Photopolymerization-based signal amplification: mechanistic characterization and practical implementation
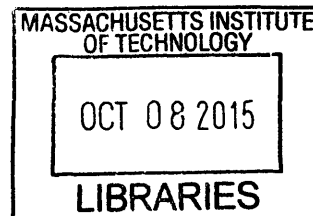
by

Kaja Kaastrup

B.S. Chemical Engineering
University of California, Berkeley, 2009

M.S. Chemical Engineering Practice
Massachusetts Institute of Technology, 2013

Submitted to the Department of Chemical Engineering in partial fulfillment of the requirements for the degree of

Doctor of Philosophy in Chemical Engineering

at the

MASSACHUSETTS INSTITUTE OF TECHNOLOGY

September 2015

Signature of Author: **Signature redacted**

Department of Chemical Engineering
July 15, 2015

Certified by: **Signature redacted**

Hadley D. Sikes
Assistant Professor of Chemical Engineering
Thesis Supervisor

Accepted by: **Signature redacted**

Richard D. Braatz
Professor of Chemical Engineering
Chairman, Committee for Graduate Students

Photopolymerization-based signal amplification: mechanistic characterization and practical implementation

by

Kaja Kaastrup

Submitted to the Department of Chemical Engineering on July 15, 2015 in Partial Fulfillment of the Requirements for the Degree of Doctor of Philosophy in Chemical Engineering

Abstract

Polymerization-based signal amplification is an approach to biosensing that leverages the amplification inherent to radical polymerization to enhance signal associated with molecular recognition. This versatile technique has been implemented with a number of radical polymerization chemistries, including atom-transfer radical polymerization (ATRP), photopolymerization, reversible addition-fragmentation chain transfer polymerization (RAFT), and enzyme-mediated redox polymerization. This thesis focuses on the development of photopolymerization-based signal amplification (PBA) as a platform technology for use at the point-of-care. We sought to build a mechanistic understanding of the system, specifically examining the effects of non-ideal binding reactions and oxygen.

One of the greatest barriers to wider implementation of polymerization-based signal amplification is the susceptibility of radical polymerization reactions to oxygen inhibition. Oxygen reacts with initiating and propagating radicals to form peroxy radicals that are unreactive towards propagation, and thus have the effect of terminating the reaction. Chapter 2 describes the development of an air-tolerant monomer solution that allows interfacial photopolymerization reactions to proceed under ambient conditions in as little as 35 seconds where previous implementations of PBA required inert gas purging to remove oxygen and reaction times of 20 minutes or longer. We showed that the inclusion of submicromolar concentrations of eosin, the photoinitiator, in the monomer solution mitigated the effects of oxygen. The ability to perform these reactions under ambient conditions increases their clinical utility by simplifying the procedure and by eliminating purging gases that might be detrimental in some biological applications, specifically those involving cells.

Intrigued by eosin's ability to overcome over 1000-fold excess of oxygen, we performed spectroscopic measurements in order to elucidate the mechanisms underlying eosin's resistance towards oxygen inhibition. A dual-monitoring system for measuring eosin consumption and monomer conversion was used to corroborate the hypothesized regeneration of eosin in the presence of oxygen (Chapter 3). This required the development of a method for analyzing absorbance data for polymerizing hydrogels. We further examined the photoactivation kinetics of the eosin/tertiary amine system and the effect of oxygen using absorbance spectroscopy and kinetic modeling (Chapter 4). The spectroscopic investigation revealed that, in addition to the previously postulated reactions in which eosin is regenerated by oxygen, additional reactions between oxygen and eosin in its triplet state and semireduced form occur and must be taken into account. The formation and consumption of the semireduced species informed the construction of a kinetic model, for which the importance of considering the reaction between triplet state eosin and the tertiary amine as two separate steps was clearly demonstrated.

Transitioning away from an examination of the amplification chemistry, we next considered the molecular recognition event, exploring the concept of the amplification threshold by investigating the impact of the binding affinity of the molecular recognition event on the limit of detection (Chapter 5). We showed that improvements in binding affinity enhance detection sensitivity. A mass action kinetics based model was used to accurately predict experimental findings and identify the key parameters for predicting the performance of PBA reactions: surface capture probe density, incubation time, concentration and binding affinity of the target molecule.

We evaluated the commonly proposed strategy of developing polymeric macrophotoinitiators for improving the sensitivity of photopolymerization-based signal amplification reactions (Chapter 6). Building on earlier work, in which solubility limits were encountered coupling eosin and neutravidin to a poly (acrylic acid-co-acrylamide) backbone, we synthesized a more water-soluble polymeric macrophotoinitiator based on a generation 7 poly (amidoamine) dendrimer scaffold. Although the solubility was improved, a new quenching limitation was identified, demonstrating the complexity of designing polymeric macrophotoinitiators that incorporate eosin as the photoinitiator. In lieu of viable photoinitiator alternatives to eosin, we concluded that future efforts to design polymeric macrophotoinitiators should include features that increase the distance between eosin molecules.

We used photopolymerization-based signal amplification to selectively encapsulate a target population of cells in a co-culture (Chapter 7). PBA allows for the selective growth of an immunoprotective hydrogel only at the surfaces of the labeled cells, even in closely contacted cell aggregates. The hydrogel protects the cells against subsequent lysis, allowing for nucleic acid extraction from the unlabeled cells without the need for cell sorting.

Finally, we consider the vast, unexplored parameter space for photopolymerization-based signal amplification, surveying alternative photoinitiation chemistries, new approaches to signal interpretation, and future applications.

Thesis Supervisor: Hadley D. Sikes
Title: Assistant Professor of Chemical Engineering

Table of Contents

List of Figures

List of Tables

1 Introduction

1.1 Motivation

The diagnosis of disease at the point-of-care is significantly enhanced by access to reliable and sensitive sensing tools. Techniques for amplifying signal are particularly valuable for applications for which low limits of detection are required. Radical polymerization has been shown to be a viable amplification technique, but barriers to implementation at the point-of-care persist.

1.2 Biosensors and amplification in sensing

Biosensors are molecular sensors that couple biological recognition events with some form of signal transduction. The basic elements of the biological recognition event are consistent across different platforms: a capture molecule, such as a nucleic acid sequence or protein, is used to specifically bind a target analyte. In some cases, this interaction is transduced directly into a signal that can be monitored in real time (Figure 1-1A). This is true for many of the biosensors employing Surface Plasmon Resonance (SPR), in which binding at an interface changes the Refractive Index and consequently the incident resonant angle at which surface plasmons are excited by plane polarized light.[1] In other cases, following capture of the target analyte by the capture molecule, a second molecule specific to the target and to which a label has been attached is introduced (Figure 1-1B). Fluorophores and gold nanoparticles are commonly used labels and can be measured directly with fluorescence scanners and absorbance spectrometers, respectively. Alternatively, the label can serve as the basis of amplification (Figure 1-1C). The enzyme-linked immunosorbent assay (ELISA) employs an enzyme as the label; following the binding steps, a substrate is introduced that the enzyme converts to a colored, fluorescent, or electrochemiluminescent product. Amplification occurs as a result of the ability of one molecule of enzyme to catalytically convert many molecules of substrate to product. Gold nanoparticles and silver salt solutions can also be used for amplification; the silver coats the gold surfaces, catalyzing the deposition of additional silver.
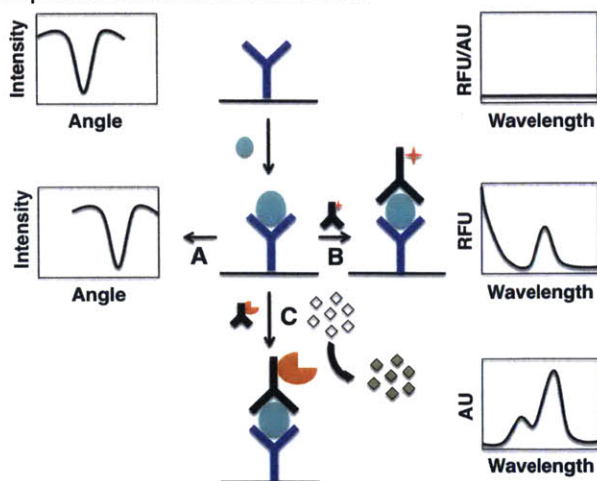
Figure 1-1. Biosensing formats depicted for antigen-antibody recognition. A) Binding of the target antigen to a capture antibody immobilized on the surface is transduced directly (e.g. surface plasmon resonance). B) A second antibody conjugated to a label (e.g. fluorophore) binds to the target antigen, producing a signal. C) The label conjugated to the second antibody serves as the basis for amplification, converting a substrate into a detectable product that can be quantitatively measured using absorbance (as shown) or fluorescence spectroscopy.

1.3 Development of photopolymerization-based signal amplification

In the last decade, polymerization-based signal amplification has emerged as a versatile and adaptable biosensing tool. It presents an alternative to commonly used amplification techniques such as ELISA. In polymerization-based signal amplification, a radical polymerization reaction amplifies the signal from a molecular recognition event. Typically, initiating molecules are conjugated to a protein or DNA probe that specifically recognizes surface-tethered proteins or DNA. This allows for the localization of the reaction to only those regions where the initiating molecule has been immobilized as a function of molecular recognition events (Figure 1-2). Amplification is inherent to radical polymerization; in response to heat, light, or catalytic activation, each initiator molecule sets off a series of propagation events that result in the conversion of many molecules of monomer to a polymer. Polymerization-based amplification has been implemented with a number of different radical polymerization chemistries, including atom-transfer radical polymerization (ATRP), photopolymerization, reversible addition-fragmentation chain transfer polymerization (RAFT), and enzyme-mediated redox polymerization. ATRP based methods have been reviewed recently[2] and photopolymerization as a biosensing tool has been discussed, although not comprehensively;[3,4] here, we consider the development of photopolymerization-based signal amplification (PBA), presenting recent advances before discussing the relative merits of the radical polymerization chemistries used for polymerization-based signal amplification in a later section.
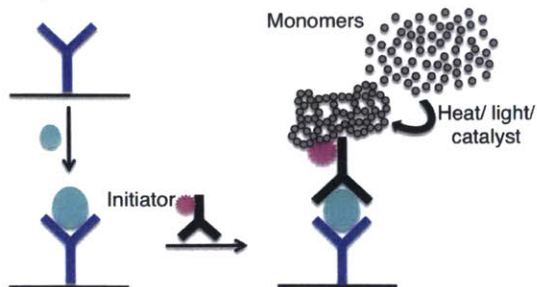
Figure 1-2. Polymerization-based signal amplification for antigen-antibody recognition. Following antigen binding to an immobilized capture antibody, a second initiator-conjugated antibody is introduced. This second antibody links polymer formation with capture of the target antigen. Polymerization occurs upon the addition of a solution of monomers and initiator activation in the form of heat, light, or a catalyst.

1.3.1 Proof of concept

Successful implementation of photopolymerization-based signal amplification hinges on the ability to localize photoinitiators at the site of molecular recognition. This is accomplished through the use of macrophotoinitiators. Macrophotoinitiator is a term that has been adopted to describe a dual-functional molecule comprised of photoinitiators and an affinity ligand. In their simplest form, these molecules consist of proteins to which the photoinitiator has been directly conjugated.

In the first demonstration of photopolymerization-based signal amplification, Sikes et al. prepared a macrophotoinitiator by coupling a protein for molecular recognition and UV activated type I initiators (Irgacure 2959) to poly (acrylic acid co-acrylamide). In this case, the molecular recognition event was between neutravidin coupled to the polymer backbone and biotinylated oligonucleotdies covalently bound to a thin-film biosensor surface.[5] The high affinity ($K_d \sim 10^{-15}$ M) biotin-neutravidin (or alternatively, streptavidin) interaction has been employed extensively in PBA;[5–12] the selection of these binding partners ensures that the amplification (or signal transduction) step rather than the molecular recognition event limits the final readout by maximizing the number of complexes formed and, consequently, the initiator surface density. The specificity of the binding interaction between biotin and

streptavidin results in the localization of initiators at the surface. A second reason for selecting these binding partners is to reduce costs during the development phase for a new technology by avoiding antibodies, which are frequently cost prohibitive and may be more sensitive to storage conditions and less reliable.

In photoinitiated polymerizations, light absorption produces radicals through the excitation of a photoinitiator that then either undergoes bond cleavage to produce radicals (type I) or interacts with a second component through an energy transfer or redox reaction to yield radicals (type II). These radicals then go on to react with carbon-carbon double bonds of monomers in solution, initiating propagation. Irgacure 2959 is a type I UV-activated photoinitiator that, upon irradiation with UV light, is cleaved into substituent radical species (Figure 1-3). The benzoyl radical initiates polymerization.
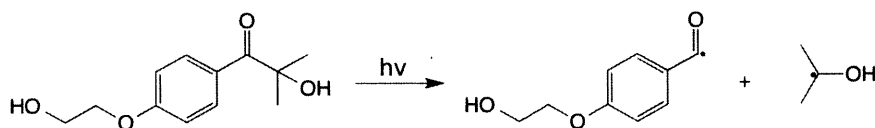
Figure 1-3. UV-activated cleavage of Irgacure 2959.

In this first implementation, the monomer solution consisted of 97 wt% hydroxyethylacrylate and 3 wt% ethyleneglycol dimethacrylate. A 10 minute dose of 5 mW/cm^2, 365 nm light produced readily visible polymer films, obviating the need for the optical properties of the biosensor surface. Though not quantitative, photopolymerization-based signal amplification in its original incarnation yielded a reliable yes/no response for as few as 1000 molecular recognition events or ~0.005 biotinylated oligonucleotides/μm^2 (based on a 600 μm diameter spot).

In an effort to expand the applicability of the approach to clinically-relevant antigen detection, Sikes et al. subtyped influenza viruses from crude lysates.[13] This study was the first instance in which specific protein detection from complex media was demonstrated using any of the published initiation chemistries for polymerization-based signal amplification. Sikes et al. replaced the enzymatic amplification used in a commercially available flu test with photopolymerization-based signal amplification. The authors used the same thin film biosensor and UV-activated macrophotoinitiator as in the proof-of-concept study,[5] with the exception that the neutravidin was replaced by monoclonal flu antibodies, and showed that photopolymerization-based signal amplification achieved the same limit of detection as enzyme-based amplification. The assay was designed so that each test contained a built-in positive control (the innermost circle where flu nucleoproteins were covalently bound to the surface as shown in Figure 1-4). Surrounding the control was the test region where subtype specific monoclonal antibodies were bound, while the remainder of the area served as a negative control. In the absence of virus, polymer was only observed within the positive control spots (Figure 1-4A). The results when either Flu A or B were present are shown in Figure 1-4B and C, respectively. The unambiguous response is one of the strengths of PBA relative to enzymatic amplification.

Figure 1-4. Subtyping influenza viruses with photopolymerization-based signal amplification. (a) No virus detected so polymer is only observed within the positive control spots. (b) Influenza A detected. (c) Influenza B detected. Reprinted with permission from Sikes et al., *Lab on a Chip*, 2009, 9, 633-656. Copyright © 2009, The Royal Society of Chemistry.[13]

1.3.2 Extension to visible light activation

While the initial development work was conducted using a photoinitiator that undergoes bond cleavage in response to UV light activation, an alternative two-component (type II) system has since gained widespread implementation. Building on work in which eosin, a xanthene dye, was covalently bound to a surface for interfacial hydrogel polymerization,[14] photopolymerization-based signal amplification was extended to visible light photoinitiators.[6] Eosin is a photoinitiator that following excitation with green light can undergo a transition to its triplet state, in which it is reactive towards reducing agents such as tertiary amines (Figure 1-5). An electron transfer from the tertiary amine to eosin in its triplet excited state is followed by a proton transfer that generates two neutral radicals, of which the tertiary amine radical initiates polymerization by reacting with a carbon-carbon double bond of one of the monomers in solution. The neutral eosin radical (the semiquinone form of eosin) is posited to participate in primary radical termination reactions,[15] but is not expected to function efficiently as an initiator due to steric hindrance and electronic delocalization.[16]
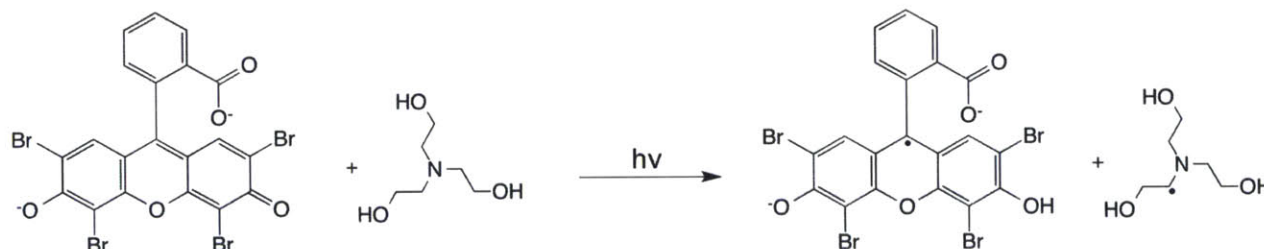
Figure 1-5. Visible-light activated energy transfer between eosin and triethanolamine. Eosin is excited by green light to its singlet state, from which it undergoes intersystem crossing to its triplet state. In its triplet state, it is reduced by triethanolamine. A subsequent proton transfer generates two neutral radials. The triethanolamine radical initiates polymerization.

Replacing Irgacure 2959 with eosin simplified the macrophotoinitiator synthesis; a commercially available isothiocyanate modified eosin was reacted with the lysine residues of streptavidin (Figure 1-6A), resulting in an average of 2.3 eosin per protein. The preparation of the Irgacure 2959 macrophotoinitiator required EDC/NHS activation of the carboxyl groups of the poly (acrylic acid co-acrylamide) prior to reaction with Irgacure 2959 and neutravidin to form ester and amide linkages, respectively (Figure 1-6B). Irgacure 2959's low molar absorptivity meant that it was necessary to conjugate 140 Irgacure 2959 initiators per polymer. Direct conjugation of 4 Irgacure 2959 molecules to neutravidin did not yield any polymer.
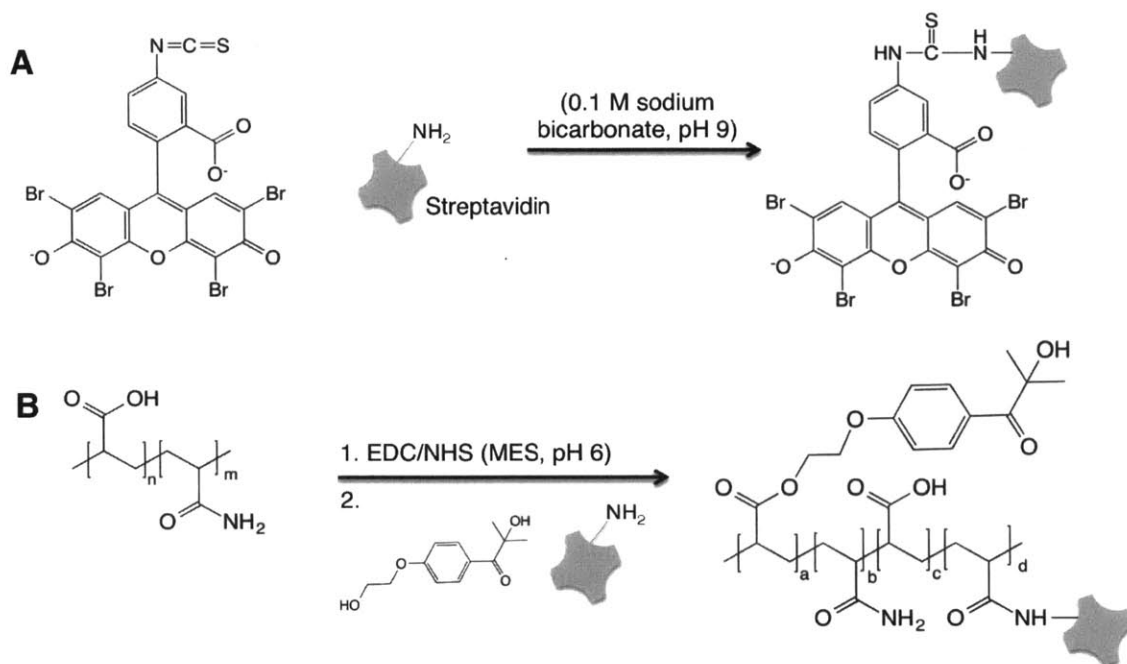
Figure 1-6. Macrophotoinitiator synthesis. A) Isothiocyanate-modified eosin reacts with the lysine groups of streptavidin. B) The carboxyl groups of poly (acrylic acid co-acrylamide) are activated by EDC/NHS for reaction with Irgacure 2959 and streptavidin (or neutravidin) to form ester and amide linkages, respectively.

In addition, the assay cost was reduced by replacing the thin-film biosensor surfaces used originally with commercially available amino and aldehyde modified glass. Previous attempts to perform the polymerization on glass using the Irgacure macrophotoinitiators yielded inconsistent results. The new initiator was also compatible with a less toxic, aqueous monomer solution, consisting of a tertiary amine coinitiator (typically methyldiethanolamine (MDEA) or trithanolamine (TEA)) and polyethyleneglycol diacrylate (PEGDA) and 1-vinyl-2-pyrrolidone (VP).

Streptavidin-eosin has become the most extensively used macrophotoinitiator, permitting the detection of biotinylated DNA hybrids[17] and antibodies.[18,19] Eosin has also been directly conjugated to antibodies without any apparent loss of protein activity.[20,21]

Johnson et al. explored an alternative method for immobilizing eosin at the site of molecular recognition, essentially constructing a macrophotoinitiator in situ for the detection of single base mutations associated with cancer. In this case, surface-bound, synthetic oligonucleotide capture probes hybridized target sequences; these target sequences were designed to emulate human genomic regions with cancer-associated point mutations. Following hybridization of a nucleic acid target with the probe, they used primer extension labeling with eosin labeled 2'-deoxyuridine-5'-triphosphate (dUTP) to facilitate the covalent incorporation of the initiator into surface-immobilized DNA sequences (Figure 1-7).[22] In primer extension labeling, deoxynucleotides are coupled to the DNA hybrids by a DNA polymerase enzyme. Primer extension labeling with photopolymerization-based signal amplification was previously demonstrated using biotinylated deoxynucleotides (dNTPs),[17] but the procedure developed by Johnson et al. reduced the number of required binding steps by eliminating the incubation with streptavidin-eosin. Direct conjugation of eosin to the dUTP did not increase the initiator density on the surface (compare Table 1 of [17] and Fig. 3 of [22]) relative to primer extension labeling with biotinylated dNTPs followed by streptavidin-eosin binding.

17
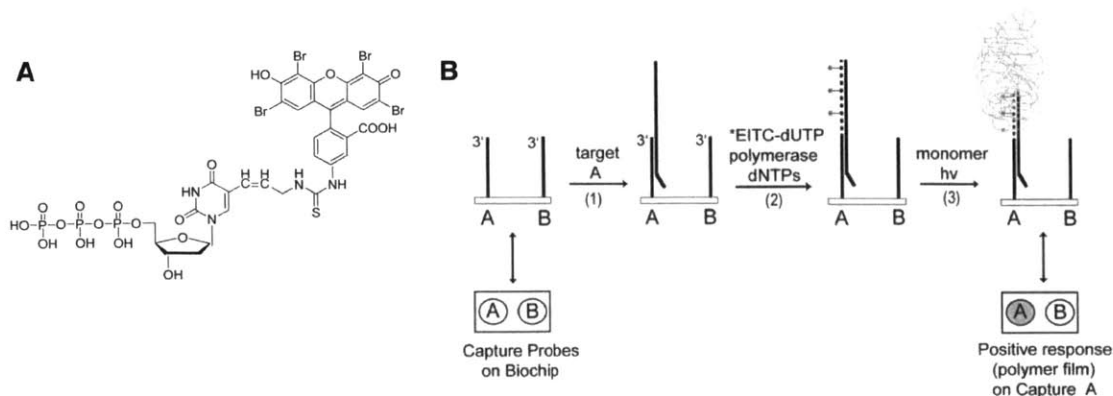
Figure 1-7. Macrophotoinitiator synthesis in situ. A) Structure of eosin-modified 2'-deoxyuridine-5'-triphosphate. B) Scheme for detection of nucleic acid hybridization. Capture probe A hybridizes the complementary sequence, target A. Primer extension labeling is used to couple the photoinitiator, eosin, to the hybridized DNA. This is followed by photopolymerization-based signal amplificiation, indicating that target A has been detected. Reprinted with permission from Johnson et al., *Biomacromolecules*, 2010, 11, 1133-1138. Copyright © 2010, American Chemical Society.[22]

1.3.3   Light activation and the tunable threshold

One of the central features of photopolymerization-based signal amplification is the ability to tune the intensity and duration of the irradiation in order to eliminate signal from nonspecific binding and thereby limit the occurrence of false positives. As depicted schematically in Figure 1-8, PBA is a threshold process; a minimum surface density of initiators is required for polymerization. Shorter reaction times and lower light intensities can be used to shift the amplification threshold, so that polymerization is only observed for initiator densities above the level of nonspecific binding.
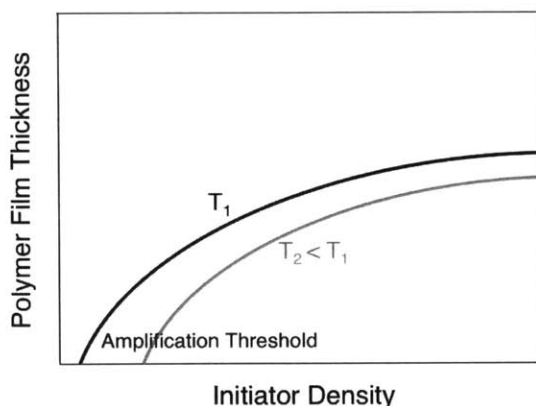
Figure 1-8. Amplification threshold. A minimum initiator surface density is required to initiate polymerization. Decreasing the reaction time increases the minimum initiator surface density, shifting the amplification threshold to the right.

Light source selection is primarily guided by the absorbance spectrum of the photoinitiator (Figure 1-9), while the duration of the irradiation is generally selected as the time beyond which there are no further gains in sensitivity. For Irgacure 2959 initiated polymerizations, high intensity UV lamps were used to produce 10 minute doses of 5 mW/cm^2 light centered around 365 nm.[5,13] With the shift to eosin-initiated reactions, high pressure mercury lamps with filters to restrict the range of irradiation wavelengths to 495-650 nm were used to deliver 20-30 minute doses of 10-40 mW/cm^2 light. The

advent of inexpensive light emitting diodes (LEDs) has permitted a transition from high pressure mercury lamps to high intensity LEDs. In addition to being less expensive than mercury lamps, LEDs have the advantage of relatively narrow bandwidths (5-20 nm).[16] This means that the full intensity of the light source is centered around the maximum absorbance wavelength of the initiator. Relative to mercury lamps, LEDs are also more efficient, both in terms of cost and energy usage, safer, and more environmentally friendly.[16]
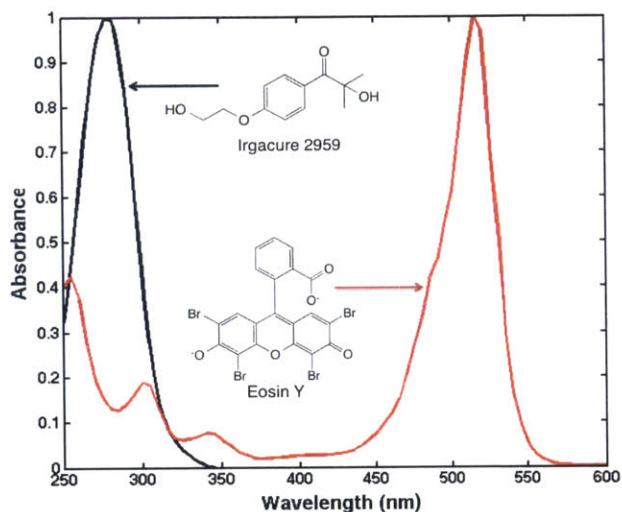
Figure 1-9. Absorbance spectra for Irgacure 2959 and Eosin.

1.3.4   Monomer composition

The criteria for monomer selection have evolved since the first demonstration of PBA. Initially, monomer compatibility with the initiating system and the formation of a polymer film were sufficient. As efforts to use PBA quantitatively and translate the technology to the point-of-care have intensified, the criteria have become more stringent.

For the Irgacure 2959 initiated system, the monomer solution consisted of 97 wt% hydroxyethylacrylate and 3 wt% ethyleneglycol dimethacrylate (Figure 1-10). [5,13] These monomers when used in conjunction with the Irgacure macrophotoinitiator provided exceptional sensitivity, generating polymers in response to 0.005 binding events/μm^2. However, this approach, in addition to requiring the use of toxic, nonaqueous monomers, produced mechanically unstable polymer films, precluding further analysis or processing steps.

With the transition to the eosin-initiated system, it became possible to employ an aqueous monomer solution consisting of 225 mM methyldiethanolamine (MDEA), 435 mM polyethyleneglycol diacrylate (PEGDA), and 37 mM 1-vinyl-2-pyrrolidone (VP) (Figure 1-10).[6] PEGDA was included as a cross-linking agent and vinyl-2-pyrrolidone (VP) as an accelerant.[23,24] MDEA has been used interchangeably with triethanolamine (TEA), a more water soluble tertiary amine. This monomer formulation, also used by Kizilel et al.,[14] was based on work from the Hubbell Group, in which porcine islets were encapsulated in hydrogels through the nonspecific adsorption of eosin onto the islet surfaces.[25–27] A critical advantage of this chemistry is that the attachment of the polymer to the surface is robust, a feature attributed to termination reactions involving the surface immobilized eosin molecules.[14] This format was shown to be approximately 1000x less sensitive compared with the UV light initiated system. However, the advantages, including a simplification of the macrophotoinitiator synthesis, use of less toxic, aqueous

monomer solutions, and compatibility with visible light and glass surfaces, outweigh the cost in sensitivity.

In an effort to optimize the composition of the monomer solution and improve the sensitivity of the signal amplification reaction, Avens et al. tested different formulations of MDEA and VP with either PEGDA or acrylamide/bisacrylamide (Figure 1-10). They compared polymer film thickness, conversion as measured by real-time IR spectroscopy, and the lowest initiator density for which polymerization was observed (or sensitivity).[28] For PBA, thick polymer films are desired as they are more easily visualized. Thicker polymer films correlate with higher conversion. IR spectroscopy is used to monitor the progression of polymerization reactions by measuring absorption from the methacrylate groups of the monomer. Total monomer conversion is taken as the fractional change in the initial area of the absorption peak of the methacrylate groups in the near IR.
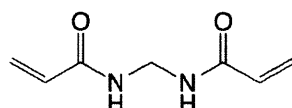
Figure 1-10. Monomers for photopolymerization-based signal amplification.

Varying the monomer composition, Avens et al. found that increasing the PEGDA concentration resulted in thicker films, but reduced sensitivity, likely a consequence of the reduced diffusivity of the amine coinitiator in the much more viscous monomer solution. They also tested the hypothesis that streptavidin rearranges in nonaqueous monomer formulations, causing eosin to become sterically inaccessible. Replacing eosin with a streptavidin-eosin conjugate in a bulk monomer solution completely inhibited the polymerization in the nonaqueous formulation. Although biocompatibility is an important consideration, it is notable that the Irgacure system, for which a nonaqueous monomer solution was used, had exceptional sensitivity.

The tertiary amine coinitiator (MDEA or TEA) also functions as a chain transfer agent, terminating propagating polymer chains and initiating the formation of new ones. This enhances film growth at an optimal concentration but can lead to increased termination and reduced sensitivity if the concentration is too high.[6] Notably, when VP was removed from the monomer solution, the sensitivity decreased slightly, while increasing the VP concentration improved the sensitivity, reducing the threshold eosin surface density. Compared with the PEGDA-based formulation, the acrylamide-based monomer (40 wt% acrylamide) produced films that were at least 4x thicker and improved the sensitivity even further, reducing the threshold surface density to 2.8 eosin/μm^2.[6] This was attributed to acrylamide's lower

molecular weight and the lower crosslinking content (bisacrylamide) of this monomer formulation promoting faster surface-mediated polymerization by allowing MDEA to more readily diffuse.[6]

In spite of the advantages of using acrylamide, aqueous, PEGDA-based monomer formulations have ultimately been favored for their lower toxicity. In addition, the PEGDA-based monomer formulation was found to perform better for applications requiring high spatial resolution, such as immunostaining; the smaller average mesh size of the polymers formed using PEGDA allows for the entrapment of a higher density of labeling agents such as nanoparticles in a thinner film.[8] However, it is possible that smaller mesh sizes could be achieved by increasing the bisacrylamide content beyond 2% as the increase from 1-2% resulted in a 60% smaller mesh. Another critical parameter that impacts mesh size is the monomer molecular weight. Higher molecular weight PEGDA produces hydrogels with larger mesh sizes.[27] A high degree of tunability is available through crosslinker content and molecular weight.

1.3.5   Signal interpretation
The polymer films generated using PBA are generally visible with the unaided eye. Profilometry and fluorescence have been explored as modalities for enabling quantitation. This section will include a brief discussion of each readout method.

Visible
The first studies using the Irgacure macrophotoinitiator and nonaqueous monomer formulation yielded reliable yes/no responses, requiring no instrumentation to detect polymer formation.[5,13] This was shown in Figure 1-4 for influenza subtyping with PBA.

Profilometry
The transition to the two-component system with eosin and a tertiary amine coinitiator enabled post-processing steps such as profilometry to measure the thickness of the polymer films.[6] The thickness of the hydrogels polymerized following a 20 minute dose of 8 mW/cm^2, 400-500 nm light ranged between 110 and 160 nm for 100 binding events/μm^2. A quantitative relationship between polymer film thickness and probe density was later established by Hansen et al.; profilometry revealed a dynamic range between 60 and 4,700 biotin/μm^2 with saturation beyond 8,300 biotin/μm^2 and a maximum polymer thickness of 250 nm.[7] The authors also showed how competitive binding between unconjugated streptavidin and streptavidin-eosin may be used to tune and extend the dynamic region.

Fluorescence
As an alternative to the expensive methods available for measuring the thickness of nanometer scale films, strategies for polymerizing fluorescent films were tested to enable quantitation through fluorescence. Fluorescent moieties were incorporated into the monomer solution to generate an amplified, fluorescent signal that could be directly correlated with the surface probe density.[7,18] Polymer films were made fluorescent through either the inclusion of fluorescent nanoparticles (initially, 20 nm Nile Red Fluospheres) in the monomer solution or the post-polymerization modification of remaining pendant double bonds with dithiothreitol for reaction with methacryloxyethyl thiocarbamoyl rhodamine B, a fluorescent dye.[7] The latter method proved insufficient for the purposes of quantification, while the addition of fluorescent nanoparticles into the PEGDA-based monomer solution reduced the polymerization kinetics and the final conversion, a possible indication of light attenuation. Hansen et al. also showed that at longer reaction times (>40 minutes), the Nile Red Fluospheres were capable of initiating polymerization. The enhanced sensitivity and thicker polymer films achieved using an acrylamide-based formulation[28] mitigated some of the detrimental effects of incorporating the fluorescent nanoparticles into the PEGDA-based monomer formulation; their inclusion in an acrylamide-

based monomer solution allowed for an improvement in sensitivity relative to direct fluorescence labeling.[18]

Using an acrylamide formulation to which yellow/green nanoparticles had been added, Avens & Bowman compared fluorescent polymerization-based signal amplification (FPBA) with direct fluorescence labeling using either a streptavidin-fluorescein conjugate or streptavidin-functionalized yellow/green nanoparticles on antibody microarrays. They showed that FPBA reduced the limit of detection by more than two orders of magnitude (to $0.16 + 0.01$ biotinylated antibody/μm^2) relative to streptavidin-fluorescein, while no positive signal was obtained using the streptavidin-functionalized nanoparticles.[18] In addition, FPBA had a wide dynamic range of 4 orders of magnitude compared with a dynamic range spanning only 2 orders of magnitude for streptavidin-fluorescein labeling. As in the earlier study, there were indications of light attenuation by the nanoparticles. The inclusion of nanoparticles resulted in thinner films, but did not compromise sensitivity. Monomers covalently attached to fluorophores were considered as an alternative strategy for creating fluorescent polymer films; however, a considerable amount of photobleaching and nonspecific polymerization were encountered.

Avens et al. demonstrated FPBA as a nonenzymatic signal amplification technique for immunostaining.[19] Eosin had previously been nonspecifically adsorbed onto the surfaces of porcine islets for the interfacial polymerization of immunoprotective hydrogels.[26] Although green light has been shown to both stimulate and suppress cell growth when delivered at high intensities over the course of several days,[29] it has been used for photopolymerizations involving mammalian cells with no adverse side effects.[26] Using FPBA, the fluorescent signal generated is comparable to tyramide signal amplification (TSA) with the advantage of not being affected by endogenous peroxidase enzymes. FPBA also appears to give better signal localization than TSA. The authors successfully labeled nuclear pore complex proteins, vimentin, and von Willebrand factor in fixed and permeabilized human endothelial colony-forming cells, also showing multicolor immunostaining of multiple antigens through sequential polymerizations using differently colored nanoparticles (Figure 1-11). In the case of the nuclear pore complex staining, FPBA was shown to reduce nonspecific signal by 5.5 fold relative to TSA.
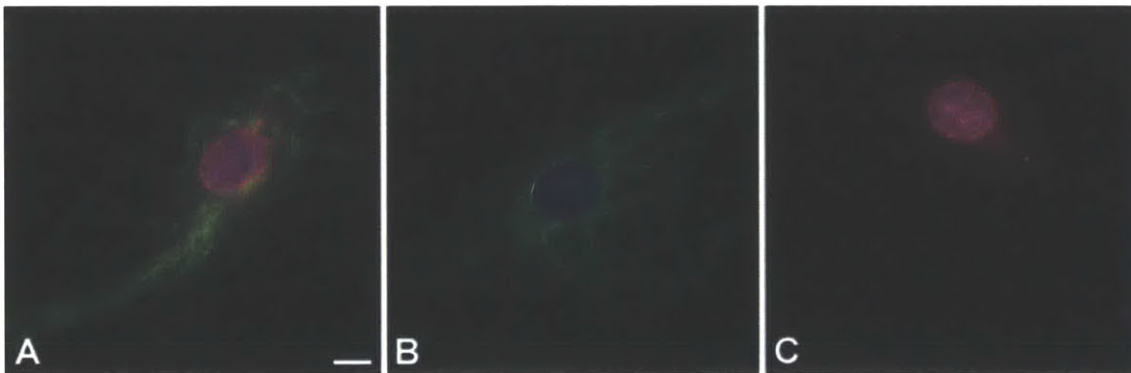
Figure 1-11. Immunostaining with sequential rounds of fluorescent polymerization-based signal amplification (FPBA). A) Nuclear pore complex proteins in fixed and permeabilized human endothelial cells were labeled using Nile red nanoparticles; vimentin was labeled in a second round of FPBA using yellow/green nanoparticles. B) Negative control in which the antibody against the nuclear pore complex protein was omitted. As a result, only the vimentin was polymerized. C) Negative control in which the vimentin antibody was omitted and only the nuclear pore complex protein was polymerized. No polymer was produced in the second round. The cell nucleus was also stained with 4', 6-diamido-2-phenylindole dihydrochloride (DAPI; blue). The scale bar is 10 microns. Reprinted with permission from Avens et al., *Journal of Histochemistry and Cytochemistry*, 2011, 59, 76-87. Copyright © 2011, Avens et al.[19]

Colorimetric

Although its quantitative potential is more limited relative to profilometry and fluorescence, colorimetric detection is preferred, particularly in point-of-care settings, as it does not require expensive equipment for the detection of polymer films. Kuck & Taylor introduced an additional assay step in which the polymer film is stained with a solution of eosin Y for the purposes of visualization, showing the potential of photopolymerizaton-based signal amplification as an inexpensive colorimetric assay and eliminating the need for profilometers or fluorescence scanners and microscopes (Figure 1-12). [20] As a stain, eosin Y outperforms hematoxylin, which requires a longer staining step and yields lower contrast. [17] Using eosin as a stain, Lee et al. showed that colorimetric intensity correlates with polymer film thickness. [9]
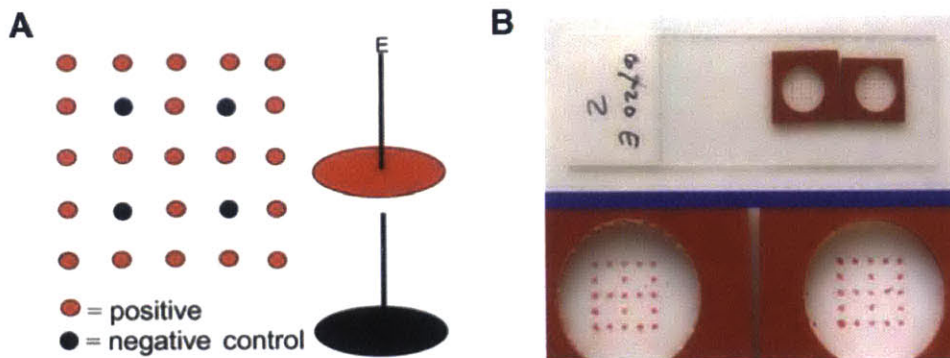
Figure 1-12. Colorimetric detection. A) Positive control eosin-labeled oligonucleotides were printed in the indicated pattern on an aldehyde functionalized glass slide. Unlabeled oligonucleotides were printed as a negative control. B) The resulting polymers were stained with an Eosin Y solution. Reprinted with permission from Kuck and Taylor, *BioTechniques*, 2008, 45, 179-186. Copyright © 2008, BioTechniques.[20]
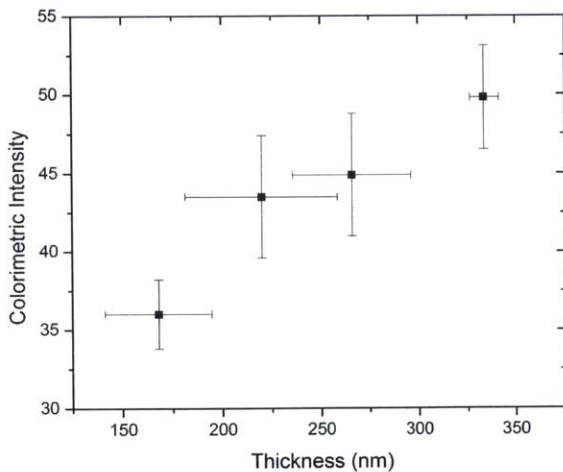
Figure 1-13. Colorimetric intensity correlates with polymer film thickness. Average colorimetric intensities were calculated from digital images of polymerized spots. The thickness of each spot was measured using profilometry. Data from Lee et al. *Biomacromolecules*, 2012, 13, 1136-1143.[9]

The immunostaining technique first demonstrated by Avens et al. using FPBA was further developed to allow for colorimetric labeling of cells, termed "Polymer Dye Labeling" (PDL).[30] Here, eosin Y was replaced as a stain with Evans Blue as eosin nonspecifically stains cytoplasmic proteins and collagen. Like FBPA, PDL has sufficient resolution to enable the identification of protein expression spatial patterns in

cells. The authors showed that the signal is stable for over 200 days (Figure 1-14). Both PDL and FPBA are reported to offer better site specificity than competing enzymatic methods. PDL was originally developed as an alternative to FPBA that is compatible with mounting media, although the authors showed that the samples fared well under dry storage as well. For PDL, the concentration of the tertiary amine was reduced by a factor of 10 relative to the FPBA monomer formulation, with TEA being used in place of MDEA. This optimized formulation may limit adverse effects from chain transfer reactions. The authors found that the dynamic range observed when the polymer thickness was measured using profilometry was lost upon staining, although, in accordance with the results of Lee et al., the colorimetric intensity of the staining loosely correlated with polymer thickness.
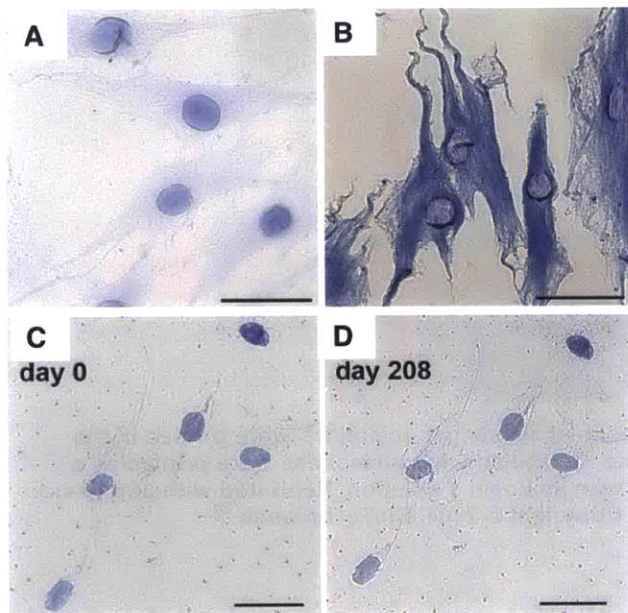
Figure 1-14. Polymer dye labeling. Evans blue-stained polymers localized in response to labeling with antibodies against nuclear pore complex (A) and vimentin (B). Polymer dye labeling of nuclear pore complex immediately following staining (C) and 208 days later (D). Reprinted with permission from Lilly et al., *PLoS ONE*, 2014, 9, e115630. Copyright © 2014, Lilly et al.[30]

1.3.6 Polymeric macrophotoinitiators

A powerful feature of this technique is the ability to shift the amplification threshold by changing the reaction time. Reducing the reaction time has the effect of shifting the amplification threshold to higher initiator densities, which has important implications for eliminating signal from nonspecifically bound molecules. However, increasing the reaction time will only improve sensitivity up to a point, beyond which no gains in sensitivity are achieved.

In order to achieve sensitivities comparable to more advanced fluorescence techniques, it is necessary to increase the number of photoinitiators per binding event. Efforts to enhance the sensitivity of photopolymerization-based amplification have thus focused on the development of polymeric macrophotoinitiators. As discussed, a polymeric macrophotoinitiator, consisting of 140 UV initiators and Neutravidin conjugated to a poly (acrylic acid co-acrylamide) backbone, was used in the first demonstration of PBA[5] and for subtyping influenza viruses from crude lysates.[13] The poly (acrylic acid co-acrylamide) backbone has also been used as the scaffold for a macroinitiator for AGET (activators generated by electron transfer) ATRP, allowing for a reduction in the reaction time.[31]

Recently, eosin was conjugated to the same poly (acrylic acid co-acrylamide) backbone. [11] Eosin's poor water solubility limited the number of eosin per polymer to 15. One of the requirements for macrophotoinitiators developed for PBA is that they must be water soluble to allow for conjugation of the protein that enables molecular recognition. Lee & Sikes varied the number of eosin per polymer between 2 and 15, obtaining a non-monotonic relationship between the number of eosin per polymer and the resulting surface initiator density. Using fluorescence to quantify eosin surface densities, they showed that a linear increase in specific signal as the number of eosin per polymer was increased from 2 to 10 was followed by a decline to background levels when the number of eosin per polymer was further increased to 15. The background signal increased dramatically when the number of initiators was increased from 6 to 10. The reduction in specific signal for 15 eosin per polymer was thought to be a consequence of eosin's poor solubility both interfering with specific binding and increasing the nonspecific adsorption. Polymerization was only observed for the polymer with 10 eosin bound with a three-fold higher detection limit than typically achieved using a streptavidin-eosin conjugate with an average of three eosin per protein, a possible indication of quenching or steric effects.

The non-monotonic trend obtained for the polymeric eosin macrophotoinitiator disagreed with previous work in which Lee et al. demonstrated how the degree of polymerization increases as the number of photoinitiators per binding event is increased.[9] In this study, a more water soluble xanthene dye, fluorescein (Figure 1-15), was used in place of eosin. The number of fluorescein per neutravidin conjugated polymer was varied between 7 and 168, beyond which a solubility limit was encountered. Surface-initiated polymerization was only observed for macrophotoinitiators with 126 and 186 fluorescein molecules for surface densities exceeding 105 biotin/μm^2. The 20% difference in the number of photoinitiators per polymer resulted in a 20% difference in polymer thickness on the surface. Because the reaction requires the diffusion of initiating radicals, propagating polymer chains, and monomers, it is expected that a diffusion limit exists, beyond which increasing the number of initiators per binding event will not increase the degree of polymerization; this limit was not encountered in this work. The colorimetric intensity and thickness of the photopolymerized hydrogels are shown in Figure 1-13. It should be noted that the polymerization reactions for the polymeric eosin and fluorescein macrophotoinitiators were activated using a 400 nm LED (1 W/cm^2). The intensity of the light (1 W/cm^2) was more than 25x higher than in previous studies where a broad spectrum of light yielded a total light intensity between 10-40 mW/cm^2. It is likely that the high light intensity compensated for the non-optimal excitation wavelength.
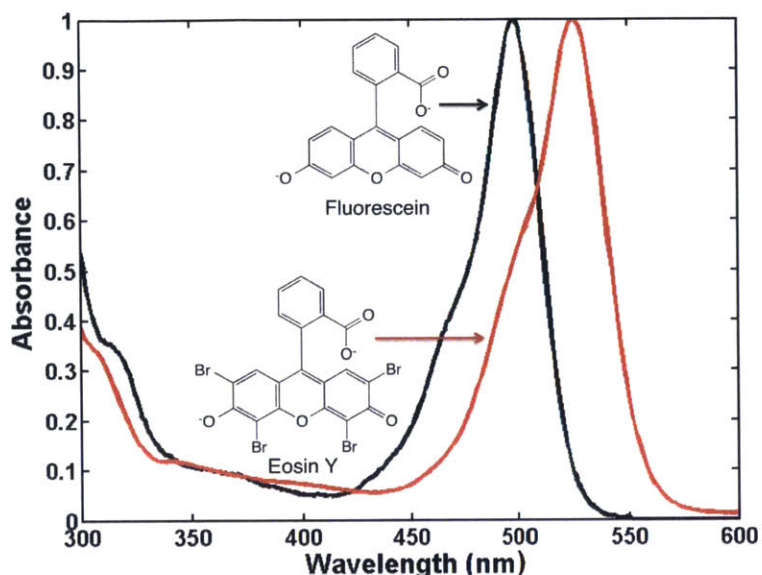
Figure 1-15. Fluorescein and Eosin Y structures and absorbance spectra.

The sensitivity achieved using fluorescein contrasts severely with the eosin-initiated system, in which 3 eosin conjugated directly to streptavidin initiate polymerization on a surface with only 15 biotin/μm^2.[10] Although fluorescein is a stronger reducing agent than eosin,[32] eosin is a more efficient photoinitiator as, due to the presence of heavy bromine atoms (Figure 1-15), it more readily undergoes intersystem crossing to the triplet state. Once in the triplet state, both fluorescein and eosin can react with a tertiary amine to form tertiary amine radicals capable of initiating the photopolymerization.[33] In a study in which the intersystem crossing quantum yields for seven xanthene dyes were measured in methanol, fluorescein was shown to have a 10-fold lower value than eosin (0.03 vs 0.32).[34] In water, the difference in intersystem crossing quantum yield increases (0.71 for eosin and 0.05 for fluorescein).[35] The difference in intersystem crossing quantum yield also explains why fluorescein was able to overcome only a 10-fold excess of inhibitor, while eosin was able to overcome a 100-fold excess in experiments exploring the cyclic regeneration of xanthene dyes as a method for overcoming oxygen inhibition.[15]

Peris et al. have also examined the efficacy of macrophotoinitiators as tools for enhancing polymer growth.[3] They compared the performance of bovine serum albumin (BSA) conjugated directly to a photoinitiator, 2- hydroxy-40-(2-hydroxyethoxy)-2-methylpropiophenone (HHMPP), with BSA and HHMPP conjugated to a 200 kDa poly(acrylic acid co-acrylamide) backbone on polycarbonate plates to which an antibody against BSA was physisorbed. They found that they were able to use 10-fold less (on a molar basis) of the polymer conjugate relative to the BSA-HHMPP conjugate to achieve polymerization. This metric for comparison differs to that traditionally used for evaluating macrophotoinitiators for PBA; typically, dilution arrays are used to determine the minimum capture probe surface density for which polymerization is achieved. Thus, it is difficult to determine whether the polymeric macrophotoinitiator developed by Peris et al. would have contributed to gains in sensitivity in biosensing assays.

1.3.7 Advances
Many of the previous studies made use of specialized surfaces and expensive equipment for detecting the formation of polymer films. As discussed, Kuck & Taylor dramatically enhanced the contrast of the visual readout by introducing an additional assay step in which the polymer film was stained with a

solution of eosin Y for the purposes of visualization. This simplification demonstrated the potential of photopolymerizaton-based signal amplification as an inexpensive colorimetric method by eliminating the need for profilometers or fluorescence scanners and microscopes.[20] Their work also provided the first demonstration of clinical samples with PBA in the context of an influenza microarray; RNA was extracted from clinical samples known to be positive for the H3N2 subtype of Influenza A for amplification by RT-PCR and subsequent digestion before hybridization on a DNA microarray with an eosin-tagged oligonucleotide label. The authors indicated that the incorporation of eosin in the PCR primer also met with success. Further advancing this technology towards implementation in point-of-care settings, the authors were able to reduce the reaction time using a PEGDA-based monomer formulation to less than 5 minutes and perform the reaction under ambient conditions, although they did not provide details explaining how this was accomplished. Kuck & Taylor also compared their results with HRP/Amplex Red amplification, replacing the eosin-tagged label with a biotinylated label for binding to a streptavidin-HRP conjugate and found that their signal amplification was 2.8x lower than the enzymatic assay and less sensitive than fluorescence by a factor of 3-4. The colorimetric assay, as described by Kuck & Taylor, has been demonstrated for the detection of S. pyogenes, which causes group A streptococcal infections, [36] and in the context of E. coli strain genotyping. [37][38]

One of the challenges with colorimetric readouts is enabling quantification. Johnson et al. showed how the thermodynamics of the binding interaction can be exploited to design an instrument-free assay capable of visual quantification of target DNA levels.[22] As shown in Figure 1-16, higher capture probe densities permit the detection of lower concentrations of target DNA in solution. The number of polymerized spots provides a quantitative estimate for the target DNA concentration in solution.
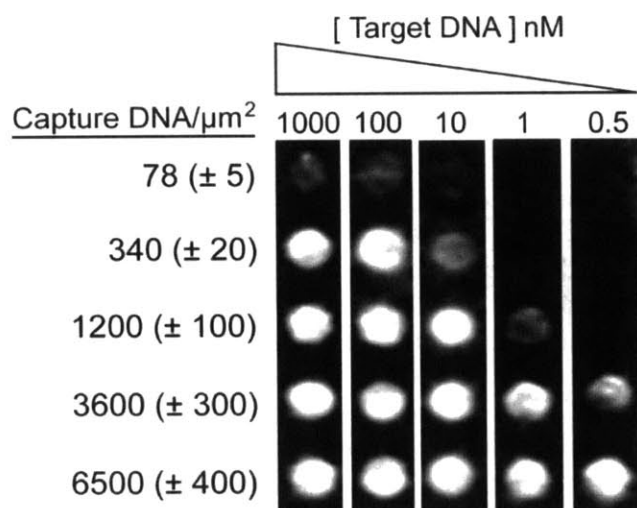
Figure 1-16. Visual quantification of target DNA solution concentrations. Biochips printed with capture probe dilution series were separately hybridized with decreasing concentrations of complementary target DNA. The polymers were stained with hematoxylin and the reverse-grayscale images were acquired with a desktop flatbed scanner. Reprinted with permission from Johnson et al., *Biomacromolecules*, 2010, 11, 1133-1138. Copyright © 2010, American Chemical Society.[22]

1.4 Comparison of polymerization-based signal amplification methods

Polymerization-based signal amplification depends on the localization of radical polymerization initiators as a function of molecular recognition events and, thus, is a fairly versatile technique as demonstrated by its implementation with other radical polymerization chemistries, including ATRP, RAFT, and enzyme-mediated redox polymerization.

A summary of the "initiators" coupled to detection probes and the corresponding molecules that initiate radical polymerization by reacting with monomers is provided in Table 1-1. As discussed previously, in the two-component initiation system used for photopolymerization-based signal amplification, eosin is attached to the surface, while the tertiary amine radical initiates polymerization (Figure 1-17A). For the enzyme-mediated method, glucose oxidase is conjugated to avidin and, thus, bound to a surface on which biotinylated antibodies are immobilized as a function of molecular recognition events.[39,40] In this case, the monomer solution contains glucose and iron. This system cleverly recasts oxygen as a participant in generating initiating radicals. After first being reduced in the process of converting β-D-glucose to δ-D-gluconolactone, glucose oxidase is regenerated following oxidation by oxygen. The oxidation reaction produces hydrogen peroxide, which is converted to hydroxyl radicals through Fenton's Chemistry. The hydroxyl radicals initiate polymerization by reacting with monomers in solution. This series of reactions is summarized in Figure 1-17B.

Table 1-1. Summary of Radical Initiator Generation Methods

Radical Generation Method	Surface immobilized molecule	Energy input	Initiating molecule
Photoactivation	Eosin	Light	Tertiary amine radical
Enzyme conversion and Fenton's chemistry	Glucose Oxidase		Hydroxyl radical
Atom transfer radical polymerization	Bromoisobutyrate		Isobutyrate radical
Reversible addition-fragmentation chain-transfer polymerization	Chain transfer agent (CMP)[1]	Heat	2-cyanoprop-2-yl radical

RAFT and ATRP are both examples of living radical polymerizations, in which bimolecular termination reactions are minimized and the lifetimes of living polymers are extended by introducing dormant states for the propagating species.[41] When ATRP is implemented for polymerization-based signal amplification, bromoisobutyrate is covalently bound to a detection probe and localized at the surface through binding events.[42] An initiating isobutryate radical is generated when the bromine is transferred to a Cu(I) catalyst in the monomer solution (Figure 1-17C). The reverse process stops the propagation.[43] With RAFT, a dithioester chain transfer agent is attached to a detection probe and radical initiators, such as azobisisobutyronitrile (AIBN), are included in the monomer solution. 2-cyanoprop-2-yl initiating radicals are formed upon the thermal decomposition of AIBN (Figure 1-17D). These radicals react with monomers in solution and the propagating chains diffuse to the surface where they then react with chain transfer agents. [44]

With the exception of ATRP, for each of the radical generation methods described, the molecules initiating polymer chains are in solution rather than tethered to the surface. In RAFT, the chain transfer agent at the surface functions to anchor the polymer. It is less clear how this is accomplished for the photopolymerization-based and enzyme-mediated methods, although, in the case of the former, it has been hypothesized that eosin radicals at the surface terminate polymer chains, thereby attaching them to the surface.

---

[1] 2-(1-Carboxy-1-methylethylsulfanylthiocarbonylsulfanyl)- 2-methyl propionic acid (CMP)
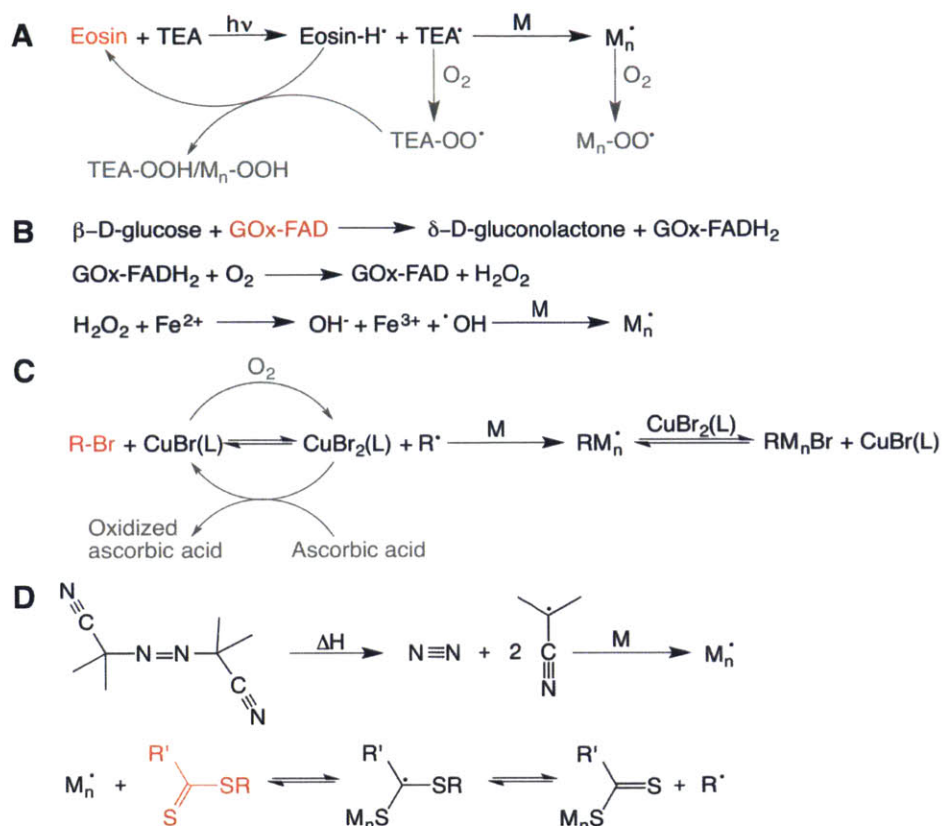
Figure 1-17. Radical polymerization chemistries for polymerization-based amplification. For each example, the surface immobilized molecule is highlighted in red. A) Photopolymerization using eosin and triethanolamine (TEA) as coinitiators. The TEA radical reacts with monomers (M) in solution to initiate polymerization. Oxygen is an inhibitor, reacting with initiating and propagating radicals to generate peroxy radicals. It has been proposed that the peroxy radicals will abstract a hydrogen from the semiquinone form of eosin (Eosin-H·), regenerating eosin.[15,45] B) Enzyme-mediated polymerization. Glucose oxidase is reduced in the process of converting β-D-glucose to δ-D-gluconolactone. Molecular oxygen oxidizes the enzyme, producing hydrogen peroxide, which is converted to hydroxyl radicals by Fenton's Chemistry. These hydroxyl radicals initiate polymerization by reacting with monomers in solution. C) Activators generated by electron transfer for atom transfer radical polymerization (AGET ATRP). In ATRP, a transition metal compound (cuprous halide) catalyzes a reversible redox process involving an organic halide, generating an initiating radical. L is the ligand that complexes the cuprous salt, thereby solubilizing it. $CuBr_2(L)$ reduces the propagating radical concentration and minimizes termination.[41] Oxygen inhibits the reaction by oxidizing the cuprous halide. In AGET ATRP, a reducing agent, such as ascorbic acid, is introduced to reduce the Cu(II) complexes to active Cu(I) complexes.[46] D) Reversible addition-fragmentation chain transfer (RAFT) polymerization. A conventional initiator is used to generate radicals in the presence of a chain transfer agent. Heat is used to decompose azobisisobutyronitrile (AIBN) into a nitrogen molecule and two 2-cyanoprop-2-yl radicals that initiate polymerization by reacting with monomers in solution. The dithioester chain transfer agent reversibly transfers a labile end to a propagating chain.[41]

One of the barriers to wider implementation of polymerization-based amplification is that radical polymerization reactions are inhibited by oxygen. Oxygen inhibition is circumvented in the enzyme-mediated system as oxygen is required for the production of initiating radicals. This thesis will describe how submicromolar concentrations of eosin in a monomer solution allow the eosin-initiated photopolymerization to be performed under ambient conditions.[10] In addition to quenching propagating radicals, oxygen inhibits ATRP by oxidizing the Cu(I) catalyst.[47] In an approach termed activators generated by electron transfer (AGET), it has become possible to perform ATRP in the presence of

oxygen through the introduction of a reducing agent such as ascorbic acid to return the Cu(II) complexes to their reactive lower oxidative state.[46–48](Figure 1-17C)

RAFT was initially explored as an alternative living polymerization method intended to address some of the limitations of ATRP, including nonspecific adsorption of metal ions to DNA molecules,[49] which contributes to elevated background signal, and the use of toxic transition metal catalysts. Although RAFT achieved an order of magnitude increase in polymer thickness (with a maximum of ~200 nm) and lower background relative to ATRP,[44] its susceptibility to oxygen inhibition and heat activation requirement have limited interest in developing the method further. Recently, Chapman et al. demonstrated the potential utility of glucose oxidase for oxygen scrubbing in open vessel RAFT polymerizations.[50] Instead of bubbling argon through the monomer solution for 10 minutes prior to heat activation of the initiator, glucose oxidase is added to the monomer solution and left at room temperature for the 10 minutes preceding activation. In another recent RAFT implementation, eosin and a tertiary amine were used to circumvent oxygen inhibition in a photoinduced electron transfer RAFT polymerization.[32] Whether these strategies would work for interfacial polymerizations remains to be seen and the long reaction times and thin films remain a limitation for RAFT.

Because polymer growth is linear with respect to time,[51] controlled radical polymerization methods such as ATRP and RAFT lend themselves to quantitative detection. AGET ATRP was implemented for quantitative electrochemical biosensing by triggering radical polymerization on an electrode surface.[52],[53] Monomers such as 2-hydroxyethyl methacrylate (HEMA) and glycidyl methacrylate (GMA) were selected to provide excess hydroxyl and epoxy groups, respectively, for the attachment of electrochemical tags (aminoferrocene). The combination of AGET ATRP with electrochemical sensing provides a linear range spanning five orders of magnitude. The electrochemical assay was clinically validated for serum tumor markers against an existing clinical electrochemiluminescent method; 100 clinical serum samples were tested for either prostate specific antigen (PSA) or carcinoembryonic antigen (CEA).[53] More recently, Wu et al. successfully implemented AGET ATRP as part of a paper-based microfluidic electrochemical immunodevice for the detection of four cancer biomarkers (Figure 1-18).[54] Looking to the future, the authors envision a portable, low-cost diagnostic enabled by the rapidly evolving electronics manufacturing landscape.
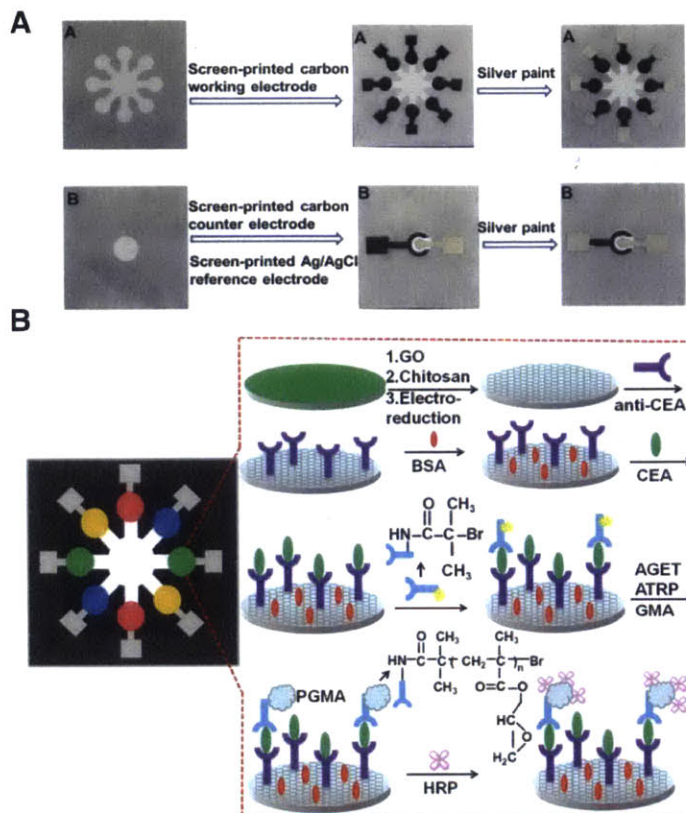
Figure 1-18. A paper-based electrochemical device integrated with AGET ATRP. A) The device consists of two layers of patterned square filter paper. Layer A consists of a central connecting zone and 8 working zones. Layer B has one connecting zone corresponding to that of layer A. The chromatography paper was impregnated with photoresist and irradiated with UV light to create the patterns. The working zones of layer A were screen-printed with carbon ink. Ag/AgCl and carbon ink were printed on layer B to form the reference and counter electrodes, respectively. **B)** The device was designed for the detection of four biomarkers: carcinoembryonic antigen (CEA), alpha-fetoprotein (AFP), cancer antigen 125 (CA125), and carbohydrate antigen 153 (CA153). The fabrication and assay procedure are shown for CEA. A solution of graphene oxide (GO) was dropped onto each working electrode, followed by a chitosan solution. The GO was then electrochemically reduced and the electrode was incubated with glutaraldehyde. Capture antibodies against each of the cancer biomarkers were applied to the corresponding working electrodes. Remaining active sites were blocked with BSA and a sample solution containing the biomarker (here, CEA) was introduced. The bromoisobutyrate (initiator)-coupled CEA antibody was added and AGET ATRP was performed. A solution of HRP (intended to react with side-chain functional groups of the polymer) was dropped onto each working electrode prior to electrochemical detection. Reprinted with permission from Wu et al., *Biosensors & Bioelectronics*, 2014, 52, 180-187. Copyright © 2014, Elsevier B.V.[54]

However, while the electrochemical output simplifies quantification relative to ellipsometry (the favored method for measuring the thickness of the films generated using ATRP), the attachment of the electrochemical tags added 10-20 hours to the assay time (on top of 2 hours of AGET ATRP followed by a 2 hour rinse), ultimately limiting its utility. In addition, although AGET ATRP was carried out in the presence of oxygen, many of the electrochemical experiments were performed under nitrogen, [53,52,55] erasing the gains achieved through the use of AGET ATRP.

AGET ATRP has also been coupled with flow injection chemiluminescent and electrochemical detection [55] and electrochemiluminescent detection [56]. Although electrochemiluminescent detection expanded

the linear range to seven orders of magnitude, neither of these methods reduced the limit of detection relative to electrochemical sensing.

AGET ATRP has been used to enhance the detection sensitivity of surface plasmon resonance (SPR) spectroscopy.[57,58]Liu & Cheng presented a membrane based biosensing interface using functional gold nanoparticles and AGET ATRP to enable ultrasensitive detection of cholera toxin (LOD=160 aM) by SPR, improving the detection limit by six orders of magnitude relative to direct measurement without amplification. In another membrane application, Liu et al. used AGET ATRP to grow a polymer at the membrane-water interface of a supported lipid bilayer by using initiator labeled trimethylammonium salts to recognize membrane-bound cavitands.[59]

Nanoparticle-based colorimetric methods have been demonstrated using both ATRP[60–62] and enzyme-mediated polymerization.[63] In all of these methods, polymerization was used to alter the optical properties of a solution of nanoparticles. The ATRP examples concentrated on the immobilization of initiators on DNA or antibody modified nanoparticles through molecular recognition events, while Gormley et al. used glucose oxidase mediated radical polymerization to entangle negatively charged gold nanoparticles. Glucose oxidase was used to eliminate oxygen from the system as well as generate hydrogen peroxide for the horseradish peroxidase-catalyzed reaction with acetylacetone. In addition to horseradish peroxidase, this concept of nanoparticle aggregation was used for the detection of catalase, iron, and copper.

It is clear that significant progress has been made in the last few years in terms of exploring novel applications, overcoming oxygen inhibition, and enabling quantitation. Each of the initiation chemistries presented has unique advantages and the selection of one amplification method over another must be driven by the end application. For colorimetric, point-of-care assays, photopolymerization is a strong candidate as it is capable of producing thick films that are readily visible to the unaided eye using inexpensive light emitting diodes for activation. The oxygen-tolerant methods, AGET ATRP and enzymatically-mediated polymerization, require hour-scale reaction times and experience sensitivity losses when the reaction time is reduced. A major advantage of photoinitiated polymerization is the ability to limit the occurrence of false positives by tuning the dose of light, thereby shifting the threshold for the positive response.

Photopolymerization-based amplification is limited by the difficulty of accessing a dynamic regime and interpreting the colorimetric readout quantitatively. Johnson et al. presented a possible solution to this problem through careful microarray design,[22] but the dynamic range and precision achieved using electrochemical detection with AGET ATRP would be challenging to match. In the published methods, quantification through the generation of an electrochemical output is achieved at the expense of assay time. However, for some applications the extra time required to generate the final output and reliance on gold substrates may be warranted.

There are many factors to consider in biosensor design: expense, time, complexity, and a requirement for equipment among them. In developing photopolymerization-based amplification, we have focused on reducing the cost and complexity of the assay with the goal of addressing some of the limitations of currently used amplification methods for point-of-care disease detection. We envision a device that can be used to screen for infectious diseases. We are also excited about new directions in the field, particularly in the area of targeted cell encapsulation.

1.5 Barriers to wider implementation of photopolymerization-based signal amplification

1.5.1 Diagnostic test criteria

In 2004, Mabey et al. summarized the need for accurate and stable diagnostic tests for the developing world.[64] In their review, they defined point-of-care tests as diagnostic tests that are "performed in the clinic, with results available within a short time so that patients can be treated without a return visit." They also identified the characteristics of the ideal diagnostic test as specified by the World Health Organization. These characteristics spell out "ASSURED" and are as follows:

- Affordable by those at risk of infection
- Sensitive (few false negatives)
- Specific (few false positives)
- User-friendly (simple to perform and requires little training)
- Rapid (enable treatment at first visit) and Robust (no requirement for refrigerated storage)
- Equipment-free
- Delivered to those who need it

These characteristics have become guiding criteria for the development of diagnostic tests, particularly for resource-limited settings. Mabey et al. emphasized that tests deployed in resource-limited settings are not necessarily competitive with laboratory-based assays, stating "the best test is not always the most useful test."

Photopolymerization-based signal amplification has the potential to transform diagnostics, both in the laboratory and at the point-of-care. Significant advances towards achieving this potential include the replacement of high-intensity mercury lamps with LEDs and the development of a colorimetric readout. However, many of the implementations of PBA discussed thus far have required inert gas purging, which increases the cost and complexity of performing the reactions. Additionally, more robust and inexpensive surfaces are required in order to facilitate translation of this technology to the point-of-care. These ideas will be discussed further in the following sections.

1.5.2 Oxygen inhibition

Radical polymerization reactions are typically inhibited by oxygen.[16,65] Oxygen reacts with propagating radicals to form peroxy-based radicals that react much more slowly with monomers than propagating radicals and thus have the effect of inhibiting the reaction.

$$R \cdot + O_2 \rightarrow ROO \cdot$$
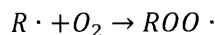
The dissolved oxygen concentration (0.3-2 mM[15]) is frequently sufficient for complete inhibition. Consequently, it is common to remove oxygen by purging both the monomer solution and the reaction chamber with an inert gas. Nitrogen and argon are most commonly used for this purpose in PBA, although helium, which is prohibitively expensive, is reported to be more efficient in displacing oxygen as a result of its high diffusivity.[16] The solubility of oxygen is lower in water than in acrylates;[66] this is another advantage of the eosin system, which uses an aqueous monomer solution.

Other strategies for limiting the impact of oxygen inhibition include increasing the light intensity and the photoinitiator concentration.[16] These solutions are impractical for PBA where the initiator concentration is limited by the number of binding events on the surface. This means that increasing the light intensity would likely only deplete the few initiating molecules at a faster rate in reactions with oxygen. It is common to employ additives and, in some cases, modify the monomers, using cationic polymerization

or multifunctional monomers, in order to overcome oxygen inhibition.[16] A common strategy unavailable to PBA is to increase the initiator concentration, making propagation reactions competitive with peroxy radical formation.[16] However, PBA is limited to what is captured on the surface. Type II systems are reported to be less affected by oxygen inhibition than type I systems as the amine coinitiators can react with peroxy radicals to reinitiate polymerization according to the expression below where DH is the hydrogen donor (the amine).[16] Hydrogens bound to carbons adjacent to an electron-rich heteroatom (oxygen, sulfur, nitrogen) tend to be abstractable.[16]

$$ROO \cdot + DH \rightarrow ROOH + D \cdot$$
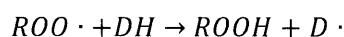
Thiols are also effective hydrogen donors, but are not as extensively used due to their strong odor.[16] Higher functionality thiols are also used to increase the viscosity of the reaction mixture and slow diffusion of oxygen.[67]

Monomer selection can also impact susceptibility to oxygen inhibition. Lee et al. showed that methacrylates are less sensitive to oxygen inhibition than acrylates.[68] In this case, the monomers contained ether groups with abstractable hydrogens that were thought to contribute to increased resistance to oxygen inhibition. Methacrylates are hypothesized to be less sensitive to oxygen due to the stability of the methacrylate radical, which makes chain transfer reaction less likely, as well as the lower solubility of oxygen in methacrylates compared with acrylates.

Because singlet oxygen is not reactive towards radicals like ground state oxygen, triplet sensitizers have been used in conjunction with singlet oxygen scavengers to overcome oxygen inhibition.[16] This concept was demonstrated by Decker in a study in which triplet excited state methylene blue reacted with oxygen to give singlet oxygen which went on to react with 1,3-diphenylisobenzofuran to give 1,2-dibenzoylbenzene and one half molecule of oxygen, thereby reducing the oxygen concentration.[69] Zinc tetrakis(tert-butyl) phthalocyanine (Zn(ttp)) was later used to excite oxygen at a rate higher than the initiation rate to favor reaction of oxygen with Zn(ttp) over initiating radicals.[70]

Padon and Scranton have proposed an oxygen scavenging pathway for the three-component radical photoinitiator system comprised of methylene blue, MDEA, and diphenyliodonium chloride (DPI).[71] In the proposed reaction, DPI regenerates methylene blue by reacting with the neutral methylene blue radical, in the process generating additional initiating phenyl radicals while the peroxyradical abstracts a hydrogen from MDEA to regenerate the MDEA radical.

Ligon et al. identified the most effective strategies as those that can either avoid peroxy radical formation entirely or reinitiate polymerization from the peroxy radicals that form. The strategy of introducing an additive followed by Decker, Shenoy and Bowman, and Padon and Scranton as described above is worthy of consideration, although other factors, such as solubility, health hazards, and the impact on sensitivity, crosslinking density, and polymer film thickness must be taken into account. In a mechanistic study of bulk polymerization reactions, Avens & Bowman found that eosin in conjunction with a tertiary amine coinitiator is able to overcome a 1000-fold excess of oxygen in solution.[15] This idea will be explored in depth in later chapters.

1.5.3   Surface compatibility and cost

In nearly every microarray implementation of polymerization-based signal amplification, self-assembled monolayer (SAM) modified glass surfaces were used to immobilize capture molecules. In the course of developing an ambient tolerant monomer solution, we found that PBA has sufficient sensitivity to report on surface inconsistencies in SAM coatings.[10] This observation led to the conclusion that a more robust,

yet inexpensive, surface was required. In addition, as many molecular diagnostic applications are based on protein binding events, a surface on which protein activity would be retained following the surface-immobilization process is required.

1.6 Thesis Overview

This thesis details the development of photopolymerization-based signal amplification as a platform technology. We leverage the amplification inherent to radical polymerization to enhance signal associated with specific molecular recognition events. The primary focus of this work was to begin the transition of photopolymerization-based signal amplification from the lab to point-of-care users by addressing some of the major limitations of the technology as originally developed in addition to improving the mechanistic understanding of the binding reaction as well as the signal amplification.

Having identified oxygen inhibition as one of the major hindrances limiting adoption of this technology in point-of-care settings, we sought to understand how eosin could be used to mitigate the effects of oxygen inhibition. Chapters 2-4 present efforts to overcome and understand the role of oxygen in our system.

Exploring the initiation threshold concept and the predictive value of known parameters, we investigated the impact of the dissociation constant on the limit of detection and identified the crucial parameters for predicting the performance of polymerization-based signal amplification reactions. This study is presented in Chapter 5.

In order to expand the realm of potential applications and maximize sensitivity, we constructed macrophotoinitiators to increase the number of initiators at the surface per binding event. Synthetic strategies and conclusions about the utility of this strategy comprise Chapter 6.

Finally, we employed photopolymerization-based signal amplification for targeted cell encapsulation, mitigating the effect of contaminating white blood cells for molecular analysis. These efforts are described in Chapter 7.

2 Development of an air tolerant monomer formulation

Some of the work, text, and figures presented in this chapter are reprinted or adapted from Kaastrup and Sikes. Polymerization-based signal amplification under ambient conditions with thirty-five second reaction times. *Lab on a Chip*, 2012, 12, 4055-4058.

2.1 Abstract

Although polymerization-based amplification (PBA) has demonstrated promise as an inexpensive technique for use in molecular diagnostics, oxygen inhibition of radical photopolymerization has hindered its implementation in point-of-care devices. The addition of 0.3-0.7 μM eosin to an aqueous acrylate monomer solution containing a tertiary amine allows an interfacial polymerization reaction to proceed in air only near regions of a test surface where additional eosin initiators coupled to proteins have been localized as a function of molecular recognition events. The dose of light required for reaction is inversely related to eosin concentration. This system achieves sensitivities comparable to those reported for inert gas-purged systems and requires significantly shorter reaction times. We provide several comparisons of this system with other implementations of polymerization-based amplification.

2.2 Introduction

The diagnosis of infectious diseases is significantly enhanced by access to point-of-care devices, particularly in resource-constrained regions. In order to diagnose and prevent the spread of disease in areas with restricted access to public health care, it is essential to develop accurate, rapid, and affordable point-of-care tests.[72] Designing diagnostic tests that satisfy all of the criteria set forth by the World Health Organization[64] has proven challenging. Many of the current systems for clinical diagnostics are PCR-based and instrument-intensive, requiring access to a hospital or laboratory as well as being expensive.[73]

A growing body of work indicates that polymerization-based amplification (PBA) addresses several of these problems and shows promise as an inexpensive technique for use in molecular diagnostics if the gap between meeting several of the criteria and all of the criteria can be bridged.[5,6,13,17–20,39,40,42,47,52] In this approach to biosensing, initiator-labeled detection reagents connect a signal amplification reaction to molecular recognition events, as depicted conceptually in Figure 2-1. Binding reactions localize initiating molecules near the test surface. With the addition of a monomer solution and light, polymerization-initiating radicals are produced and a crosslinked, hydrogel forms provided the number of binding events exceeds a certain threshold. In addition to being low cost and simple to perform, this process also tolerates complex analytes.[13,17,19] However, limitations stand in the way of widespread use in field and point-of-care settings. Chain growth reactions that proceed through radical mechanisms are inhibited by oxygen, and previous implementations of photoinitiated PBA have made use of inert gas-purged reaction vessels.[5,6,13,17–19,28,42] Molecular oxygen inhibits radical polymerization by reacting with initiators and propagating radicals to form peroxy radicals, which are unreactive towards further propagation and thus terminate chain growth.[65] This termination reaction is particularly important for surface-initiated polymerization where the ratio of atmosphere-exposed surface area to reaction volume is high and, consequently, oxygen is readily replenished even as it is consumed. In the present work, we address the oxygen inhibition problem in a visible-light, photo-reducible dye initiation system.

Eosin Y has been used as a coinitiator for the photopolymerization of acrylate monomers in visible-light initiated systems for decades,[14,25,26,74] but it is only in the last few years that its role in preventing oxygen

inhibition has been appreciated.[15,75] Eosin is a photoreducible dye that reacts with a tertiary amine to form an initiating species for free radical polymerization. The tertiary amine, typically either methyldiethanolamine (MDEA) or triethanolamine (TEA), forms an initiating radical as a result of charge transfer from the triplet excited state of eosin. Recently, Avens et al. proposed a mechanism by which eosin is able to initiate polymerization in the presence of oxygen. They demonstrated that 0.4 µM eosin in combination with 210 mM MDEA is able to initiate polymerization of an aqueous poly(ethyleneglycol) diacrylate (PEGDA) solution containing 1000-fold excess of dissolved oxygen after a 2.5 minute inhibition period.[15] These experiments were conducted using homogeneous, rather than interfacial polymerization reactions, and molecular recognition events were not involved. According to the proposed mechanism, eosin reacts with inhibitors through a process in which it is cyclically regenerated. A peroxy radical, formed in the reaction between molecular oxygen and a propagating chain, abstracts hydrogen from an eosin radical, regenerating eosin in the process:

$$TEA-M_n \bullet + O_2 \rightarrow TEA-M_nOO \bullet \tag{1}$$

$$TEA-M_nOO \bullet + H-Eosin \bullet \rightarrow TEA-M_nOOH + Eosin \tag{2}$$

In this article, we systematically investigate the idea of including sub-micromolar concentrations of free eosin in the monomer solution during a PBA reaction. The resulting reaction mixture contains eosin in two forms: unconjugated eosin that is homogenously distributed throughout the system, and eosin coupled to proteins that are localized at a test surface as a function of specific molecular recognition events (
Figure 2-1). We show that this approach allows the detection of molecular recognition events without inert gas purging. We demonstrate that sensitivity is not compromised relative to earlier reports on a similar photopolymerization system with an inert gas-purge,[6] and that no trade-off exists between reaction time and assay sensitivity as has been observed in air-tolerant ATRP[47] and enzymatic PBA systems.[39]
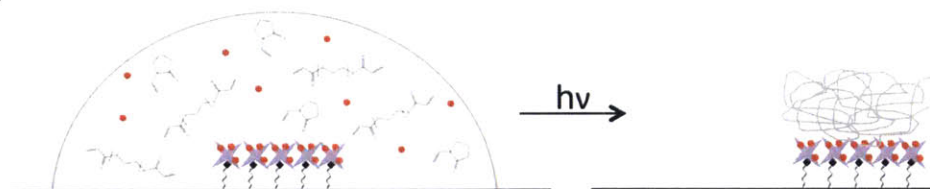
Figure 2-1. Molecular recognition events increase the local concentration of initiator (represented by a red diamond) at the surface relative to the bulk. Bulk initiator concentrations that allow rapid hydrogel readouts in an air environment only in regions of a biochip where molecular recognition occurs have been identified. Without initiators in the bulk solution, inert gas purging is required for reaction.

2.3 Experimental

2.3.1 Materials
Poly(ethylene glycol) diacrylate (M_n=575), triethanolamine, 1-vinyl-2-pyrrolidinone, eosin Y disodium salt, 10x phosphate buffered saline, Triton® X-100, and Tween® 20 were purchased from Sigma Aldrich and used without further purification. Eosin 5-isothiocyanate was obtained from Marker Gene Technology. Streptavidin was purchased from Rockland Immunochemicals Inc. 10x bovine serum albumin blocker solution and EZ-Link Sulfo-NHS-LC biotin were purchased from Pierce/Thermo Scientific. 100x Denhardt's solution was obtained from Bioexpress. Biochip test surfaces containing biotin-functionalized DNA were purchased from InDevR, Inc. Cy3 NHS ester was purchased from Lumiprobe. UltraCruz™ Micro G-25 Spin Columns were purchased from Santa Cruz Biotechnology, Inc. Dulbecco's Modified Eagle's Medium was purchased from Lonza Group, Ltd. Fetal bovine serum was purchased

from ATCC and penicillin/streptomycin was purchased from EMD Millipore. A BCA Protein Assay Kit with bovine serum albumin standards was obtained from Pierce/Thermo Scientific.

2.3.2 Preparation of Detection Reagents

Eosin initiators were coupled to binding events by reaction of eosin 5-isothiocyanate with a fraction of the solvent-accessible lysine residues of streptavidin as previously described.[6] Streptavidin (1 mg) was dissolved in 100 uL of 0.1 M sodium bicarbonate buffer, pH9. Eosin 5-isothiocyanate (EITC, 1 mg) was dissolved in 100 uL of DMSO. 10 uL of the EITC solution was added to the streptavidin solution (100 uL) for a total reaction volume of 110 uL. After gentle pipetting to mix, the reaction was protected from light and maintained at 4°C overnight. Remaining 10 uL aliquots of EITC in DMSO were stored at -80°C for future use. Following overnight reaction, pre-packed Sephadex gel filtration columns for use in microcentrifuges were used to separate unreacted EITC from SA-EITC conjugates. Performing a buffer exchange of the column material into 0.1 M sodium bicarbonate buffer was important for obtaining optimal product recovery, and 1/3 of the reaction mixture was loaded onto each of three Sephadex spin columns. Three columns were used at this scale to avoid overloading the column with uncoupled EITC. The recovered streptavidin-EITC conjugates were pooled and diluted with 890 uL of phosphate buffered saline. UV-visible absorbance spectroscopy was used to determine the average number of eosin molecules covalently coupled to each protein. Measured absorbance values at 280 nm and 525 nm and measured extinction coefficients in the stated buffer system were used in the following equation to determine an average number of EITC per protein:

$$n_{EITC}/n_{SA} = (Abs_{EITC,525}/ \varepsilon_{EITC,525})/[(Abs_{SA,280}-Abs_{EITC,280})/\varepsilon_{SA,280}],$$ and $\varepsilon_{EITC,525}$ = 90,200 $M^{-1}cm^{-1}$, $\varepsilon_{EITC,280}$ = 26,800 $M^{-1}cm^{-1}$, $\varepsilon_{SA,280}$ = 173,000 $M^{-1}cm^{-1}$. Following characterization, the streptavidin-EITC solution was diluted (1:1 on a volume basis) with glycerol and stored in aliquots at -20°C for a period of up to six months without an observed loss of binding activity when used as specified in the text of this paper.

Stock solutions of free, unconjugated eosin-Y solubilized at a concentration of 5 µM in 1% methanol in distilled water were used to facilitate preparation of three monomer solutions containing final eosin concentrations of 0.3 µM, 0.5 µM, and 0.7 µM. The concentrations of PEGDA, VP, and TEA in these monomer solutions were, respectively, 200 mM, 100 mM, and 150 mM with distilled water as a solvent. PEGDA (M_n=575) as purchased contains 400-600 ppm MEHQ as an inhibitor, and additional purification steps to remove this inhibitor proved unnecessary for polymerization. TEA was used as an alternative to MDEA for its improved water solubility.

2.3.3 Quantification of test surfaces

Test surfaces consisting of 5' amino-50 mer ssDNA-TEG biotin 3' spotted onto aldehyde-functionalized glass at various dilutions[20] were purchased from InDevR, Inc. We quantified the number of binding-accessible ssDNA-biotin per square micron in each surface feature using a Cy3-streptavidin conjugate and fluorescence analysis (Agilent microarray scanner) against a Cy3 calibration array (Full Moon Biosystems). Prior to use, surfaces were rinsed with distilled water to remove residual salts and unreacted oligos. The test surface was contacted with 7.5 µg/ml Cy3-streptavidin in 0.75% BSA in 1.5x PBS, 5x Denhardts for five minutes in a humid chamber. This concentration is within the previously determined range of concentrations (1-10 ug/mL) that ensure signals dominated by specific rather than nonspecific binding.[6,19] Sequential rinses with PBST (1x PBS, 0.1% Tween 20), 1x PBS, and ddH$_2$O were used to remove unbound Cy3-streptavidin. Background-corrected fluorescence signals were compared with a standard curve generated using the Full Moon Biosystems calibration array where features containing only spotting buffer were used to calculate background signal.

2.3.4 Detection of molecular recognition using PBA under ambient conditions

The design of the present study was modeled after previous studies of labeled oligonucleotides covalently coupled to surfaces[5,6] so that sensitivity and other observables with the monomer solution and reaction conditions reported here could be compared with previous work.[6] In order to identify air-tolerant polymerization conditions, test surfaces containing a dilution array of biotinylated DNA features were contacted with 40 μL of 7.5 μg/ml eosin-streptavidin in 0.75% BSA, 1.5x PBS and 5x Denhardt's Solution for 5 minutes in a humid chamber. To remove unbound initiator, surfaces were rinsed with PBST (1x PBS, 0.1% Tween 20), 1x PBS, and distilled water and wicked dry. Once dry, 40 μL of the prepared monomer solution was contacted with the surface and the surface was irradiated with 522 nm light (30 mW/cm^2, measured using a SPER Scientific Light Meter) from an array of LEDs (InDevR). Unreacted monomer solution was removed by rinsing the surface with distilled water. Remaining hydrogel surface features, if present, were stained with 25 mM eosin (50% methanol, 50% distilled water) for 2 minutes and subsequently rinsed with water to allow visualization of the polymer on the slide surface. Each condition was repeated a minimum of 5 times. To verify the specificity of binding, competitive binding assays using eosin-streptavidin conjugates that were pre-incubated with an excess of free biotin were performed. To pre-block the eosin-streptavidin conjugates with free biotin, biotin dissolved in DMSO (22 mM) was added to the macrophotoinitiator solution to achieve a final concentration of 550 μM, a >1000-fold excess relative to streptavidin. The final DMSO concentration of the solution incubated with biochip surfaces was 2.5% on a volume basis, and biochips were developed as described above.

2.3.5 Assessing tolerance for complex analyte solutions

A431 cells were maintained in Dulbecco's Modified Eagle's Medium supplemented with 10% fetal bovine serum and 1% penicillin/streptomycin. The cells were lysed with Triton X-100 using standard protocols.[76] In brief, A431 cells were grown to confluence on a 100 mm culture plate. The culture medium was discarded and the cells were washed twice with 1xPBS prior to the addition of 1 mL chilled lysis buffer (150 mM NaCl, 1% Triton X-100, 50 mM Tris-HCl, pH 7.4). The cells were incubated on ice with occasional rocking for 25 minutes. The lysate was transferred to a microcentrifuge tube and centrifuged at 18,000xg for 10 minutes at 4°C. The supernatant was then removed and the total protein concentration, quantified with a BCA assay, was determined to be 0.9 mg/ml. The lysate was diluted to 0.5 mg/mL with BSA in 1x PBS (for a final concentration of 0.75% BSA in 0.5x PBS) and macrophotoinitiator was added to a final concentration of 375 nM (or 7.5 μg/mL streptavidin). The surfaces were contacted with the macrophotoinitiator in lysate for 5 minutes and developed normally. Macrophotoinitiator was also added directly to undiluted cell lysate for comparison.

2.3.6 Analysis

Each surface was imaged using the digital camera built into the IntelliChip Reader (InDevR) imaging bay. Mean intensity and standard deviation values were calculated for every surface feature and for the background in an automated fashion using software that accompanies the IntelliChip Reader. Hydrogel thickness profiles were obtained using a Dektak Stylus Surface Profiler with a 2.5 μm stylus applying a force of 98 μN. Hydrogels were in the dry state.

2.4 Results and Discussion

Figure 2-2 demonstrates that the inclusion of 0.3 μM eosin in the monomer solution allows the formation of visible hydrogels only in the regions of the dilution-series biochip where molecular recognition events have localized additional eosin. The interfacial polymerization reaction proceeds in an ambient environment without the need for inert gas purging or removal of MEHQ inhibitors used to stabilize acrylate monomers. A colorimetric response was observed in all features where at least 15

molecular recognition events per square micron were possible, and a complete lack of a response was observed in negative control regions including the unmodified surface area between features and the bottom row of features that were treated with oligo-spotting buffer only. In 7/15 cases, colorimetric responses from the row of features containing 6 possible molecular recognition events per square micron were observed (not shown in quantitative details below). Figure 2-3 provides characterization data indicating that an average of three eosin molecules were coupled to each protein, and Figure 2-4 supports the assertion that the dilution series biochip contains the stated number of biotin-labeled oligos per square micron. Figure 2-5 provides evidence for specific binding in all regions of the biochip that showed a polymerization response; biochips treated with eosin-streptavidin initiators that were pre-incubated with an excess of free biotin prior to contact with the surface did not yield polymerization responses.

Position	Biotin/μm^2	Average Intensity	Average Thickness
0	110	66.7 ± 11.6	597.6 ± 267.5
1	100	73.3 ± 5.7	1007.7 ± 68.5
2	50	61.7 ± 6.0	531.9 ± 73.5
3	27	41.7 ± 2.9	230.4 ± 30.2
4	15	35.8 ± 2.0	117.8 ± 9.2
5	6	25.8 ± 1.2	
6		23.6 ± 1.0	
7	0 (spotting buffer)	25 ± 1.1	
Background	N/A	26 ± 1.8	
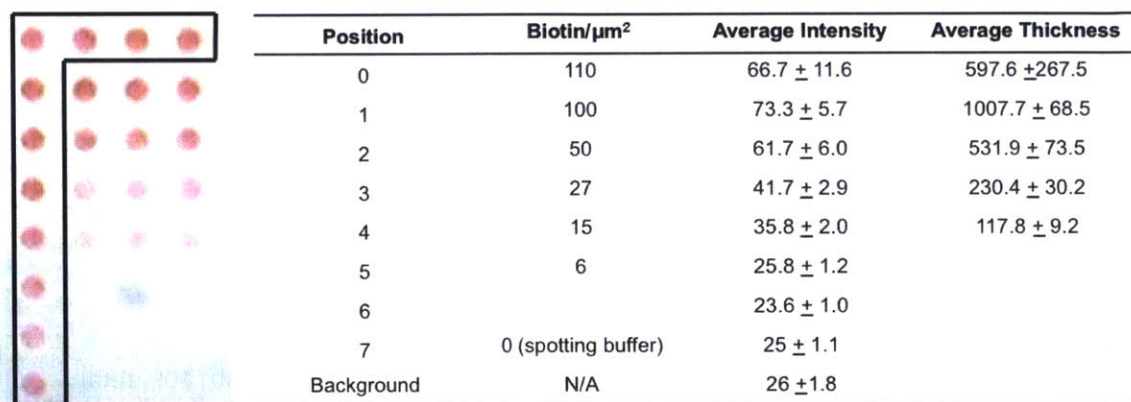
Figure 2-2. Colorimetric detection of molecular recognition using PBA under ambient conditions. The monomer solution contained a bulk concentration of 0.3 µM eosin and the irradiation time was 100 seconds with 522 nm light from LEDs (30 mW/cm^2). This table includes average thickness data as determined using profilometry.
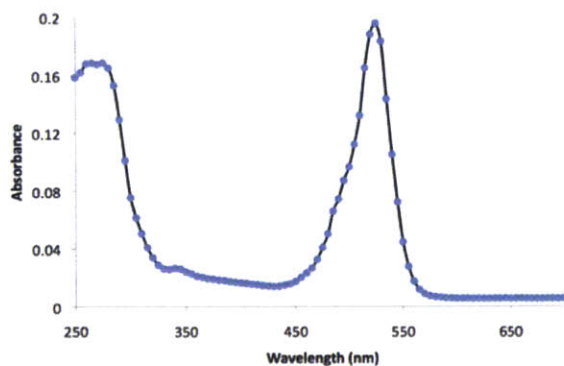
Figure 2-3. UV-visible absorbance spectrum for Streptavidin-Eosin conjugate.

A

Absorbance vs Wavelength (nm)

B

C

Position	SNR	#Biotin/μm²
0	113	110
1	103	100
2	54	50
3	29	27
4	16	15
5	7	6
6	2	
7	1	

D

SNR vs Fluorophores per square micron

$y = 0.5317x$
$R^2 = 0.99732$
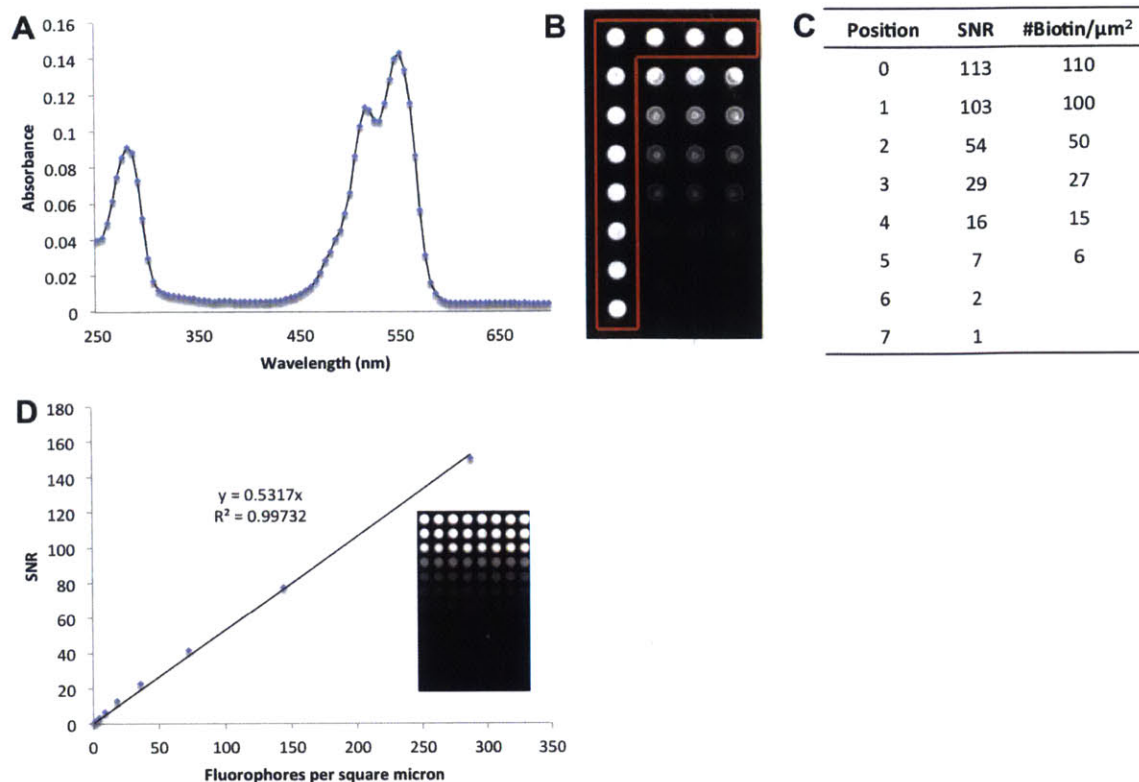
Figure 2-4. The number of binding-accessible ssDNA-biotin in each set of features of the test surface was quantified using a Cy3-Streptavidin conjugate, a scanner calibration array and fluorescence analysis. (A) A streptavidin-Cy3 conjugate with a known average number of Cy3 molecules per streptavidin was prepared using the same method outlined above, though with a NHS ester-functional dye in the place of an isothiocyanate dye. An average of two Cy3 were coupled to each protein according to the provided spectral data and the following extinction coefficients: $\varepsilon_{cy3,552} = 150,000$ M⁻¹cm⁻¹, $\varepsilon_{cy3,280} = 12,000$ M⁻¹cm⁻¹ $\varepsilon_{SA,280} = 173,000$ M⁻¹cm⁻¹. (B) A biochip test surface was reacted with the Cy3-streptavidin conjugate as described in the text and imaged. The average signal to noise ratios (C) were compared with a standard curve generated using a Full Moon Biosystems calibration array (D). The signal intensities on the surface were determined using Metamorph Basic to compute average intensities within specified regions of constant area. The signal to noise ratio is defined as the difference between the signal and the background (in this case, the average signal of the three buffer spots) divided by the standard deviation of the background $\left(\frac{signal-background}{\sigma_{background}}\right)$. The fluorescence images were obtained using an Agilent microarray scanner with an excitation wavelength of 532 nm (20 mW) and emission wavelengths between 550 nm and 610 nm. The intensity scale is 0 to 10000 and the PMT setting was 10%.
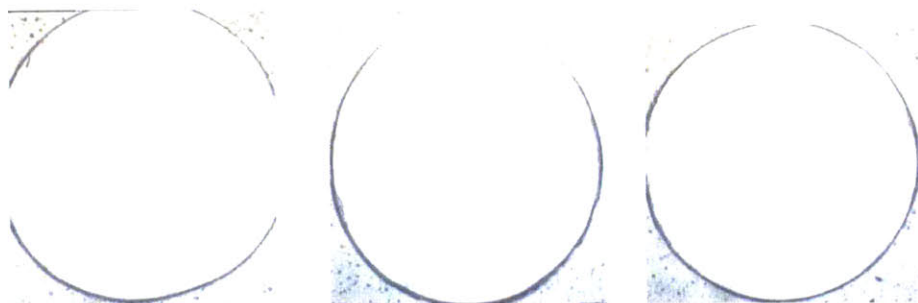
Figure 2-5. Competitive binding assays using eosin-streptavidin pre-incubated with a 70-fold excess of free biotin confirmed the specificity of the binding interaction. Displayed are the negative controls for monomer solutions containing 0.3 μM, 0.5 μM, and 0.7 μM eosin, respectively.

Figure 2-2 contains a table that collects average colorimetric intensity data and average polymer film thickness data for each set of features in the biochip. The top row and left-most column of features (boxed, position 0) were spotted with an identical concentration of biotin-labeled oligonucleotides; this design provides a means to assess variability over the length and width of the array. DNA density decreases in each successive row from the top with three replicate spots representing each dilution. A t-test performed on the colorimetric intensity data suggests that differences between features in positions 0, 1, and 2 are not statistically significant, while those between positions 2, 3 and 4 are statistically significant. The average pixel intensity of the accompanying digital image correlates with the average hydrogel thickness. The dried polymer films ranged between an average thickness of 0.12 ± 0.01 μm for a surface density of 15 biotin/μm^2 up to 0.60 ± 0.27 μm for 110 biotin/μm^2 for the surface shown in Figure 2-2.

Monomer solutions containing higher concentrations of free eosin (0.5 μM and 0.7 μM) produced similar results to those shown in Figure 2-2; however, the reaction time required to achieve these results decreased with increasing dissolved eosin concentration (Figure 2-6). Without compromising sensitivity, it was possible to decrease the reaction time from 100 to 35 seconds by increasing the free eosin concentration in the monomer solution from 0.3 μM to 0.7 μM. Average film thicknesses and colorimetric intensities for all fifteen samples (five samples for each of three monomer solutions with varying dissolved eosin content) are collected in

Table 2-1 and Table 2-2. These tables include data for the features that presented 6 possible molecular recognition events per square micron; this row generated a colorimetric response on seven out of the fifteen samples that were tested. These tables include data for the features that presented 6 possible molecular recognition events per square micron; this row generated a colorimetric response on seven out of the fifteen samples that were tested. Including less than 0.3 μM of free eosin in the monomer solution did not allow hydrogel growth in an air environment with irradiation times of up to 150 s, and including 0.9 μM of free eosin resulted in difficulty finding a reaction time that led to surface-localized rather than bulk polymerization.
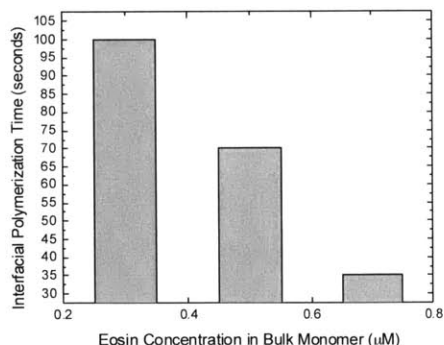
Figure 2-6. The reaction time required for interfacial polymerization decreases as the eosin concentration in the bulk monomer solution increases in the range from 0.3-0.7 μM. A crosslinked hydrogel forms at the interface only in regions where molecular recognition events have increased the local initiator concentration with these monomer compositions and reaction times.

Table 2-1. Average Film Thickness

Position	Biotin/μm^2	Film Thickness (nm) (0.3 µM Eosin)	Film Thickness (nm) (0.5 µM Eosin)	Film Thickness (nm) (0.7 µM Eosin)
0	110	747.3 + 211.6	868.5 + 226.2	560.6 + 165.5
1	100	844.7 + 230.5	707.5 + 55.3	546.1 + 344.5
2	50	468.0 + 90.3	744.0 + 353.3	466.5 + 47.4
3	27	271.3 + 57.8	389.6 + 246.6	401.8 + 130.5
4	15	238.1 + 170.1	334.3 + 42.1	336.8 +91.8
5	6	327.1 + 18.4	533.0 + 334.9	440.7 + 249.5

Table 2-2. Average Pixel Intensity

Position	Biotin/μm^2	Average Pixel Intensity (0.3 µM Eosin)	Average Pixel Intensity (0.5 µM Eosin)	Average Pixel Intensity (0.7 µM Eosin)
0	110	63.5 + 6.0	49.5 + 5.5	56.1 + 3.5
1	100	67.1 + 9.0	47.5 + 7.6	54.8 + 3.1
2	50	59.1 + 10.4	51.3 + 10.3	49.8 + 5.1
3	27	42.7 + 5.0	44.8 + 3.2	46.8 + 6.0
4	15	39.6 + 6.6	41.9 + 7.8	38.6 + 6.6
5	6	30.2 + 10.6	44.6 + 10.3	37.0 + 14.5
6		24.4 + 1.0	25.0 + 0.7	25.4 + 1.3
7	0 (spotting buffer)	24.4 + 0.8	25.0 + 0.8	24.6 + 0.9
Background	N/A	25.6 + 0.3	25.4 + 0.3	25.5 + 0.3

Figure 2-7 shows that monomer solutions containing free eosin and our reported reaction conditions are compatible with lysates of an immortalized human cell line (A431), a representative complex analyte solution. This representative complex analyte solution does not interfere with the readout; it did not increase the level of background signal or cause false positive results.

Position	Biotin/μm^2	Average Intensity
0	170	69.6 + 9.0
1	150	69.1 + 3.6
2	80	67.6 + 4.7
3	40	61.4 + 8.7
4	20	38.5 + 4.7
5	10	25.8 + 1.2
6		25.0 + 1.3
7	0 (spotting buffer)	24.6 + 1.0
Background	N/A	25.0 + 1.7
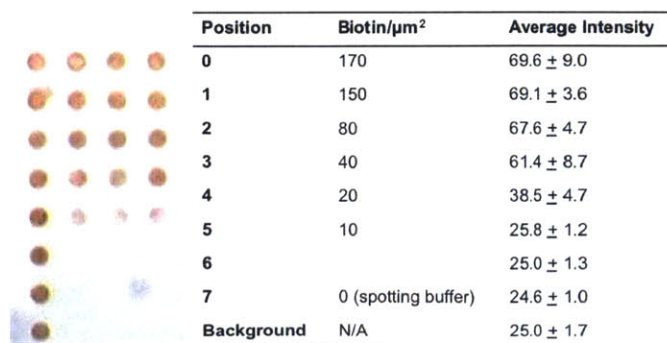
Figure 2-7. Providing the macrophotoinitiator in a mammalian cell lysate solution rather than in buffer has a negligible effect on the system sensitivity. The surface was contacted with macrophotoinitiator in A431 cell

lysate diluted to 0.5 mg/mL with BSA in PBS. The surface was then developed using an aqueous monomer solution containing 0.5 µM eosin and irradiated for 70 seconds. An identical sensitivity of ≥ 15 possible molecular recognition events per square micron was observed without any increase in background (non-specific signal). For macrophotoinitiator spiked directly into undiluted lysate, sensitivity decreased to ≥ 27 possible molecular recognition events per square micron without an increase in background signal.

Our results are consistent with the findings of Avens, et al., indicating that sub-micromolar eosin concentrations may be used to overcome oxygen inhibition during polymerization of aqueous acrylate monomers. These dissolved eosin concentrations are significantly lower than the expected dissolved oxygen concentration in the monomer solution (1.5 mM [77]), supporting the cyclic eosin regeneration mechanism proposed in reactions 1 and 2 above. Our system differs from that reported by Avens and coworkers: in addition to free eosin throughout the monomer solution, we have localized eosin-protein conjugates at the surface of a biochip as a result of specific molecular interactions. High local eosin concentrations lead to a decreased inhibition time in our system, <70 or <100 seconds for the 0.5 µM and 0.3 µM cases, respectively, compared with the 150 second inhibition period observed by Avens. One caveat of these comparisons is that Avens et al. used a high pressure mercury lamp and selected wavelengths from 490 nm - 650 nm with a total intensity of 75 mW/cm^2 and used a monomer solution containing 420 mM PEGDA, 35 mM VP, and 210 mM MDEA.

Previous work has shown that increasing the concentration of the tertiary amine co-initiator can result in thinner films, a consequence of the amine's propensity to act as a chain-transfer agent, slowing network formation and facilitating termination at higher concentrations.[28] The lack of change in hydrogel thickness in response to dissolved eosin concentration observed in this study suggests that eosin does not act as a chain-transfer agent in a manner similar to the tertiary amine, at least not within the range of concentrations tested.

In the context of previous reports of using visible light initiated polymerization reactions to detect molecular recognition, our present implementation provides several advantages. The reaction proceeds under ambient conditions within 35-100 seconds, a substantial improvement on the previously reported 20 minute reaction periods for argon-purged systems.[6] In addition, the threshold surface density of targets required for a response (15 biotin/µm^2) is comparable to that reported for previous systems (9.8 targets/µm^2 [6] and 17 targets/µm^2 [20]). Table 2-3 provides a compact comparison of our study with previous approaches to PBA, including AGET ATRP and enzymatically-mediated polymerization. Both AGET ATRP and enzymatically-mediated polymerization require reaction times on the hour time-scale for maximum sensitivity with sensitivity losses at shorter reaction times.

Table 2-3. Comparison of PBA Methods

System	Surface	Inert-Gas Purge	Reaction Time[†]	Thickness
Photopolymerization (this report)	Glass	No	35-100 sec.	0.12-0.60 µm
Photopolymerization[13‡] (without inert gas purge)	Glass	No	(minutes)	Not measured
Photopolymerization[6] (with inert gas purge)	Glass	Yes	20 minutes	0.12-0.54 µm
AGET ATRP[15]	Gold	No	10-120 minutes	4-16 nm

| Enzymatically mediated polymerization [8] | Polystyrene | No | 15-60 minutes | Not measured |

The covalent model system used in this work allows comparison of amplification techniques without confounding variables. Straightforward comparisons of sensitivity are complicated by differing association constants for different binding events, additional assay steps that may increase or decrease capture efficiency, and the fact that capture molecule density is not usually well-characterized but is known to impact capture efficiency and detection sensitivity. A striking example of the impact of capture molecule density on detection sensitivity of a target molecule captured from solution may be found in Figure 5 of reference 26. Of course, in contrast to the covalent model system, real assays require capture of a target molecule from solution. Previous work indicates that trends identified in covalent model systems hold in real assays involving additional non-covalent binding events.[13,17,19]

The present covalent model system does have drawbacks. PBA has sufficient sensitivity so that it reports on surface inconsistencies caused by variability in the SAM coatings of modified glass, small differences in oligonucleotide spotting procedures, and post-spotting processing procedures used to prepare biochips. Surface quality and uniformity are important factors in obtaining reliable results, and we believe that these factors currently determine the degree of variation in the results presented herein (i.e. standard deviations). Uniform, robust, low-cost test surfaces are a prime area for improvement. To date, visible-light initiated PBA has detected binding events at SAM modified glass, polystyrene, nitrocellulose and polysiloxane surfaces and should be easily adaptable to others.

2.5 Conclusion

The inclusion of sub-micromolar concentrations of free eosin in aqueous acrylate monomer solutions has been demonstrated to successfully overcome oxygen inhibition and allow detection of molecular recognition at biochip surfaces using surface-localized photopolymerization reactions. The reaction time can be tuned by adjusting the eosin concentration, higher concentrations yielding shorter reaction times. The system presented produces thicker hydrogels with shorter reaction times than other implementations of polymerization-based amplification,[39,47] and sensitivity is equivalent to a similar previously reported system that required an inert gas purge and longer reaction times.[6] In addition, the introduction of a complex analyte doesn't negatively impact assay performance. The system's speed, tolerance for complex analytes and ability to perform under ambient conditions suggest its utility for point-of-care devices.

3   Spectroscopic Investigation

3.1   Abstract

Techniques that promise real time monitoring of polymerization reactions in situ have the potential to dramatically simplify the kinetic characterization of new reactions. A novel system for monitoring photoinitiator consumption and double bond conversion for photopolymerizations in situ and real time was recently reported. Here, we employ this system to investigate the eosin-activated photopolymerization of hydrogels. In examining spectroscopic challenges associated with the polymerization of largely aqueous systems, three metrics for quantifying the extent of light scattering are identified and their relation to phase changes discussed. In addition, the dual-monitoring system is applied to the study of dye regeneration by oxygen.

3.2   Introduction

Radical photopolymerization is an essential and commonly used tool in a wide range of industries including microelectronics, laser imaging, and the production of coatings and adhesives.[78,79] Photopolymerization offers a number of advantages over alternative radical polymerization chemistries such as reversible addition-fragmentation chain-transfer polymerization and atom transfer radical polymerization; the reactions can be performed at room temperature and provide spatial and temporal control.[79]

Spectroscopic monitoring of polymerization allows for the elucidation of reaction kinetics and characterization of the polymers as they grow. An early approach to monitoring polymerization kinetics was to take periodic measurements; in an example of this, Shen et al. performed interval measurements of the propagating radical concentration and the monomer conversion for the bulk polymerization of methyl methacrylate.[80] Real-time monitoring of polymerization, and particularly monomer conversion using FT-NIR, has since become routine. Wayne Reed and colleagues developed an online polymerization monitoring system that operated through the continuous withdrawal of a small stream of the sample that was then diluted with solvent for light scattering and viscometric measurements.[81,82] A system based on light scattering for in-situ monitoring of parallel polymerization reactions was also developed.[83,84] Absorbance spectroscopy has been used to measure photoinitiator consumption and track changes in refractive index during polymerization reactions. In a study examining the polymerization kinetics of acrylic resins, Schmitt used a UV-Vis spectrometer to correlate changes in refractive index with double bond conversion.[85] Kang et al. presented a method for determining the chemical cross-link density in real time using UV-Vis spectroscopy in the context of the redox reaction between phenol groups and eosin for the polymerization of tyramine modified sodium alginate.[86] In situ UV-vis and FT-IR spectroscopy has been used to monitor the copolymerization of furan and thiophene; polyfuran and polythiophene have characteristic absorption bands depending on their band gaps so the UV-vis spectra provide an indication of the relative incorporation of thiophene and furan.[87] Decker performed separate measurements with real-time UV spectroscopy and IR spectroscopy to study the photolysis kinetics of a UV initiator and monitor conversion, respectively.[88]

Recently, Aguirre-Soto et al. demonstrated a custom coupled UV-Vis/FT-NIR set-up that permits simultaneous monitoring of photoinitiator consumption and monomer conversion (Figure 3-1). This system offers myriad advantages, including the ability to monitor a broad range of wavelengths extending from the UV to the NIR in situ, without the need for sample extraction. This set-up has previously been demonstrated for the polymerization of bulk monomer solutions. Here, we apply it to the study of eosin-activated photopolymerization of hydrogels.

Hydrogels are hydrophilic, cross-linked polymers that have been used extensively in tissue engineering,[89–91] protein delivery,[92] three-dimensional cell culture,[93] and as adhesives for wound closure.[94] Because of their swelling properties as well as the reduced toxicity of aqueous monomer solutions relative to bulk monomer solutions, hydrogel systems have also been used for photopolymerization-based signal amplification reactions.[6,10,21] These are reactions in which hydrogel formation is localized at a surface as a function of molecular recognition events; a photoinitiator is coupled to a molecule that specifically binds to a target molecule immobilized at a surface.

Hydrogels present a particular challenge in absorbance spectroscopy as the lower monomer concentrations result in slower rates of polymerization and more gradual transitions from liquid to gel. This often results in increased light scatter. Here, we demonstrate some of the spectroscopic challenges unique to hydrogel polymerizations and how to address them. In addition, we show how the dual monitoring set-up can be used to examine the effect of oxygen on radical polymerization reactions by measuring eosin consumption in the visible range and monomer conversion in the near IR.

Eosin has gained favor as a photoinitiator for photopolymerization-based signal amplification reactions as it is activated by visible light, contributes to the formation of gels that are firmly attached to the surface,[14] and is able to circumvent oxygen inhibition.[10] Oxygen reacts with initiating or propagating radicals to produce peroxy radicals that are unreactive towards propagation,[16,65] and, thus, have the effect of terminating the reaction. The exact mechanism through which eosin is able to overcome oxygen inhibition is unknown, although a possible route through which eosin is regenerated in a reaction between peroxy radicals and the semiquinone form of eosin has been proposed.[15]

Absorbance and fluorescence spectroscopy have been used previously to investigate dye regeneration. Slower rates of absorbance and fluorescence decay have been associated with dye regeneration.[71,95] Evidence of eosin regeneration in the presence of oxygen was presented by Chesneau and Fouassier. Comparing the absorbance at 546 nm for purged and laminated solutions of eosin, methyldiethanolamine (MDEA), and an oxime ester, they saw a plateau region during which the absorbance of the nonpurged solution was constant before rapidly decreasing.[45] By contrast, the absorbance of the corresponding purged solution decreased immediately. The regeneration of eosin, as indicated by the delayed decrease in absorbance for the nonpurged solution, was attributed to hydrogen abstraction from the semiquinone form of eosin by peroxy radicals in solution and the reaction between the semiquinone form and oxygen that produces eosin in its ground state and $HOO^{\bullet}$.[45]

Previous studies have been limited to monitoring either double bond conversion[15] or photoinitiator consumption[45] in examining the role of oxygen in the photopolymerization of hydrogels. The advantage of using a set-up that allows for simultaneous monitoring of the dye consumption and conversion is that it becomes possible to measure how the dye is consumed specifically during the inhibition period. Here, we will first discuss the treatment of the absorbance data for hydrogel systems before showing evidence of eosin regeneration by oxygen.
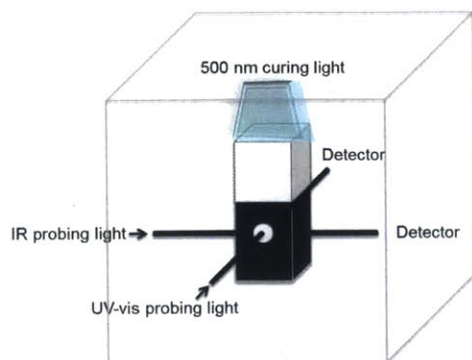
Figure 3-1. Set-up for simultaneous monitoring of near-infrared absorbance and uv/visible absorbance or fluorescence. Monomer samples in a cuvette are place in a holder with pinholes to restrict light to the detector which is transmitted by fiber optic cables. The curing light is shone from above and the entire set-up is encased within an air-excluding case to enable purged polymerization reactions.

3.3 Experimental

3.3.1 Materials

Poly(ethylene glycol) diacrylate, triethanolamine, 1-vinyl-2-pyrrolidone, 1-ethyl-2-pyrrolidone, and eosin Y disodium salt were purchased from Sigma Aldrich. PMMA cuvettes were purchased from Eppendorf.

3.3.2 FT-NIR and UV-Vis Monitoring

A multi-wavelength light emitting diode box containing a green 500 nm LED (FC8-LED, Prizmatix, Southfield, MI) was used to excite the photoinitiator, eosin. Irradiance or power density was controlled with a potentiometer and measured with a radiometer (6253, International Light Technologies, Peabody, MA) within the 400-700 nm range.

A fiber optic coupled UV-Vis spectrometer (USB4000-FL Miniature Fiber Optic Spectrometer, Ocean Optics, Dunedin, FL) was used to monitor absorbance within the 350-1000 nm range through a 10 mm pathlength. The acquisition time for the UV-Vis spectrometer was set to ~ 0.5 s (50 ms integration time, 10 scans to average) and a boxcar width of 4 was used. A water reference spectrum was collected prior to each experiment. The monomer solution consisting of 420 mM PEGDA, 35 mM VP, and 210 mM TEA did not absorb over the range of wavelengths being probed. The probing light was consistently adjusted to the same threshold intensity.

A fiber optic coupled FT-NIR spectrometer (Nicolet Magna-IR Series II, Thermo Scientific, West Palm Beach, FL) was used to track the vinyl group concentration. A pathlength of 2 mm was used for the NIR spectroscopy to avoid saturation by the O-H bands from the water. FT-NIR spectra were collected with a resolution of 8, a gain of 1, and an optical aperture of 10 with 4 scans at each time point. Acquisition time for the FT-NIR was between 0.5 and 3 seconds.

10 x 2 mm PMMA cuvettes were used inside an adaptor with custom-made optical apertures. A 3D printed cap was placed on top of the cuvette to restrict the curing light to the sample volume. The sample volume was 50 µL, which results in sample dimensions of 2 mm x 10 mm x 2.5 mm, where the latter is the thickness in the direction of the excitation light from the LED. Samples were placed inside a CUV-ALL-UV 4-Way Cuvette Holder (Ocean Optics, Dunedin, FL) with SMA connectors for fiber integration. Fiber optic cables were connected perpendicularly for UV-Vis and FT-NIR analysis. For the FT-NIR, two 1000 nm fibers were used to feed the IR light from the spectrometer to the sample, and from the sample back into the InGaAs detector. The UV-Vis probing light was fed into the cuvette holder

via a 600 nm solarization resistant fiber optic cable (QP-600-1-SR, Ocean Optics, Dunedin, FL), and a 50 micron receiving fiber optic cable (P50-1-Vis-NIR, Ocean Optics, Dunedin, FL) was connected to the UV-Vis spectrometer.

Monomer solutions were prepared with 420 mM PEGDA, 35 mM VP, 210 mM TEA, and 5 µM Eosin Y in water (equivalent to 21.6% PEGDA, 2.8% TEA, 0.4% VP, 75.2% water). In the case of the purged samples, Argon was bubbled through the solution for 5 minutes prior to transfer to a PMMA cuvette for polymerization. These samples were polymerized under Nitrogen flow (8 psi). Between three and five replicates were performed at each condition.

3.3.3   Processing of UV-Vis Spectra

For each time point, baselines were fit to 10 points at each end of the wavelength range for peaks between 430 and 650 nm. The baseline-adjusted absorbance at the wavelength corresponding to the initial maximum peak height (523 nm) was monitored as a function of time.

During the polymerization reactions, the solutions underwent a phase change to a hydrogel, resulting in significant light scatter. To determine the point at which the absorbance signal is dominated by light scatter, the "cloudiness" of the solution was monitored by tracking the absolute absorbance at 430 nm. In addition, to account for contamination from the curing light, the ratio of the baseline-corrected absorbance at 500 nm to the absorbance at 523 nm was monitored. 500 nm is the wavelength of the curing light. When the ratio of 500 nm to 523 nm changes substantially, it is an indication that there is increased contamination from the curing light. The time point for this transition was found by fitting a spline to the ratio as a function of time and then calculating the maximum second derivative.

Single exponentials were fit to the inhibition periods and the periods immediately following the onset of polymerization. To ensure that the curing light infiltration and increased light scatter did not interfere with the ground state eosin absorbance measurements, the end point of the second regime was determined by finding the maximum of the second derivative of the absorbance at 523 nm and then fitting 80% of the absorbance data between the end of the inhibition period and the second derivative maximum. The maximum second derivative of the absorbance at 523 nm occurs before the change in the ratio of the absorbance at 500 nm and 523 nm. Fitting 80% of the data in this regime serves as an added precaution against inadvertently misinterpreting artifacts resulting from the light scatter caused by the polymerization.

3.3.4   Processing of FT-NIR Spectra

The vinyl group concentration was determined by integrating the peak area between 6229 and 6128.8 cm^{-1} for the first overtone of the =C-H bond(s) associated with the acrylate group at approximately 6160 cm^{-1}.

The inhibition periods were determined by first plotting the conversion (defined as $\frac{A_0-A}{A_0}$) as a function of time. The largest time for which a conversion of 0 was obtained was determined numerically and used as the starting point for 200 points to which a second order polynomial was fit as well as the initial guess to find the root (conversion=0) of the function. This fitting procedure was performed iteratively until the difference between two consecutive roots was less than 0.1 seconds.

The rate of polymerization was determined by differentiating the function generated by fitting a smoothing spline with smoothing parameter=1×10^{-5} to the raw conversion data starting near the root found through the iterative process. The resulting derivative was multiplied by the initial peak area to give the rate of polymerization. The intercept of the spline was also calculated and found to agree with the value determined through iteratively fitting a second order polynomial.

3.4   Results and Discussion

Eosin consumption was measured by monitoring the maximum absorbance peak for the ground state of eosin at 523 nm. This process is complicated by the gelation of the monomer solution as the polymerization progresses. As shown in Figure 3-2, the baseline shifts as the polymerization proceeds and contaminating light from the 500 nm curing light passes through to the detector (Figure 3-3), reducing the absorbance at 500 nm below the baseline. There is also an inversion in the absorbance at the peak fluorescence emission wavelength of eosin, 550 nm. The increased baseline absorbance is a result of increased probing light scatter as the polymer chains propagate and crosslink. The accompanying phase change permits additional light from the curing light through to the detector. It is necessary to account for these phenomena in interpreting the absorbance signal.
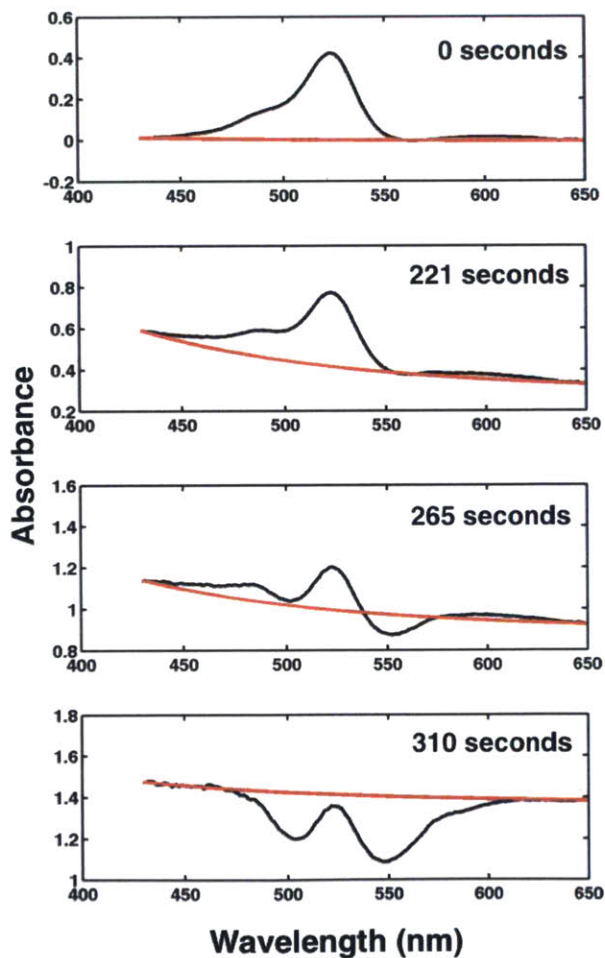
Figure 3-2. Baseline shifting and curing light contamination as polymerization progresses for solution of eosin, TEA, PEGDA, and VP illuminated with 500 nm light (3.7 mW/cm^2).
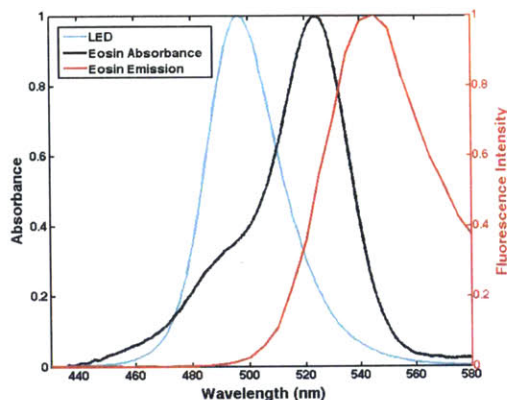
Figure 3-3. Absorbance spectra for the curing LED and the ground state of eosin in the monomer solution. The fluorescence emission spectrum for eosin is also shown. The spectra are normalized to the maximum peak absorbance.

As the polymerization proceeds, oligomers in solution scatter light, shifting the baseline absorbance (Figure 3-2). A wavelength dependence of the scattering is apparent with higher absorbance at shorter wavelengths (~430 nm) compared with longer wavelengths (~650 nm). This form of wavelength dependence is frequently indicative of Rayleigh scattering, for which the intensity of the scattered light scales with the inverse of λ^4.[96]

An examination of the absorbance spectra suggests that a combination of light scattering phenomena is taking place. To account for the wavelength independent absorbance as well as the apparent wavelength dependent scattering, the intensity of the transmitted light can be expressed as follows:

$$I = (aI_0)\left(1 - b/_{\lambda^4}\right)$$

where I_0 is the intensity of the probing light, a is a constant that accounts for the amount of wavelength-independent light scatter ($a=0$ corresponds to complete scatter or zero transmission), and $b/_{\lambda^4}$ represents the fraction of the remaining light that is scattered with a Rayleigh wavelength dependence.[96] This expression can be rewritten in terms of absorbance:

$$A = log_{10}\left(\frac{I_0}{I}\right) = -log_{10}(a) - log_{10}\left(1 - b/_{\lambda^4}\right)$$

If $b/_{\lambda^4} \ll 1$, the second term can be approximated as

$$log_{10}\left(1 - b/_{\lambda^4}\right) \approx \frac{1}{\ln(10)}\left(-b/_{\lambda^4}\right)$$

Reinserting into the expression for absorbance:

$$A = log_{10}\left(\frac{I_0}{I}\right) = log_{10}\left(\frac{1}{a}\right) + \frac{\left(b/_{\lambda^4}\right)}{\ln(10)} = a' + b'/_{\lambda^4}$$

51

Baselines were fit to the absorbance spectra, assuming the above dependence on wavelength. This allows for an assessment of the relative contributions of the wavelength independent and dependent scatter in the form of a' and b'. Figure 3-4 shows these constants as a function of time for the sample presented in Figure 3-2. In order to permit a comparison of the magnitudes of the constants, b' was normalized by the average of $1/_{\lambda^4}$. As shown, the wavelength-dependent scattering, as represented by b', comprises less than 20% of the total scattering reflected in the increased baseline absorbance. The wavelength-dependent parameter goes through a maximum at 235 seconds before decreasing. This behavior was consistent across all of the samples, under different curing light intensities and purging conditions, and suggests that the concentration and/or size of the light scattering oligomers is steadily increasing, finally reaching a point where the oligomers exceed the size for which Rayleigh scattering is possible, i.e. smaller than the probing wavelength, and the contribution from wavelength-dependent scattering consequently diminishes. The maximum could correspond to the point at which a phase change occurs and shorter oligomers react to form a cross-linked polymer network.
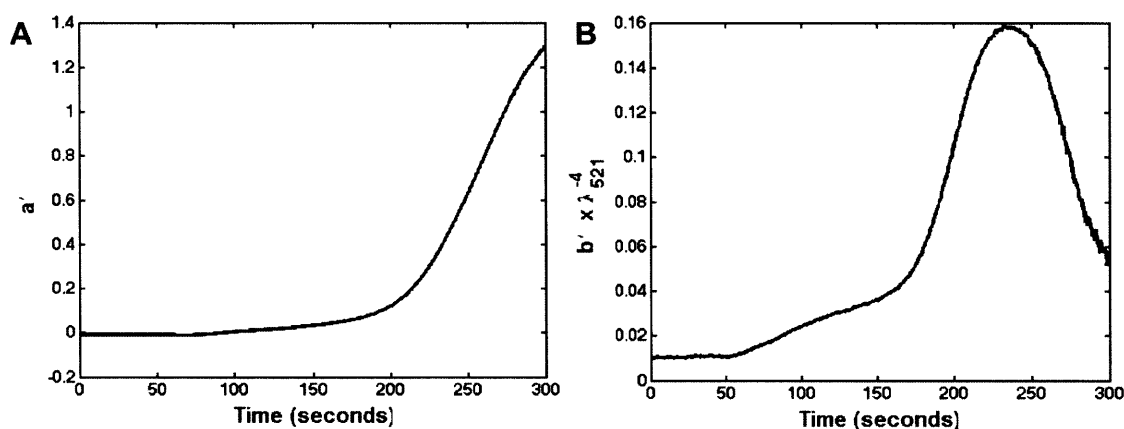
Figure 3-4. Baseline fitting parameters for solution of eosin, TEA, PEGDA, and VP illuminated with 500 nm light (3.7 mW/cm^2). A) Baseline fitting parameter, a', representing wavelength-independent scatter. B) Baseline fitting parameter, b', representing wavelength-dependent scatter and normalized by the average of 1/λ^4 (1/521nm^4).

The time at which b' reached its maximum and the conversion at that time are summarized in Table 3-1 for the different conditions tested. For both ambient and purged conditions, the time at which b' passes through a maximum decreases as the light intensity increases and the rate of polymerization increases. The conversion when b' is at a maximum is consistently between 0.27 and 0.37, further indicating that the change in b' is reflective of a phase change.

Table 3-1. Wavelength-dependent parameter: time and conversion at b' maximum

Intensity (mW/cm^2)	Time (b'$_{max}$) (seconds)		Conversion (b'$_{max}$) (seconds)	
	Ambient	Argon-purged	Ambient	Argon-purged
1.5	373 ± 37.9	181 ± 29.5	0.27 ± 0.03	0.33 ± 0.02
3.7	230 ± 11.8	147 ± 12.6	0.37 ± 0.003	0.31 ± 0.01
6	173 ± 29.5	111 ± 6.4	0.33 ± 0.01	0.30 ± 0.01
9.6	153 ± 29.5	103 ± 9.8	0.30 ± 0.02	0.29 ± 0.02

Figure 3-5 shows the absorbance at 523 nm and conversion as a function of time (A) and the rate of polymerization and absorbance as a function of conversion (B) for a representative sample that was irradiated with 500 nm light (3.7 mW/cm^2) under ambient conditions. The sample is the same one

presented in Figure 3-2. The first 43 seconds during which there is no polymerization (the conversion is 0) is the inhibition period. During this time, the oxygen present in solution reacts with radicals to form peroxy radicals,[41] which are fairly unreactive towards propagation and thus effectively inhibit the polymerization. Before the onset of polymerization, the absorbance at 523 nm decays at a nearly imperceptible rate (Figure 3-5). Once the oxygen in the system has been depleted, the polymerization begins and the maximum rate is achieved immediately, as shown in Figure 3-5B. The absorbance at 523 nm begins to decay more rapidly with the onset of polymerization. As the polymerization proceeds and the double bond conversion increases, the rate of polymerization slows. This rate reduction occurs as the polymer chains become cross-linked and a gel (polymer network) forms, slowing the diffusion of the monomers and propagating radicals. After 240 seconds, the rate of absorbance decay increases. As shown in Figure 3-2, at this point in the polymerization, an increase in the baseline absorbance and contamination from the curing light are already evident. This transition corresponds closely with the maximum in the wavelength-dependent parameter b', which occurs at 235 seconds, further suggesting an increase in the size of oligomers in solution are contributing to significant light scatter.
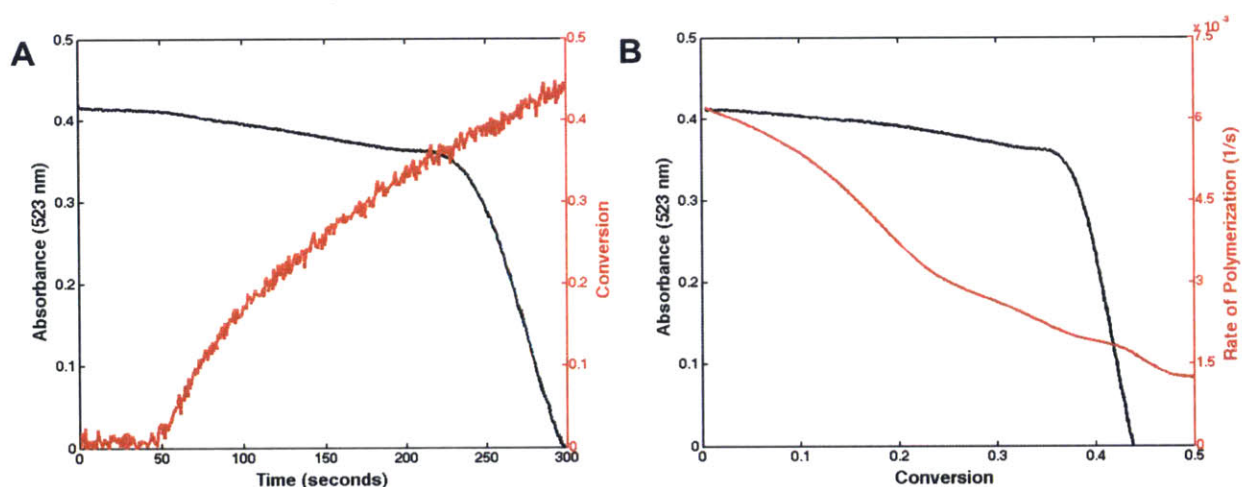
Figure 3-5. A) Absorbance at 523 nm and conversion as a function of time and B) absorbance and rate of polymerization as a function of conversion for a solution of eosin, TEA, PEGDA, and VP illuminated with 500 nm light (3.7 mW/cm2).

In order to assess the extent of the probing light scatter during the polymerization, the absolute absorbance (not baseline corrected) at a wavelength in the visible range was monitored. 430 nm was selected for this purpose as none of the species present in solution absorb at this wavelength and also because Rayleigh scattering effects are more pronounced at shorter wavelengths. As the reaction proceeds, the polymer chains grow and form cross-links, scattering the probing light and thereby increasing the absolute absorbance at 430 nm.

To determine the point at which infiltration of the curing light is first observed, the ratio of the peak height at 500 nm (the wavelength of the LED curing light) to the peak height at 523 nm (the wavelength at which the eosin absorbance is at a maximum) was tracked. A reduction in the absorbance at 500 nm relative to the absorbance at 523 nm indicates that light from the LED curing light is reaching the detector, altering the characteristic absorbance spectrum for eosin. It is worth noting that as eosin is consumed and the absorbance decreases, some peak broadening is expected and, consequently, a change in the ratio of the absorbance at 500 nm to that at 523 nm. However, peak broadening has the opposite effect, contributing to a slight increase in the ratio of the absorbance at 500 nm to that at 523 nm.

Figure 3-6 shows the absolute absorbance at 430 nm and the ratio of the absorbance at 500 nm to 523 nm for the sample in Figure 3-2. Around 240 seconds, where the rate of decay of the absorbance at 523 nm increases (Figure 3-5), the ratio of the absorbance at 500 nm to the absorbance at 523 nm begins a precipitous descent. Referencing Figure 3-5, it is also evident that the absorbance at 430 nm begins to increase when the conversion approaches ~10% with an even sharper increase when the conversion approaches 0.3 and the rate of polymerization begins to decrease. The rate reduction and the increased absorbance are both indicative of the formation of larger cross-linked polymer chains that likely serve to scatter light and hinder diffusion and consequently contribute to a reduced rate of polymerization.
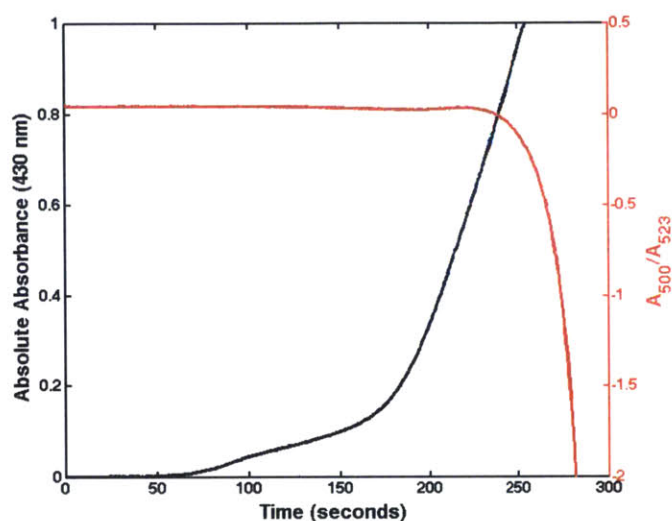
Figure 3-6. Monitoring baseline shifting (absorbance at 430 nm) and curing light contamination (ratio of absorbance at 500 nm to absorbance at 523 nm) for a solution of eosin, TEA, PEGDA, and VP illuminated with 500 nm light (3.7 mW/cm2).

The onset of the decrease in the ratio of the absorbance at 500 nm to 523 nm was determined by calculating the maximum of the second derivative. For the curve shown in Figure 3-6, this onset occurs at 250 seconds where the absorbance at 430 nm is equal to 1 (10% of the probing light transmitted). As shown in Table 3-2 for different curing light intensities under both ambient and argon purged conditions, there is a correlation between the change in the ratio of the absorbance at 500 nm to 523 nm and the absolute absorbance at 430 nm. The correlation between the absolute absorbance at 430 nm and the ratio of the absorbance at 500 nm to 523 nm suggests that a critical point is reached at which some fraction of the monomers in solution have been incorporated into a light-scattering, cross-linked polymer network.

Table 3-2. Baseline shift and curing light contamination: transition times

Intensity (mW/cm^2)	Time (A_{500}/ A_{523} maximum of 2nd derivative) (seconds)		Time (A_{430}=1) (seconds)	
	Ambient	Argon-purged	Ambient	Argon-purged
1.5	389 + 22.5	195 + 33.0	414 + 42.7	211 + 37.1
3.7	235 + 15.1	178 + 18.6	238 + 16.3	186 + 14.8
6	191 + 23.6	120 + 6.8	207 + 22.0	139 + 3.9
9.6	184 + 52.1	98 + 16.9	214 + 45.9	138 + 6.5

Table 3-3 shows the average conversions corresponding to the transition times summarized in Table 3-2. The onset of the sharp decline in the ratio of the absorbance at 500 nm to 523 nm and the point at which the absorbance at 430 nm is 1 consistently occur when the conversion is between 0.3 and 0.4, closely following the maximum in the wavelength-dependent light scattering parameter b'. Beyond this conversion, it is difficult to reliably determine the absorbance at 523 nm resulting from eosin in its ground state. However, it is still possible to draw conclusions from the change in absorbance prior to this transition and this analysis demonstrates the wealth of information contained within the absorbance data.

Table 3-3. Baseline shift and curing light contamination: conversion at transition times

Intensity (mW/cm^2)	Conversion (A_{500}/ A_{523} maximum of 2nd derivative)		Conversion (A_{430}=1)	
	Ambient	Argon-purged	Ambient	Argon-purged
1.5	0.31 + 0.04	0.35 + 0.02	0.32 + 0.04	0.37 + 0.02
3.7	0.38 + 0.01	0.34 + 0.01	0.38 + 0.01	0.35 + 0.01
6	0.35 + 0.01	0.31 + 0.01	0.37 + 0.01	0.34 + 0.01
9.6	0.33 + 0.04	0.29 + 0.03	0.37 + 0.02	0.35 + 0.01

As previously noted and shown in Figure 3-5, the rate of absorbance decay accelerates with the onset of polymerization. As shown in Figure 3-7, this acceleration was captured quantitatively by fitting single exponentials to the inhibition period (region 1) and the period immediately following the onset of the polymerization (region 2), but prior to the infiltration of the curing light and the sharp increase in the baseline absorbance (region 3). The single exponentials are shown in red and cyan.

For the representative sample shown throughout, the exponential decay constants during the inhibition period (the first 43 seconds) and the initial polymerization are, respectively 2.3 x 10^{-4} seconds^{-1} and 8.5 x 10^{-4} seconds^{-1}. The rate of decay increases 3.8x with the onset of polymerization.
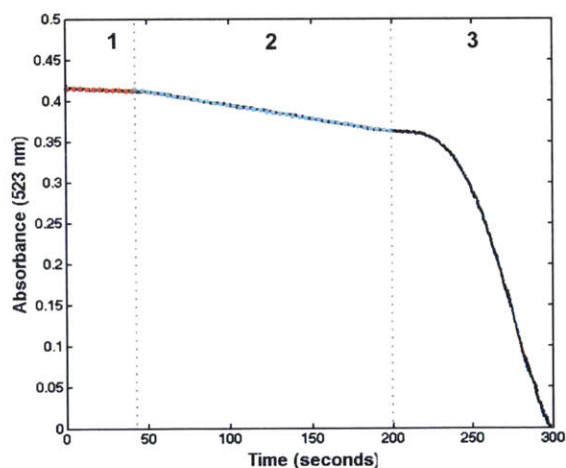
Figure 3-7. Fitting single exponentials to the inhibition period (region 1) and initial polymerization (region 2) for a solution of eosin, TEA, PEGDA, and VP illuminated with 500 nm light (3.7 mW/cm2) under ambient conditions. The black curve is the baseline-corrected absorbance at 523 nm. The red curve is a single exponential fit to the inhibition period, the first 43 seconds preceding polymerization. The cyan curve is a single exponential fit to the period immediately following the onset of polymerization, between 43 and 202 seconds. Curing light contamination affects the absorbance signal in region 3, which is excluded from the single exponential fitting.

Exponential decay constants measured under ambient and argon-purged conditions for increasing curing light intensities are shown in Figure 3-8 and Table 3-4. The decay constants increase with light intensity for both the inhibition period and initial polymerization period under ambient and argon-purged conditions. The dependence on light intensity appears exponential; a linear relationship between the decay rate constant and light intensity has previously been observed for photoinitiators that undergo direct photolysis.[88] A nonlinear dependence indicates that the number of photoinitiator molecules destroyed per photon absorbed increases with light intensity.[88] As more light reaches the sample, more of the eosin is excited from its ground state to its singlet state. From its singlet state, eosin can relax back to its ground state, react with TEA or oxygen, or undergo intersystem crossing to its triplet state. Once in its triplet state, eosin can react with itself, oxygen, or TEA. The exchange of an electron and proton with TEA produces the semiquinone form of eosin and a TEA radical, which can react with a monomer to initiate polymerization or react with oxygen to form a peroxy radical. Increasing the light intensity increases the rate at which eosin is excited and consequently the rates of the subsequent reactions. Thus, more of the eosin is irreversibly photobleached as it is consumed in termination reactions that convert it to its leuco form.

The onset of polymerization also has the effect of increasing the decay constant. The decay constants during the initial polymerization are between 3-6.3x greater than those during the inhibition period. At a curing light intensity of 1.5 mW/cm^2, the increase is most pronounced with the polymerization decay constant 5.5x higher than the inhibition period decay constant. As the curing light intensity is increased to 3.7, 6, and 9.6 mW/cm^2, the decay constant increases by a factor of 4.5, 3.7 and 3, respectively, with the onset of polymerization.

For the two higher curing light intensities (6 and 9.6 mW/cm^2), the average decay constant for the polymerization under argon-purged conditions is 1.3-2.1x higher than under ambient conditions, whereas at the other curing light intensities used, the polymerization decay constants for ambient and purged conditions were similar.

The experiments performed under ambient conditions were conducted in open vessels, permitting the diffusion of oxygen into the solution, although, as the polymerization progresses and the hydrogel forms, the rate of oxygen diffusion will slow. The initial concentration of dissolved oxygen should be close to 0.5 mM, the solubility in water; this is 100x greater than the concentration of eosin. For polymerization to occur, the oxygen concentration must be decreased to a level at which radical propagation reactions are favored over inhibition reactions. Independent of the curing light intensity, the absorbance decreases by 1% during the inhibition period. The consistency of this decrease reflects how the oxygen concentration must be reduced below a threshold level for the polymerization to proceed.

The slower rate of absorbance decay during the inhibition period suggests that ground state eosin is being regenerated in the presence of oxygen. In addition, the less rapid decay of the eosin absorbance with the onset of polymerization under ambient conditions relative to purged conditions is likely a consequence of the replenishment of oxygen by diffusion as it is consumed. This effect becomes more apparent as the light intensity is increased and the initiation rate and rate of oxygen consumption increase.

Slower rates of fluorescence decay have been associated with dye regeneration.[71] Xanthene dyes, such as eosin, are well known oxygen sensitizers. Oxygen has been reported to react with the triplet state of

eosin with a rate constant of $1.1 \times 10^9 \, M^{-1} s^{-1}$.[97] The two most commonly presented reactions between triplet eosin and oxygen are as follows:[98]

$$E^{3*} + O_2 \rightarrow E^{\cdot+} + O_2^{\cdot-}$$
$$E^{3*} + O_2 \rightarrow E + {}^1O_2$$
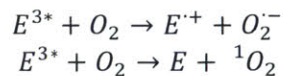
Of these, the second is considered to be the predominant reaction with a rate constant at least two orders of magnitude greater than the first reaction.[99] This is one pathway through which ground state eosin can be regenerated by oxygen. However, Avens & Bowman have presented an alternative route through which eosin can be regenerated:[15]

$$E^{3*} + TEA \rightarrow EH^{\cdot} + TEA^{\cdot}$$
$$R^{\cdot} + O_2 \rightarrow ROO^{\cdot}$$
$$EH^{\cdot} + ROO^{\cdot} \rightarrow ROOH + E$$
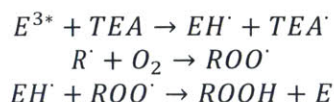
According to this mechanism, the semiquinone eosin ($EH^{\cdot}$) resulting from the reaction with TEA is susceptible to hydrogen abstraction by the peroxy radicals ($ROO^{\cdot}$) that result from the reaction of an initiating TEA radical or propagating radical (here, presented as $R^{\cdot}$) with oxygen. This regenerates the ground state eosin. Whether this reaction or the reaction that produces singlet oxygen is primarily responsible for the regeneration of eosin depends on the relative concentrations of TEA and oxygen as well as the rate constants for the reactions between the triplet state of eosin and oxygen and TEA. The initial concentration of TEA is 210 mM, 700x the concentration of oxygen. Thus, the probability of a triplet eosin encountering TEA is higher. However, the rate constant for the reaction between triplet eosin and oxygen is reported to be at least two orders of magnitude higher than that between triplet eosin and TEA,[97,98] which means that these reactions occur at comparable rates and likely both contribute to oxygen regeneration. This would be consistent with Avens & Bowman's suggestion that additional regeneration pathways, beyond the peroxy radical hydrogen abstraction, available to eosin in the presence of oxygen account for its ability to overcome 1000-fold excess oxygen as compared with only 100-fold excess 2,2,6,6-Tetramethyl-1-piperidinyloxy (TEMPO) inhibitor.[15]
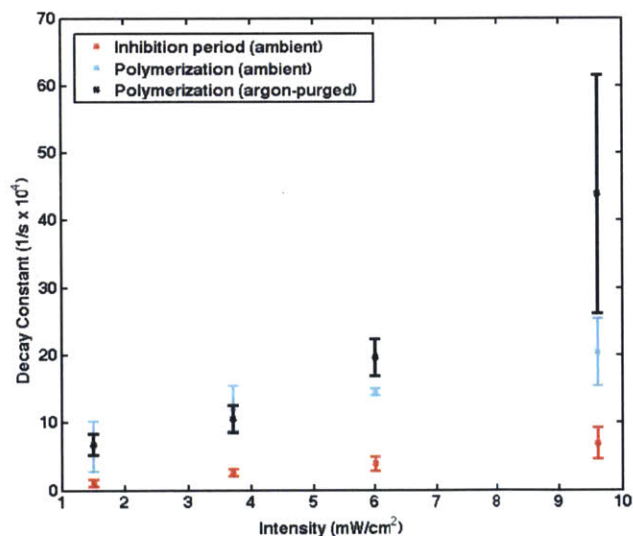
Figure 3-8. Exponential decay constants (τ, $A(t) = A_0 e^{-\tau t}$) for ambient and argon-purged conditions as a function of curing light intensity.

Table 3-4. Exponential decay constants for ambient and purged conditions at different curing light intensities

Intensity (mW/cm^2)	Inhibition Time (seconds)		τ (inhibition period, 1/s x10^4)	τ (polymerization, 1/s x10^4)	
	Ambient	Argon-purged	Ambient	Ambient	Argon-purged
1.5	142 + 25	17.8 + 2.7	1.2 + 0.5	6.6 + 3.7	6.8 + 1.5
3.7	42.2 + 1.2	5.6 + 2.4	2.7 + 0.5	12.2 + 3.3	10.5 + 2.0
6	27.7 + 4.0	0	4.0 + 1.0	14.6 + 0.5	19.6 + 2.8
9.6	20.0 + 3.5	0	7.0 + 2.3	20.5 + 5.0	43.9 + 17.7

Exponential Decay Constant, τ, $A(t) = A_0 e^{-\tau t}$

Assuming no primary termination reactions, the concentration of TEA radicals participating in initiation reactions at the onset of polymerization is 1.5-2x higher with argon purging. The maximum rates of polymerization (also the initial rates) are presented in Figure 3-9. The initial TEA radial concentration can be approximated based on the following expression for the rate of polymerization: [25]

$$R_p = k_p[M]\left(\frac{R_i}{2k_t}\right)^{0.5} = k_p[M]\left(\frac{k_i[M][TEA \cdot]}{2k_t}\right)^{0.5}$$

From this, it follows that $\frac{R_{p,1}}{R_{p,2}} = \left(\frac{[TEA\cdot]_1}{[TEA\cdot]_2}\right)^{0.5}$. The lower rate of polymerization under ambient conditions indicates that fewer TEA radicals are being formed as oxygen reacts with eosin in its singlet or triplet excited state and/or that oxygen is reacting with TEA radicals, preventing them from reacting with monomers and initiating polymerization. The lower polymerization rates and the lower absorbance decay rates under ambient conditions suggest that oxygen is being replenished by diffusion even as it is consumed and that it is regenerating eosin.
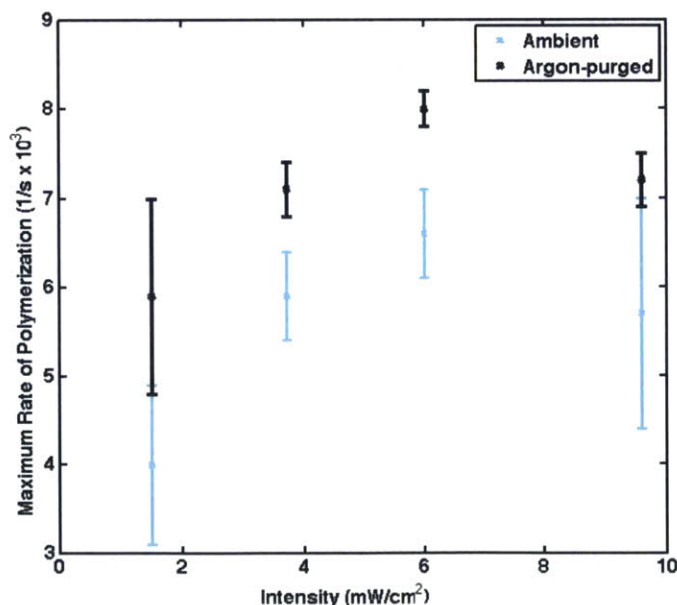
Figure 3-9. Maximum rate of polymerization as a function of curing light intensity for ambient and argon-purged conditions.

3.5 Conclusion

Dual monitoring with UV-Vis and FT-NIR allows for a more detailed understanding of polymerization kinetics and the properties of the growing polymer network. Here, we showed how light scattering in the visible spectrum can interfere with the absorbance signal from the photoinitiator in the photopolymerization of hydrogels, presenting a strategy for baseline fitting that accounts for both wavelength-dependent and wavelength-independent light scatter. In addition, we introduced three metrics for monitoring the extent of light scatter: a wavelength-dependent baseline fitting parameter b', the absolute absorbance at a wavelength in the visible range (430 nm), and the ratio of the absorbance at the wavelength of the curing light to the peak absorbance of the photoinitiator. These three metrics underwent significant transitions when the monomer conversion was between 0.3 and 0.4, implying the existence of critical phase change. Practically, these metrics were used to establish an upper bound on the reliability of the absorbance data. Having established a method for treating the data, we demonstrated how the coupled technique can be effectively used to investigate oxygen inhibition and dye regeneration. We showed that the consumption of eosin increases by a factor of 3 or more following the inhibition period, a finding consistent with previous reports of eosin regeneration by oxygen.

4 Photoinitiation Kinetics: Spectroscopy and Kinetic Model

4.1 Abstract

Eosin, a photoreducible dye, has been instrumental in enabling photopolymerization-based signal amplification reactions to be performed under ambient conditions; the mechanism through which eosin is able to circumvent oxygen inhibition is poorly understood. As a commonly used photosensitizer, the study of eosin's photochemistry dates back to the 1950s, and has revealed a complex network of reactions involving various excited species and producing reactive oxygen species. Here, we use absorbance spectroscopy to inform the development of a kinetic model, demonstrating the importance of modeling the reaction between triplet state eosin and its tertiary amine coinitiator as a two step process and hypothesizing the existence of additional photobleaching reactions as well as reactions involving the semireduced form of eosin.

4.2 Introduction

In its original form, polymerization-based signal amplification required inert gas purging to overcome oxygen inhibition. As described in earlier chapters, oxygen reacts with initiating and propagating radicals to give peroxy radicals that are essentially unreactive towards propagation and thus have the effect of terminating polymerization reactions.[16,65] Many strategies for overcoming oxygen inhibition in radical polymerization reactions have been investigated.[16] In addition to the common tactics of increasing the initiator concentration and light intensity and purging oxygen from the system with inert gases, UV initiators have been included along with visible-light initiators to consume oxygen and aid the production of thick films with tack free surfaces.[98] However, the majority of the UV initiators used also served as radical traps, reducing the rate of polymerization. In an example of one such system, Chesneau and Fouassier introduced an α-oxo oxime ester into a solution of eosin and methyldiethanolamine (MDEA) to mitigate the effects of oxygen inhibition.[45] Strikingly, they showed that the rate of photobleaching of eosin in a solution also containing oxime ester and MDEA was reduced when the monomer solution was not purged.[45] Avens and Bowman later published a study in which they showed that eosin is able to overcome a 1000-fold excess of oxygen and proposed a mechanism through which eosin is cyclically regenerated.[15] In the proposed mechanism, the peroxy radical abstracts a hydrogen from the semiquinone form of eosin produced in the reaction between triplet eosin and the tertiary amine. This has the effect of regenerating eosin in its ground state as shown below.

$$R - OO^{\cdot} + EH^{\cdot} \rightarrow R - OOH + E$$
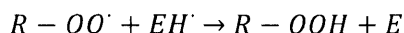
In a recently published study,[100] we showed that this mechanism for eosin regeneration in the presence of oxygen[15] is insufficient for capturing the role of oxygen in the system. As hypothesized by Avens and Bowman when they compared eosin's reduced ability to overcome a different inhibitor (2,2,6,6-Tetramethyl-1-piperidinyloxy or TEMPO) with its ability to overcome oxygen inhibition, this suggests that additional reaction pathways involving oxygen need to be included. Previous work has shown that singlet oxygen generation competes with electron transfer in amine activated Rose Bengal sensitized photochemistry.[101] Oxygen quenching of Rose Bengal has been studied quantitatively, revealing singlet oxygen as the main product with a small amount of superoxide radical anion produced as well.[102–104] Like Rose Bengal, eosin is a xanthene dye, and thus a singlet oxygen generator (the structures for both dyes are shown in Figure 4-1). The difference in heavy atom substitution reduces eosin's singlet oxygen quantum yield relative to Rose Bengal (0.39 vs. 0.76) as well as its triplet state quantum yield (0.28 vs. 0.75), while increasing its fluorescence quantum yield (0.63 vs. 0.08).[98]
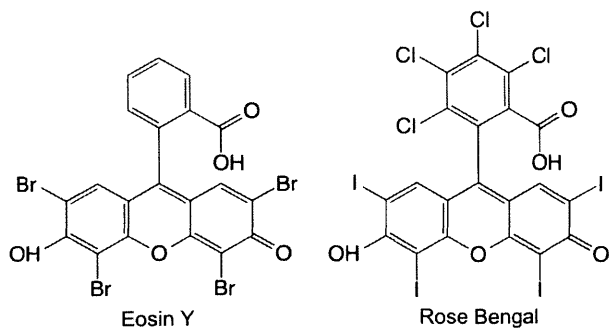
Figure 4-1. Eosin Y and Rose Bengal.

Eosin has been instrumental in enabling the performance of polymerization-based signal amplification under ambient conditions.[10,21,105] We have shown that the inclusion of a submicromolar concentration of eosin in a monomer solution allows these reactions to proceed without inert gas purging, producing sensitivities on par with those achieved with the original purged system.[6]

We are interested in developing an improved understanding of the role of oxygen in the eosin-activated system not only to facilitate the construction of a predictive model, but also to identify characteristics of eosin that may be shared by alternative photoinitiators. Steady-state fluorescence spectroscopy experiments have been used previously to study initiation mechanisms of three-component systems.[71,106,107] Slower rates of fluorescence decay have been associated with dye regeneration.[71] We used absorbance spectroscopy to investigate the effect of oxygen on eosin/ triethanolamine (TEA) initiation kinetics, measuring the decay in ground state eosin absorbance under irradiation and examining the contribution of oxygen as well as each component of the monomer solution individually.

As part of our study of the initiation kinetics and the impact of oxygen, we wanted to more fully examine the role of 1-vinyl-2-pyrrolidone (VP) in the system. Previous work has posited that VP functions as an accelerant with a more pronounced effect for systems that are constrained by diffusion limitations.[24] VP facilitates propagation through its high mobility and through the reactivity between N-vinyl amide and acrylate functionalities.[24] There is an optimum concentration both for accelerating the rate of polymerization[24] and, in the context of PBA, maximizing film thickness.[28] In addition to abstracting hydrogen from the semiquinone form of eosin, it is possible that peroxy radicals formed through the reaction of oxygen and propagating or initiating radicals may abstract hydrogen from VP. To test this theory, we replaced VP with 1-ethyl-2-pyrrolidone (EP), thereby eliminating the reactivity towards propagation while maintaining the potential susceptibility to hydrogen abstraction.

Here, we will first present the independent effects of oxygen, TEA, VP, EP, and poly (ethyleneglycol) diacrylate (PEGDA) on the absorbance decay of eosin before showing the combined effects of these various components. We will then summarize the reactions proposed in the literature relating to the photoactivation of eosin and its reduction by TEA and compare the results of a kinetic model based on the proposed reactions with the empirical observations.

4.3 Experimental

4.3.1 Materials

Poly (ethyleneglycol) diacrylate (PEGDA), 1-vinyl-2-pyrrolidone (VP), 1-ethyl-2-pyrrolidone (EP), triethanolamine (TEA), and Eosin Y were purchased from Sigma Aldrich. PMMA cuvettes were purchased from Eppendorf.

4.3.2 UV-Vis Monitoring

A multi-wavelength light emitting diode box containing a green 500 nm LED (FC8-LED, Prizmatix, Southfield, MI) was used to excite eosin to its singlet state. Irradiance or power density was controlled with a potentiometer and measured with a radiometer (6253, International Light Technologies, Peabody, MA) within the 400-700 nm range. In the case of the purged samples, Argon was bubbled through the solution for 5 minutes prior to transfer to a PMMA cuvette for monitoring. These samples were irradiated under Nitrogen flow (8 psi). A minimum of three replicates was performed at each condition.

10 x 2 mm PMMA cuvettes (UVette, Eppendorf, Hauppauge, NY) were used inside an adaptor with custom-made optical apertures. A 3D printed cap was placed on top of the cuvette to restrict the light from the LED to the sample volume. The sample volume used was 50 μL, which lead to sample dimensions of 2 mm x 10 mm x 2.5 mm, where the latter is the thickness in the direction of the excitation light from the LED. Samples were placed inside a CUV-ALL-UV 4-Way Cuvette Holder (Ocean Optics, Dunedin, FL) with SMA connectors for fiber integration. Fiber optic cables were connected perpendicularly for UV-Vis analysis. The UV-Vis probing light was fed into the cuvette holder via a 600 nm solarization resistant fiber optic (QP-600-1-SR, Ocean Optics, Dunedin, FL), and a 50 micron receiving fiber optic cable (P50-1-Vis-NIR, Ocean Optics, Dunedin, FL) was connected to the UV-Vis spectrometer. A fiber optic coupled UV-Vis spectrometer (USB4000-FL Miniature Fiber Optic Spectrometer, Ocean Optics, Dunedin, FL) was used to monitor absorbance within the 350-1000 nm range through a 10 mm pathlength. The acquisition time for the UV-Vis was set to ~ 0.5 s (50 ms integration time, 10 scans to average) with a boxcar width of 4. A water reference spectrum was collected prior to each experiment; the lack of absorbance of a solution of 420 mM PEGDA, 35 mM VP, 210 mM TEA was verified. The intensity of the probing light was adjusted to a threshold of ~5500.

Solutions consisting of 5 μM Eosin Y and 5 μM Eosin Y and 210 mM TEA were prepared and monitored at 4 irradiance levels (1.5, 3.7, 6, and 9.6 mW/cm^2). To look at the combined effects of various components on the absorbance of eosin, the following additional solutions were monitored at 3.7 mW/cm^2:

- 5 μM Eosin Y, 35 mM VP
- 5 μM Eosin Y, 420 mM PEGDA
- 5 μM Eosin Y, 210 mM TEA, 35 mM VP
- 5 μM Eosin Y, 35 mM EP
- 5 μM Eosin Y, 210 mM TEA, 35 mM EP

An aqueous solution of 5 μM Eosin Y and 210 mM TEA was monitored with the deuterium bulb off (only the halogen lamp emitting light) with the LED intensity set to 3.7 mW/cm^2 as well as turned off. These experiments were performed in order to verify that the probing light was not exciting eosin and contributing to spectra irregularities. This solution was also monitored in a diffusion experiment in

which the solution was purged for the first 14 minutes, after which the system was opened to allow for the diffusion of oxygen into the solution.

4.3.3 Processing of UV-Vis Spectra

For each time point, baselines were fit to 10 points at each end of the wavelength range for peaks between 360 and 430 nm and 430 and 560 nm. For the peak between 430 and 560 nm, the baseline-adjusted absorbance at the wavelength corresponding to the initial maximum peak height was monitored as a function of time. Between 360 and 430 nm, the peak at 410 nm was monitored.

4.3.4 Model Development

A system of ordinary differential equations was solved using ode15s.m in Matlab. The reactions and rate constants obtained from the literature are summarized in Table 4-1 at the end of the chapter.

4.4 Results and Discussion

4.4.1 Absorbance Spectroscopy

The absorbance spectrum between 380 nm and 600 nm was measured as a function of time under constant irradiation. The effect of each component on the absorbance decay of the ground state of eosin (517 nm) was assessed. A shown in Figure 4-2 and Figure 4-3, EP, VP, and PEGDA have an imperceptible effect. As evident in Figure 4-2 and Figure 4-3, there was more variability across the replicates in the purged experiments. This was likely a consequence of variations in the extent of oxygen uptake during the process of transferring the purged solution to the cuvette for spectroscopic monitoring.
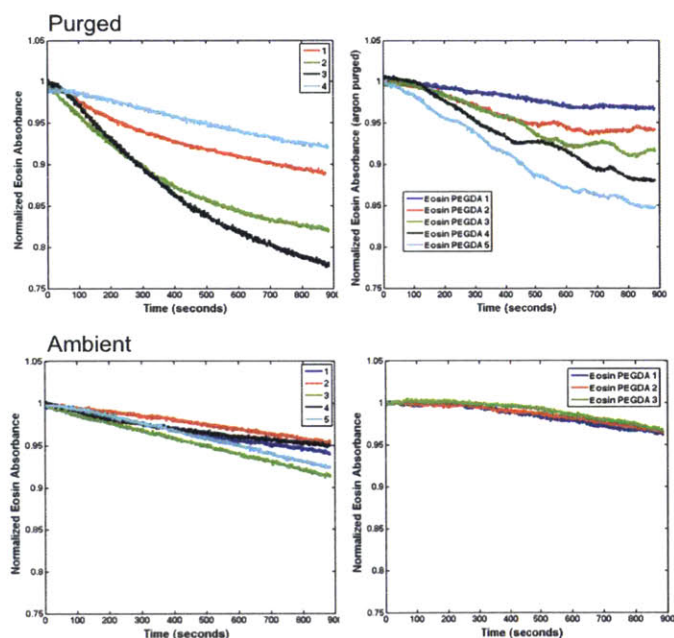
Figure 4-2. Effect of PEGDA (right) on the absorbance decay of eosin (517 nm) irradiated with 500 nm light (3.7 mW/cm^2) under argon purging (top row) and under ambient conditions (bottom row). The absorbance has been normalized by the initial absorbance. Each plot shows several replicate measurements.

Figure 4-3. Effect of EP (center) and VP (right) on the absorbance decay of eosin (517 nm) irradiated with 500 nm light (3.7 mW/cm^2) under argon purging (top row) and under ambient conditions (bottom row). The absorbance has been normalized by the initial absorbance. Each plot shows several replicate measurements.

As shown in Figure 4-4, the rate of decay of eosin absorbance at 517 nm increases with increasing curing light intensity; this could be a consequence of an increase in the rate of triplet-triplet annihilation reactions relative to first-order deactivation reactions.[103] The effect of light intensity is more pronounced under ambient conditions (bottom row) than for purged solutions (top row). In fact, at the maximum light intensity used (9.6 mW/cm^2), the profile for ambient conditions closely resembles that for purged conditions. At the lowest light intensity (1.5 mW/cm^2), the effect of oxygen on the rate of decay is more apparent; the rate is significantly reduced under ambient conditions. This could be a result of eosin regeneration through the reaction between the eosin triplet state and oxygen that also produces singlet oxygen.[98]
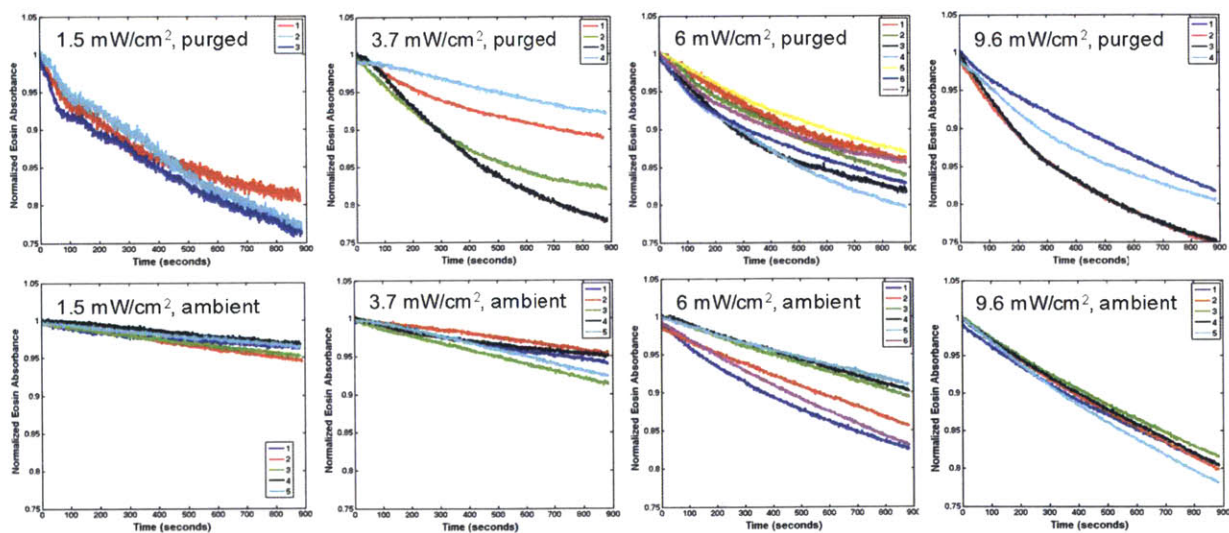
Figure 4-4. Effect of light intensity (increasing left to right) on the absorbance decay of eosin (517 nm) irradiated with 500 nm light under argon purging (top row) and under ambient conditions (bottom row). The absorbance has been normalized by the initial absorbance. Each plot shows several replicate measurements.

Having ascertained the extent of photobleaching for eosin in response to irradiation with 500 nm light at increasing intensity, a reducing agent, TEA, was introduced. It should be noted that the addition of TEA increases the pH from 7 to 9. Although xanthene dyes are known to undergo color changes in response to changes in pH,[108] it has been established that eosin is present only in its dianionic form at pH values greater than 6.[109] The addition of TEA also did not shift the maximum absorbance peak as would be expected if the pH were causing the dianionic eosin to assume a different form. The amine reduces the triplet state of eosin to give an amine radical cation and the semireduced form of eosin. The amine radical cation can either transfer a proton to the semireduced eosin to give the semiquinone and an α-aminoalkyl radical or back electron transfer can occur. As shown in Figure 4-5, the rate of decay of the absorbance at 517 nm increases substantially as the amine reacts with eosin. At the higher light intensities, the eosin is nearly completely consumed. It is evident that oxygen reduces the rate of decay significantly. Similar to a previous report with eosin, methyldiethanolamine, and a UV initiator (α-oxo oxime ester),[45] the absorbance decay of eosin with the amine is slower in nonpurged solutions. This suggests that eosin is being regenerated in the presence of oxygen.
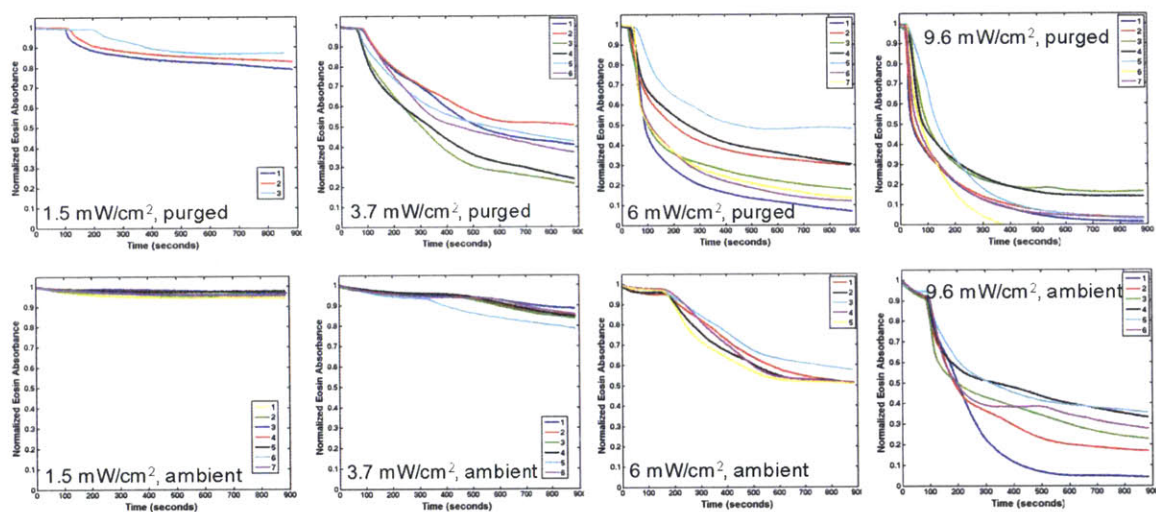
Figure 4-5. Effect of light intensity (increasing left to right) on the absorbance decay of eosin (517 nm) irradiated with 500 nm light in the presence of TEA under argon purging (top row) and under ambient conditions (bottom row). The absorbance has been normalized by the initial absorbance. Each plot shows several replicate measurements.

Each absorbance decay curve consists of two regimes; slow decay followed by more rapid decay. It is possible that oxygen is consumed during the first regime allowing for the much more rapid photobleaching of the second regime. For the argon-purged samples, this would mean that the appearance of the first regime is an indication that there is some residual oxygen present in the solution.

In addition to the peak for the ground state eosin at 517 nm, with the addition of the amine, a small peak at 410 nm was evident. This peak corresponds to the semireduced form of eosin,[110] which is the intermediate formed following electron transfer from the amine. Figure 4-6 shows the absorbance at 410 nm for the samples shown in Figure 4-5. Here, we see that more of the semireduced species is produced and more rapidly at higher light intensities. The absorbance of the semireduced species increases as the ground state absorbance decreases. The semireduced species is also consumed more rapidly at higher light intensities. As demonstrated in Figure 4-5, this is likely a result of the consumption of the ground state eosin, from which the semireduced species is derived. The absorbance from the semireduced species is significantly reduced in the presence of oxygen. It appears that oxygen either

rapidly consumes the semireduced species or prevents its formation. Even in the cases in which the ground state eosin absorbance decay is more rapid under ambient conditions, less of the semireduced species is observed in the presence of oxygen (compare 6 mW/cm^2 with 1.5 mW/cm^2 with argon purging). This suggests that the semireduced absorbance is not solely dependent on the amount of ground state eosin that has been reacted, but that there is also a separate effect of oxygen. In 1962, Oster et al. reported a reduced lifetime for an intermediate species (possibly the semireduced eosin) in the presence of oxygen.[111] It has been proposed that the semireduced species will react with oxygen, regenerating eosin and producing superoxide in the process.[112] The rate at which the eosin absorbance decays is likely significant; faster rates result in a faster rate of formation of the semireduced species, which could mean that the semireduced species is generated at a faster rate than it is consumed.
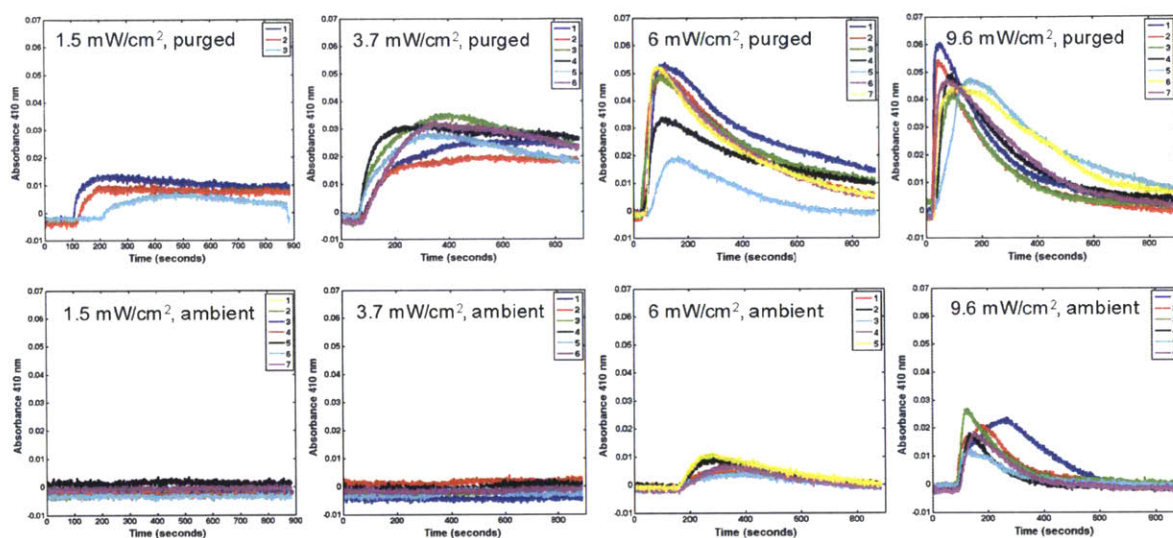
Figure 4-6. Appearance of peak at 410 nm for solutions of eosin and TEA irradiated with 500 nm light at increasing light intensities (left to right) under argon purging (top row) and under ambient conditions (bottom row). Each plot shows several replicate measurements.

It should be noted that in the presence of amine, the absorbance peak underwent a hypsochromic shift with in some cases, shifts from 517 nm to 493 nm (the absorbance maximum of fluorescein). This is shown in Figure 4-7 for a solution of eosin and TEA that was irradiated under nitrogen purging for 14 minutes (840 seconds), after which the system was opened to the atmosphere, allowing for the diffusion of oxygen into the solution. The absorbance spectra are shown for 6 different time points; for the first 4 time points shown, the absorbance maximum shifts to shorter wavelengths and the absorbance decreases as the eosin is consumed. Once the system is open to the atmosphere, the absorbance increases at the shifted maximum. Such shifts have previously been attributed to eosin debromination, which is a result of the photochemical decomposition of semireduced eosin.[111,113–115] Kimura et al. reported that debromination requires the photoexcitation of the semireduced species,[115] which could potentially occur as a result of excitation by the UV-Vis probing light. Loss of its bromine atoms would decrease the triplet state quantum yield of eosin and, consequently, its photoinitiation efficiency.[98] Hypsochromic shifts have also been associated with dimerization;[116] however, the absorbance maximum of the eosin dimer occurs at 480 nm.[117,118]
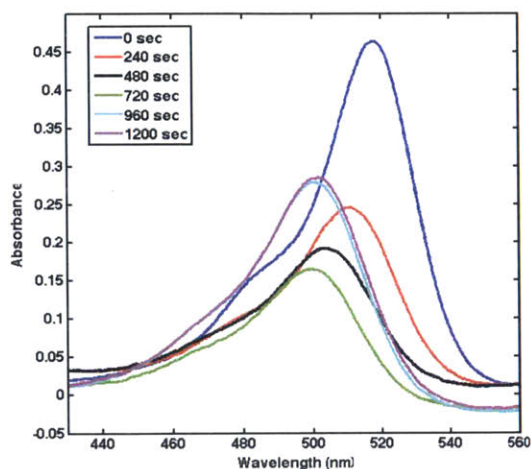
Figure 4-7. Hypsochromic shift and regeneration upon introduction of oxygen for a solution of eosin and TEA irradiated with 3.7 mW/cm^2 500 nm light.

The results of three replicate experiments in which solutions of eosin and TEA were irradiated under nitrogen purging for 840 seconds, after which the system was opened to the atmosphere are shown in Figure 4-8. The normalized absorbance of the eosin ground state is shown in Figure 4-8A. Reintroducing oxygen at 840 seconds results in an increase in the absorbance at 517 nm at ~900 seconds, indicating that some of the ground state is regenerated. Figure 4-8B shows the normalized absorbance at 500 nm. The hyposochromic shift results in a 20% increase in absorbance relative to the initial absorbance when the reaction was stopped at 1200 seconds. The shift in the maximum absorbance is shown in Figure 4-8D, where it is apparent that under purging, the peak steadily shifts to shorter wavelengths, and stops upon the reintroduction of oxygen. The effect of introducing oxygen on the semireduced species is shown in Figure 4-8C. As the absorbance increases at 500 nm and 517 nm, the absorbance at 410 nm decreases. This could indicate that oxygen reacts with the semireduced species and effectively competes with the debromination reaction, for which the semireduced species is also the precursor. Alternatively, the disappearance of the semireduced species once oxygen is reintroduced could indicate that the semireduced species is not formed if the triplet state eosin preferentially reacts with oxygen rather than TEA. Hypsochromic shifts were observed for purged solutions of eosin and TEA for each irradiation condition, but only at higher light intensities (6 and 9.6 mW/cm^2) for solutions irradiated under ambient conditions. This is consistent with the debromination reaction occurring as a result of the photochemical decomposition of the semireduced species, which was only observed at higher light intensities under ambient conditions.
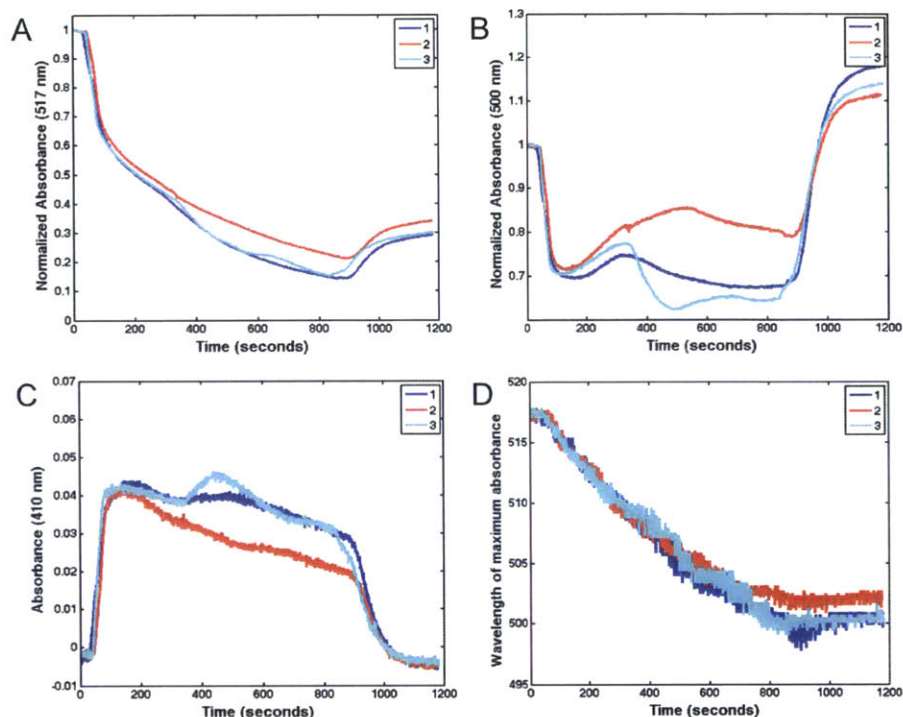
Figure 4-8. Regeneration by oxygen. Solutions of eosin and TEA were irradiated with 3.7 mW/cm^2 500 nm light under nitrogen purging for 840 seconds, after which the system was opened to the atmosphere to allow for the diffusion of oxygen into the solutions. A) The absorbance at 517 nm normalized by the initial absorbance for three replicate measurements. B) The absorbance at 500 nm normalized by the initial absorbance for three replicate measurements. C) The absorbance at 410 nm for three replicate measurements. D) The hypsochromic shift of the maximum absorbance wavelength.

The absorbance at 517 nm and 410 nm for eosin and TEA solutions to which EP or VP have been added are shown in Figure 4-9 and Figure 4-10, respectively. EP, which lacks a carbon-carbon double bond and hence should be unreactive towards propagation, appears to accelerate the absorbance decay of eosin slightly under both purged and ambient conditions. The increased decay under ambient conditions would be consistent with the hypothesized peroxy radical hydrogen abstraction from EP. If peroxy radicals abstract hydrogens from both the semiquinone form of eosin and EP, less eosin will be regenerated when EP is added to the solution, as appears to be the case. The increase in the semireduced species with the addition of EP under ambient conditions suggests that EP may also react directly with one of the species competing for reaction with the semireduced species (namely oxygen and the triethanolamine radical cation), and thereby inhibit the ability of that species to react with the semireduced eosin. If EP reacts with the triethanolamine radical cation, the peroxy radical concentration would decrease, which could also result in less regeneration of eosin.

VP accelerates the absorbance decay of eosin in a much more marked fashion, increasing the percentage of eosin that is consumed from ~15% to more than 40% under ambient conditions after 900 seconds. Under purged conditions, nearly all of the eosin is consumed in under 200 seconds in comparison with between 50% and 80% after 900 seconds without VP (Figure 4-9). Whereas in the absence of VP, an accelerated rate of disappearance of eosin appears to correlate with an accelerated rate of appearance of the semireduced species, when VP is added to the solution, the semireduced species is not observed. This suggests that, like oxygen, VP either reacts with semireduced eosin and that eosin is not regenerated in the process or that VP reacts with a precursor to semireduced eosin.
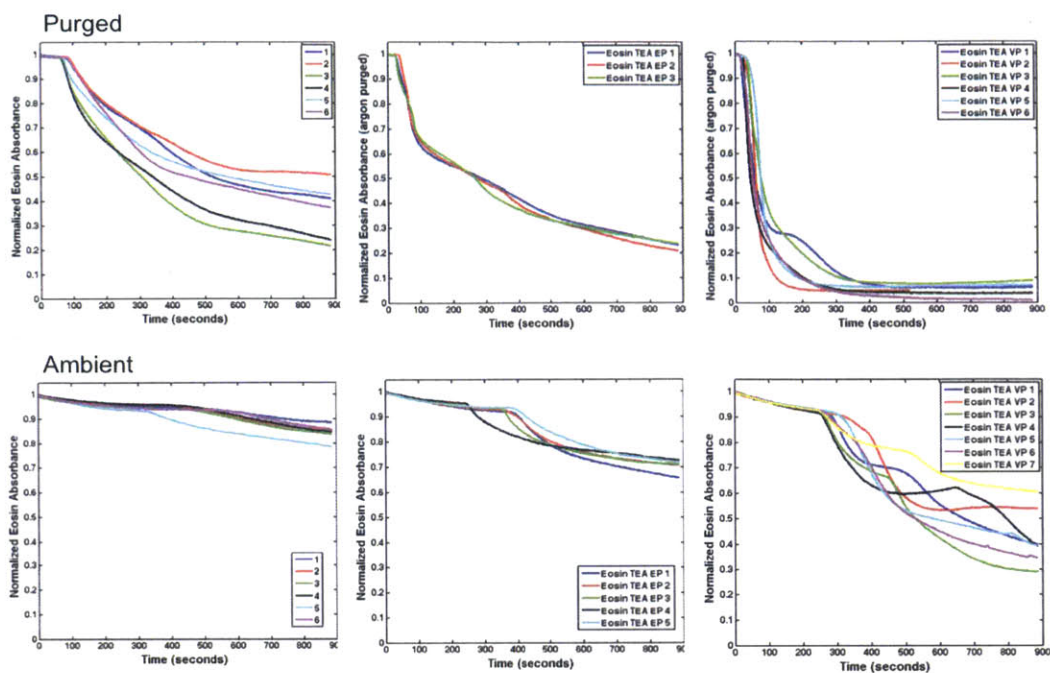
Figure 4-9. Effect of EP (center) and VP (right) on the absorbance decay of eosin (517 nm) irradiated with 500 nm light (3.7 mW/cm^2) in the presence of TEA under argon purging (top row) and under ambient conditions (bottom row). The absorbance has been normalized by the initial absorbance. Each plot shows several replicate measurements.
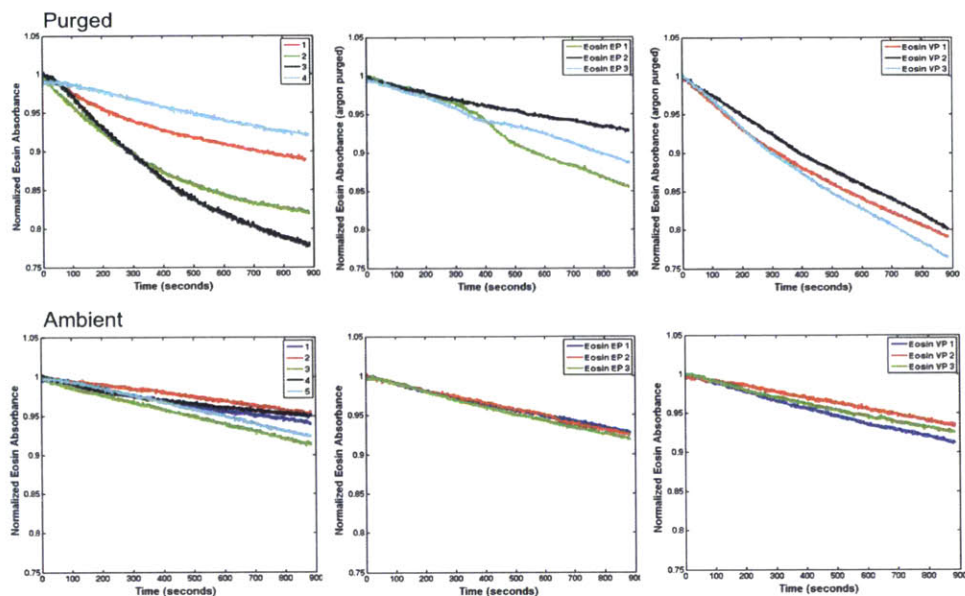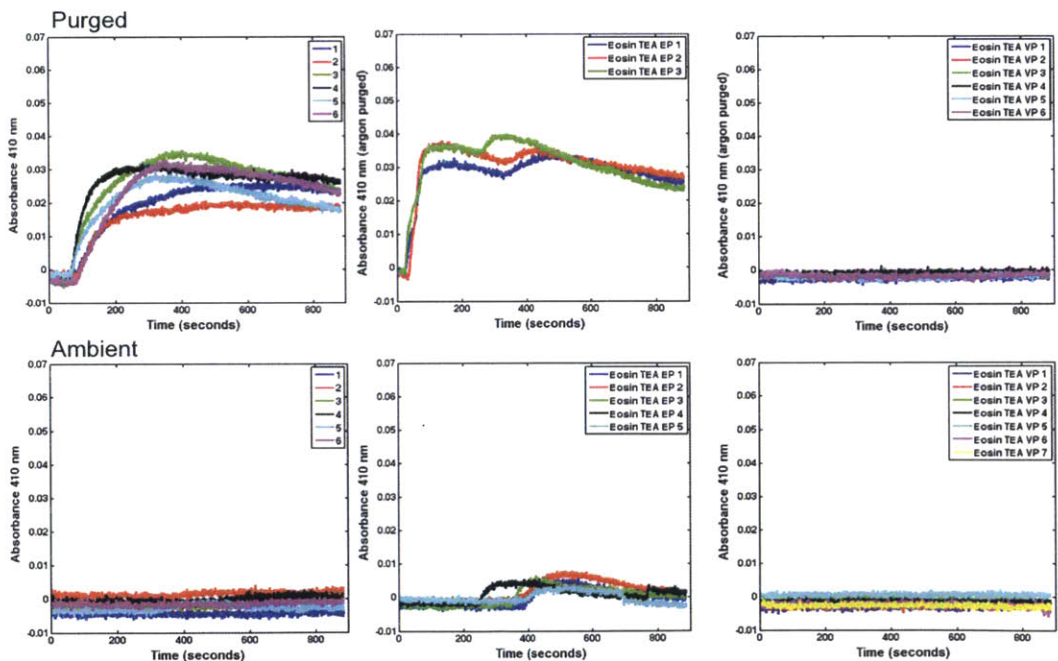

Figure 4-10. Effect of EP (center) and VP (right) on the appearance of the peak at 410 nm for solutions of eosin and TEA irradiated with 500 nm light (3.7 mW/cm^2) under argon purging (top row) and under ambient conditions (bottom row). Each plot shows several replicate measurements.

4.4.2 Model discussion and results

Flash photolysis experiments to investigate the photochemical reactions of eosin date back to the 1950s. The primary reactions involving eosin, tertiary amines, and oxygen identified over the course of the last several decades are summarized in Table 4-1 at the end of this section. The table is formatted so that reactions involving only eosin species are listed first, followed by reactions involving eosin and oxygen, eosin and TEA, and, finally, eosin, TEA, and oxygen. Reported rate constants, half-lives, and the corresponding references are also listed.

Upon the absorption of photons, eosin is excited to its singlet state according to the following rate expression:

$$R_0 = \frac{\varepsilon I_0 [E]}{E'}$$

where ε is the absorptivity of eosin at the wavelength of irradiation, I_0 is the light intensity, [E] is the concentration of eosin in its ground state, and E' is the photon energy at the wavelength of irradiation. The values used in the model for these parameters as well as the initial concentrations of the reactants are summarized in Table 4-2. As shown in Table 4-1, once in its singlet state, the excited eosin molecule can either return to the ground state or undergo intersystem crossing to its triplet state. In the triplet state, eosin can participate in quenching reactions with the ground state and the triplet state and form semireduced and semioxidized eosin. The triplet eosin reaction with ground state eosin (reaction 8) was proposed in 1956 when it was shown that the overall quantum yield decreased with increasing eosin concentration.[119] Only the reactions in black were included in the model; the reactions in gray are included to give a complete picture of the reactions that have been proposed in the literature. Reactions 4, 5, 6, 10, and 11 were excluded because the concentrations of the participating species were so low that the contributions from these reactions were imperceptible. Reaction 13 was originally proposed on the basis of Lindqvist's early work studying fluorescein;[120] however, Lindqvist did not include this reaction in his later study of the transient species of eosin[110] and we have found no other reports of dimer formation, so this reaction was excluded. As the semireduced and semixoxidized species do not decay by first order kinetics,[121] decay of these species to ground state eosin was not included in the model, although approximate half-lives for these species are included in the table (14, 15 in Table 4-1).[121]

Reactions 20 and 21 were not included in the model as there is little evidence for these reactions in the literature and they have been proposed by few sources.[97,122] Reaction 22 was excluded as the eosin species quenching the singlet oxygen was not identified and the reactions were conducted under illumination.[123,124] Second-order self-dismutation of superoxide has been found to be negligible,[125] and thus was not included. Reaction 26 was excluded as the excited singlet state of eosin is extremely short lived and, therefore, this reaction makes no perceptible contribution. Finally, reactions 30 and 32 were not included in the model as hydrogen abstraction from the semiquinone form of eosin by oxygen (reaction 30) is expected to occur at a much slower rate than the peroxy radical hydrogen abstraction and without this reaction generating hydroperoxyl radicals, reaction 32 cannot occur.
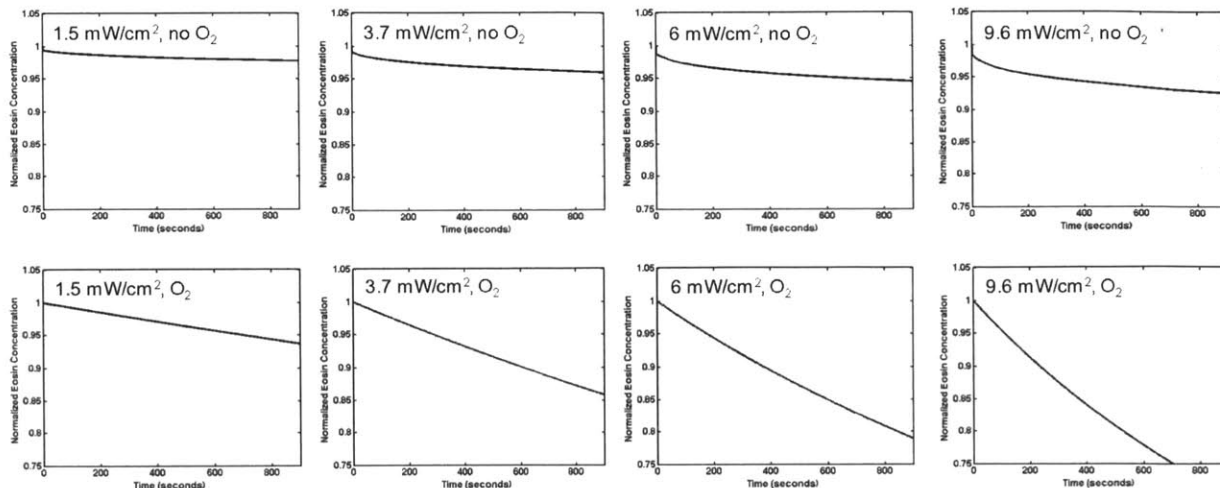
Figure 4-11. Simulation of the effect of light intensity (increasing left to right) on the consumption of eosin irradiated with 500 nm light (top row). The effect of adding oxygen is shown in the bottom row. The eosin concentration is normalized by the initial concentration (5 µM).

The model's predictions for the consumption of eosin in a solution being irradiated with increasing light intensity and with the addition of oxygen are presented in Figure 4-11. As observed experimentally, the eosin concentration decreases more rapidly as the light intensity is increased. In the model, this is a consequence of the increased concentration of semireduced eosin, which reacts with itself to give the leuco form of eosin (reaction 12). The rate constant for reaction 12 is an upper estimate based on a calculation of the encounter rate of two semireduced eosin molecules.[120] This reaction presents the only route for irreversible photobleaching of eosin to the leuco form. The discrepancy between the model's predictions for eosin consumption in the presence of oxygen with the experimental absorbance profiles suggests the existence of additional photobleaching reactions or reactions involving semioxidized eosin. The model does not predict the reduced consumption of eosin in the presence of oxygen observed experimentally, which is a consequence of oxygen reacting with semireduced eosin (reaction 19) and thereby preventing the semireduced eosin from reacting with the semioxidized eosin to produce two eosin molecules in the ground state (reaction 9). This results in an accumulation of the semioxidized species and less regeneration of the ground state. The existence of other photobleaching reactions is implied by the model's prediction of less than 10% consumption of eosin at the highest light intensity as compared with a 25% decrease in the absorbance (Figure 4-4) even with the rate constant for reaction 12 set at the encounter rate. It has been shown that the photobleaching of eosin is related to the accumulation of the triplet state;[126] this possibly suggests that additional photobleaching reactions should involve the triple state eosin.
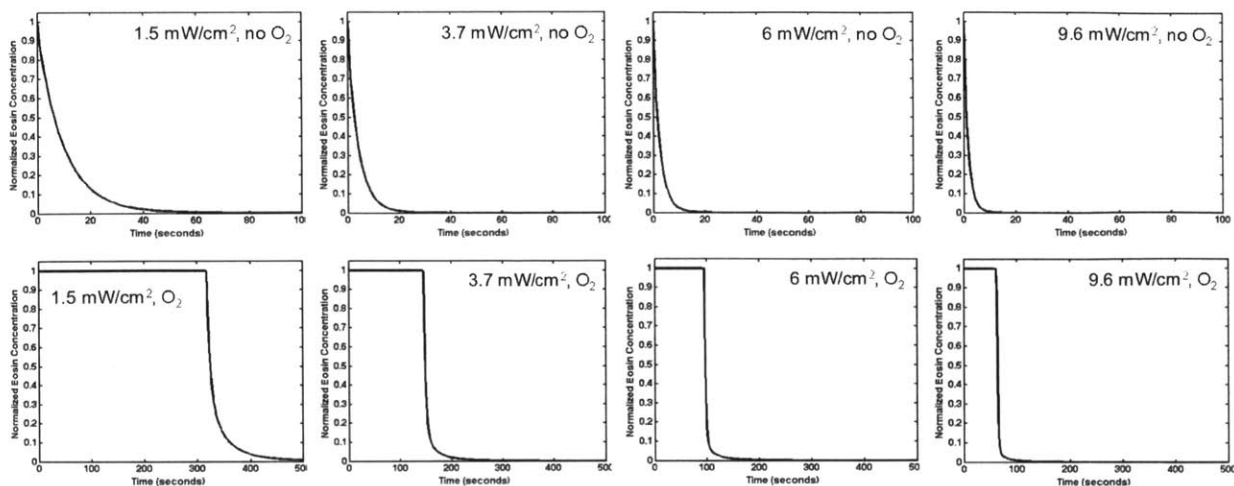
Figure 4-12. Simulation of the effect of light intensity (increasing left to right) on the consumption of eosin irradiated with 500 nm light with TEA (top row). The effect of adding oxygen is shown in the bottom row. The eosin concentration is normalized by the initial concentration (5 µM).

The normalized eosin concentration profiles when TEA is added for increasing light intensity and with oxygen are shown in Figure 4-12. The rate constant for reaction 25 was determined from literature values reported for triplet state quenching by the amine where the decay of the triplet state was monitored.[127–129] Rather than simplifying the eosin/TEA reaction to directly give the semiquinone and TEA radical, reactions 28 and 29 were included in order to capture the appearance of the semireduced species seen experimentally. Comparing the model predictions with the absorbance profiles in Figure 4-5, it is first apparent that the model overpredicts the consumption of eosin as well as the rate of consumption. The time scales on the plots in Figure 4-12 have been adjusted to show the effect of light intensity. The absorbance profiles all consisted of an initial plateau region followed by a more dramatic decline in absorbance. This plateau region was likely due to residual oxygen, which would account for its absence in the model results when the initial oxygen concentration is set to 0. For the simulations in which oxygen is included, the model underestimates the duration of the plateau region by approximately 50-70%. At 1.5 mW/cm^2, the model predicts ~300 seconds as compared with the experimentally observed 900 seconds or more. At 9.6 mW/cm^2, the model predicts ~60 seconds relative to ~100 seconds obtained experimentally. For every condition simulated, the model predicts complete consumption of eosin. This is at odds with the experimental observations, where complete consumption was only achieved at the highest light intensity. The accelerated consumption predicted by the model could be a result of an overestimate of the activation rate R_0.
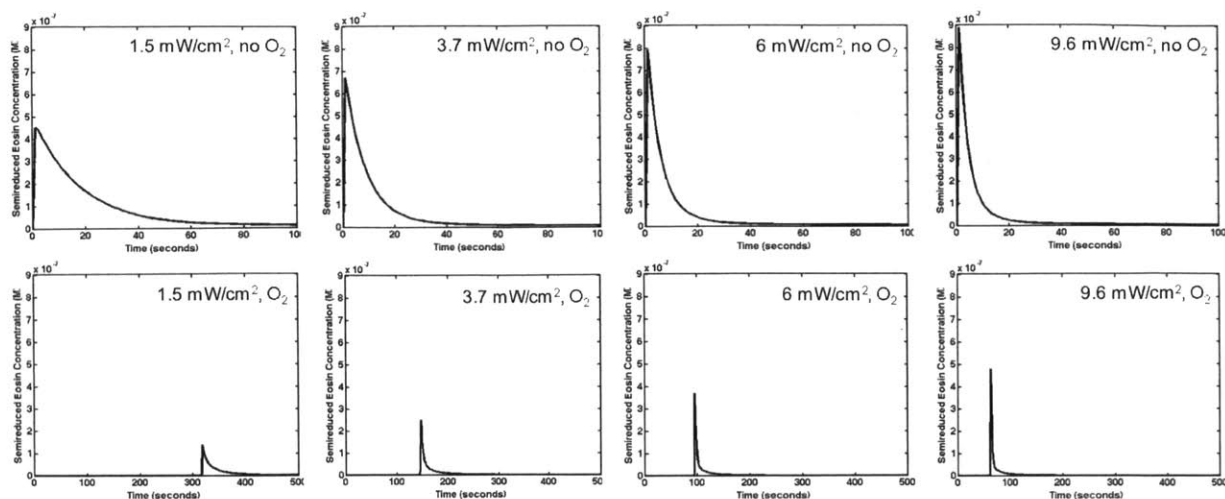
Figure 4-13. Simulation of the concentration of semireduced eosin in a solution of eosin and TEA irradiated with 500 nm light at the indicated light intensities. The effect of adding oxygen is shown in the bottom row.

The model's predictions for the semireduced species are shown in Figure 4-13. In order to capture the experimentally observed trends, the uncertain rate constants (reactions 28, 29, 33, 34) had to be adjusted to fall within certain ranges. The targeted experimental trends include the reduction in the semireduced eosin concentration in the presence of oxygen, the increase in the semireduced eosin concentration with increasing light intensity, and, for the cases in which oxygen is present, the appearance of the semireduced species once the oxygen is sufficiently depleted. In addition, the model was designed to capture the relative concentrations of semireduced eosin at the various conditions simulated; for example, Figure 4-6 shows that the semireduced eosin absorbance for a solution irradiated with 6 mW/cm^2 light under ambient conditions approached the absorbance measured for a solution irradiated with 1.5 mW/cm^2 under purged conditions. The extinction coefficient for the semireduced species has been reported as 40,000 M^{-1}cm^{-1}.[110] Using this value and assuming that Beer's Law applies, the maximum concentration of the semireduced species varies between 0.25 µM (1.25 mW/cm^2) and 1.5 µM (9.6 mW/cm^2).

The accumulation of a detectable amount of the semireduced species when TEA is present in the solution and its disappearance under ambient conditions imply a competition between several reactions. The amine reduces the triplet state of eosin to give an amine radical cation and the semireduced form of eosin. The semireduced species can then react with the amine radical cation to give the semiquinone and an α-aminoalkyl radical (reaction 28) or it can transfer the electron back to the amine radical cation (reaction 29). The reduction of the semireduced species in the presence of oxygen suggests that oxygen also reacts with the semireduced eosin (reaction 19) and that this reaction occurs at a faster rate than either of the reactions with the amine radical cation. Alternatively, as previously noted, the reduction in the semireduced eosin concentration in the presence of oxygen could suggest that oxygen prevents the formation of the semireduced species by reacting with its precursors. We tested the first alternative.

In order to capture the concentration trends, it was critical that the reaction between the semireduced eosin and oxygen (reaction 19) be favored over the reactions between the semireduced eosin and the TEA radical cation (reactions 28 and 29). The rate constant for reaction 19 has previously been estimated to fall within the range 10^7-10^9 M^{-1}cm^{-1}.[112] Here, the value was set to 10^8 M^{-1}cm^{-1} as increasing the rate constant to 10^9 M^{-1}cm^{-1} decreased the maximum concentration of semireduced eosin at 9.6

73

mW/cm^2 relative to 6 mW/cm^2. The rate constants for reactions 28 and 29 were set to 10^4 M^{-1}cm^{-1}. Increasing either of these rate constants by an order of magnitude decreases the maximum concentration of semireduced eosin by a factor of 4 or more when oxygen is included with less than 6% decrease when oxygen is not included. This suggests that the rate constant for reaction 19 must be several orders of magnitude higher than those for reactions 28 and 29 in order for the reaction between the semireduced eosin and oxygen to occur preferentially and produce the experimentally observed trend.

The final two reactions in the model are the reaction between the peroxy radical and the semiquinone form of eosin to regenerate ground state eosin (reaction 33) and an additional reaction in which the peroxy radical abstracts a hydrogen from TEA (reaction 34). The rate constant for reaction 34 was set to 10^4 M^{-1}s^{-1} in line with the slow oxidation rates reported for tertiary amines,[130] while the rate constant for reaction 33 was set at the diffusion limit.[100] Increasing the rate constant for reaction 34 accelerated the rate of oxygen consumption, reducing the duration of the initial plateau period. This is due to the fact that the TEA concentration is several orders of magnitude higher than the semiquinone concentration. In order to see any eosin regeneration, it follows, therefore, that the rate of reaction 34 must be smaller that the rate of reaction 33. Otherwise, the oxygen would be completely consumed without any eosin regeneration and the large excess of TEA would entirely prevent any oxygen inhibition. The sensitivity of photopolymerization-based signal amplification reactions to small changes in eosin concentration indicates that this is not the case.[10] Reducing the rate constant for reaction 33 from 10^9 to 10^7 M^{-1}cm^{-1} had the effect of reducing the duration of the initial plateau period slightly; the effect was not as pronounced as for the case in which the rate constant of reaction 34 was increased. Both increasing the rate constant for reaction 34 and decreasing the rate constant for reaction 33 led to a slight increase in the semireduced species. Completely eliminating reaction 34 extended the plateau period by ~30%, while the semireduced eosin concentration was unaffected. Thus, in order to achieve the longer periods of slow eosin consumption and capture the trends in the concentration of the semireduced species observed experimentally, it is important to minimize the reaction 34 rate constant relative to the reaction 33 rate constant.

Table 4-1. Reaction summary

Reaction	Range	Rate constant	References
1. $E^{1*} \rightarrow E$	1×10^8 s^{-1}	1.3×10^8 s^{-1} (water)	113
		$\leq 1.05 \times 10^8$ s^{-1} (water)	131
2. $E^{1*} \rightarrow E^{3*}$	8×10^8 s^{-1}	5.8×10^7 s^{-1} (water)	113
		$(8.4 \pm 0.8) \times 10^8$ s^{-1} (water)	131
3. $E^{3*} \rightarrow E$	540 s^{-1}	6×10^3 s^{-1}	132
		420 s^{-1}	113
		540 s^{-1}	110
		550 s^{-1} (pH 8), 540 s^{-1} (pH 11)	133
4. $E^{3*} + E^{3*} \rightarrow E^{3*} + E$	10^9 M^{-1}s^{-1}	1.2×10^9 M^{-1}s^{-1} (pH 8), 9.8×10^8 M^{-1}s^{-1} (pH 11)	133
		1.1×10^9 M^{-1}s^{-1}	110
5. $E^{3*} + E^{3*} \rightarrow E^{-} + E^{+}$	1.2×10^8 M^{-1}s^{-1}	1.2×10^8 M^{-1}s^{-1} (pH 8),	133

Reaction			
		1.3×10^8 M^{-1}s^{-1} (pH 11)	
		1×10^8 M^{-1}s^{-1}	[110]
		$< 3 \times 10^4$ M^{-1}s^{-1}	[97]
6. $E^{3*} + E^{3*} \rightarrow 2E$	1×10^9 M^{-1}s^{-1}	1.9×10^9 M^{-1}s^{-1}	[134]
		$2k = 2.4 \times 10^9$ M^{-1}s^{-1}	[113]
7. $E^{3*} + E \rightarrow E^{\cdot -} + E^{\cdot +}$	7×10^7 M^{-1}s^{-1}	0.7×10^8 M^{-1}s^{-1}	[110]
		7.3×10^7 M^{-1}s^{-1} (pH 8), 7.1×10^7 M^{-1}s^{-1} (pH 11)	[133]
8. $E^{3*} + E \rightarrow 2E$	3×10^8 M^{-1}s^{-1}	3×10^8 M^{-1}s^{-1}	[110]
		3.3×10^8 M^{-1}s^{-1} (pH 8), 7.9×10^8 M^{-1}s^{-1} (pH 11)	[133]
9. $E^{\cdot -} + E^{\cdot +} \rightarrow 2E$	8×10^8 M^{-1}s^{-1}	0.75×10^3 M^{-1}s^{-1} (ethanol)	[135]
		8×10^8 M^{-1}s^{-1} (pH 8.5)	[120]
10. $F^{3*} + F^{\cdot -} \xrightarrow{k_1} F^{\cdot -} + F$		$k_{10} + k_{11} = 1 \times 10^9$ M^{-1}s^{-1}	[136] (Fluorescein)
11. $F^{3*} + F^{\cdot +} \xrightarrow{k_2} F + F^{\cdot +}$			
12. $E^{\cdot -} + E^{\cdot -} \rightarrow E + EH_2$	2.1×10^6 M^{-1}s^{-1}	2.1×10^6 M^{-1}s^{-1} (pH 8.5)	[120] (encounter rate)
		1×10^7 M^{-1}s^{-1}	[137] (fluorescein)
13. $E^{\cdot +} + E^{\cdot +} \rightarrow P$	1×10^8 M^{-1}s^{-1}	1×10^8 M^{-1}s^{-1}	[120] (P identified as possibly dimer)
14. $E^{\cdot -}$	1980 s^{-1}	1980 s^{-1}	[121] ($t_{1/2} = 0.35$ ms, $k = \ln(2)/t_{1/2}$)
15. $E^{\cdot +}$	1155 s^{-1}	1155 s^{-1}	[121] ($t_{1/2} = 0.6$ ms, $k = \ln(2)/t_{1/2}$)
16. $E^{3*} + O_2(^3\Sigma_g^-) \rightarrow E + O_2(^1\Delta_g)$	1×10^9 M^{-1}s^{-1}	1×10^9 M^{-1}s^{-1} (pH 8), 1.8×10^9 M^{-1}s^{-1} (pH 11)	[133]
		7×10^8 M^{-1}s^{-1}	[99]
		$(1.3-2.1) \times 10^9$ M^{-1}s^{-1}	[112] aqueous, attributing all of triplet/oxygen reaction to singlet oxygen
17. $E^{3*} + O_2(^3\Sigma_g^-) \rightarrow E + O_2$	10^9 M^{-1}s^{-1}	$< 10^8$ M^{-1}s^{-1}	[134]
		1.1×10^9 M^{-1}s^{-1}	[138][139][140]
		1.56×10^9 M^{-1}s^{-1}	[136] (Fluorescein)
		1.6×10^6 M^{-1}s^{-1} (water)	[113]
18. $E^{3*} + O_2(^3\Sigma_g^-) \rightarrow E^{\cdot +} + O_2^{\cdot -}$	10^4 M^{-1}s^{-1}	6×10^6 M^{-1}s^{-1} (pH 6-8), $< 10^7$ M^{-1}s^{-1}	[138][139]
		$< 10^7$ M^{-1}s^{-1}	[99]
		9.1×10^3 M^{-1}s^{-1} (water)	[113][86]
19. $E^{\cdot -} + O_2 \rightarrow E + O_2^{\cdot -}$	10^8 M^{-1}s^{-1}	10^7-10^9 M^{-1}s^{-1}	[112] (uncertain)
20. $E^{\cdot +} + O_2 \rightarrow P_2$		8×10^8 M^{-1}s^{-1} (70% acetonitrile)	[97] (P_2 unidentified)

Reaction			
21. $F^{\cdot+} + O_2^{\cdot-} \rightarrow F + O_2(\,^3\Sigma_g^-)$			Hypothesized for fluorescein[122]
22. $E + O_2(\,^1\Delta_g) \rightarrow E + O_2(\,^3\Sigma_g^-)$		$\sim 10^7\,M^{-1}s^{-1}$	[123] (methanol or acetonitrile) [141 124] (50% acetonitrile/water)
23. $O_2(\,^1\Delta_g) \rightarrow O_2(\,^3\Sigma_g^-)$	$2.4 \times 10^5\,s^{-1}$	$4.4 \times 10^5\,s^{-1}$ (water)	[142]
		$5.2 \times 10^4\,s^{-1}$ (DMSO)	[143]
		$3.3 \times 10^4\,s^{-1}$ (acetonitrile)	[143]
		$2.4 \times 10^5\,s^{-1}$	[141]
24. $O_2(\,^1\Delta_g) + O_2^{\cdot-} \rightarrow O_2(\,^3\Sigma_g^-) + O_2^{\cdot-}$	$10^9\,M^{-1}s^{-1}$	$1.6 \times 10^9\,M^{-1}s^{-1}$ (DMSO)	[143]
		$(3.6\pm0.1)\,10^7\,M^{-1}s^{-1}$	[144]
		$(7\pm6) \times 10^9\,M^{-1}s^{-1}$ (acetonitrile)	[143]
25. $E^{3*} + TEA \xrightarrow{k} E^{\cdot-} + TEA^{\cdot+}$	4×10^7	$7.3 \times 10^7\,M^{-1}s^{-1}$ (water)	[127]
		$4.2 \times 10^7\,M^{-1}s^{-1}$ (water, pH 9.5)	[128]
		$1.8 \times 10^8\,M^{-1}s^{-1}$ (water, pH 9.5)	[129]
		$6 \times 10^5\,M^{-1}s^{-1}$ (eythl acetate/20% methanol)	[98]
26. $E^{1*} + TEA$	$10^9\,M^{-1}s^{-1}$	$3.4 \times 10^9\,M^{-1}s^{-1}$ (water, pH 9.5)	[128]
		$2.1 \times 10^9\,M^{-1}s^{-1}$ (water, pH 9.5)	[129]
27. $EH^{\cdot} + EH^{\cdot} \rightarrow EH_2 + E$ [107 145 146]	$10^4\,M^{-1}s^{-1}$	$1.1 \times 10^4\,M^{-1}s^{-1}$	[147] (Fluorescein)
28. $E^{\cdot-} + TEA^{\cdot+} \rightarrow EH^{\cdot} + TEA^{\cdot}$	$10^4\,M^{-1}s^{-1}$		[145]
29. $E^{\cdot-} + TEA^{\cdot+} \rightarrow E + TEA$	$10^4\,M^{-1}s^{-1}$		
30. $EH^{\cdot} + O_2 \rightarrow E + HOO^{\cdot}$			Proposed by [148 45]
31. $TEA\cdot + O_2 \rightarrow TEA-OO^{\cdot}$	$5 \times 10^9\,M^{-1}s^{-1}$	$4.9 \times 10^9\,M^{-1}s^{-1}$	[149] (tertiary amine in benzene or cyclohexane)
32. $HO_2^{\cdot} + HO_2^{\cdot} \rightarrow O_2(\,^3\Sigma_g^-) + H_2O_2$	$10^6\,M^{-1}s^{-1}$	$7.6 \times 10^5\,M^{-1}s^{-1}$	[150 151]
		$2 \times 10^6\,M^{-1}s^{-1}$	[152]
33. $TEA-OO^{\cdot} + EH^{\cdot} \rightarrow TEA-OOH + E$ [45 15]	$10^9\,M^{-1}s^{-1}$		

34.	10^4 M^{-1}s^{-1}		
$TEA - OO^. + TEA \rightarrow TEA - OOH + TEA^.$			

Table 4-2. Physical properties and model parameters

Parameter	Value
ε, Absorptivity of eosin in water at 500 nm	3.78×10^7 M^{-1}cm^{-1}
I_0, light intensity	1.5-9.6 mW/cm^2
E', photon energy at 500 nm	2.39×10^8 mW s mol^{-1}
$[E]_0$, initial concentration of eosin	5×10^{-6} M
$[TEA]_0$, initial concentration of TEA	2.10×10^{-1} M
$[O_2]_0$, initial concentration of oxygen	5×10^{-4} M

4.5 Conclusion

The effect of oxygen on the photoinitiation kinetics of a two-component system (eosin and triethanolamine) was investigated spectroscopically and through the construction of a kinetic model based on reactions reported in the literature. The spectroscopic investigation showed that oxygen has a regenerative effect on eosin and suggested that semireduced eosin reacts directly with oxygen and 1-vinyl-2-pyrrolidone in addition to the triethanolamine radical cation. These observations were crucial in the development of the kinetic model. Although the model imperfectly captures the photobleaching of eosin in response to irradiation, it has revealed some of the shortcomings of previous approaches to modeling the photoinitiation kinetics of this system. The discrepancies between the experimentally measured photobleaching of eosin and that predicted by the model suggest that additional pathways for irreversible photobleaching are missing. In addition, the effect of oxygen on the semireduced eosin reveals the importance of modeling the reaction between triplet state eosin and triethanolamine as two separate steps (electron transfer followed by proton transfer).

5 Impact of dissociation constant on the detection sensitivity of polymerization-based signal amplification reactions

Some of the work, text, and figures presented in this chapter are reprinted or adapted from Kaastrup, K.; Chan, L.; Sikes, H.D. Impact of dissociation constant on the detection sensitivity of polymerization-based signal amplification reactions. *Analytical Chemistry*, 2013, 85, 8055-8060.

5.1 Abstract

Many studies have demonstrated the concept of using free-radical polymerization reactions to provide signal amplification so that molecular recognition events indicative of disease states may be detected in a simple and low-cost manner. We provide the first systematic study of how dissociation constant impacts detection sensitivity in these assays, having chosen a range of dissociation constants (nanomolar to picomolar) that is typical of those encountered in molecular diagnostic applications that detect protein-protein binding events. In addition, we use experimental results to validate a mass-action kinetic model that may be used to predict assay performance as an alternative or supplement to the empirical approach to developing new polymerization-based amplification assays that has characterized the field to date.

5.2 Introduction

Polymerization-based amplification has been established as a sensitive signal amplification technique for use in molecular diagnostics.[5–10,13,17–20,22,28,39,40,42,44,47,48,153–155] Amplification is achieved through the initiation of radical polymerization coupled to molecular recognition at a surface. Initiating molecules immobilized at a surface generate radical species that react with carbon-carbon double bonds of acrylate monomers, a process that results in polymer formation. Various chemistries have been implemented, including atom transfer radical polymerization (ATRP),[42,47,48,52,53] photopolymerization,[5–10,13,17,19,20,22,28,153] reversible addition-fragmentation chain transfer polymerization (RAFT),[44,154,155] and enzyme-mediated redox polymerization.[39,40] Of these methods, photopolymerization has shown promise as a point-of-care technology as it allows for the formation of micron scale hydrogels in as little as thirty-five seconds under ambient conditions.[10]

Photopolymerization-based amplification requires the localization of photoinitiators at a surface through binding events (typically DNA hybridization or protein binding). Much of the previous work studying photopolymerization-based amplification has explored the case in which signal amplification, rather than the thermodynamics or kinetics of the binding event, is limiting.[5–10,20,28,39,40,153] These studies have made use of the high-affinity biotin-avidin interaction (dissociation constant~10^{-15} M)[156] as a model recognition event that is particularly well suited to studying the effects of varying different aspects of the chemistry, such as monomer composition or initiator type. However, in order to implement this technology for clinical diagnostics, it is necessary to employ biological recognition events for which dissociation constants (K_d) are typically in the nanomolar to picomolar range (e.g. antibody-antigen complex formation).[157]

Although there are several examples of polymerization-based amplification studies involving antibody-antigen complex formation,[8,13,18–20,39,40,48,52] a systematic investigation of the effect of varying the dissociation constant on assay sensitivity has never been performed. In the absence of signal amplification, it is expected that increasing the binding affinity should enhance the sensitivity of an

assay. However, the coupling of a binding event with an amplification reaction introduces additional complexities. For amplification processes, there are generally three distinct signal regimes. The first regime, near the limit of detection, is set by the amplification threshold. In the case of photopolymerization, this threshold corresponds to the minimum initiator density required to induce polymerization. For enzyme-linked immunosorbent assay (ELISA), the threshold is set by the minimum amount of enzyme necessary for sufficient substrate conversion for a detectable readout, and for immuno-PCR, the threshold is the minimum DNA concentration required for PCR. The second signal regime is characterized by dynamic change in the signal in response to initiator, enzyme, or DNA concentration changes, and in the final regime, above a certain initiator, enzyme, or DNA surface concentration, amplification based assays tend to exhibit signal plateaus.[28,158] In this final regime, there may be no apparent difference between binding molecules with different dissociation constants depending on the concentration used and whether that concentration results in a fraction bound that is within the plateau region. For the purposes of bioassay development, quantitatively establishing how these signal regimes relate to K_d values is useful, particularly in the nanomolar to picomolar range.

Binding affinity studies of ELISAs have predominantly shown that assay sensitivity improves as the dissociation constant for the interaction decreases.[159,160] However, in a study by Glass et al. in which the least detectable concentration (LDC) was measured for four antibodies for estradiol with different affinities (K_d=0.006 to 1.4 nM as measured by kinetic exclusion), the authors measured the same LDC for the two highest affinity binders.[160] In the absence of experimental details such as the length of the incubation periods (data collection was contracted out to the biosensor manufacturer), it is difficult to speculate as to why the LDC did not change when the K_d was reduced from 0.039 to 0.006 nM.

In this study, we investigate the impact of varying binding affinity on the sensitivity of photopolymerization-based amplification using three fibronectin clones that have been engineered to bind to the epidermal growth factor receptor (EGFR) ectodomain with different affinities (K_d=250 pM-30 nM).[161] The proteins are engineered such that mutations of a small subset of amino acids alter binding affinity without dramatically changing other properties of the protein; this allows for an evaluation based on binding affinity without the introduction of additional variables. Keeping other parameters constant, the concentration of each of the clones was reduced until polymerization was no longer observed. We then tested the applicability of a mass-action kinetic model of protein binding for predicting the minimum surface initiator density required for polymerization.

5.3 Experimental

5.3.1 Materials
Poly(ethylene glycol) diacrylate (PEGDA) (M_n=575), triethanolamine (TEA), 1-vinyl-2-pyrrolidinone (VP), eosin Y disodium salt, sodium (meta) periodate, HABA, 10x phosphate buffered saline (PBS), 4'-hydroxyazobenzene-2-carboxylic acid (HABA), Triton® X-100, and Tween® 20 were purchased from Sigma Aldrich and used without further purification. Eosin 5-isothiocyanate was obtained from Marker Gene Technology. Streptavidin was purchased from Rockland Immunochemicals Inc. 10x bovine serum albumin blocker solution, EZ-Link NHS-LC biotin, and a BCA Protein Assay Kit with bovine serum albumin standards were purchased from Pierce/Thermo Scientific. 100x Denhardt's solution and Coomassie Brilliant Blue were obtained from Bioexpress. Glass slides (75x25x1 mm) were purchased from VWR. Seakem LE Agarose was purchased from Lonza. Imidazole (99%) was obtained from Alfa Aesar and cOmplete Mini Protease Inhibitor Cocktail was purchased from Roche. Rosetta™ host strains were

purchased from Novagen. Sodium chloride, sodium phosphate monobasic, and sodium phosphate dibasic were purchased from Mallinckrodt Chemicals. Bacto agar and Difco LB broth were purchased from Becton, Dickinson, and Company. Chloramphenicol and kanamycin sulphate were obtained from Calbiochem. Isopropyl β-D-1 thiogalactopyranoside (IPTG) was purchased from Omega Bio-Tek. HisTrap™ FF crude 1 mL columns were purchased from GE Healthcare. Silicone isolators (9 mm diameter, 1 mm well depth) were obtained from Electron Microscopy Sciences. Cy3 NHS ester was purchased from Lumiprobe. UltraCruz™ Micro G-25 Spin Columns were purchased from Santa Cruz Biotechnology, Inc. 4-15% Mini-PROTEAN® TGX™ Precast Gels were purchased from Bio-Rad Laboratories, Inc.

5.3.2   Protein expression and biotinylation

Plasmids (pEThK-Fn3 clones B, D, and E)[161] were obtained from the K.D. Wittrup Lab. To express each clone, plasmids were transformed into Rosetta (DE3) E. coli, which were then grown on LB agar plates (with 30 mg/mL kanamycin and 25 mg/mL chloramphenicol) at 37°C. Starter cultures were prepared by transferring single colonies to 5 mL of LB media (with 30 mg/L kanamycin and 25 mg/mL chloramphenicol). These cultures were grown at 37°C at 250 rpm for ~16 hours and then added to 100 mL of LB media (with 30 mg/L kanamycin and 25 mg/mL chloramphenicol) in a 250 mL flask to be grown at 37°C and 250 rpm. Once the absorbance at 600 nm had reached ~1, expression was induced by adding IPTG to a final concentration of 0.5 mM. The cells were then incubated for a further 24 hours at 37°C and 250 rpm. At this point, the cells were pelleted at 15,000xg for 15 minutes (4°C). The supernatant was decanted and the cells were resuspended in 25 mL wash buffer (300 mM NaCl, 50 mM sodium phosphate, 10 mM imidazole, pH 7.4). A cOmplete Mini protease inhibitor cocktail tablet was added to the cell suspension. The sample tube containing the cell mixture was placed in a container packed with ice and sonicated 3 times for 60 seconds each (Branson sonifier 250, output control set to 5, 50% duty cycle). The sample was centrifuged at 15,000xg for 15 minutes (4°C) and the supernatant was filter sterilized with a 0.2 μm filter in preparation for metal affinity purification. The proteins were purified using an ÄKTAFPLC and HisTrap FF Crude columns. The elution buffer consisted of 300 mM NaCl, 50 mM sodium phosphate, 300 mM imidazole (pH 7.6). The results are summarized in Figure 5-1.
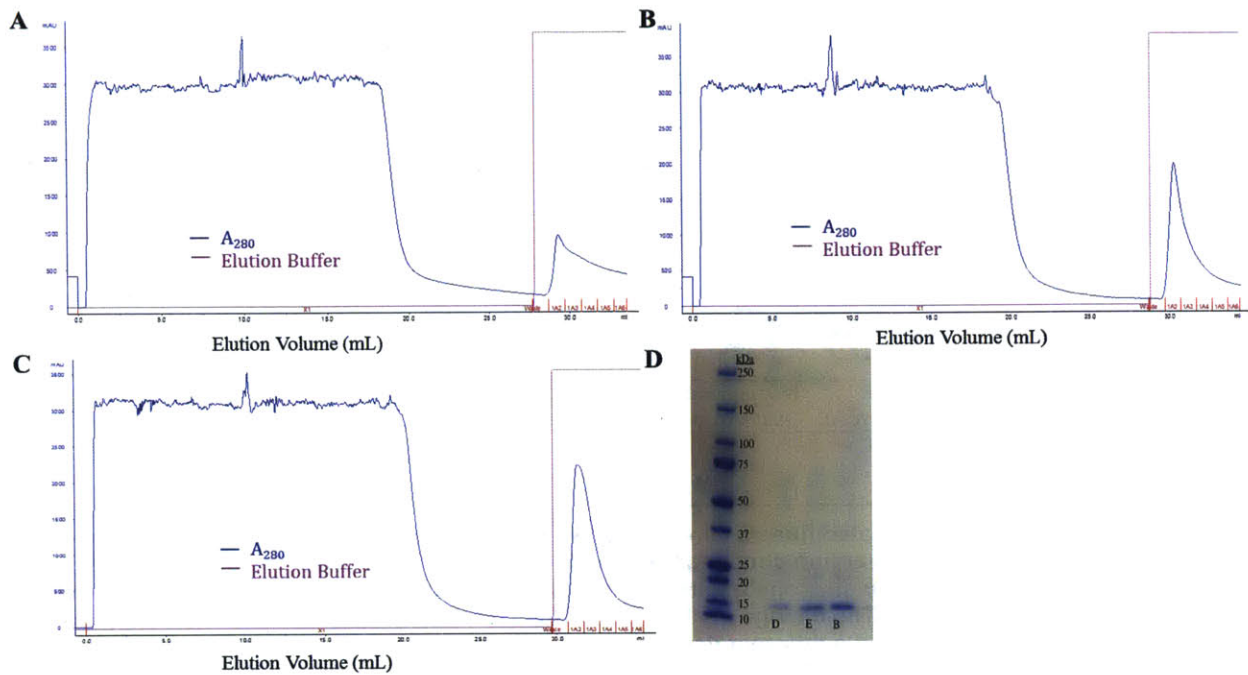
Figure 5-1. Fibronectin clone purifications. (A) Chromatogram for metal affinity purification of clone B showing the absorbance at 280 nm and the introduction of elution buffer. The fractions eluted (in red) were pooled and the amount of protein was quantified using a BCA assay. (B) Chromatogram for metal affinity purification of clone D showing the absorbance at 280 nm and the introduction of elution buffer. The fractions eluted (in red) were pooled and the amount of protein was quantified using a BCA assay. (C) Chromatogram for metal affinity purification of clone E showing the absorbance at 280 nm and the introduction of elution buffer. The fractions eluted (in red) were pooled and the amount of protein was quantified using a BCA assay. (D) SDS-PAGE gel. Based on total protein quantification (BCA assay), 1.5 µg of each of the protein purifications was loaded onto an SDS-PAGE gel, which was then run for 30 minutes at 150 V.

Following purification, the proteins were biotinylated with the EZ-Link NHS-LC-Biotin and subsequently purified using UltraCruz™ Micro G-25 Spin Columns. Total protein was quantified using a BCA assay with BSA standards.

5.3.3 HABA assay for determining relative degree of biotinylation

A standard curve for determining the degree of biotinylation was generated by adding varying concentrations of biotin to HABA-streptavidin solutions. The standards were prepared in a 96-well microplate format; 20 µL of various concentrations of biotin stock solutions in pH 6, 0.05 M sodium phosphate, 0.15 M NaCl buffer were added to 180 µL HABA-streptavidin (175.6 µL 0.5 mg/mL streptavidin in pH 6, 0.05 M sodium phosphate, 0.15 M NaCl buffer and 4.4 µL 2.42 mg/mL HABA in 10 mM NaOH). The samples were prepared by mixing 20 µL of each biotinylated protein with 180 µL of the HABA-streptavidin solution. The samples were mixed for 5 minutes prior to reading the absorbance at 500 nm using a Plate Reader. The standard curve was constructed by plotting the change in absorbance for the biotin dilutions (relative to a sample to which 20 µL of buffer had been added) as a function of biotin concentration. The HABA assay results are presented in **Figure 5-2**.

A

y = 0.0118x + 0.0031
R² = 0.9971

■ Clone B ▲ Clone E ● Clone D

B

y = 0.0105x - 0.0071
R² = 0.9978

■ Clone B ▲ Clone E ● Clone D

C

Fibronectin clone	Biotin/protein (standard curve A)	Biotin/protein (standard curve B)
D	10	10
E	8	7
B	12	11
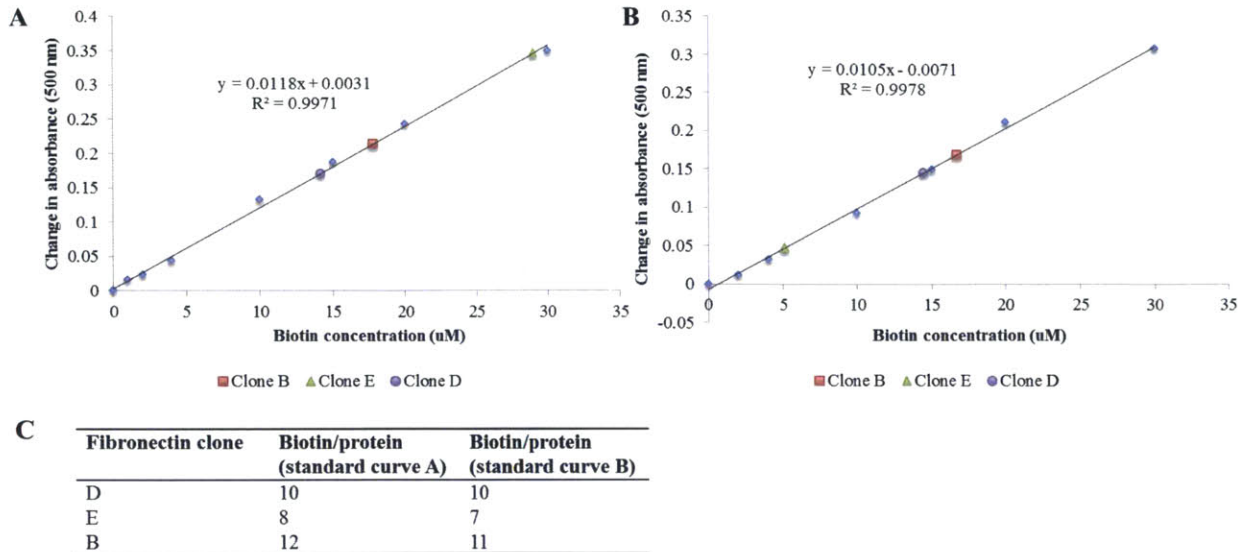
Figure 5-2. HABA assay on biotinylated fibronectin clones. (A) Standard curve for determining the degree of biotinylation generated by adding varying concentrations of biotin to HABA-streptavidin solutions. The change in absorbance for the biotin dilutions (relative to a sample to which no biotin was added) is plotted as a function of biotin concentration. The change in absorbance for each of the clones is shown on the plot. (B) Replicate HABA assay performed on a different day. (C) Table summarizing the number of biotin per protein determined using the two separate standard curves. The number of biotin per protein is defined as the moles of biotin (as indicated by the assay) divided by the moles of protein (based on a BCA assay and assuming that there are not any contaminating proteins present). Because the proteins differ only with respect to a small subset of amino acids, it is reasonable to assume that they are similarly reactive; therefore, we hypothesize that the differences in the number of biotin per protein are attributable to differences in the relative purities of the protein preparations.

5.3.4 Densitometry

Because the BCA assay determines the total amount of protein, the fraction of the total corresponding to each of the fibronectin clones was estimated using densitometry. Duplicate samples of each of the fibronectin clone protein purifications were run at a total protein concentration of 1.5 µg on an SDS-PAGE gel along with BSA standards (2 µg, 1.5 µg, and 1 µg). Following Coomassie staining, the gel was imaged and analyzed using ImageJ. The image was inverted and the integrated intensities of equal areas fully encompassing each of the protein bands as well as an area removed from the bands (to be used as the background intensity) were measured. The integrated intensities were then background corrected and the quantity of each of the fibronectin clones was determined through normalization by the integrated intensity of the BSA standard bands. The densitometry analysis is presented in Figure 5-3.
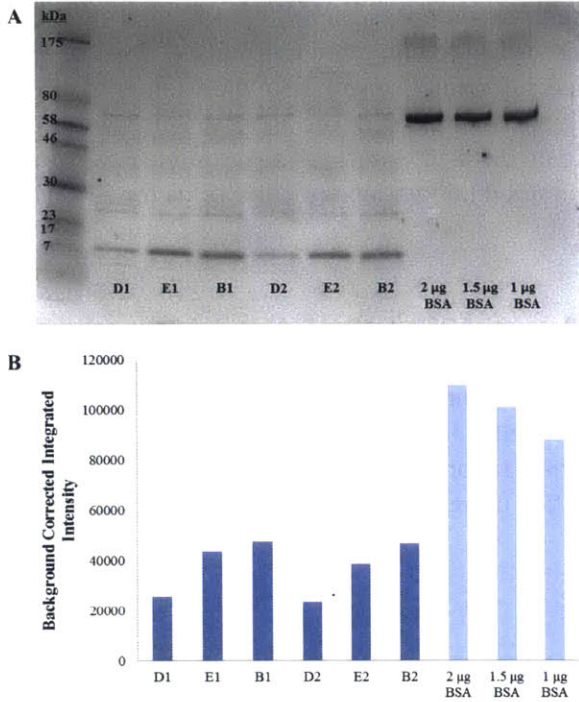
Figure 5-3. Densitometric analysis. (A) SDS-PAGE gel. 1.5 µg total protein (based on a BCA assay) of each fibronectin clone protein preparation was loaded in duplicate onto an SDS-PAGE gel along with a protein ladder and BSA standards at the indicated quantities. The gel was imaged and densitometric analysis was performed in order to determine the amount of each fibronectin clone in the respective protein preparations. (B) Quantification of the SDS-PAGE gel presented in A. Using ImageJ, the image was inverted and the integrated intensities of equal areas fully encompassing the bands as well as an area removed from the bands (to be used as the background intensity) were measured. The integrated intensities were then background corrected (shown above) and the quantity of each of the fibronectin clones was determined through normalization by the integrated intensity of the BSA standard bands.

5.3.5 EGFR/FC purification

An EGFR (extracellular domain)-Fc receptor fusion was isolated from a mixture of EGFR-Fc fusion and Fc receptor using size exclusion chromatography (Superdex 75 10/300 GL gel filtration column). The resulting fractions were collected and run on an SDS-PAGE gel to identify the fraction containing the fusion. Fraction 7 contained the fusion without any contaminating Fc. The purification chromatogram and SDS-PAGE gel are shown in Figure 5-4.
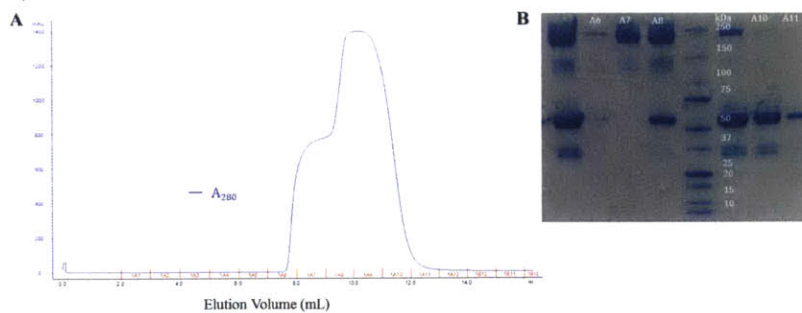
Figure 5-4. EGFR-Fc fusion purification. (A) Chromatogram for size exclusion purification of the EGFR-Fc fusion showing the absorbance at 280 nm. (B) SDS-PAGE gel of fractions collected during the size exclusion purification. The fractions collected from the size exclusion purification of the EGFR-Fc fusion were diluted 1:1 with Laemmli buffer and loaded onto an SDS-PAGE gel (run at 150 V for 30 minutes). The fraction collected of the EGFR-FC fusion and used in this study is labeled A7.

5.3.6 Details of aldehyde functionalized agarose surface preparation

Aldehyde functionalized agarose surfaces were prepared according to published methods.[162] 2 mL of a solution of 0.2 wt% agarose in distilled water (briefly heated in the microwave) were pipetted onto a glass slide and dehydrated overnight under ambient conditions. Activation of the agarose was achieved by immersing the slides in 20 mM sodium (meta) periodate (in distilled water) for 30 minutes. Following activation, the surfaces were rinsed with distilled water and dried under ambient conditions for 2 hours prior to protein printing.

5.3.7 Test surface preparation

Each test surface consisted of duplicate spots of 0.1 µL 250 µg/mL EGFR (Figure 5-4) in PBS, one spot of BSA (0.1 µL 250 µg/mL in PBS) as a negative control, and one spot of biotinylated fibronectin clone B (0.1 µL 250 µg/mL in PBS) as a positive control for macrophotoinitator binding and polymerization. Post-spotting, the surfaces were kept at ambient conditions overnight. Silicone isolator wells were applied in order to confine the monomer to the test area during polymerization. The number of binding-accessible EGFR molecules per square micron in each spot was quantified using a streptavidin-Cy3 conjugate and fluorescence analysis.

5.3.8 Antigen density determination

We quantified the number of binding-accessible EGFR molecules per square micron in each spot using a streptavidin-Cy3 conjugate and fluorescence analysis (Agilent microarray scanner) against a Cy3 calibration array (Full Moon Biosystems). The surfaces were developed according to the standard protocol; in brief, the surfaces were blocked for 10 minutes with 1% BSA in 1x PBS and rinsed with 1x PBS, 40 µL of each of the biotinylated fibronectin clones (10 µg/mL total protein) was added to separate isolators and the binding interaction was given 30 minutes to reach completion before unbound protein was rinsed away using 1x PBS. At this point, the test surfaces were contacted with 0.1 µM streptavidin-Cy3 in 0.75% BSA in 1.5x PBS, 5x Denhardts for five minutes in a humid chamber. Sequential rinses with PBST (1x PBS, 0.1% Tween 20), 1x PBS, and ddH$_2$O were used to remove unbound streptavidin-Cy3. The background fluorescence was determined by preparing surfaces with the corresponding unbiotinylated fibronectin clones in place of the biotinylated binders. The fluorescence intensity of the EGFR spots was then quantified and subtracted from the fluorescence intensity of features contacted with the biotinylated binders. These background-corrected fluorescence signals were compared with a standard curve generated using the Full Moon Biosystems calibration array where features containing only spotting buffer were used to calculate background signal. The arrays were scanned at 100% PMT with an excitation wavelength of 532 nm (20 mW) and emission wavelengths between 550 and 610 nm.

5.3.9 Preparation of detection reagents

A macrophotoinitiator capable of binding biotin was prepared by coupling eosin initiators to streptavidin by reaction of eosin 5-isothiocyanate with a fraction of the solvent-accessible lysine residues of streptavidin as previously described.[6] The aqueous monomer solution consisted of 0.5 µM eosin, 200 mM poly(ethylene glycol) diacrylate (PEGDA) (M$_n$=575), 100 mM triethanolamine (TEA), and 150 mM 1-vinyl-2-pyrrolidinone (VP).

5.3.10 Detection of molecular recognition using PBA

To reduce the incidence of nonspecific binding, the test surfaces were first blocked with 1% BSA in 1x PBS for 10 minutes. Following a rinse with PBS, the surfaces were contacted with one of the three biotinylated fibronectin clones at total protein concentrations ranging between 0.1 and 10 µg/mL. The

total protein concentration (as measured with a BCA assay) was kept constant, rather than the concentrations of the individual clones, in recognition of the fact that any contaminant proteins present would have also been functionalized with biotin. Keeping total protein concentration constant ensured that levels of non-specific binding would be held constant. To begin an assay, 40 μL of one of the biotinylated fibronectin clones (0.1-10 μg/mL with 1% BSA in 1x PBS) was added to each of the isolators wells. After 30 minutes (at which point it was assumed that binding was complete), the surfaces were rinsed once more with 1x PBS and contacted with 40 μL of 0.1 μM (6 μg/mL streptavidin) streptavidin-eosin in 0.75% BSA, 1.5x PBS and 5x Denhardt's Solution for 5 minutes in a humid chamber. To remove unbound initiator, surfaces were rinsed with PBST (1x PBS, 0.1% Tween 20), 1x PBS, and distilled water and wicked dry. Once dry, 40 μL of the prepared monomer solution was contacted with the surface and the surface was irradiated with 522 nm light (30 mW/cm^2, measured using a SPER Scientific Light Meter) from an array of LEDs housed in an ampliPHOX® reader (InDevR) for 100 seconds. Unreacted monomer solution was removed by rinsing the surface with distilled water. Remaining hydrogel surface features, if present, were stained with 50 mM eosin (50% methanol, 50% distilled water) for 2 minutes and subsequently rinsed with water to allow visualization of the polymer on the slide surface. Each condition was repeated a minimum of 5 times. Two control experiments were performed to verify the specificity of the interaction between surface immobilized biotin and the macrophotoinitiator as well as that between EGFR and the three fibronectin clones. In the first experiment, 10 μg/mL of each of the *unbiotinylated* fibronectin clones was used in place of their biotinylated counterparts. In the second experiment, the test surface development was performed omitting the fibronectin binding step so that the surfaces were only contacted with streptavidin-eosin. These experiments were performed to assess the specificity of the polymerization response; assay conditions must be chosen such that streptavidin-eosin does not nonspecifically bind EGFR or the fibronectin clones at a level sufficient for the initiation of polymerization.

5.3.11 Analysis
Each surface was imaged using the digital camera built into the ampliPHOX® Reader (InDevR) imaging bay. Mean intensity and standard deviation values were calculated for every surface feature and for the background in an automated fashion using the ampliVIEW® software that accompanies the instrument.

5.4 Results and Discussion
A schematic of the binding events resulting in polymerization is presented in Figure 5-5. As depicted, biotinylated fibronectin binds to EGFR immobilized on activated agarose (K_d=0.25-30 nM depending on the clone), and this is followed by the binding reaction between biotin and the streptavidin of the macrophotoinitiator. Streptavidin is coupled to a photoinitiator, eosin, which, in the presence of a co-initiator (triethanolamine), can induce radical polymerization in response to light in the visible range (522 nm). The resulting hydrogel is stained with a dye for ease of visualization; the final result is depicted in Figure 5-6 for fibronectin clone D. For the radical polymerization reaction, eosin is present both at the surface as a function of the sequential binding events as well as in the bulk monomer solution in order to circumvent the oxygen inhibition typical of radical photopolymerization reactions.[10] The polymerization is a threshold process, and thus will be limited to the surface where the local concentration of eosin is higher than in the bulk solution provided that local concentration exceeds a minimum initiator threshold. Thresholds are also encountered in ELISA and immuno-PCR[158] for which signal plateaus are observed above a certain enzyme or DNA concentration.
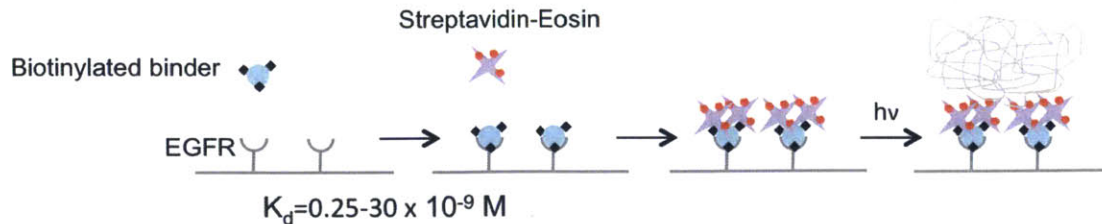
Figure 5-5. Schematic of the binding interactions that lead to polymerization. Biotinylated fibronectin clones engineered to bind with varying affinities to EGFR are bound by the surface-immobilized EGFR. A photoinitiator, eosin, is then tethered at the surface through the binding of a streptavidin-eosin conjugate to biotin. With the addition of a monomer solution containing a co-initiator (triethanolamine), eosin then induces radical polymerization in response to light in the visible range (522 nm). This results in a visible hydrogel confined to regions where initiating molecules have been immobilized.

The schematic shows: $K_d = 0.25\text{–}30 \times 10^{-9}$ M

Feature	Mean Colorimetric Intensity	Standard Deviation	Recognition Event
1	135.1	3.5	EGFR : Fn3-b : SA
2	130.4	7.2	EGFR : Fn3-b : SA
3	131.7	3.7	Fn3-b : SA
4	23.4	1.1	BSA

Figure 5-6. Colorimetric detection of clone D binding to surface immobilized EGFR. The concentration of clone D in solution was 1 uM. Features 1 and 2 are stained hydrogels generated in response to two subsequent binding events. First, biotinylated clone D binds to surface immobilized EGFR. This is followed by the binding of streptavidin-eosin. Feature 3 is a positive control for the polymerization reaction. In this case, streptavidin-eosin binds to biotinylated protein immobilized on the surface. Feature 4 is a negative control consisting of surface immobilized BSA. The mean and standard deviation values reported in the accompanying table derive from the quantification of the pixel intensities comprising each feature in the digital image and are based on areas incorporating the majority of each feature, but excluding edge effects.

Figure 5-6 shows that polymerization is restricted to those areas in which eosin has been immobilized as function of the two binding events. There is no polymerization on the surface where BSA has been immobilized; BSA should have little affinity for the EGFR binders and streptavidin-eosin. The positive control spot consisting of biotinylated protein serves to validate the activity of the macrophotoinitiator as well as of the monomer solution. To ensure that polymerization is obtained only in response to the two sequential binding interactions, two control experiments were performed (Figure 5-7). In the first, unbiotinylated fibronectin clones were used in place of the biotinylated clones to confirm that the macrophotoinitiator binding is a result of the interaction between biotin and streptavidin. In order to exclude the possibility of polymerization resulting from nonspecific binding of streptavidin-eosin to EGFR, a second control experiment was performed in which the fibronectin was excluded.

A   **B**   **C**   **D**

Figure 5-7. Negative and positive controls. (A) The test surface was prepared omitting the incubation with a biotinylated fibronectin clone. This demonstrates that nonspecific binding of streptavidin-eosin to EGFR does not result in a false positive. (B) The test surface was prepared with 1 uM unbiotinylated clone B in place of its biotinylated counterpart. (C) The test surface was prepared with 1 uM unbiotinylated clone E in place of its biotinylated counterpart. (D) The test surface was prepared with 1 uM unbiotinylated clone D in

place of its biotinylated counterpart. The latter three cases demonstrate that nonspecific binding of streptavidin-eosin to the fibronectin clones does not result in a false positive. In all cases, polymerization is observed in response to the binding of the streptavidin-eosin conjugate to the biotin covalently coupled to the surface as the positive control spot.

The colorimetric intensity of the stained hydrogels was averaged (5 trials) for the EGFR binders at each of the concentrations assayed (Figure 5-8). The correlation between binder affinity and the concentration required to achieve sufficient surface coverage to initiate polymerization is apparent. Polymerization was observed for concentrations of the highest affinity binder (clone D, K_d=0.25 nM) at a concentration as low as 6 nM. For both clones E (K_d=2.9 nM) and B (K_d=30 nM), no polymerization was observed below 10 nM. However, sufficient binding for polymerization was achieved for surfaces contacted with 20 nM clone E. It is noteworthy that both clone D and clone B performed inconsistently at their respective concentration limits (6 nM and 47 nM), initiating polymerization in 3 of 5 trials. This suggests that the complex concentration (number of biotinylated fibronectins bound) on the surface approaches the initiator threshold that must be exceeded for polymerization at these concentrations and the amount of active EGFR immobilized on the surface is limiting.
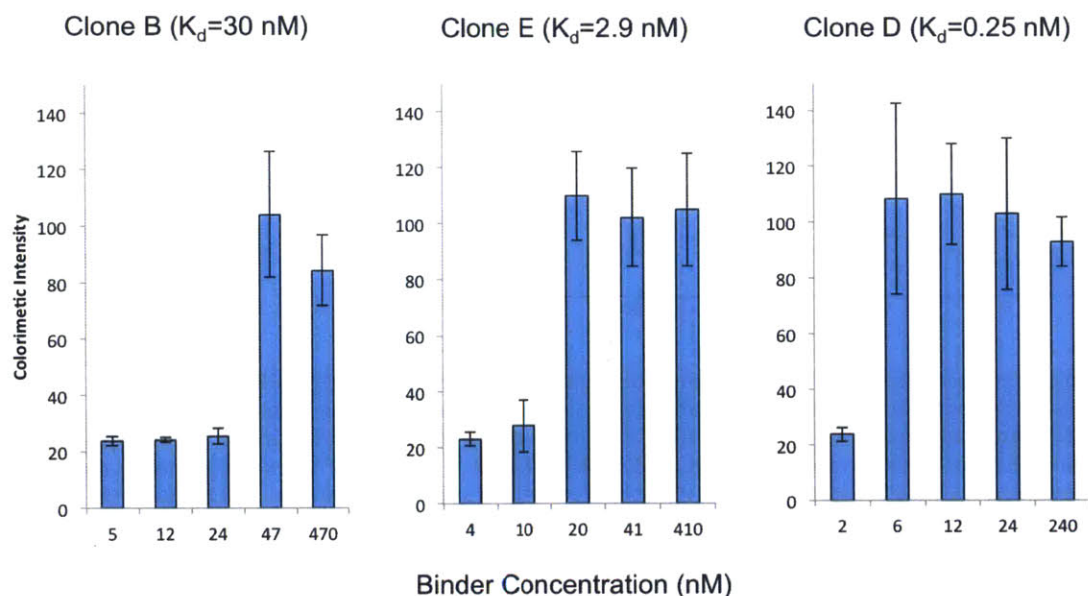
Figure 5-8. Colorimetric intensity of the polymerization response for each of the fibronectin clones as a function of concentration. The concentrations are calculated from the total protein concentration based on SDS-PAGE gel densitometry. In the case of clone D at a concentration of 6 nM, a positive response was obtained in 3 of 5 trials. Similarly, for 47 nM clone B, a positive response was obtained in 3 of 5 trials. The colorimetric intensity of the agarose surface (the background) was ~25.

Near the limit of detection, small differences in the number of protein molecules bound (or immobilized on the surface) dictate whether or not the threshold for polymerization is exceeded. The threshold nature of the polymeric amplification[5,22] is also seen in the lack of correlation between the extent of the polymerization (as indicated by the colorimetric intensity[9]) and the binder concentration used, although it is likely that the fractional surface coverage increases with binder concentration. Further indication that a threshold limit based on the number of surface-immobilized protein molecules has been reached, the concentration limit for clone B is approximately 1.5 times its dissociation constant, while the concentration limit for clone D is more than an order of magnitude greater than its dissociation

constant. This suggests that increasing the concentration of active surface immobilized EGFR would allow for further reductions in the fibronectin clone concentrations necessary for achieving a surface initiator density sufficient for polymerization. Johnson et al. demonstrated the effects of altering the relative concentrations of the capture and probe molecules for a nucleic acid hybridization study.[22] Near the limit of detection (78 capture DNA/ μm^2), they found that a concentration of 10 nM target DNA is necessary for the formation of a polymer film, while increasing the capture density to 6500/ μm^2 allows for a reduction in the target DNA concentration to below 0.5 nM.[22] Similarly, simulation shows that as the EGFR surface density is increased, the fraction of available binding sites occupied remains the same, but the overall number of fibronectin clones bound per unit area increases (Figure 5-9).
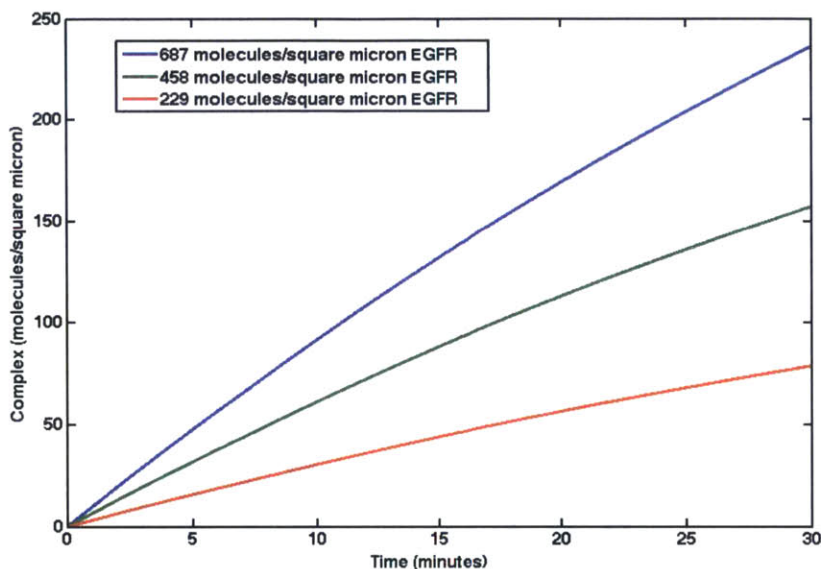
Figure 5-9. Complex concentration increases as the concentration of immobilized EGFR molecules increases. Complex concentration as a function of time is shown for the EGFR surface density determined experimentally (229 molecules/μm^2) as well as double and triple this concentration. For the results generated above, the concentration of fibronectin clone D (K_d=0.25 nM) was set to 2.4 nM. The experimental data (Figure 3 in the text) shows that the initiator density achieved with a surface density of 229 molecules EGFR/μm^2 and 2.4 nM of clone D in solution is not sufficient after a 30-minute incubation to initiate polymerization. This simulation shows that one way to achieve an initiator density above the threshold required for polymerization while holding the solution concentration of the target biomolecule (clone D) constant would be to increase the surface density of EGFR.

In order to determine the surface initiator density threshold for polymerization, it is useful to calculate the theoretical fraction of EGFR molecules bound for each of the clones at the concentrations assayed. The reversible bimolecular interaction at the surface can be written as $L + P \rightleftarrows C$ where L represents the binding ligand, P the surface-immobilized protein, and C the complex formed at the surface. Assuming mass action kinetics, the rate of association takes the form $k_{on}[L][P]$ and the dissociation rate takes the form $k_{off}[C]$ (where brackets are used to indicate concentration and k_{on} and k_{off} are kinetic constants with units of $M^{-1}s^{-1}$ and s^{-1}, respectively). The rate of change of complex can be expressed as follows:

$$\frac{dC}{dt} = k_{on}[L][P] - k_{off}[C]$$

Provided that the ligand is present in excess of the protein immobilized on the surface and the rate of ligand diffusion to the surface is faster than the rate of association, the ligand concentration can be

taken as constant. An analysis of the Damkohler number, which is defined as the ratio of the reaction velocity $k_{on}[L]$ to the diffusion velocity D/h (where k_{on} is the on-rate for ligand binding, $[L]$ is the concentration of ligand a distance h away from the surface, and D is the diffusivity of the ligand through the medium) supports this simplification. An approximation for the Damkohler number $\left(k_{on}[L]h^2/D\right)$ over the depth of the liquid was obtained by calculating the ligand diffusivity according to the Stokes-Einstein equation (Figure 5-10). Over the range of ligand concentrations and depths assayed, the Damkohler number is much less than 1, indicating that the rate of diffusion to the surface is significantly faster than the reaction at the surface; binding is reaction-limited and the ligand concentration at the surface is essentially constant.
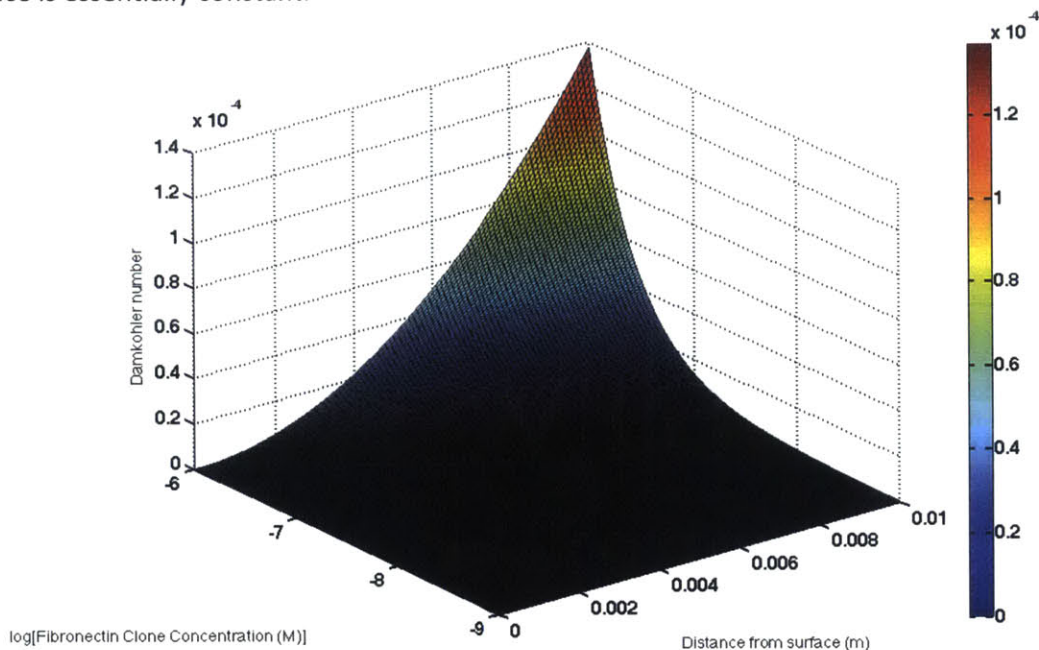
Figure 5-10. Damkohler number as a function of both fibronectin clone concentration and the distance between the fibronectin clone in solution and the EGFR on the surface.

Assuming ligand excess and a typical order-of-magnitude value of 10^5 $M^{-1}s^{-1}$ for k_{on}[163] and using the dissociation constant to determine k_{off} ($K_d = \frac{k_{off}}{k_{on}}$), a plot showing the complex concentration after a 30-minute incubation period as a function of fibronectin clone concentration for each of the three binders was generated (Figure 5-11). Comparing the experimental results with the complex concentrations output by this model indicates that the threshold for polymerization is 140 protein molecules/μm^2. The EGFR density on the surface was set at 230 molecules/μm^2 based on fluorescent labeling and comparison with a calibration array (Figure 5-12). This model shows that the theoretical complex concentration for surfaces contacted with 10 nM clone E is greater than that for 6 nM clone D, although polymerization was only observed in the case of the latter. This discrepancy could be explained by the assumption of an on-rate of 10^5 $M^{-1}s^{-1}$ for all clones. These clones were selected using equilibrium screening and the on-rates were never directly determined,[161] so it is possible that the on-rates could differ slightly for any of the three clones. A reduced on-rate for clone E would result in a lower surface complex concentration (Figure 5-13). Assuming an on-rate of 10^5 $M^{-1}s^{-1}$, the model predicts a complex concentration of 160 molecules/μm^2, which is above the threshold for polymerization. However, fluorescence-based surface density quantification (Figure 5-14) reveals that only 70 molecules/μm^2 are bound, a result consistent with a lower on-rate and the absence of polymerization.
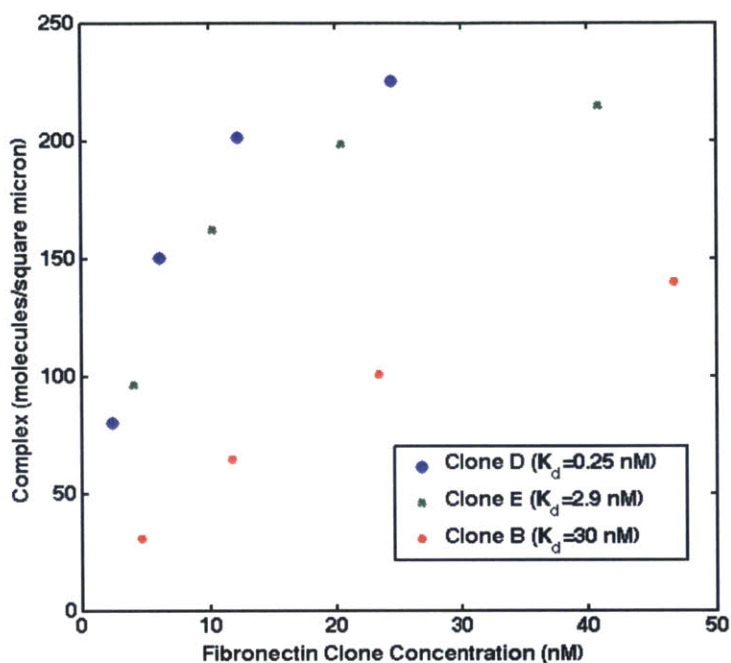
Figure 5-11. Theoretical surface concentrations of the EGFR-fibronectin complex as a function of solution concentration of the fibronectin clone following a 30 minute incubation period. The complex concentration is calculated assuming that the rate diffusion of the fibronectin clones to the EGFR at the surface is faster than the binding reaction (Da<<1), and thus, it can be assumed that the fibronectin concentration is constant. For this simulation, in the absence of measured values, all clones were assumed to have the same association rate (10^5 M^{-1}s^{-1}).

D

Streptavidin per square micron

Fibronectin Clone	EGFR (1)	EGFR (2)	Positive Control	Negative Control
10 μg/mL B-b	220	230	270	60
10 μg/mL E-b	260	260	270	30
10 μg/mL D-b	230	180	240	70
Average	230		260	50
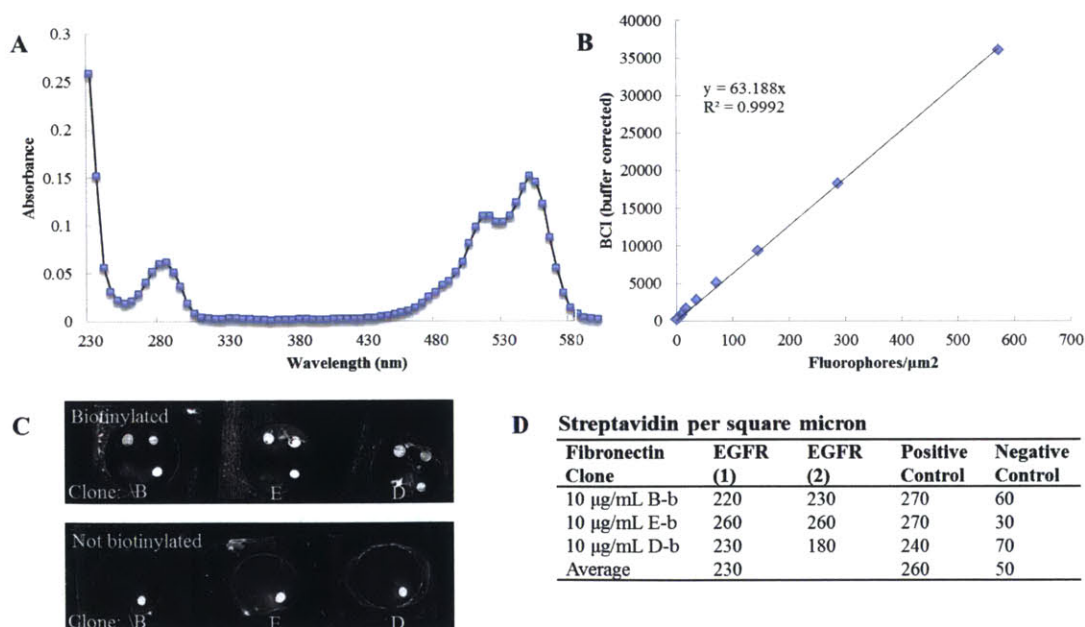
Figure 5-12. Protein surface density quantification. (A) A streptavidin-Cy3 conjugate with 3.5 Cy3 molecules per streptavidin was prepared using the same method outlined above, though with a NHS ester-functional dye in the place of an isothiocyanate dye. Extinction coefficients used in the analysis: $\varepsilon_{cy3,552}$ = 150,000 M^{-1}cm^{-1}, $\varepsilon_{cy3,280}$ = 12,000 M^{-1}cm^{-1} $\varepsilon_{SA,280}$ = 173,000 M^{-1}cm^{-1}. (B) Standard curve generated using a Full Moon Biosystems calibration array. The signal intensities were determined using ImageJ to compute average

intensities within specified regions of constant area. BCI (background corrected intensity) is defined as the difference between the signal and the background (in the case of the calibration array, an array of buffer spots). The array was scanned at 100% PMT with an excitation wavelength of 532 nm (20 mW) and emission wavelengths between 550 and 610 nm. (C) (Top) A biochip test surface reacted with 10 µg/mL (total protein) of each of the biotinylated fibronectin clones (from left to right: clones B, E, and D) followed by 0.1 µM streptavidin-Cy3 conjugate as described in the text and imaged using an Agilent microarray scanner with an excitation wavelength of 532 nm (20 mW) and emission wavelengths between 550 nm and 610 nm. The PMT setting was 100%. The top two features in each array correspond to the EGFR-Fc fusion immobilized on the surface, while the bottom right feature is the positive control spot (biotinylated clone B). The rightmost array demonstrates how surface defects (arising through contact with the end of a pipet tip, for example) can result in false positives. (Bottom) A biochip test surface developed in the same way as the top image with the exception that the surface has been reacted with 10 µg/mL (total protein) of each of the unbiotinylated fibronectin clones (from left to right: clones B, E, and D). (D) Table summarizing the number of streptavidin bound per square micron for the indicated surface features based on average signal intensities determined using the images presented in (C). The bottom image in (C) was used as the background correction for the top image and the intensity values were converted to the number of streptavidin bound per square micron using the calibration array standard curve (B).
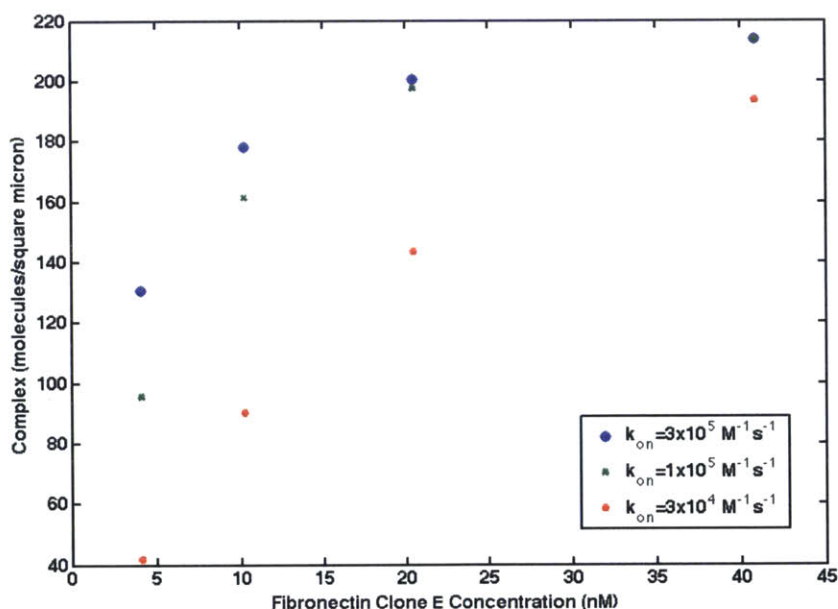
Figure 5-13. Reducing the on-rate below 10^5 $M^{-1}s^{-1}$ results in a reduction in the complex concentration for lower concentrations of the fibronectin clone. For the results generated above, K_d=2.9 nM (fibronectin clone E) and the binding reaction time was set to 30 minutes. This simulation shows the extent to which slight changes in the on-rate (which may occur from clone to clone as clones were selected using equilibrium titrations rather than kinetic screens) result in changes in the surface concentration of the EGFR-Fn complex. For example, looking at the 10 nM points, a deviation of the on-rate from the standard order-of-magnitude assumption of 10^5 $M^{-1}s^{-1}$ could place the initiator density either well above or well below the observed threshold required for polymerization.

A Biotinylated Clone E

10 μg/mL   0.25 μg/mL   10 μg/mL   0.25 μg/mL

B Clone E (not biotinylated)

10 μg/mL   0.25 μg/mL

C Streptavidin per square micron

Fibronectin Clone	EGFR (average of 4)
10 μg/mL E-b	240
0.25 μg/mL E-b	70
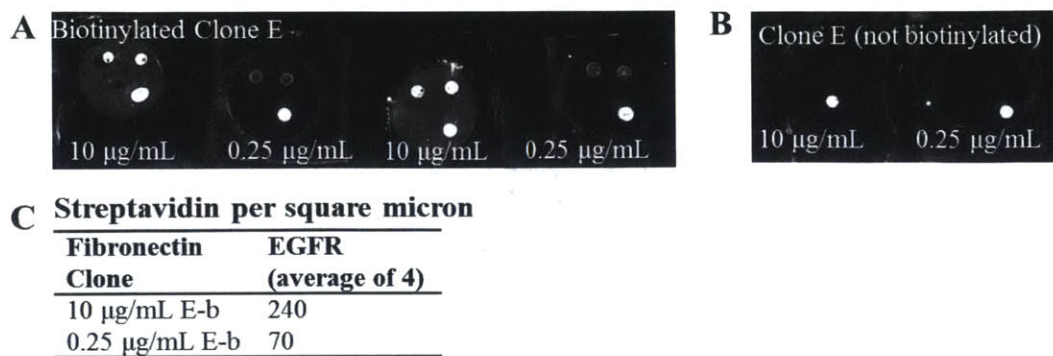
Figure 5-14. Protein surface density quantification for clone E. (A) A biochip test surface reacted with the indicated concentration (total protein) of biotinylated fibronectin clone E followed by 0.1 μM streptavidin-Cy3 conjugate as described in the text and imaged using an Agilent microarray scanner with an excitation wavelength of 532 nm (20 mW) and emission wavelengths between 550 nm and 610 nm. The PMT setting was 100%. The top two features in each array correspond to the EGFR-Fc fusion immobilized on the surface, while the bottom right feature is the positive control spot (biotinylated clone B). Based on densitometry, 10 μg/mL clone E corresponds to 410 nM and 0.25 μg/mL corresponds to 10 nM. (B) A biochip test surface developed as described for A, with the exception that unbiotinylated clone E was used in place of the biotinylated clone. (C) Table summarizing the number of streptavidin bound per square micron for the EGFR surface features based on average signal intensities determined using the images presented in A and B. The fluorescence intensities of the relevant features in the image in B were used as the background correction for the image in A and the intensity values were converted to the number of streptavidin bound per square micron using the calibration array standard curve shown in Figure 5-12.

5.5 Conclusion

In the study of the impact of dissociation constant on the observed detection sensitivity using polymerization-based signal amplification reactions presented here, our key findings are that within the parameter space investigated, improvements in binding affinity lead to marked improvements in detection sensitivity. Experimental findings were accurately predicted using a mass action kinetic model. Combined model and experimental findings support the idea that in polymerization-based amplification assays, detection sensitivity for a solution phase molecule is determined by whether a threshold initiator surface density is attained as a result of the kinetic and thermodynamic characteristics of the chosen recognition events and the chosen assay conditions (incubation time, surface capture probe density). Bioassay development is typically an empirical process that can be time consuming and costly. The ability to predict assay performance greatly enhances the efficiency of this process. As presented here, a simple kinetic model can be used to predict assay performance given a minimal set of experimentally accessible parameters (surface capture probe density and binding affinity).

In addition, experimental validation of this simple model in the context of polymerization-based amplification assays is valuable for future efforts to engineer binding reagents since improved assay performance as a function of improvements in binding affinity may be quantitatively predicted prior to committing resources to a protein engineering effort. This work also provides guidance in assessing whether commercial binding reagents are likely to provide adequate sensitivity in a given application.

6 Investigation of macrophotoinitiators for polymerization-based signal amplification reactions

6.1 Abstract

Polymerization-based signal amplification, a technique developed for use in rapid diagnostic tests, hinges on the ability to localize initiators as a function of interfacial binding events. A number of strategies are available for increasing this local concentration, including increasing the capture probe density, using higher affinity binding molecules, or, as presented here, directly conjugating additional initiators to the detection reagent through the use of functionalized polymers. We have previously considered poly(acrylic acid-*co*-acrylamide) backbones for this purpose; with eosin as the photoinitiator, these efforts were hindered by solubility limitations. Here, we use a poly(amidoamine) dendrimer as a scaffold to produce conjugates with enhanced solubility. Through an investigation into the surface binding and solution-phase properties of these conjugates, we show that quenching effects impact the efficacy of these conjugates as macrophotoinitiators.

6.2 Introduction

Photopolymerization-based signal amplification[5,6,10,20] is an inexpensive and rapid technique that presents an alternative to traditional methods for signal amplification[164,165] in molecular diagnostics. This technique links a radical polymerization reaction with molecular recognition at a surface through the use of photoinitiator-coupled affinity reagents. With an adequate dose of light and multi-acrylate monomers, the resulting hydrogel is visible to the unaided eye and easy to interpret. This technique has been demonstrated in a variety of contexts, including the detection of proteins,[8,13,18–20,166] DNA hybridization,[17,20,22,153] and epigenetic modifications of DNA using protein-DNA binding events.[105]

The polymerization reaction in these assays is dependent on whether the minimum surface initiator density required for propagation reactions to become competitive with inhibition reactions is exceeded. Reducing the number of binding events required to achieve this threshold initiator density could improve sensitivity and enable the extension of this technique to a number of clinical assays, including epigenotyping assays, for which the currently reported sensitivity precludes analysis of samples derived from needle biopsies.[105]

The relevant tunable parameters for improving assay sensitivity have been outlined in previous work;[166] these include kinetic and thermodynamic characteristics of the molecular recognition events, surface density of capture probes, and assay conditions such as incubation time. We and others have made efforts to improve sensitivity by increasing the number of initiators localized per binding event using macroinitiators for both photopolymerization-based [5,9,11] and ATRP-based signal amplification reactions.[31] These macroinitiators consist of a poly (acrylic acid-co-acrylamide) backbone conjugated to initiating molecules and neutravidin or streptavidin (proteins for molecular recognition). Streptavidin and neutravidin are used for their high affinity for biotin ($K_d \sim 10^{-15}$ M). As an alternative to molecular recognition, the He Group has also employed electrostatic interactions in the construction of an ATRP

macroinitiator for universal DNA detection with peptide nucleic acid probes. The ATRP macroinitiator improved the limit of detection by 60 times in comparison with single-initiator tagged DNA detection.[167]

Efforts to further improve the sensitivity of photoinitiated polymerization-based signal amplification through the synthesis of more densely photoinitiator-labeled macroinitiators have been stymied by the poor solubility of eosin, a photoinitiator, in water.[11] A more water soluble xanthene derivative, fluorescein, was used in the first demonstration of how sensitivity improves as the number of photoinitiators localized per recognition event increases.[9] However, in order to initiate polymerization localized near a surface with 105 biotin/μm^2, it was necessary to couple more than 70 fluorescein substituents to the polymer. This contrasts sharply with the sensitivity achieved using eosin; a conjugate consisting of just three eosin coupled to avidin is able to initiate polymerization from surfaces with only 15 biotin/μm^2.[10] Fluorescein is a less efficient photoinitiator as it lacks eosin's heavy bromine atoms and thus less readily undergoes intersystem crossing to the triplet state, from which it can react with a tertiary amine coinitiator to form tertiary amine radicals capable of initiating the polymerization reaction.[168]

More recently, Lee and Sikes showed that for the same poly (acrylic acid-co-acrylamide) backbone, solubility limitations restricted the maximum average number of eosin per chain to 15.[11] Lee and Sikes varied the number of eosin per polymer between 2 and 15, finding that the fluorescence intensity of the target spots attained a maximum for a polymer with 10 eosin but, counter-intuitively, decreased when the number of eosin was further increased to 15. In this case, poor solubility suggested the possibility of solution phase aggregates that would be expected to decrease the level of specific binding of the macroinitiator to the surface, leading to decreased sensitivity.

We hypothesize that an alternative scaffold may enable an increase in the number of initiators localized per binding event while, critically, remaining sufficiently soluble to enable surface binding. Towards this end, we conjugated eosin and neutravidin to poly (amidoamine) (PAMAM) dendrimers. Dendrimers present an attractive scaffold for initiator coupling as their exterior layer contains functional groups that lend themselves to modification. Dendrimers have been used in the construction of fluorescent probes for biological applications, including the fluorescence labeling of antibodies,[169] as scaffolds for conjugating two different dyes to produce a ratiometric sensor,[170,171] and as photostable nanoprobes for high-resolution imaging.[172] In addition to increasing the number of fluorophores per protein, one of the potential advantages of using fluorescent dendrimers conjugated to proteins rather than directly derivatizing the protein is preservation of its activity.[169] Here, we varied the number of eosin substituents conjugated per dendrimer and tested the conjugates in photopolymerization-based signal amplification reactions. As hypothesized, using dendrimer scaffolds improved solubility and allowed for a greater extent of eosin derivatization. However, photophysical factors interfered with their photoinitiation capability. We used solution-phase spectroscopy to elucidate these factors.

6.3 Experimental

6.3.1 Materials
Poly (amidoamine) (PAMAM) dendrimer (ethylenediamine core, generation 7), N-(3-dimethlaminopropyl)-N'-ethylcarbodiimide hydrochloride (EDC), dimethyl sulfoxide, poly(ethylene glycol) diacrylate, triethanolamine, 1-vinyl-2-pyrrolidinone, Eosin Y disodium salt, succinic anhydride, Tween® 20, and MES solution were purchased from Sigma Aldrich. N-hydroxysulfosuccinimide (NHSS), no-weigh format, NeutrAvidin Protein, and Blocker BSA in PBS (10x) were purchased from Thermo

Scientific. Eosin 5-isothiocyanate (EITC) was obtained from Marker Gene Technologies. Calibration chips were purchased from InDevR. Amicon Ultra-4 Centrifugal Filter Units with Ultracel-100 membranes and Amicon Ultra-0.5 Centrifugal Filter Units with Ultracel-30 membranes were purchased from EMD Millipore. PD-10 desalting columns were purchased from GE Healthcare. UltraCruz™ Micro G-25 Spin Columns were obtained from Santa Cruz Biotechnology. Black 96-well microplates were purchased from Corning. Clear 96-well microplates were purchased from Grenier Bio-One. AMRESCO Denhardt's solution (100x) was purchased from BioExpress. AMRESCO phosphate buffered saline (10x) was purchased from VWR. ACS grade methanol and 2 N hydrochloric acid were purchased from BDH. Sodium chloride, sodium phosphate monobasic, and sodium phosphate dibasic were purchased from Mallinckrodt Chemicals.

6.3.2   Coupling of eosin to dendrimers

In order to improve water solubility, a generation 7 PAMAM dendrimer (0.043 µmol) was partially carboxylated with a 512-fold excess of succinic anhydride (22 µmol) in DMSO (1:1 ratio of dendrimer amines:succinic anhydride). The reaction was stirred overnight at room temperature, after which unreacted succinic anhydride was removed by gel filtration. A 10, 16, or 40 fold excess (based on the initial mass of dendrimer reacted) of eosin 5-isothiocyanate (EITC) was then introduced and the reaction was once again stirred overnight at room temperature. Unreacted EITC was removed by gel filtration. The eosin-conjugated dendrimers were then dialyzed against water for 2 days and lyophilized. As the fold excess of eosin was increased, the fraction of conjugates that precipitated during dialysis increased. Because of this solubility limitation, increasing the fold excess further did not produce conjugates with higher eosin densities.

6.3.3   Conjugation of neutravidin to dendrimers

Prior to protein conjugation, ~1 mg of the lyophilized product (conjugates **1-3**) was dissolved in 50 µL water and characterized using absorbance spectroscopy. 0.2-0.5 mg of **1-3** was then reacted with a 500-fold excess of EDC and sulfo-NHS in pH 6 0.1 M MES, 0.5 M NaCl buffer. In the final reaction volume, the dendrimer concentration was 6 µM with 3 mM EDC and 3 mM sulfo-NHS. After 15 minutes, a 2-fold molar excess of neutravidin dissolved in pH 7.5 0.1 M sodium phosphate buffer was introduced and the reaction was incubated at 4°C overnight. The reaction volume was doubled during the neutravidin addition, thereby increasing the pH to favor the reaction between the neutravidin amines and the NHS-ester. As described, this conjugation resulted in conjugates with between 0.5 and 2 neutravidin per dendrimer. Variability in the number of neutravidin conjugated per dendrimer is likely a consequence of uncertainty in the initial mass measurements of **1-3**. To avoid complications due to potential avidity effects, only conjugates with 1 or less neutravidin per dendrimer were used. For the purposes of assessing signal from polymers bound to a surface, a lower coupling efficiency is preferable as unconjugated dendrimers do not bind to the surface. All dilutions were prepared on a neutravidin basis and, for the solution spectroscopy, absorbance and emission values were normalized by the number of neutravidin per dendrimer. A scheme summarizing the preparation is shown in Figure 6-1.

Following the overnight reaction, the samples were purified using a 100 kDa molecular weight cut-off centrifugal filter device to remove unreacted neutravidin. The samples were centrifuged at 4°C according to the manufacturer's instructions and the filtration was repeated 5 times with pH 7 PBS.
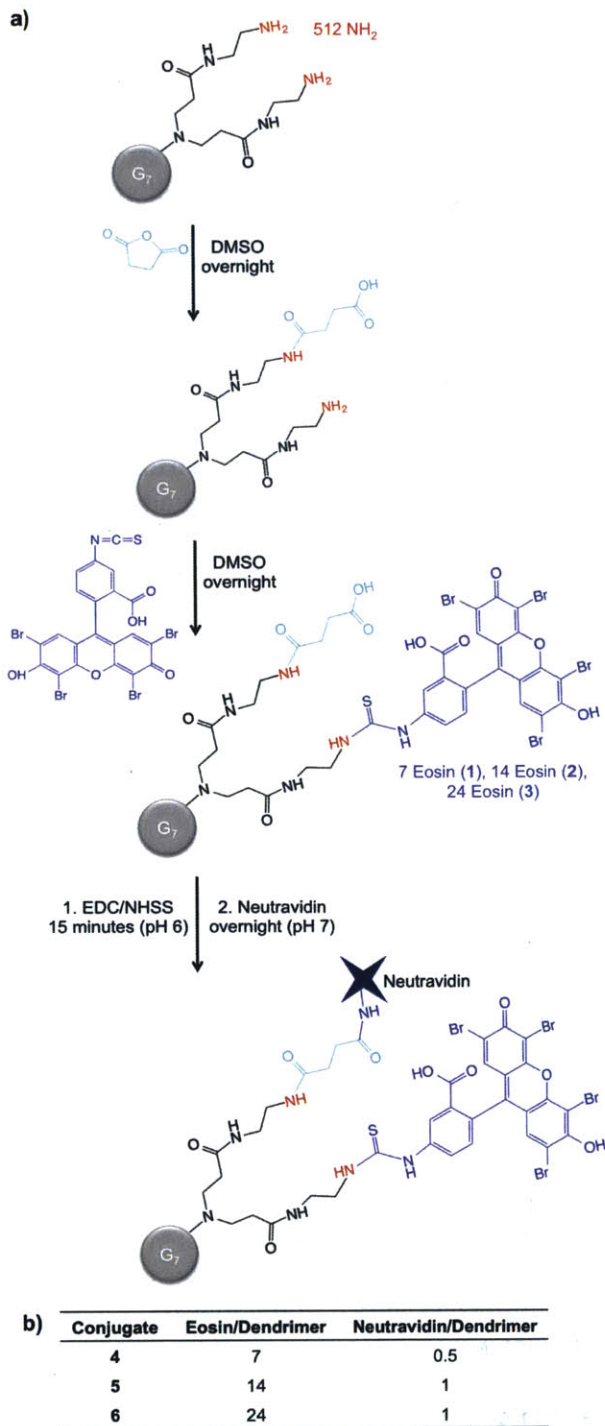
Figure 6-1. Preparation of conjugates 1-6. a) Generation 7 poly (amidoamine) dendrimers were partially carboxylated via reaction with succinic anhydride. Following removal of unreacted succinic ahydride by gel filtration, the dendrimers were reacted with 10, 16, or 40-fold excess of eosin-5-isothiocyanate. The dendrimers were subsequently purified by gel filtration and dialysis and lyophilized prior to conjugation with neutravidin using EDC/NHSS to activate the dendrimers' carboxylic acid functional groups. **b)** Summary of the calculated number of eosin and neutravidin per dendrimer for conjugates 4-6.

DMSO: dimethyl sulfoxide, EDC: N-(3-dimethlaminopropyl)-N'-ethylcarbodiimide hydrochloride, NHSS: N-hydroxysulfosuccinimide

6.3.4 Conjugate characterization

The filtered solutions were characterized using absorbance spectroscopy with a Tecan Infinite m200 microplate reader and a NanoQuant plate (path length=0.05 cm). Extinction coefficients were determined from absorbance standard curves for the dendrimer, eosin, and neutravidin in PBS (Figure 6-2). In each case, the absorbance standard curves were based on a minimum of two separate dilution sets. Absorbance spectroscopy was favored over H-NMR as it has been shown to be a more reliable method for quantifying the number of fluorophores conjugated per polymer. H-NMR analysis has also been shown to suffer in accuracy for the analysis of dendrimers due to the large difference in the number of dendrimer and dye protons. The number of eosin per dendrimer was determined from absorbance spectra collected for the lyophilized eosin-dendrimer products (conjugates **1-3**). Prior to characterization, stock solutions were prepared with the lyophilized products; ~1 mg was resuspended in 50 μL water. These stock solutions were then diluted by at least a factor of 10 with PBS so as to be within the linear range for absorbance measurements. The absorbance at 525 nm was used to determine the eosin concentration and the absorbance at 280 nm was used for the dendrimer concentration, accounting for eosin's absorbance at 280 nm. Following the neutravidin conjugation, the absorbance spectra for the purified samples (conjugates **4-6**) were measured. The eosin concentration was determined from the absorbance at 525 nm and the concentration of the dendrimer was then calculated based on the previously determined number of eosin per dendrimer (for the corresponding conjugates **1-3**). The 280 nm absorbance was used to determine the neutravidin concentration, this time accounting for absorbance by both eosin and the dendrimer. For each conjugate, a minimum of three absorbance spectra were collected and averaged. The concentrations, as calculated using the standard curves, are presented in Table 6-1. Finally, the samples were diluted with an equal volume of glycerol, aliquoted, and stored at -20°C.
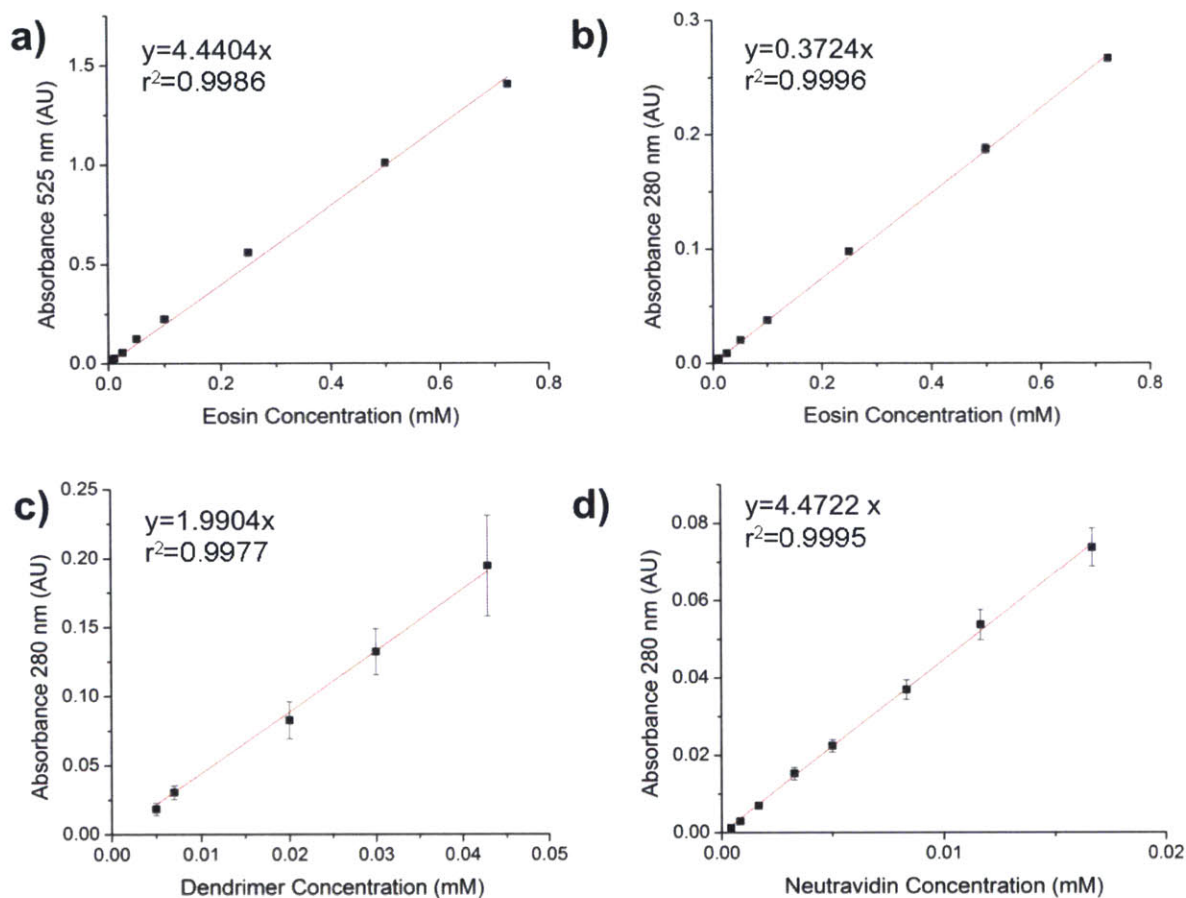
Figure 6-2. Absorbance standard curves. a) Absorbance standard curve for eosin at 525 nm (2 replicates). b) Absorbance standard curve for eosin at 280 nm (2 replicates). c) Absorbance standard curve for the poly (amidoamine) dendrimer at 280 nm (4 replicates). d) Absorbance standard curve for neutravidin at 280 nm (4 replicates). In all instances, the black squares represent the absorbances at the indicated wavelength for dilutions prepared in PBS.

Table 6-1. Conjugate Concentrations from Characterization

Summary of concentrations for the components comprising each conjugate as calculated using the standard curves based on absorbance measurements obtained using the Tecan Infinite m200 microplate reader and a NanoQuant plate (path length=0.05 cm). The final row shows the concentration range of the standards used for generating the standard curves.

Conjugate	Eosin (mM)	G_7 PAMAM Dendrimer (mM)	Neutravidin (mM)
1	0.102	0.015	N/A
2	0.103	0.0076	N/A
3	0.287	0.012	N/A
4	0.077	0.011	0.0056
5	0.091	0.0067	0.0080
6	0.186	0.0077	0.0092
NAv-Eosin	0.039	N/A	0.0066
Linear Range	*0.005-0.725*	*0.005-0.0429*	*0.0004-0.017*

6.3.5   Preparation of neutravidin-eosin conjugates

To serve as a reference conjugate, eosin was conjugated directly to neutravidin. This reaction was performed according to the protocol outlined previously for streptavidin.[6] 1 mL of a 1 mg/mL solution of neutravidin was concentrated with 30 kDa centrifuge filters and then diluted to 10 mg/mL with pH 9 0.1 M sodium bicarbonate buffer for a final volume of 100 µL. 10 µL of 10 mg/mL eosin 5-isothiocyanate (EITC) was then added and the reaction was placed at 4°C overnight. Finally, the reaction was purified by gel filtration, characterized by absorbance spectroscopy (6 replicate measurements), and diluted with glycerol for storage at -20°C.

6.3.6   Interfacial analysis using fluorescence

In order to verify the binding activity of **4-6** as well as compare the surface initiator density achieved using the dendrimer conjugates relative to a neutravidin-eosin conjugate, glass surfaces consisting of dilution arrays of biotinylated oligonucleotides were incubated with conjugate dilutions. The dilutions were prepared based on the neutravidin concentrations in order to normalize for the number of potential binding events as the biomolecular interaction of interest is neutravidin binding to surface immobilized biotin. Three concentrations (5, 10, 20 µg/mL) were selected based on previous work in which 10 µg/mL of a streptavidin-eosin conjugate was shown to effectively saturate the binding sites on the surface.[10] The dilutions were prepared in 0.5% BSA, 1.5x PBS, and 5x Denhardt's solution. The test surfaces were rinsed with water to remove residual salts prior to a 5-minute incubation with the dilutions. Following the incubation, the surfaces were rinsed sequentially with 0.1% Tween® 20 in PBS, PBS, and ddH$_2$O to remove unbound conjugates. Once dry, the surfaces were scanned with a GenePix 4000B Microarray scanner (Molecular Devices, LLC). The wavelength was set to 532 nm with 500 PMT gain at 100% power. The fluorescence intensity of the arrays was later quantified in ImageJ. A minimum of 2 arrays was scanned for each condition. On each array, the highest density of biotin (row 1) is printed in an "L" comprising 11 spots. The following 7 dilutions as well as the final negative control row consisting of spotting buffer each comprise 3 spots.

The specificity of the dendrimer conjugates for biotin was verified by repeating the surface incubation with 0.27 µM of neutravidin-free dendrimer conjugate **3**. This dendrimer was selected on the basis that it has the highest number of eosin per dendrimer and is thus the most likely to nonspecifically adhere to the surface. The concentration corresponds to the highest concentration of dendrimer used in the surface binding experiments (the dendrimer concentration when 20 µg/mL of neutravidin is used).

6.3.7   Interfacial polymerization

An aqueous monomer solution consisting of 200 mM poly(ethylene glycol) diacrylate (PEGDA), 150 mM triethanolamine (TEA), 100 mM vinyl-2-pyrrolidinone (VP), and 0.5 µM eosin Y was prepared. Following incubation with the conjugate dilutions described above and the subsequent rinsing steps, each array was contacted with 40 µL of this monomer solution and irradiated for 70 seconds with 522 nm light (30 mW/cm^2) from an array of LEDs housed in an ampliPHOX reader (InDevR). The arrays were then rinsed with water at room temperature and stained with a 50 mM eosin Y solution in 50% methanol, 50% ddH$_2$O for 2 minutes, after which the surfaces were rinsed one final time with water at room temperature and dried with compressed air. Each surface was imaged using the digital camera built into the ampliPHOX reader (InDevR) imaging bay. Four surfaces were polymerized for each conjugate dilution prepared at 10 µg/mL neutravidin (the concentration at which each conjugate saturated the available binding sites). Two surfaces each were polymerized for 5 and 20 µg/mL.

6.3.8 Solution spectroscopy

The dilutions prepared above were analyzed by absorbance and fluorescence spectroscopy using a Tecan Infinite m200 microplate reader. The concentrations for each component are summarized in Table 6-2. 80 µL of the dilutions were added to clear and black 96-well plates for absorbance and fluorescence measurements, respectively. A volume of 80 µL results in a path length of approximately 0.23 cm. Absorbance was measured at 5 nm steps between 400 and 700 nm. Emission scans were performed for excitation at 525, 450, and 260 nm with emission measured at 5 nm steps between 545-650 nm, 500-600 nm, and 450-650 nm, respectively. 525 nm is eosin's peak absorbance wavelength, but measurements were performed for excitation at 450 and 260 nm in order to obtain a complete emission spectrum around the maximum emission peak at 545 nm. The absorbance at 525 nm and emission at 545 nm (for excitation at 450 nm) were normalized by the number of neutravidin coupled per dendrimer. Three separate trials (performed on separate days) were averaged in each case.

Table 6-2. Conjugate Concentrations for Solution Spectroscopy

Summary of concentration ranges for the components comprising each conjugate for the solution spectroscopy experiments, which were performed in 96 well plates (path length=0.23 cm).

Conjugate	Eosin (mM)	G_7 PAMAM Dendrimer (mM)	Neutravidin (mM)
4	5.83×10^{-4}-2.33×10^{-3}	1.67×10^{-4}-6.67×10^{-4}	8.33×10^{-5}-3.33×10^{-4}
5	1.17×10^{-3}-4.67×10^{-3}	8.33×10^{-5}-3.33×10^{-4}	8.33×10^{-5}-3.33×10^{-4}
6	2×10^{-3}-8×10^{-3}	8.33×10^{-5}-3.33×10^{-4}	8.33×10^{-5}-3.33×10^{-4}
NAv-Eosin	5×10^{-4}-2×10^{-3}	N/A	8.33×10^{-5}-3.33×10^{-4}

6.4 Results and Discussion

6.4.1 Conjugates

A generation 7 (G_7) poly (amidoamine) (PAMAM) dendrimer was partially carboxylated[173] prior to reaction of the remaining amines with eosin 5-isothiocyanate (EITC). Carbodiimide coupling chemistry was then employed to activate the carboxylic groups of the dendrimers for reaction with neutravidin. The preparation of these conjugates is summarized in Figure 6-1. After thorough purification, the conjugates were characterized by absorbance spectroscopy (Figure 6-2 and Figure 6-3). Dendrimer conjugates (**1-3**) were prepared with an average of 7, 14, and 24 eosin per dendrimer, respectively. Conjugation of neutravidin to conjugates **1-3** resulted in conjugates **4-6**. On average, no more than one neutravidin was coupled per dendrimer. In addition to the three conjugates, eosin was coupled directly to neutravidin (Figure 6-3) to serve as a reference conjugate with an average of 6 eosin per neutravidin. Because neutravidin binding to surface immobilized biotin is the relevant biomolecular interaction, dilutions were prepared at neutravidin-matched concentrations and we report all concentrations throughout on a mass of neutravidin per volume basis.
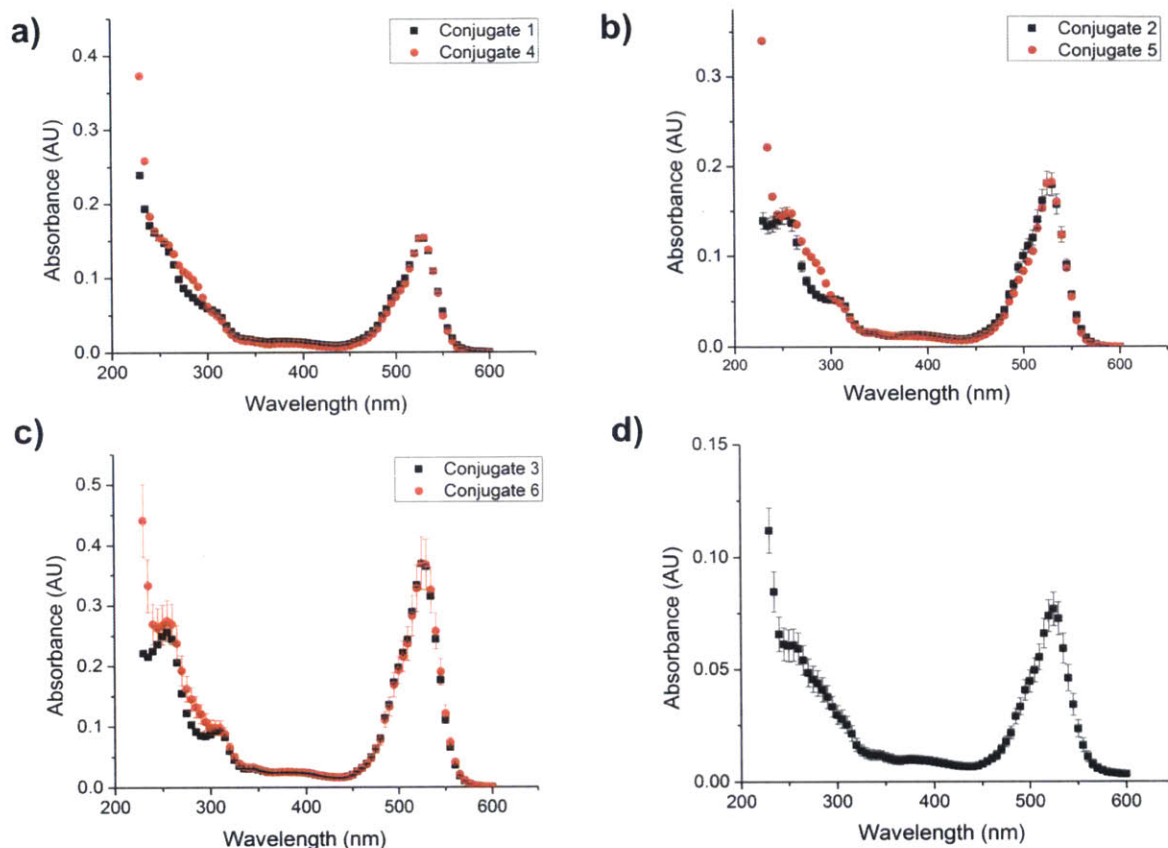
Figure 6-3. Conjugate characterization. Conjugates 1-3 were coupled to neutravidin to produce the corresponding conjugates 4-6. a) Absorbance spectra for conjugates 1 and 4. b) Absorbance spectra for conjugates 2 and 5. c) Absorbance spectra for conjugates 3 and 6. d) Absorbance spectrum for Neutravidin-eosin. Using the standard curves shown in supplementary figure 1, the number of eosin conjugated per dendrimer for conjugates 1-3 was determined. The characteristic absorbance of eosin at 525 nm allows for the subsequent determination of the number of neutravidin conjugated per dendrimer for conjugates 4-6 as the eosin densities for each dendrimer are known.

6.4.2   Interfacial performance

In the assessment of new conjugates for polymerization-based signal amplification reactions, the primary functional properties of interest include the level of specific binding and the level of nonspecific binding. To date, the fluorescence signal of conjugates bound to surface- immobilized DNA labeled with biotin (Figure 6-4 a) has served as a useful metric for comparing the performance of different conjugates.[9,11]
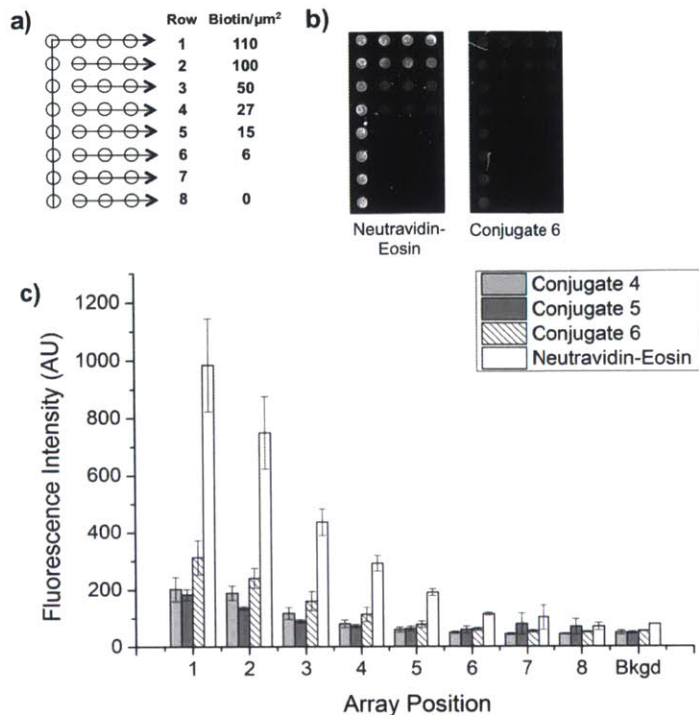
Figure 6-4. Interfacial binding. a) Schematic diagram of a test surface. The outer "Γ" is designated row 1 and contains the highest interfacial density of biotin-labeled oligonucleotides. The interfacial concentration of biotin decreases with each subsequent row consisting of three spots. The final row contains three spots of buffer without any biotinylated oligonucleotide. b) Fluorescence image of test surfaces following incubation with neutravidin-eosin (left) and conjugate 6 (right), each 10 µg/mL on a neutravidin basis (intensity scale: 0-1500). c) Summary of the mean fluorescence intensities for each set of replicate features from the array. The mean fluorescence intensities comprise the surface features from two test surfaces with error bars denoting the standard deviation about the mean.

Bkgd: background (area surrounding surface features)

Figure 6-4 b shows that binding of **4-6** was specific to those areas with chemically coupled biotin. This specificity was further corroborated by the lack of surface binding observed for (neutravidin-free) **3** (Figure 6-5).
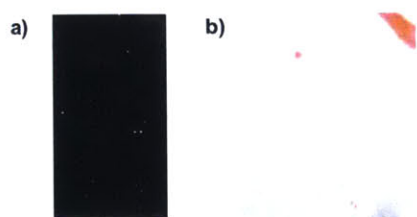
Figure 6-5. Negative control experiment. To verify the specificity of conjugate binding as well as investigate the possibility of eosin conjugation increasing the hydrophobicity of the conjugates and thus contributing to nonspecific binding, a test surface was incubated with 0.27 µM dendrimer conjugate 3. Conjugate 3 was selected as it has the highest number of eosin per dendrimer, and is thus the most likely to exhibit nonspecific binding, and a concentration of 0.27 µM was used as it corresponds to the dendrimer concentration present for 20 µg/mL of conjugate 6 (the highest concentration assayed). a) Fluorescence image of test surface following incubation with conjugate 3 (intensity scale: 0-1500). The background intensity level is 83 ± 31. b) Polymerization result for test surface incubated with conjugate 3. No polymerization was observed.

To be sure that the concentrations used in Figure 6-4 were sufficient to saturate the available interfacial binding sites, test surfaces were incubated with conjugate dilutions prepared at 5, 10, and 20 µg/mL prior to fluorescence scanning. With **4-6**, increasing the neutravidin concentration from 5 to 20 µg/mL did not produce a statistically significant increase in fluorescence intensity across the surface (Figure 6-4c and Figure 6-6), suggesting that binding site saturation was effectively achieved at 5 µg/mL. For the neutravidin-eosin conjugate, however, increasing the concentration from 5 to 10 µg/mL resulted in a doubling of the fluorescence intensity, while further increasing the concentration had no effect on the specific signal, indicating saturation at 10 µg/mL. Figure 6-4c shows that increasing the number of eosin per dendrimer by a factor of 2 from 7 (**4**) to 14 (**5**) did not result in an increase in fluorescence intensity, possibly indicating that **4** has a smaller hydrodynamic radius, thereby allowing more conjugate binding at the surface relative to **5**. Further increasing the number of eosin per dendrimer to 24 (**6**) resulted in an increase in the fluorescence intensity. However, the signal from the neutravidin-eosin conjugate was more than three times that of **6**.
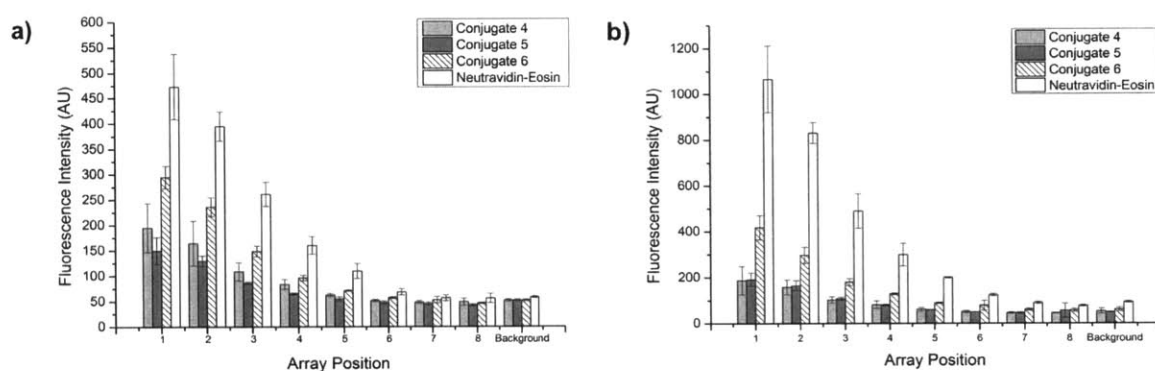
Figure 6-6. a) Summary of the average fluorescence intensities for each biotin dilution on test surfaces contacted with 5 µg/mL of each conjugate. b) Summary of the average fluorescence intensities for each biotin dilution on test surfaces contacted with 20 µg/mL of each conjugate. In both cases, the average comprises the surface features from two test surfaces.

Bkgd: background (area surrounding surface features).

The average background fluorescence intensities are presented in Figure 6-7. The background fluorescence intensity for the neutravidin-eosin conjugate increases with increasing concentration, following the expected trend for nonspecific adsorption. In contrast with previous work in which increasing the number of eosin per polymer from 2 to 15 resulted in an increase in nonspecific adsorption,[11] neither increasing the concentration of the conjugates nor the number of eosin substituents resulted in an increase in the background fluorescence intensity. This deviation from the expected trend could indicate fluorescence quenching or that the dendrimer conjugates are less hydrophobic than the polymers prepared in earlier work or a combination of the two.
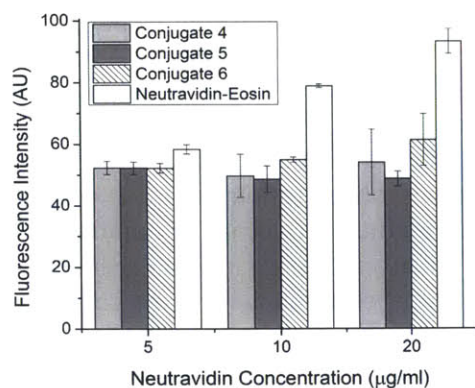
Figure 6-7. Mean background fluorescence intensity for each conjugate for increasing neutravidin concentration. The background fluorescence intensity for the neutravidin-eosin conjugate follows the expected trend, increasing with increasing concentration. However, the background fluorescence intensities for the dendrimer conjugates do not follow any clear trend.

Following interfacial fluorescence analysis, the conjugate-bound test surfaces were contacted with aqueous solutions of monomers and amine coinitiators and initiating light as previously described.[10] The binding of the dendrimer conjugates to surface-immobilized biotin and subsequent photopolymerization are illustrated in Figure 6-8. At 10 µg/mL neutravidin, the limit of detection for the neutravidin-eosin conjugate was 15 biotin/μm^2 (Figure 6-9a). As shown in Figure 6-4c, this limit corresponds to a fluorescence intensity of 190 $\pm$ 12, implying that for features with higher fluorescence intensities, the initiator density should be above the threshold for polymerization. Only **6** produced fluorescence intensities above this level and only for features with more than 100 biotin/μm^2. One of four surfaces tested resulted in polymerization for these features (Figure 6-9b), suggesting that the initiator density is near the threshold for polymerization[10] where inhibition reactions compete effectively with initiation and propagation reactions. We have observed similar stochastic outcomes with replicates in past work just below the reported limits of detection.[10,166]
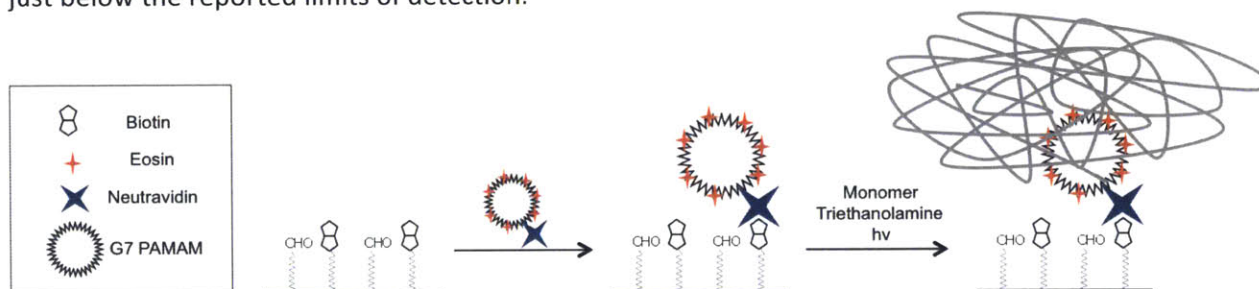
Figure 6-8. Using dendrimer conjugates for colorimetric detection of molecular recognition. Generation 7 poly (amidoamine) dendrimers conjugated to a photoinitiator (eosin) and neutravidin bind to biotinylated oligonucleotides immobilized at a glass surface. Following the addition of an aqueous monomer solution and 522 nm light, a hydrogel forms in areas specifically bound by the conjugate.

a) Neutravidin-Eosin   b) Conjugate 6
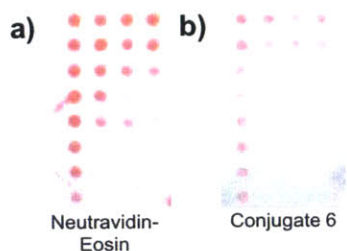
Figure 6-9. Polymerization results for surfaces incubated with a) neutravidin-eosin and b) conjugate 6 (each 10 µg/mL on a neutravidin basis). The hydrogels on the surface incubated with conjugate 6 are thinner than those on the surface incubated with the neutravidin-eosin as indicated by the intensity of the staining.

6.4.3   Solution-phase spectroscopy

To better understand the results presented in Figure 6-4 and Figure 6-7, the conjugate dilutions were evaluated using solution-phase spectroscopy. We wished to assess whether the formation of aggregates in solution or a quenching phenomenon may explain the reduced surface fluorescence observed using **4-6** relative to eosin coupled directly to neutravidin (Figure 6-4c). In comparison with much of the previous work with modified dendrimers and in particular those looking at dendrimer aggregation,[174] we were operating in a relatively dilute regime (0.2 µM versus 86 µM[174]), precluding the use of common methods such as dynamic light scattering for assessing whether aggregates were present. Both absorbance and fluorescence measurements were performed. For the fluorescence measurements, emission was monitored between 500 and 600 nm with excitation at 450 nm. Neither the presence of the dendrimer nor the progressive increase in the number of eosin per conjugate produced spectral shifts (Figure 6-10), which can be indicative of chromophore aggregation.[175,176] Upon excitation, conjugates **4-6** and the physical mixture of the dendrimer and neutravidin-eosin each emitted less light than neutravidin-eosin alone, a finding that we investigated further as a function of concentration (Figure 6-11).
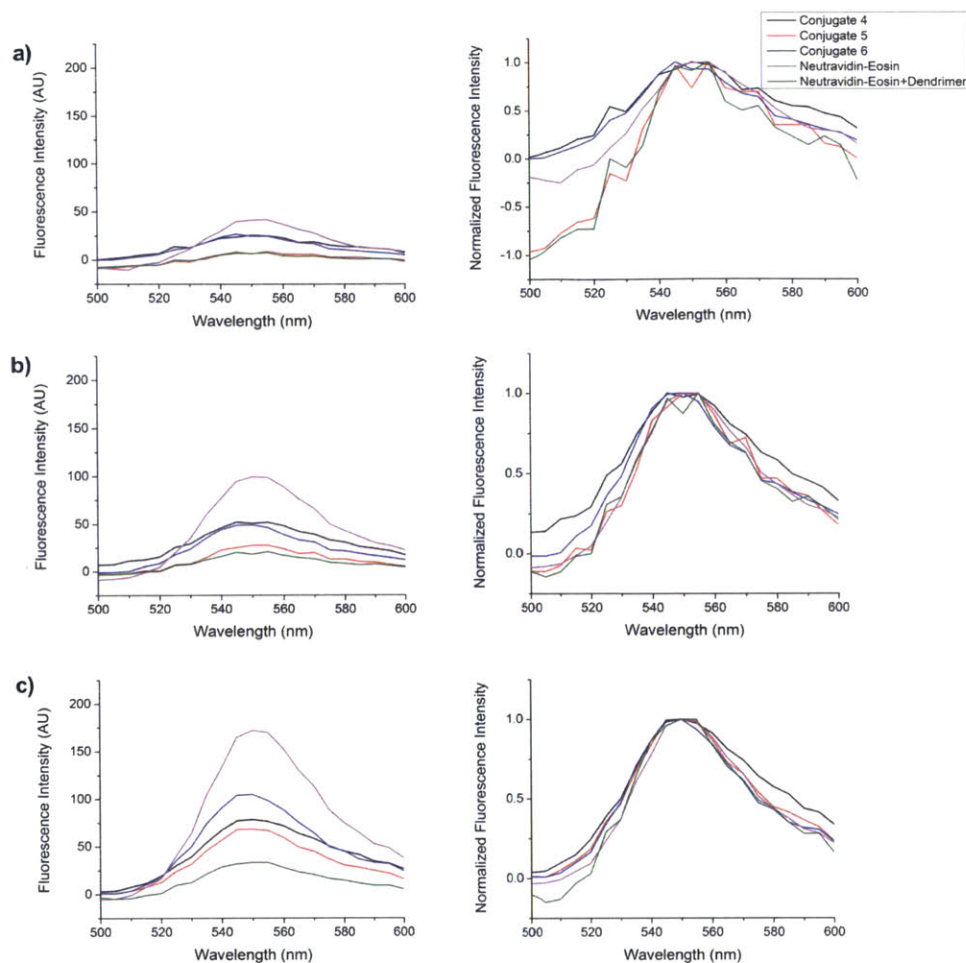
Figure 6-10. Emission spectra following excitation at 450 nm for 5 and 10 µg/mL of the conjugates as well as a dilution of neutravidin-eosin to which an equimolar amount of free dendrimer had been added. The spectra are corrected for the background fluorescence of the buffer solution (left column) and then normalized by peak height (right column). Note that these results are not normalized by the number of neutravidin conjugated per dendrimer, which is why the fluorescence intensities for conjugate 4 are higher than for conjugate 5. Conjugate 4 has approximately half the number of neutravidin conjugated compared with conjugate 5, so there are unconjugated dendrimers present and these contribute to an increase in the fluorescence intensity. a) Spectra for 5 µg/mL neutravidin. The normalized spectra (right) show that there is no shift in the maximum peak wavelength. b) Spectra for 10 µg/mL neutravidin. c) Spectra for 20 µg/mL neutravidin. Progressively increasing the concentration of eosin more clearly demonstrates that there is no peak shift as the fluorescence intensity increases and the effect of noise is diminished. The higher concentrations are also more relevant from the perspective that aggregate formation is a concentration driven process and more likely to be observed at higher concentrations. The spectra are the average of three trials.
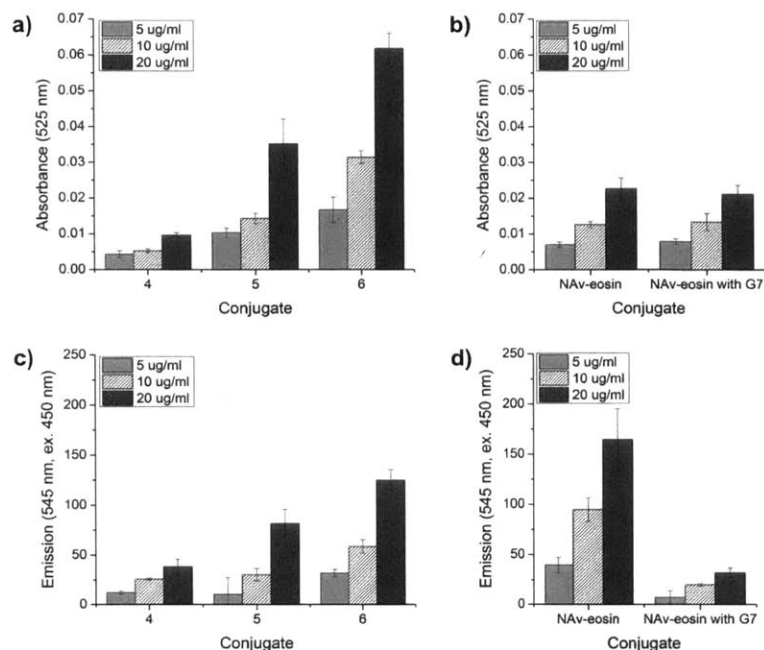
Figure 6-11. Solution spectroscopy. a) Peak absorbances (525 nm) for dilutions of conjugates 4-6 with concentrations given on a neutravidin basis. b) Peak absorbances (525 nm) for dilutions of neutravidin-eosin alone and, as an additional comparison, neutravidin-eosin to which an equimolar concentration of free dendrimer (G_7) was added. c) Fluorescence emission at 545 nm (excitation at 450 nm) for the dilution series presented in (a). d) Fluorescence emission at 545 nm (excitation at 450 nm) for the dilution series presented in (b). The absorbance and fluorescence emission values have been normalized by multiplication with the number of neutravidin conjugated per dendrimer. Three trials were averaged in all cases. Mechanisms underlying the observed trends are considered in the text.

Figure 6-11 shows the peak absorbance at 525 nm as well as the peak fluorescence emission at 545 nm for the conjugate dilutions at 5, 10, and 20 µg/mL neutravidin (full emission spectra presented in Figure 6-10). For comparison, results for dilutions of neutravidin-eosin, both with and without an equimolar amount of free dendrimer added, are included (Figure 6-11 b, d). Although the absorbance values for **5** and **6** (Figure 6-11 a) were higher than for the corresponding neutravidin-eosin dilutions (Figure 6-11 b), in both cases, the emission was lower than for the neutravidin-eosin conjugate (Figure 6-11 c vs d). The emission measurements suggest that, rather than relaxing from the excited state to the ground state via fluorescence, the eosin molecules lost energy nonradiatively. The reduction in emission upon the addition of the free dendrimer to the neutravidin-eosin dilutions indicates that the dendrimer quenched eosin fluorescence. Quenching is frequently characterized using Stern-Volmer plots; these have been used previously to characterize quenching of BSA fluorescence by PAMAM dendrimers.[177] Here, the Stern-Volmer plot generated for eosin with increasing amounts of dendrimer added is nonlinear (Figure 6-12), indicating that quenching is likely not the result of a diffusive process.[178]
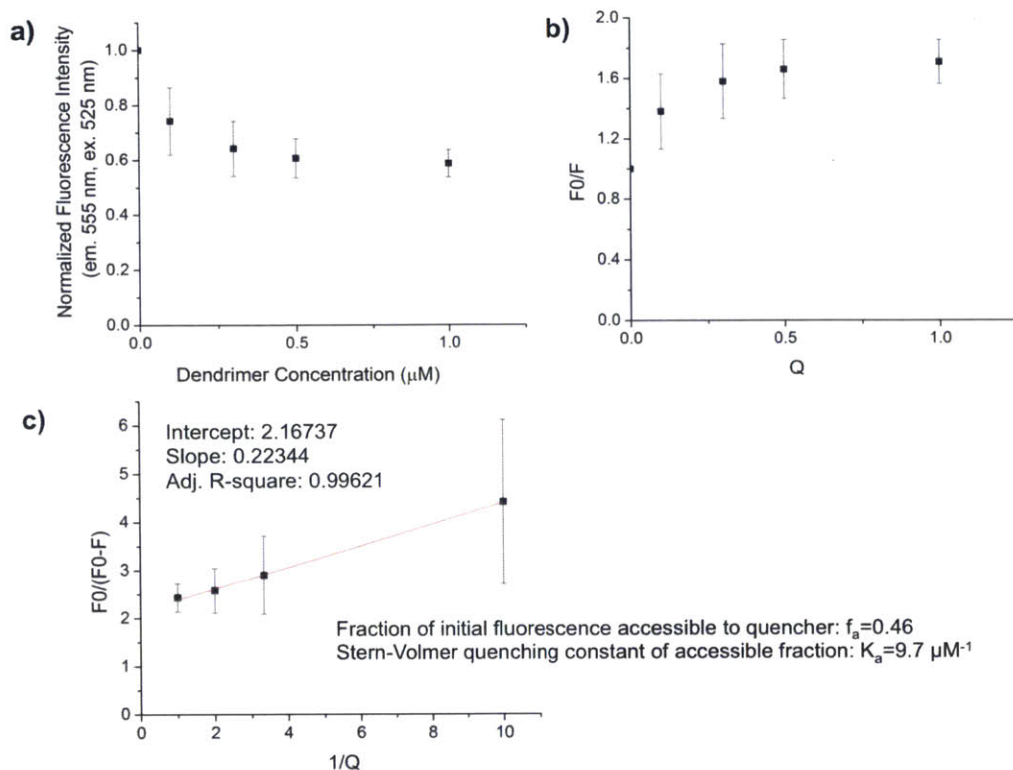
Figure 6-12. Stern-Volmer Plots. a) The concentration of free dendrimer in a 1 µM eosin solution was varied between 0.1 and 1 µM (three trials). b) The ratio of the fluorescence intensity in the absence of quencher, F_0, to the fluorescence intensity, F, was plotted as a function of quencher concentration, $|Q|$, in accordance with the Stern-Volmer equation:

$$\frac{F_0}{F} = 1 + k_q\tau_0|Q|^{178}$$

In the above expression, k_q is the bimolecular quenching constant, and τ_0 is the lifetime of the fluorophore in the absence of quencher. The nonlinearity of the Stern-Volmer plot indicates that more than one type of quenching may have occurred. The downward curvature of this plot suggests that the quenching observed here might be better described by a modified Stern-Volmer equation that allows for two fluorophore populations, one accessible to the quencher and the other inaccessible. In this expression (below), f_a is the fraction of initial fluorescence that is accessible to the quencher and K_a is the Stern-Volmer quenching constant of the accessible fraction.

$$\frac{F_0}{F_0-F} = \frac{1}{f_aK_a|Q|} + \frac{1}{f_a}^{178}$$

c) The modified Stern-Volmer plot. While quenching was consistently observed, the linear fit for the modified plot is not convincing. For each plot, the error bars represent the standard deviation of the dependent variable across three trials.

To further investigate the mechanism of quenching, the pH of the dilutions was reduced. Previous work has shown that the tertiary amines of dendrimers are capable of reductively quenching the excited states of fluorescent molecules.[179,180] Approaching pH 4, all of the primary and tertiary amines are protonated,[181] so the pH was reduced to 3.5. This reduction in pH increased the emission from mixtures of neutravidin-eosin with free dendrimer added to the levels measured for dilutions of neutravidin-eosin alone (Figure 6-13). However, reducing the pH did not have a similar effect on the emission from **6**, implying the existence of an alternative quenching mechanism for eosin covalently bound to a dendrimer.
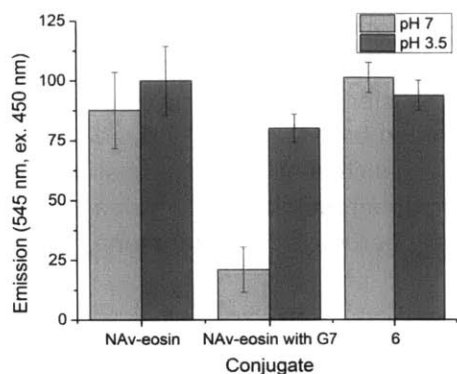
Figure 6-13. Effect of pH on fluorescence intensity. Dilutions of neutravidin-eosin, both with and without an equimolar concentration of free dendrimer (G₇), and conjugate 6 were prepared at 10 µg/mL in the original buffer (pH 7) and in a second buffer for which the pH had been reduced to 3.5 with HCl. The samples were excited with 450 nm light and the resulting emission at 545 nm measured. Reducing the pH should protonate the tertiary amines of the dendrimer and suppress quenching if the quenching mechanism involves an electron transfer from the tertiary amines to the excited state of eosin. Reducing the pH increased the fluorescence emission for the dilution of neutravidin-eosin with free dendrimer, but had no effect on dendrimer conjugate 6.

The reduced fluorescence of the dendrimer conjugates relative to the neutravidin-eosin conjugate could be an indication that locally high concentrations of eosin on the dendrimer surfaces promote self-quenching. The reduction in fluorescence intensity observed when increasing amounts of fluorescein were coupled to G_0-G_2[169] and G_5[182] PAMAM dendrimers was attributed to self-quenching. Here, increasing the number of fluorophores enhanced the signal. Yet, if we normalize the emission by each conjugate's absorbance, we see that the normalized emission decreased as the number of eosin substituents per dendrimer increased (Figure 6-14). Kim et al. also observed a reduction in normalized emission when the number of Cy5 coupled to G_5 PAMAM dendrimers was increased from 0.8 to 8; this was attributed to weak excitonic coupling between the dye molecules on the dendrimers.[172]
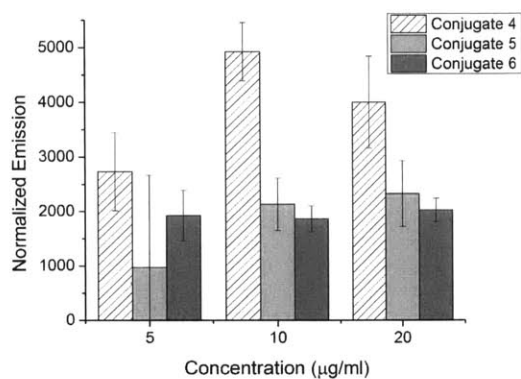
Figure 6-14. Emission normalized by absorbance. The emission at 545 nm (ex. 450 nm) was normalized by the peak absorbance at 525 nm for each dendrimer conjugate. As the number of eosin substituents per dendrimer increases, the normalized emission decreases.

Finally, for both the dendrimer and poly (acrylic acid-co-acrylamide) conjugates, the limit of detection for the polymer conjugates was higher than for neutravidin directly coupled to eosin. For the poly (acrylic acid-co-acrylamide) system, the observations of decreased solubility and increasing levels of nonspecific binding with increasing eosin substitution suggested the possibility of solution phase

aggregates. In this work, solubility was improved even for higher degrees of eosin labeling; however, fluorescence quenching mechanisms were evident in solution-phase measurements. Susceptibility to quenching is a feature that distinguishes photopolymerization from the other chemistries that have been used for polymerization-based signal amplification; these include atom-transfer radical polymerization (ATRP),[42,52] reversible addition-fragmentation chain transfer polymerization (RAFT),[44] and enzyme-mediated redox polymerization.[39] For both photopolymerization-based and RAFT-based signal amplification, macroinitiators have been shown to contribute to an enhancement in photoinitiation efficiency. [9,31,167] This work provides the first demonstration of a macrophotoinitiator for which a quenching limit was encountered, highlighting the impact of complex photophysical phenomena on macrophotoinitiator performance.

6.5 Conclusion

A body of work has established that the interfacial density of initiators determines the sensitivity obtained when polymerization reactions are used to provide signal amplification in bioassays. It follows that increasing the number of initiators localized per binding event may improve sensitivity. This strategy has provided improved sensitivity for several combinations of initiators (2-hydroxy-1-[4-(2-hydroxyethoxy)phenyl]-2-methyl-1-propanone, fluorescein/tertiary amine, bromoisobutyrate) and polymeric scaffolds (poly (acrylic acid-co-acrylamide), polylysine) that present functional groups for modification with both initiators and moieties that are capable of either molecular recognition or useful electrostatic interactions. The eosin/tertiary amine initiation system is attractive in comparison with the above-mentioned initiators because it allows for reaction times on the seconds timescale under ambient conditions. However, eosin has exhibited more complex behavior than these other initiation systems upon incorporation into macroinitiators. Coupling eosin directly to proteins has provided superior sensitivity. The partially carboxylated G_7 PAMAM dendrimer scaffold solved the solubility limitation that was encountered in past work with poly (acrylic acid-co-acrylamide) scaffolds, but a new quenching limitation has been identified here and investigated mechanistically. Future efforts to design eosin macroinitiators should include a feature that increases the separation between eosin molecules, or conjugation of eosin directly to proteins should be accepted as the design that provides the greatest sensitivity.

7 Application to selective cell lysis

This work was completed in collaboration with Xiaocheng Jiang and Aimal Khankhel.

7.1 Abstract

Co-cultures are essential to the study of heterotypic cell interactions and for the creation of biomimetic microenvironments that facilitate cell growth. Nucleic acid enrichment from co-cultures is important for elucidating cell signaling mechanisms as well as verifying the accurate recapitulation of human cell biology by model systems. Here, we present a strategy for the selective lysis of a target cell population in a co-culture. Cells are labeled with photoinitiators and subsequently irradiated to induce crosslinking of membrane proteins and photopolymerize a protective hydrogel barrier, allowing for RNA extraction from the unlabeled cells. The process is complete within 5 seconds and selective even in closely contacted cell aggregates.

7.2 Introduction

Co-cultures have been used to study heterotypic cell interactions in the context of tumor angiogenesis,[183,184] cell migration,[185] cancer metastasis,[186–188] immune responses,[189] wound healing,[190,191] stem cell maintenance,[192] and the assembly of neural circuits.[193] Micropatterned cocultures have also enabled the creation of biomimetic environments for cell growth.[194]

In some cases, the co-culture functions to facilitate the growth of a particular cell type by providing a supportive microenvironment. The cocultivation of hepatocytes with nonparenchymal cells has proven critical for maintaining hepatocyte viability and function.[195,196] Microscale co-cultures of hepatocytes with fibroblasts,[197] which synthesize the connective tissue of the stroma, have been developed for studying the biology and treatment of malaria,[198] hepatitis C,[199] and hepatitis B.[200] The ability of the co-culture system to accurately recapitulate human hepatocyte biology has been verified through gene expression profiling.

Co-cultures commonly feature in mechanistic studies of cell signaling. Co-cultures of cancer stems cells and monocytes were used to elucidate the interactions between cancer stem cells and their microenvironment.[187] Following 3 hours of co-culture, the cells were separated using fluorescence-activated cell sorting (FACS) in order to measure the expression of cytokine mRNAs.

The enrichment of nucleic acids from a single population of cells in a co-culture is complicated by the need for trpysinization and separation by FACS. In the case of hepatocyte co-cultures, the fibroblasts that are essential for stabilized function over longer periods of time contribute contaminating RNA when the cells are lysed. Methods for selective lysis and RNA extraction in situ have the potential to vastly simplify the nucleic acid enrichment process and improve signal-to-noise ratios, while also eliminating complicating factors from trypsinization.

Photopolymerized hydrogels have been used extensively in tissue engineering to encapsulate cells.[25,26,89–91] Photopolymerization has been favored over alternative polymerization chemistries for its spatial and temporal control,[89] low heat generation,[25] and demonstrated cytocompatibility.[201] Hydrogels serve as immunoprotective barriers by enabling size selective transport,[25,26] even in the case of nanoscale films.[202] The targeted interfacial photopolymerization of hydrogels offers a route through which selective lysis and RNA extraction can be achieved. Here, cells are pre-labeled with fluorescent dyes that freely pass through the cell membrane into the cytoplasm, where they are converted into cell-impermeant products. In addition, photoinitiator conjugated probes are used to label transmembrane

proteins in the targeted cell population. We show that the fluorescent dyes in the cytoplasm and the membrane bound photoinitiators have a combined effect, protecting the target population from lysis. The former produce singlet oxygen upon irradiation, resulting in cross-linking of the membrane, while the latter initiate polymerization localized to the surfaces of the targeted cells.

7.3 Experimental

7.3.1 Materials
CellTracker Red CMTPX and CellTracker Green CMFDA were purchased from Life Technologies. Poly(ethylene glycol) diacrylate, triethanolamine, 1-vinyl-2-pyrrolidinone, and Eosin Y disodium salt were purchased from Sigma Aldrich. Lysis buffer was obtained from Qiagen. Poly-l-lysine, tissue culture plates, phosphate buffered saline (PBS), dimethyl sulfoxide, neutravidin, eosin-5-isothiocyanate, and Hoechst 33342 were purchased from Sigma Aldrich. H1975 cells were obtained from ATCC. Biotinylated anti-CD45 antibody was purchased from Abcam.

7.3.2 Cell culture and sample preparation
H1975 cells were maintained in RPMI 1640 medium supplemented with 10% fetal bovine serum (FBS) at 37°C and 5% CO_2. Whole blood from healthy donors was processed according to published methods[203] to isolate white blood cells from red blood cells and platelets. Following isolation, the white blood cells were stained with 1 µg/mL (2.2 µM) CellTracker Green CMFDA in serum-free medium following the manufacturer's protocol. In brief, CellTracker Green CMFDA was dissolved in DMSO to a final concentration of 10 mM. A working solution with 2.2 µM CellTracker Green CMFDA in serum-free medium was prepared from the stock solution. The cells were incubated in the working solution for 30 minutes at 37°C. The cells were then centrifuged and the working solution was removed. The cells were resuspended in media supplemented with serum. The H1975 cells were stained with CellTracker Red CMTPX in parallel. Once labeled, the cells were combined in a 5:1 ratio of white blood cells: H1975 cells for a final concentration of 6x10⁶ cells/mL in PBS. The nuclei were then stained with 1 µg/mL Hoechst 33342 in PBS for 5-10 minutes and rinsed.

Biotinylated anti-CD45 antibody was added to the cell suspension for a final concentration of 5 µg/mL. The cells were incubated with the antibody for 30 minutes and then washed with PBS. Neutravidin-eosin with 4 eosin per protein was prepared according to published methods.[10] The cells were incubated with neutravidin-eosin at a final concentration of 1 µg/mL for 20 minutes and then washed three times with PBS. The final concentration of cells in suspension was 1x10⁶ cells/mL.

96-well culture dishes were coated with 0.1 mg/mL poly-l-lysine for 20 minutes and rinsed with water. 100 µL of the combined cell suspension was then added to the wells and the plates were centrifuged for 2 minutes at 100xg to accelerate cell attachment to the coated surfaces.

7.3.3 Polymerization and Lysis
A monomer solution consisting of 200 mM PEGDA, 150 mM TEA, 100 mM VP, and 0.3 µM eosin Y[10] in PBS was prepared. The cells were imaged prior to polymerization with the 20x objective and DAPI, FITC, and Texas Red filters of a Nikon microscope. 10 µL of the monomer solution was added to the well containing the cells and 100 µL of PBS for a final concentration of 20 mM PEGDA, 10 mM VP, 15 mM TEA, and 0.03 µM eosin in PBS. The well was subsequently illuminated using the Cy3 filter and the 20x objective for 5-15 seconds with the lamp intensity at its maximum setting. The buffer and residual monomer solution were removed from the well by pipette and lysis buffer was added and immediately removed after 5 seconds. 100 µL of PBS was added to the well. The cells were then imaged again to verify the specificity of the lysis.

7.4 Results and Discussion

As depicted in Figure 7-1, white blood cells and H1975 cells were labeled with 5-chloromethylfluorescein diacetate (CellTracker Green CMFDA) and CellTracker Red CMTPX, respectively. The structures of the two dyes are shown in Figure 7-1A and B. CMFDA is a fluorescein dye with a chloromethyl group and two acetate groups appended. The purpose of the chloromethyl group is to improve retention of the dye within the cell by reacting with thiol groups in a glutathione S-transferase-mediated reaction that produces membrane-impermeant glutathione-fluorescent dye adducts. The fluorescence of the dye is activated when the actetate groups are cleaved by intracellular esterases to produce fluorescein.[204] The difference in polarity between fluorescein diacetate and fluorescein also contributes to retention of the dye within the cell; fluorescein diacetate is nonpolar, while fluorescein is polar and, therefore, passes more slowly through the cell membrane.[204] Following labeling with the CellTracker dyes, the cells were combined and incubated with a biotinylated anti-CD45 antibody that binds to CD45 antigen expressed in the white blood cell membranes. The cells were subsequently incubated with a neutravidin-eosin conjugate to localize eosin to the surfaces of the white blood cells (Figure 7-1C).

Fluorescein, like eosin, is a xanthene dye that is commonly used as a fluorescent label[205,206] and tracer.[98] Both fluorescein and eosin function as photoinitiators;[9,15] upon irradiation with green light, the dye is excited to its singlet state, from which it can undergo intersystem crossing to its triplet state. In its triplet state, it is reactive towards reducing agents, such as tertiary amines, which are included in a monomer solution as coinitiators. Electron transfer to the triplet state fluorescein from the tertiary amine is followed by proton loss from the tertiary amine radical cation.[33] This sequence produces two neutral radicals, of which the tertiary amine radical initiates polymerization by reacting with carbon-carbon double bonds of monomers in solution. As schematically represented in Figure 7-1C, with the addition of a monomer solution and exposure to light, only the cells labeled with CMFDA and eosin are expected to be encapsulated within a hydrogel that protects them against subsequent lysis.
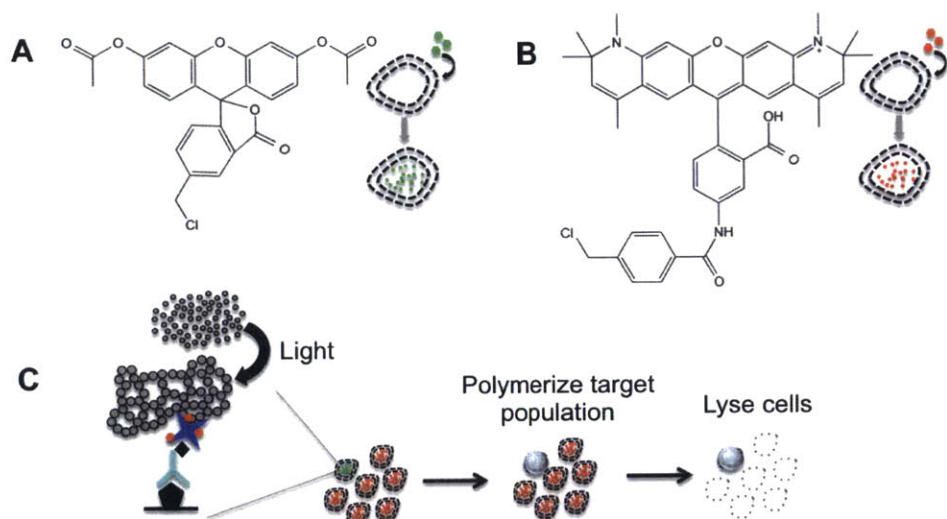
Figure 7-1. Schematic for cell labeling, polymerization, and lysis. A) White blood cells are labeled with 5-chloromethylfluorescein diacetate (CellTracker Green CMFDA) and H1975 cells are labeled with CellTracker Red CMTPX. B) Once labeled, the cells are combined and incubated with a biotinylated anti-CD45 antibody, washed, and subsequently incubated with a neutravidin-eosin conjugate. This series of steps results in eosin localized to the membranes of the white blood cells. The cells are then plated in a poly-l-lysine coated 96-well polystyrene plate. Upon the addition of monomer and light, the white blood cell membranes are crosslinked and encapsulated within a hydrogel, so that only the H1975 cells are lysed when lysis buffer is added to the well.

113

Because fluorescein undergoes intersystem crossing less readily than eosin, its tetrabromo derivative, with a triplet state quantum yield of 0.05 relative to eosin's 0.61,[207] it is a less efficient photoinitiator.[9,15] Its lower rate of intersystem crossing is why it is favored as a fluorescent tracer; its aqueous fluorescence quantum yield, which increases with pH,[122] is 0.92 compared with 0.2 for eosin.[208]

Using CMFDA and CD45 targeting to immobilize eosin on the cell surfaces, it is possible to load a sufficient level of photoinitiator in the cytoplasm and on the membranes of white blood cells to selectively protect only the white blood cells in a mixed population of white blood cells and H1975 tumor cells in as little as 5 seconds (Figure 7-2). As shown in Figure 7-2B, more than 94% of the white blood cells remain following lysis. Initially, we believed that a hydrogel interfacially polymerized on the white blood cell membranes served as the only protection against lysis. However, control experiments revealed that irradiation of the CMFDA in the cytoplasm without eosin immobilized on the surface and in the absence of monomers prevented lysis. Both fluorescein and eosin are singlet oxygen sensitizers.[98] In the triplet state, these dyes react with oxygen to produce singlet oxygen and regenerate the ground state. The singlet oxygen quantum yields in water are 0.03 (fluorescein) and 0.57 (eosin).[35,98] Singlet oxygen has been implicated in the crosslinking of membrane proteins for cell membranes that have been reacted with fluorescein isothiocyanate and irradiated with 488 nm laser light (1.9 W/cm^2) for 15-165 seconds.[209] The addition of sodium azide, a singlet oxygen quencher, was shown to inhibit the crosslinking.[209] It should be noted that sodium azide can also react with sensitizer triplets and, as a hydrophilic anion, is excluded from the membrane interior and repelled by the negative charge on most biological membranes.[210] Singlet oxygen is longer lived than the other excited states of oxygen,[211] and singlet oxygen lifetimes have been shown to be longer in model membranes, possibly facilitating reactions with membrane proteins.[210] In another example of photosensitizer initiated crosslinking, membrane protein aggregation was induced upon the irradiation (15 W/cm^2, 488 nm) of fluorescein-conjugated concanavalin A, a carbohydrate-binding protein, bound to erythrocyte membranes.[212] The integrity of the membrane permeability barrier was not compromised and reducing the concentration of oxygen was found to reduce the extent of the crosslinking. 2-mercaptoethanol was also shown to disaggregate some of the crosslinked material, indicating the formation of oxidative crosslinks.[212] In a different application, fluorescein-dextran conjugates were introduced intravascularly to induce platelet aggregation in arterioles of the hamster cheek pouch in response to irradiation.[213] Singlet oxygen scavengers (sodium azide, trans-beta-carotene) delayed the time to aggregate appearance while hydroxyl radical scavengers had no effect. Rose Bengal, another xanthene dye, and more efficient singlet oxygen sensitizer (quantum yield=0.75[98]) has been used in a light initiated bonding technique intended to replace suturing.[214–218] The protein crosslinking has been shown to be mediated by singlet oxygen; Verter et al. showed that the extent of crosslinking decreased under nitrogen purging and increased in D$_2$O, in which singlet oxygen is longer lived.[218]

Efforts have been made to elucidate the mechanism for this photoinduced crosslinking. The photooxidation products of histidine are thought to undergo crosslinking via a nucelophilic addition by amino groups.[211,219,220] These products can also react with cysteine or other histidine residues to form crosslinks.[211] The photooxidation products of tyrosine and tryptophan also react with amino groups.[211,220] In addition to the singlet oxygen mediated pathway, aromatic amino acids such as tyrosine and tryptophan are oxidized in reactions with the triplet state and semioxidized form of eosin.[138,139] Radical formation can also lead to peptide bond cleavage.[211] Aggregation via intermolecular disulphide bond formation and radical-radical termination reactions can result as well.

Increasing the irradiation time from 5 to 60 seconds resulted in retention of the cells labeled with CMTPX (Figure 7-2); the percentage of H1975 cells remaining post-lysis increases from 4% to 88%. This

suggests that the CMTPX may also function as a singlet oxygen photosensitizer. It is also possible that as the irradiation time is increased, nonspecific polymerization occurs. Radical polymerization is a threshold process; a minimum concentration of initiating radicals is required for initiation and propagation reactions to be competitive with inhibition reactions. For less efficient photoinitiators as well as those present at lower concentrations, it is possible to increase the initiating radical concentration by increasing the light dosage.[16]
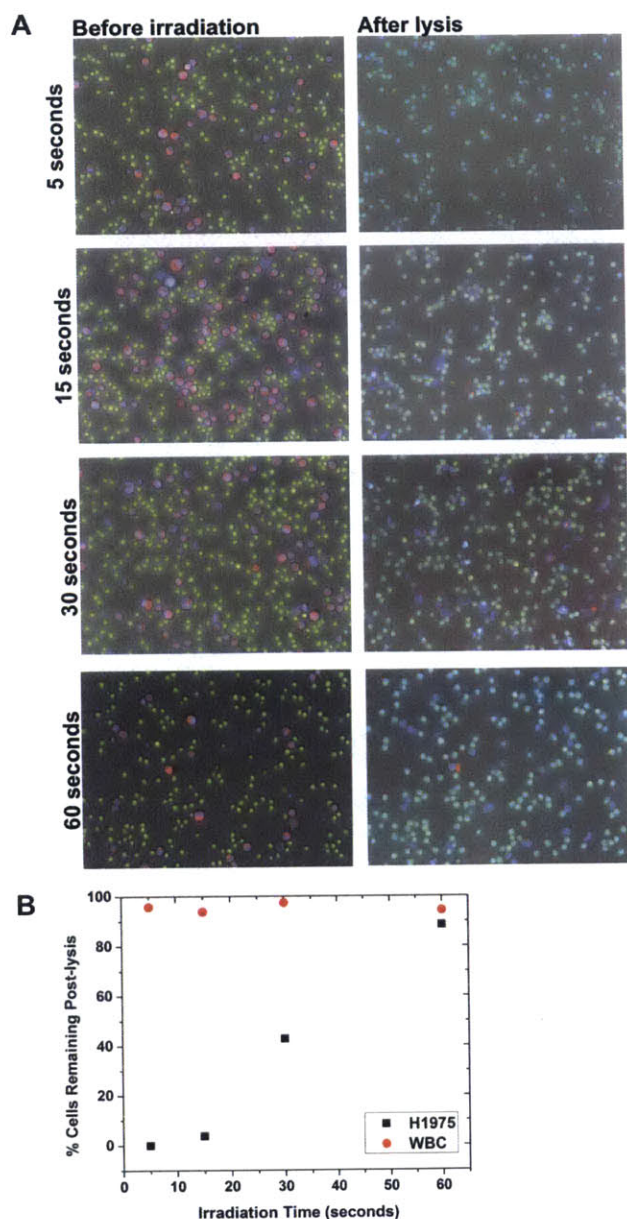
Figure 7-2. Adjusting the lysis threshold. A) Cells are shown before irradiation and after lysis for progressively longer irradiation times. The white blood cells (WBC) are stained with CellTracker Green CMFDA and the H1975 cells are stained with CellTracker Red CMTPX. The nuclei are stained with Hoechst; the signal from the Hoechst dominates post-lysis as the CellTracker dyes are photobleached during the irradiation. B) Quantitative analysis of the percentage of each cell type remaining post-lysis for increasing irradiation times.

Figure 7-3A shows that the specificity of the technique is not impacted by varying the ratio of H1975 cells to white blood cells. As the ratio is varied from 1:2 to 1:25, only the white blood cells remain following lysis for a 5 second irradiation time. This has important implications for applications in which the cell type intended for RNA extraction is present at a much lower density than other cell types.

The strength of this technique for selective lysis lies in its ability to protect the target population from lysis even in closely contacted cell aggregates (Figure 7-3 B and C). As shown, even white blood cells in close proximity to H1975 cells remain intact following introduction of the lysis buffer. Figure 7-3C presents SEM images of white blood cells before and after irradiation and shows white blood cells in contact with an H1975 cell post-irradiation in a demonstration of the resolution achievable using this method.
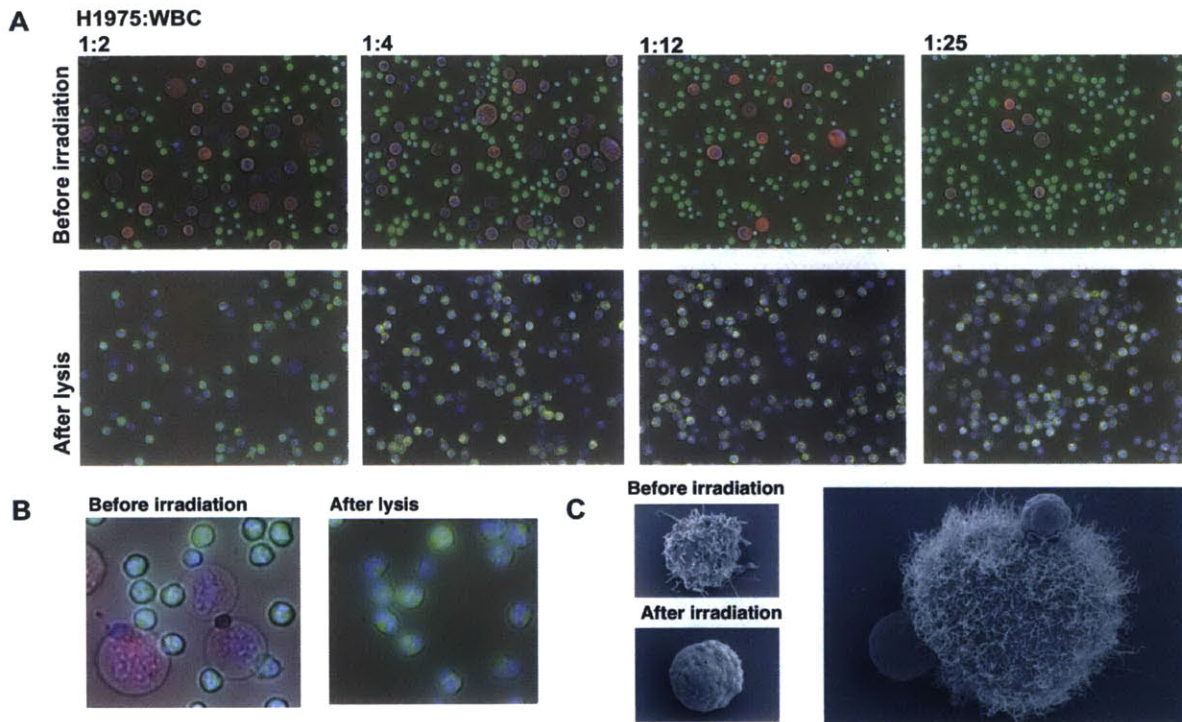
Figure 7-3. Lysis in closely contacted cell aggregates of white blood cells (WBC) and H1975 tumor cells. A) The ratio of H1975 tumor cells (red) to white blood cells (green) was varied. Varying the ratio of the cells did not impact the performance of the technique; approximately 90% of the white blood cells remained post-lysis for each ratio and an irradiation time of 5 seconds. The nuclei are stained with Hoechst (blue); the signal from the Hoechst dominates post-lysis as the CellTracker dyes are photobleached during the irradiation. B) White blood cells and H1975 cells shown in close proximity. Only the white blood cells remain post-lysis. C) SEM images of a white blood cell before and after irradiation (left) and crosslinked/polymerized white blood cells in contact with an H1975 cell.

Pre-labeling cells with photosensitizers prior to co-culture allows for selective lysis of and nucleic acid extraction from the unlabeled cells. This is a significant improvement over currently available methods for nucleic acid analysis in co-culture, which require trypsinization and FACS or suffer from low signal-to-noise ratios.

7.5   Conclusion

The enrichment of nucleic acids from a target cell population in a co-culture requires trypsinization and cell sorting and is hindered by low signal-to-noise ratios when attempted in situ. Photoinduced membrane crosslinking and targeted interfacial polymerization present efficient strategies for selective

cell lysis and RNA enrichment in co-cultures. Cells are pre-labeled with a commercially available dye that passes through the cell membrane and is converted into a cell impermeant product in the cytoplasm. In response to irradiation, the dye converts oxygen to singlet oxygen, which induces crosslinking of the membrane proteins. In addition, photoinitiators immobilized on the cell surface initiate polymerization upon the addition of a solution of monomers and exposure to light, forming hydrogels that are localized to the surfaces of the labeled cells, further protecting the cells against lysis. Future work will concentrate on determining the relative contribution of the photoinduced crosslinking and interfacial polymerization to protecting the cells against lysis.

8 Conclusion and Outlook

8.1 Summary

Photopolymerization-based signal amplification (PBA) is an approach to biosensing that leverages the amplification inherent to radical photopolymerization to enhance signal associated with specific molecular recognition events. The main objective of this thesis was to expand the range of relevant applications for PBA by addressing some the limitations of the technique as originally developed. In addition, we sought to build a mechanistic understanding of the method, specifically examining the effects of nonideal binding reactions and oxygen. Chapter 2 describes the development of an air-tolerant monomer solution that allows interfacial photopolymerization reactions to proceed under ambient conditions in as little as 35 seconds.[10] Previous implementations of PBA required inert gas purging to eliminate the inhibitory effects of oxygen. We showed that the inclusion of submicromolar concentrations of eosin, the photoinitiator, in the monomer solution mitigated these effects. The ability to perform these reactions under ambient conditions increases their clinical utility by simplifying the procedure and by removing purging gases that might be detrimental in some biological applications, specifically those involving cells.

Chapters 3 and 4 detail spectroscopic investigations into the mechanisms underlying eosin's ability to overcome oxygen inhibition. In Chapter 3, a dual-monitoring system for measuring eosin consumption and monomer conversion is used to corroborate the hypothesized regeneration of eosin in the presence of oxygen. A method for analyzing absorbance data for polymerizing hydrogels is also presented. In Chapter 4, we examine the photoinitiation kinetics of the eosin/tertiary amine system and the effect of oxygen using absorbance spectroscopy and kinetic modeling. The spectroscopic investigation revealed that, in addition to the previously postulated reactions in which eosin is regenerated by oxygen, additional reactions between oxygen and eosin in its triplet state and semireduced form occur and must be taken into account. The formation and consumption of the semireduced species informed the construction of a kinetic model, for which the importance of considering the reaction between triplet state eosin and the tertiary amine as two separate steps was clearly demonstrated.

Chapter 5 considers the molecular recognition event, rather than the amplification chemistry examined in the preceding two chapters. This chapter explores the concept of the amplification threshold in photopolymerization-based signal amplification by investigating the impact of the binding affinity of the molecular recognition event on the limit of detection. We showed that improvements in binding affinity enhance detection sensitivity. A mass action kinetics based model was used to accurately predict experimental findings and identify the key parameters for predicting the performance of PBA reactions: surface capture probe density, incubation time, concentration and binding affinity of the target molecule.

Chapter 6 evaluates the widely advocated strategy of developing polymeric macrophotoinitiators for improving the sensitivity of photopolymerization-based signal amplification reactions. Building on earlier work, in which solubility limits were encountered coupling eosin and neutravidin to a poly (acrylic acid-co-acrylamide) backbone,[221] we synthesized a more water-soluble polymeric macrophotoinitiator based on a generation 7 poly (amidoamine) dendrimer scaffold. Although the solubility was improved, a new quenching limitation was identified, demonstrating the complexity of designing polymeric macrophotoinitiators that incorporate eosin as the photoinitiator. In lieu of viable photoinitiator alternatives to eosin, we concluded that future efforts to design polymeric macrophotoinitiators should include features that increase the distance between eosin molecules. However, it is also possible that

the polymeric macrophotoinitiators are sterically hindered and that fewer bind to the surface. Considering the excellent performance of the eosin-avidin conjugate, efforts to improve the sensitivity of PBA reactions would be better spent on increasing the density of the capture probe.

Finally, in Chapter 7, we used PBA and photoactivated membrane crosslinking to selectively encapsulate a target population of cells in a co-culture. In addition to labeling cell membranes with photoinitiator, cells were pre-labeled with photoinitiators that are able to pass through the cell membrane into the cytoplasm where they are converted to cell-impermeant products. This form of labeling and subsequent illumination protects the cells against lysis, allowing for nucleic acid extraction from the unlabeled cells without the need for cell sorting.

8.2 Recent advances

In the course of completing this thesis, a number of additional improvements reducing the cost associated PBA were made. We found that coating glass slides with an activated agarose film[162] facilitated a retention of binding activity for proteins that were denatured on SAM-modified glass.[105,166] In addition to providing a more hydrophilic environment, we hypothesize that the agarose coatings shield the proteins from the charged glass surface. These surfaces have the added advantage of being significantly less expensive than SAM-modified glass (83% cheaper).

The agarose surfaces were critical to the development of a photopolymerization-based epigenotyping assay using methyl binding domain (MBD) proteins.[105] Photopolymerization-based signal amplification enhances the suitability of MBD proteins for the detection of methylated DNA fragments by reducing the cost and complexity of the assay relative to previously proposed methods.

More recently, photopolymerization-based signal amplification was demonstrated as part of a paper-based immunoassay.[21] Photopolymerization-based signal amplification was used to enhance the visual contrast of the colorimetric readout and accelerate the color development process relative to existing enzyme and nanoparticle based technologies. High visual contrast between negative and positive results was achieved through the formulation of a pH-responsive monomer solution; 1.6 mM phenolphthalein was incorporated into the acrylate monomer solution[10] and the pH was reduced to 7.9 to eliminate light absorption by phenolphthalein during the polymerization. The phenolphthalein becomes entrapped within the polymer network; a basic rinse post-polymerization permits visualization by the unaided eye as the polymer goes from colorless to bright pink. The immunodetection of plasmodium falciparum histidine-rich protein 2 in human serum was used as an example. This method was shown to be quantitative when combined with cellphone-based imaging (Figure 8-1). Indicative of the flexibility of this assay, it was also possible for the user to decouple the analyte capture from the amplification and visualization; eosin is stable on the surface and is able to initiate polymerization after 130 days of storage and the hydrogel post-polymerization can be rehydrated with NaOH after 130 days to generate a strong colorimetric response.
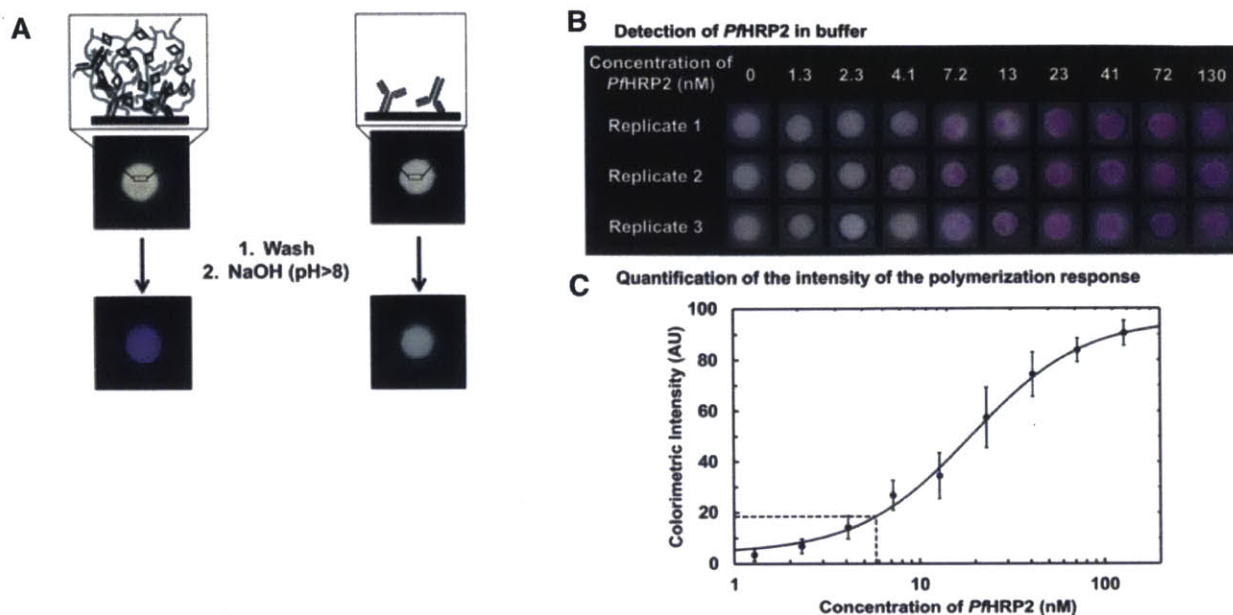
Figure 8-1. Photopolymerization-based signal amplification for a paper-based immunoassay. A) Hydrophilic test zones were created by wax printing chromatography paper. Capture antibodies against *Pf*HRP2 were covalently coupled to aldehyde groups within the test zone, allowing for the subsequent capture of *Pf*HRP2. A second eosin-modified reporter antibody was introduced to form a complex with the surface-immobilized *Pf*HRP2 and restrict polymerization to test zones in which *Pf*HRP2 was captured. In order to visualize the polymer that formed, phenolphthalein was included in the monomer solution. As shown, the phenolpthalien became entrapped within the cross-linked polymer network. A colorimetric readout was achieved when a basic solution was dropped onto the surface, causing the phenolphthalein to become pink. A similar color change was not observed on surfaces on which no *Pf*HRP2 was captured and, consequently, no polymer formed. B) Detection of *Pf*HRP2 in a buffered solution at various concentrations. C) Quantitation of the colorimetric results shown in (B). Images were taken using a cell phone camera and the colorimetric intensity was calculated using ImageJ. The vertical line indicates the calculated limit of detection. Reprinted with permission from Badu-Tawiah and Lathwal et al., *Lab on a Chip*, 2015, 15, 655-659. Copyright © 2015, The Royal Society of Chemistry.[21]

8.3 Outlook

As a novel technology platform, the unexplored parameter space for PBA is vast. The photoinitiation chemistry, monomer composition, and signal interpretation are all areas for continued research.

Alternative photoinitiation chemistries, in particular, are worthy of further exploration; to date, only Irgacure 2959, Irgacure 184, fluorescein, and eosin have been tested. Eosin is one of several xanthene dyes.[98] Its superior performance as a photoinitiator relative to fluorescein has been explained by its higher intersystem crossing quantum yield.[98] The heavy atom content of erythrosin B and Rose Bengal results in still higher intersystem crossing quantum yields, potentially indicating the potential of these two xanthene dyes as alternative photoinitiators for PBA. It is generally accepted that to be considered effective, photosensitizers should have high molar extinction coefficients at the wavelength of the excitation light, high yields of intersystem crossing to the triplet state, and long triplet lifetimes to allow sufficient time for reaction.[222] However, the heavy atoms that drive intersystem crossing, also favor back electron transfer from the semireduced eosin to the tertiary amine radical cation, ultimately reducing the photoinitiation efficiency.[207] The opposing effects of the xanthene dye heavy atoms highlight the complexity of evaluating photoinitiators. The coupled system for dual-monitoring of UV-Vis and FT-NIR presented in Chapter 3 presents an effective screening method for assessing photoinitiation systems.

Eosin's use as a photoinitiator dates back to the 1950s;[223] in the last 20 years, significant advancements in photoinitiator efficiency have been achieved through the use of three-component systems. Three-component photoinitiation systems include a light absorbing moiety (dye), an electron donor (amine), and an iodonium salt.[106,107] The hypothesized mechanism through which these reactions proceed involves first the bimolecular initiation reaction between the dye and the amine, producing an amine radical capable of initiating polymerization and an inactive dye radical. The iodonium salt is posited to oxidize the inactive dye radical, regenerating the original dye, while also producing an active phenyl radical.[106] A more efficient photo-oxidizable mechanism has also been proposed; the route through which the reaction proceeds depends on the reactants.[224] Advantages of three-component systems include better absorption, enhanced photochemical and chemical reactivity, higher polymerization rates and conversions, and lower oxygen sensitivity.[71,225] Lower oxygen sensitivity is especially significant in the context of photopolymerization-based signal amplification where the surface-to-volume ratio is high, resulting in rapid replenishment of oxygen even as it is consumed in inhibition reactions. Replacing the coinitiator also has the potential to yield significant gains in terms of photoinitiation efficiency. In a study of the effect of coinitiator type on the initiation efficiency of two-component systems employing eosin, Popielarz and Vogt showed that eosin used with an iodonium salt was 28x more efficient that eosin used with triethanolamine.[226]

One of the disadvantages of employing eosin to overcome oxygen inhibition is that the limit of detection is essentially set by the concentration of eosin in the monomer solution. When the effective eosin surface concentration approaches the solution concentration, the entire solution polymerizes and no surface localized polymerization is observed. Another alternative for overcoming oxygen inhibition is to employ glucose oxidase to "scrub" oxygen from the system.[50]

Alternative methods for generating quantitative readouts have been explored in the context of AGET ATRP. Photopolymerization has been most effective for enabling colorimetric readouts by producing thick films that are readily visible to the unaided eye; the use of cell phone based imaging also allows for quantitation with relative ease. Resistance-based measurements may permit quantitation with increased sensitivity and precision. Chemiresistive biosensing is an area of growing interest as it allows for label-free, rapid detection; analyte binding to the sensor surface changes the resistance, which can be measured using an inexpensive multimeter.[227] Recently, conducting polymers have been used in the fabrication of chemiresistive biosensors.[227] In addition to providing mechanical flexibility (permitting a range of novel substrates as surfaces), tunability, and low cost, these conducting polymers can be easily modified to facilitate the covalent bonding of probe molecules. Photopolymerization-based signal amplification has the potential to enhance the sensitivity of chemiresistive biosensors based on conducting polymers. Polymer formation triggered by photoinitiators immobilized on the surface as a function of binding events would amplify the change in resistance, enabling the detection of lower concentrations of analyte.

In addition to resistance based sensing, we can also envision detecting the growth of polymer films using microfluidic methods based on changes in size (film thickness), density, or surface friction. For these applications, the polymerization may be performed on functionalized beads, rather than planar substrates. Inertial focusing allows for the passive ordering of particles of different sizes at high rates in microchannels.[228] PBA can be used to effect a change in size through the growth of a polymer film. This change can then be detected using inertial focusing. Microchannel resonators can also be used to detect changes in size.[229] Alternatively, the Manalis Group has developed microfluidic mass sensors capable of measuring the density of single cells with a precision of 0.001 g/mL.[230] Provided the polymer is sufficiently thick, polymer film growth is likely to alter particle density, enabling this form of sensing.

Surface friction is yet another possible metric and would depend on the hydrogel's surface friction being different to that of the underlying substrate.[231]

Two of the most critical parameters in determining the sensitivity of photopolymerization-based signal amplification reactions are the capture probe density and its affinity for the target of interest. Efforts are underway to engineer better capture probe molecules with higher affinities. However, as shown in Chapter 5, the gains achievable using higher affinity capture probes are limited, and, ultimately, assay sensitivity is determined by the capture probe density. Three-dimensional substrates, of which the agarose surfaces are an example, offer a potential route towards increasing the density of capture probes on the surface. The agarose-coated surfaces were optimized with the intent of minimizing stain uptake on the surface. This resulted in a lower concentration of agarose being used than might be most favorable for achieving high capture probe densities. The lower concentration of agarose implies a lower concentration of functional groups and larger pores. As alternative staining strategies, such as the phenolphthalein system, are developed, a reoptimization of the agarose-coated surfaces may be warranted. Polymer brushes have been used extensively to produce functionalized surfaces.[232] However, it is difficult to rival the simplicity and low cost of the agarose-coated surfaces.

There are a number of potential applications that can benefit from the selective cell lysis protocol presented, including drug screening for liver toxicity[197] as well as studies of tumor angiogenesis,[183,184] cell migration,[185] cancer metastasis,[186–188] immune responses,[189] wound healing,[190,191] stem cell maintenance,[192] and the assembly of neural circuits.[193] As presented, the demonstration of selective lysis made use of a commercially available modified-fluorescein. This dye is only one of many commercially available dyes, and further studies could identify an alternative that is retained for longer periods within the cell, allowing for longer-term co-culture experiments.

The discovery of more efficient photoinitiators or the development of a water-soluble polymeric macrophotoinitiator that is impervious to quenching could improve the reproducibility of molecular recognition event-triggered cell encapsulation. This advance would widen the field of potential applications for PBA. One application of particular interest is the selective extraction of nucleic acids from circulating tumor cells (CTCs) in a mixed population with white blood cells. Over the past few years, significant progress has been made in capturing CTCs from the peripheral blood of patients with metastatic cancers.[203,233–235] There is interest in RNA-based characterization of the isolated CTCs. This is complicated by the presence of contaminating white blood cells.[233] Photopolymerization-based signal amplification offers a strategy for selectively polymerizing white blood cells in response to labeling with photoinitiator conjugated anti-CD45 antibodies, thereby enabling the extraction of RNA from only the CTCs. By incorporating cleavable monomers,[236] it should be possible to remove the polymers from the encapsulated cells, allowing for molecular analysis of both cell populations.

Efforts are underway to model the interfacial polymerization activated by eosin. This is a challenging problem due to the complexity of the photoinitiation kinetics involved. This thesis has provided some clues as to which reactions must be included in order to more fully capture the behavior observed experimentally. The development of a representative and predictive model would permit a design-based approach, eliminating the need for tedious trial and error based experimentation. Strides have already been made in this direction, in particular concerning the binding reaction at the surface.

8.4 Concluding remarks

This thesis describes the development of photopolymerization-based signal amplification as a platform technology for use at the point-of-care. The development of an oxygen tolerant monomer formulation for radical photopolymerization provided the impetus for spectroscopic investigations into photoinitiation kinetics and the effect of oxygen. The factors determining the sensitivity of photopolymerization-based amplification reactions were elucidated and novel synthetic strategies for macrophotoinitiators were explored. Finally, interfacial photopolymerization and photoactivated membrane cross-linking was implemented for the selective lysis of a target cell population in a co-culture. This thesis provides the basis for future work evaluating alternative photoinitiation chemistries, monomer compositions, detection reagents, and signal interpretation methodologies.

References

(1)   Turner, A. P. F. *Chem. Soc. Rev.* **2013**, *42*, 3184–3196.

(2)   Wu, Y.; Wei, W.; Liu, S. *Acc. Chem. Res.* **2012**, *45*, 1441–1450.

(3)   Peris, E.; Bañuls, M.-J.; Maquieira, Á.; Puchades, R. *Trends Anal. Chem.* **2012**, *41*, 86–104.

(4)   Yuan, L.; Hua, X.; Xu, L.; Liu, S. *Anal. Chim. Acta* **2015**.

(5)   Sikes, H. D.; Hansen, R. R.; Johnson, L. M.; Jenison, R.; Birks, J. W.; Rowlen, K. L.; Bowman, C. N. *Nat. Mater.* **2008**, *7*, 52–56.

(6)   Hansen, R. R.; Sikes, H. D.; Bowman, C. N. *Biomacromolecules* **2008**, *9*, 355–362.

(7)   Hansen, R. R.; Avens, H. J.; Shenoy, R.; Bowman, C. N. *Anal. Bioanal. Chem.* **2008**, *392*, 167–175.

(8)   Avens, H. J.; Chang, E. L.; May, A. M.; Berron, B. J.; Seedorf, G. J.; Balasubramaniam, V.; Bowman, C. N. *J. Nanoparticle Res.* **2011**, *13*, 331–346.

(9)   Lee, J. K.; Heimer, B. W.; Sikes, H. D. *Biomacromolecules* **2012**, *13*, 1136–1143.

(10)   Kaastrup, K.; Sikes, H. D. *Lab Chip* **2012**, *12*, 4055–4058.

(11)   Lee, J. K.; Sikes, H. D. *Macromol. Rapid Commun.* **2014**, *35*, 981–986.

(12)   Kaastrup, K.; Sikes, H. D. *RSC Adv.* **2015**, *5*, 15652–15659.

(13)   Sikes, H. D.; Jenison, R.; Bowman, C. N. *Lab Chip* **2009**, *9*, 653–656.

(14)   Kizilel, S.; Pérez-Luna, V. H.; Teymour, F. *Langmuir* **2004**, *20*, 8652–8658.

(15)   Avens, H. J.; Bowman, C. N. *J. Polym. Sci. Part A Polym. Chem.* **2009**, *47*, 6083–6094.

(16)   Ligon, S. C.; Husár, B.; Wutzel, H.; Holman, R.; Liska, R. *Chem. Rev.* **2014**, *114*, 577–589.

(17)   Hansen, R. R.; Johnson, L. M.; Bowman, C. N. *Anal. Biochem.* **2009**, *386*, 285–287.

(18)   Avens, H. J.; Bowman, C. N. *Acta Biomater.* **2010**, *6*, 83–89.

(19)   Avens, H. J.; Berron, B. J.; May, A. M.; Voigt, K. R.; Seedorf, G. J.; Balasubramaniam, V.; Bowman, C. N. *J. Histochem. Cytochem.* **2011**, *59*, 76–87.

(20)   Kuck, L. R.; Taylor, A. W. *Biotechniques* **2008**, *45*, 179–186.

(21)   Badu-Tawiah, A. K.; Lathwal, S.; Kaastrup, K.; Al-Sayah, M.; Christodouleas, D. C.; Smith, B. S.; Whitesides, G. M.; Sikes, H. D. *Lab Chip* **2015**, *15*, 655–659.

(22)   Johnson, L. M.; Hansen, R. R.; Urban, M.; Kuchta, R. D.; Bowman, C. N. *Biomacromolecules* **2010**, *11*, 1133–1138.

(23)   Lorenz, D. H.; Azorlosa, J. L.; Tu, R. S. *Radiat. Phys. Chem.* **1977**, *9*, 843–849.

(24)   White, T. J.; Liechty, W. B.; Guymon, C. A. *J. Polym. Sci. Part A Polym. Chem.* **2007**, *45*, 4062–4073.

(25)   Pathak, C. P.; Sawhney, A. S.; Hubbell, J. A. *J. Am. Chem. Soc.* **1992**, *114*, 8311–8312.

(26)   Cruise, G. M.; Hegre, O. D.; Scharp, D. S.; Hubbell, J. A. *Biotechnol. Bioeng.* **1998**, *57*, 655–665.

(27)   Cruise, G. M.; Scharp, D. S.; Hubbell, J. a. *Biomaterials* **1998**, *19*, 1287–1294.

(28)   Avens, H. J.; Randle, T. J.; Bowman, C. N. *Polymer (Guildf).* **2008**, *49*, 4762–4768.

(29)   Karu, T. I. *Photochem. Photobiol.* **1990**, *52*, 1089–1098.

(30)   Lilly, J. L.; Sheldon, P. R.; Hoversten, L. J.; Romero, G.; Balasubramaniam, V.; Berron, B. J. *PLoS One* **2014**, *9*, e115630.

(31)   Xu, L.; Yuan, L.; Liu, S. *RSC Adv.* **2014**, *4*, 140–146.

(32)   Xu, J.; Shanmugam, S.; Duong, H. T.; Boyer, C. *Polym. Chem.* **2014**.

(33)   Valdes-Aguilera, O.; Pathak, P. C.; Shi, J.; Watson, D.; Neckers, D. C. *Macromolecules* **1992**, *25*, 541–547.

(34)   Zhang, X.-F.; Zhang, I.; Liu, L. *Photochem. Photobiol.* **2010**, *86*, 492–498.

(35)   Gandin, E.; Lion, Y.; van de Vorst, a. *Photochem. Photobiol.* **1983**, *37*, 271–278.

(36)   Dawson, E. D.; Taylor, A. W.; Smagala, J. a.; Rowlen, K. L. *Mol. Biotechnol.* **2009**, *42*, 117–127.

(37)   Quiñones, B.; Swimley, M. S.; Taylor, A. W.; Dawson, E. D. *Foodborne Pathog. Dis.* **2011**, *8*, 705–711.

(38)   Quiñones, B.; Swimley, M. S.; Narm, K.-E.; Patel, R. N.; Cooley, M. B.; Mandrell, R. E. *Front. Cell. Infect. Microbiol.* **2012**, *2*, 1–10.

(39)   Berron, B. J.; Johnson, L. M.; Ba, X.; McCall, J. D.; Alvey, N. J.; Anseth, K. S.; Bowman, C. N. *Biotechnol. Bioeng.* **2011**, *108*, 1521–1528.

(40)   Berron, B. J.; May, A. M.; Zheng, Z.; Balasubramaniam, V.; Bowman, C. N. *Lab Chip* **2012**, *12*, 708–710.

(41)   Odian, G. *Principles of Polymerization*; 4th ed.; John Wiley & Sons, Inc.: Hoboken, NJ, 2004.

(42)   Lou, X.; Lewis, M. S.; Gorman, C. B.; He, L. *Anal. Chem.* **2005**, *77*, 4698–4705.

(43)   Lou, X.; He, P.; Okelo, G. O.; He, L. *Anal. Bioanal. Chem.* **2006**, *386*, 525–531.

(44)   He, P.; Zheng, W.; Tucker, E. Z.; Gorman, C. B.; He, L. *Anal. Chem.* **2008**, *80*, 3633–3639.

(45)   Chesneau, E.; Fouassier, J. P. *Die Angew. Makromol. Chemie* **1985**, *135*, 41–64.

(46)   Jakubowski, W.; Matyjaszewski, K. *Macromolecules* **2005**, *38*, 4139–4146.

(47)   Qian, H.; He, L. *Anal. Chem.* **2009**, *81*, 4536–4542.

(48)   Qian, H.; He, L. *Anal. Chem.* **2009**, *81*, 9824–9827.

(49)   Lou, X.; He, L. *Langmuir* **2006**, *22*, 2640–2646.

(50)   Chapman, R.; Gormley, A. J.; Herpoldt, K.; Stevens, M. M. *Macromolecules* **2014**.

(51)   Edmondson, S.; Osborne, V. L.; Huck, W. T. S. *Chem. Soc. Rev.* **2004**, *33*, 14–22.

(52)   Wu, Y.; Liu, S.; He, L. *Anal. Chem.* **2009**, *81*, 7015–7021.

(53)   Wu, Y.; Liu, S.; He, L. *Analyst* **2011**, *136*, 2558–2563.

(54)   Wu, Y.; Xue, P.; Hui, K. M.; Kang, Y. *Biosens. Bioelectron.* **2014**, *52*, 180–187.

(55)   Wu, Y.; Liu, S.; He, L. *Biosens. Bioelectron.* **2010**, *26*, 970–975.

(56)   Wu, Y.; Shi, H.; Yuan, L.; Liu, S. *Chem. Commun. (Camb).* **2010**, *46*, 7763–7765.

(57)   Liu, Y.; Dong, Y.; Jauw, J.; Linman, M. J.; Cheng, Q. *Anal. Chem.* **2010**, *82*, 3679–3685.

(58)   Liu, Y.; Cheng, Q. *Anal. Chem.* **2012**, *84*, 3179–3186.

(59)   Liu, Y.; Young, M. C.; Moshe, O.; Cheng, Q.; Hooley, R. J. *Angew. Chemie - Int. Ed.* **2012**, *51*, 7748–7751.

(60)   Lou, X.; Wang, C.; He, L. *Biomacromolecules* **2007**, *8*, 1385–1390.

(61)   Zheng, W.; He, L. *Anal. Bioanal. Chem.* **2009**, *393*, 1305–1313.

(62)   Shi, H.; Yuan, L.; Wu, Y.; Liu, S. *Biosens. Bioelectron.* **2011**, *26*, 3788–3793.

(63)   Gormley, A. J.; Chapman, R.; Stevens, M. M. *Nano Lett.* **2014**, 1–11.

(64)   Mabey, D.; Peeling, R. W.; Ustianowski, A.; Perkins, M. D. *Nat. Rev. Microbiol.* **2004**, *2*, 231–240.

(65)   Bowman, C. N.; Kloxin, C. J. *AIChE J.* **2008**, *54*, 2775–2795.

(66)   Gou, L.; Coretsopoulos, C. N.; Scranton, A. B. *J. Polym. Sci. Part A Polym. Chem.* **2003**, *42*, 1285–1292.

(67)   Kwisnek, L.; Heinz, S.; Wiggins, J. S.; Nazarenko, S. *J. Memb. Sci.* **2011**, *369*, 429–436.

(68)   Lee, T. Y.; Guymon, C. a.; Jönsson, E. S.; Hoyle, C. E. *Polymer (Guildf).* **2004**, *45*, 6155–6162.

(69)   Decker, C. *Macromol. Chem. Phys.* **1979**, *180*, 2027–2030.

(70)   Shenoy, R.; Bowman, C. N. *Macromolecules* **2010**, *43*, 7964–7970.

(71)   Padon, K. S.; Scranton, A. B. *J. Polym. Sci. Part A Polym. Chem.* **2000**, *38*, 3336–3346.

(72)   Anderson, D. A.; Crowe, S. M.; Garcia, M. *Curr. HIV/AIDS Rep.* **2011**, *8*, 31–37.

(73)   Niemz, A.; Ferguson, T. M.; Boyle, D. S. *Trends Biotechnol.* **2011**, *29*, 240–250.

(74)   Valdes-Aguilera, O.; Pathak, C. P.; Shi, J.; Watson, D.; Neckers, D. C. *Macromolecules* **1992**, *25*, 541–547.

(75)   Kuck, L. R. Signal Amplification of Biorecognition Events Using Photopolymerization in the Presence of Air. App. No. 12/279,523, Pub. No. 20090005263A1, 2009.

(76)   Simpson, R. J. *Proteins and Proteomics: A Laboratory Manual*; Cold Spring Harbor Laboratory Press: Cold Spring Harbor, NY, 2002; Vol. 0879695536.

(77)   Dendukuri, D.; Panda, P.; Haghgooie, R.; Kim, J. M.; Hatton, T. A.; Doyle, P. S. *Macromolecules* **2008**, *41*, 8547–8556.

(78)   Fouassier, J. .; Allonas, X.; Burget, D. *Prog. Org. Coatings* **2003**, *47*, 16–36.

(79)   Yagci, Y.; Jockusch, S.; Turro, N. J. *Macromolecules* **2010**, *43*, 6245–6260.

(80)   Shen, J.; Tian, Y.; Zeng, Y.; Qiu, Z. *Macromol. Rapid Commun.* **1987**, *8*, 615–620.

(81)   Florenzano, F. H.; Strelitzki, R.; Reed, W. F. *Macromolecules* **1998**, *31*, 7226–7238.

(82)   Giz, A.; Çatalgil-Giz, H.; Alb, A.; Brousseau, J. L.; Reed, W. F. *Macromolecules* **2001**, *34*, 1180–1191.

(83)   Drenski, M. F.; Reed, W. F. *J. Appl. Polym. Sci.* **2004**, *92*, 2724–2732.

(84)   Drenski, M. F.; Mignard, E.; Alb, A. M.; Reed, W. F. *J. Comb. Chem.* **2004**, *6*, 710–716.

(85)   Schmitt, M. *Macromol. Chem. Phys.* **2011**, *212*, 1276–1283.

(86)   Kang, X.; Yu, Y.; Bao, Y.; Cai, W.; Cui, S. *Polym. Chem.* **2015**.

(87)   Alakhras, F.; Holze, R. *Synth. Met.* **2007**, *157*, 109–119.

(88)   Decker, C. *J. Polym. Sci. Part A Polym. Chem.* **1992**, *30*, 913–928.

(89)   Nguyen, K. T.; West, J. L. *Biomaterials* **2002**, *23*, 4307–4314.

(90)   Koh, W.-G.; Revzin, A.; Pishko, M. V. *Langmuir* **2002**, *18*, 2459–2462.

(91)   Balakrishnan, B.; Banerjee, R. *Chem. Rev.* **2011**, *111*, 4453–4474.

(92)   Vermonden, T.; Censi, R.; Hennink, W. E. *Chem. Rev.* **2012**, *112*, 2853–2888.

(93)   Kharkar, P. M.; Kiick, K. L.; Kloxin, A. M. *Chem. Soc. Rev.* **2013**, *42*, 7335–7372.

(94)   Ghobril, C.; Grinstaff, M. W. *Chem. Soc. Rev.* **2015**, *44*, 1820–1835.

(95)   Cook, W. D.; Chen, F. *Polym. Chem.* **2015**, *6*, 1325–1338.

(96)   Kerker, M. *The Scattering of Light and Other Electromagnetic Radiation*; Academic Press, Inc.: New York, NY, 1969.

(97)   Fouassier, J. P.; Chesneau, E. *Macromol. Chem. Phys.* **1991**, *192*, 245–260.

(98)   Neckers, D. C.; Valdes-Aguilera, O. M. In *Advances in Photochemistry*; Volman, D. H.; Hammond, G. S.; Neckers, D. C., Eds.; John Wiley & Sons, Inc., 1993; Vol. 18, pp. 315–394.

(99)   Natera, J. E.; Massad, W. a.; Amat-Guerri, F.; García, N. a. *J. Photochem. Photobiol. A Chem.* **2011**, *220*, 25–30.

(100)   Wong, J.; Kaastrup, K.; Aguirre-Soto, A.; Sikes, H. D. *Polymer (Guildf).* **2015**, *69*, 169–177.

(101)   Davidson, R. S.; Trethewey, K. R. *J. Am. Chem. Soc.* **1976**, *98*, 4008–4009.

(102)   Srinivasan, V. S.; Podolski, D.; Westrick, N. J.; Neckers, D. C. *J. Am. Chem. Soc.* **1978**, *100*, 6513–6515.

(103)   Lee, P. C. C.; Rodgers, M. A. *J. Photochem. Photobiol.* **1987**, *45*, 79–86.

(104)   Lambert, C. R.; Kochevar, I. E. *J. Am. Chem. Soc.* **1996**, *118*, 3297–3298.

(105)   Heimer, B. W.; Shatova, T. A.; Lee, J. K.; Kaastrup, K.; Sikes, H. D. *Analyst* **2014**, *139*, 3695–3701.

(106)   Padon, K. S.; Scranton, A. B. *J. Polym. Sci. Part A Polym. Chem.* **2000**, *38*, 2057–2066.

(107)   Padon, K. S.; Scranton, A. B. *J. Polym. Sci. Part A Polym. Chem.* **2001**, *39*, 715–723.

(108) Neckers, D. C. *J. Chem. Educ.* **1987**, *64*, 649.

(109) Levillain, P.; Fompeydie, D. *Anal. Chem.* **1985**, *2563*, 2561–2563.

(110) Kasche, V.; Lindqvist, L. *Photochem. Photobiol.* **1965**, *4*, 923–933.

(111) Oster, G.; Oster, G. K.; Karg, G. *J. Phys. Chem.* **1962**, *66*, 2514–2517.

(112) Görner, H. *Photochem. Photobiol. Sci.* **2008**, *7*, 371–376.

(113) Zwicker, E. F.; Grossweiner, L. I. *J. Phys. Chem.* **1963**, *67*, 549–555.

(114) Kimura, K.; Miwa, T.; Imamura, M. *Chem. Commun.* **1968**, 1619–1621.

(115) Kimura, K.; Miwa, T.; Imamura, M. *Bull. Chem. Soc. Jpn.* **1970**, *43*, 1337–1342.

(116) Chambers, R. W.; Kajiwara, T.; Kearns, D. R. *J. Phys. Chem.* **1974**, *78*, 380–387.

(117) Rohatgi, K. K.; Mukhopadhyay, a. K. *Photochem. Photobiol.* **1971**, *14*, 551–559.

(118) López Arbeloa, I. *Dye. Pigment.* **1983**, *4*, 213–220.

(119) Oster, G.; Adelman, A. H. *J. Am. Chem. Soc.* **1956**, *78*, 913–916.

(120) Chrysochoos, J.; Ovadia, J.; Grossweiner, L. I. *J. Phys. Chem.* **1967**, *71*, 1629–1636.

(121) Fisher, G. J.; Lewis, C.; Madill, D. *Photochem. Photobiol.* **1976**, *24*, 223–228.

(122) Kasche, V.; Liindqvist, L. *J. Phys. Chem.* **1964**, *68*.

(123) Tanielian, C.; Golder, L.; Wolff, C. *J. Photochem.* **1984**, *25*, 117–125.

(124) Martinez, G.; Bertolotti, S. G.; Zimerman, O. E.; Martire, D. O.; Braslavsky, S. E.; Garcia, N. a. *J. Photochem. Photobiol. B Biol.* **1993**, *17*, 247–255.

(125) Riley, D. P.; Rivers, W. J.; Weiss, R. H. *Anal. Biochem.* **1991**, *196*, 344–349.

(126) Song, L.; Varma, C. A.; Verhoeven, J. W.; Tanke, H. J. *Biophys. J.* **1996**, *70*, 2959–2968.

(127) Islam, S. D. M.; Yoshikawa, Y.; Fujitsuka, M.; Watanabe, A.; Ito, O. Studies on Photochemical Processes of Xanthene Dyes by Means of the Transient Absorption Spectra in the Visible/Near-IR Regions. *Bulletin of the Chemical Society of Japan*, 1998, *71*, 1543–1548.

(128) Encinas, M. V.; Rufs, a. M.; Bertolotti, S. G.; Previtali, C. M. *Polymer (Guildf).* **2009**, *50*, 2762–2767.

(129) Valdebenito, A.; Encinas, M. V. *J. Photochem. Photobiol. A Chem.* **2008**, *194*, 206–211.

(130) Bartholomew, R. F.; Davidson, R. S. *J. Chem. Soc. C Org.* **1971**, 2347–2351.

(131) Penzkofer, a.; Beidoun, a.; Daiber, M. *J. Lumin.* **1992**, *51*, 297–314.

(132) Ohno, T.; Kato, S.; Koizumi, M. *Bull. Chem. Soc. Jpn.* **1966**, *39*, 232–239.

(133) Rizzuto, F.; Spikes, J. D. *Photochem. Photobiol.* **1977**, *25*, 465–476.

(134) Grossweiner, L. I.; Zwicker, E. F. *J. Chem. Phys.* **1961**, *34*, 1411–1417.

(135) Penzkofer, a.; Beidoun, a. *Chem. Phys.* **1993**, *177*, 203–216.

(136) Song, L.; Hennink, E. J.; Young, I. T.; Tanke, H. J. *Biophys. J.* **1995**, *68*, 2588–2600.

(137) Cordier, P.; Grossweiner, L. I. *J. Phys. Chem.* **1968**, *72*, 2018–2026.

(138) Grossweiner, L. I.; Kepka, A. G. *Photochem. Photobiol.* **1972**, *16*, 305–314.

(139) Kepka, A. G.; Grossweiner, L. I. *Photochem. Photobiol.* **1971**, *14*, 621–639.

(140) Kraljic, I. **1974**, *20*, 351–355.

(141) Wilkinson, F.; Helman, W. P.; Ross, A. B. *J. Phys. Chem. Ref. Data* **1995**, *24*, 663–911.

(142) Wilkinson, F.; Brummer, J. G. *J. Phys. Chem. Ref. Data* **1981**, *10*, 809–999.

(143) Guiraud, H. J.; Foote, C. S. *J. Am. Chem. Soc.* **1976**, *98*, 1968–1970.

(144) Koppenol, W. H.; Butler, J. *FEBS Lett.* **1977**, *83*, 1–6.

(145) Kato, S.; Watanabe, T.; Nagaki, S.; Koizumi, M. *Bull. Chem. Soc. Jpn.* **1960**, *33*, 262–265.

(146) Grotzinger, C.; Burget, D.; Jacques, P.; Fouassier, J. P. *Macromol. Chem. Phys.* **2001**, *202*, 3513–3522.

(147) Mills, A.; Lawrence, C.; Douglas, P. *J. Chem. Soc. Faraday Trans. 2* **1986**, *82*, 2291.

(148) Imamura, M.; Koizumi, M. *Bull. Chem. Soc. Jpn.* **1956**, *29*, 899–903.

(149) Maillard, B.; Ingold, K. U.; Scaiano, J. C. *J. Am. Chem. Soc.* **1983**, *105*, 5095–5099.

(150) Marklund, S. *J. Biol. Chem.* **1976**, *251*, 7504–7507.

(151) Fridovich, I. *Science (80-.).* **1978**, *201*, 875–880.

(152) Ingold, K. U. *Acc. Chem. Res.* **1968**, *2*, 1–9.

(153) Johnson, L. M.; Avens, H. J.; Hansen, R. R.; Sewell, H. L.; Bowman, C. N. *Aust. J. Chem.* **2009**, *62*, 877–884.

(154) He, P.; He, L. *Biomacromolecules* **2009**, *10*, 1804–1809.

(155) He, P.; Tucker, E. Z.; Gorman, C. B.; He, L. *Anal. Methods* **2011**, *3*, 2463.

(156) Green, N. M. *Methods Enzymol.* **1970**, *18*, 418–424.

(157) Kuriyan, J.; Konforti, B.; Wemmer, D. In *The Molecules of Life*; Taylor & Francis Group, 2012.

(158) Sano, T.; Smith, C. L.; Cantor, C. R. *Science* **1992**, *258*, 120–122.

(159) Liang, M.; Klakamp, S. L.; Funelas, C.; Lu, H.; Lam, B.; Herl, C.; Umble, A.; Drake, A. W.; Pak, M.; Ageyeva, N.; Pasumarthi, R.; Roskos, L. K. *Assay Drug Dev. Technol.* **2007**, *5*, 655–662.

(160) Glass, T. R.; Ohmura, N.; Saiki, H. *Anal. Chem.* **2007**, *79*, 1954–1960.

(161) Hackel, B. J.; Ackerman, M. E.; Howland, S. W.; Wittrup, K. D. *J. Mol. Biol.* **2010**, *401*, 84–96.

(162) Afanassiev, V.; Hanemann, V.; Wölfl, S. *Nucleic Acids Res.* **2000**, *28*, E66.

(163) Janin, J.; Chothia, C. *J. Biol. Chem.* **1990**, *265*, 16027–16030.

(164) Valencia, C. A.; Coffee, B. *Modern Clinical Molecular Techniques*; Hu, P. C.; Hegde, M. R.; Lennon, P. A., Eds.; Springer: New York, NY, 2012.

(165) Lei, J.; Ju, H. *Chem. Soc. Rev.* **2012**, *41*, 2122–2134.

(166) Kaastrup, K.; Chan, L.; Sikes, H. D. *Anal. Chem.* **2013**, *85*, 8055–8060.

(167) Qian, H.; He, L. *Sensors Actuators B Chem.* **2010**, *150*, 594–600.

(168) Zakrzewski, A.; Neckers, D. C. *Tetrahedron* **1987**, *43*, 4507–4512.

(169) Wängler, C.; Moldenhauer, G.; Saffrich, R.; Knapp, E.-M.; Beijer, B.; Schnölzer, M.; Wängler, B.; Eisenhut, M.; Haberkorn, U.; Mier, W. *Chem. -A Eur. J.* **2008**, *14*, 8116–8130.

(170) Albertazzi, L.; Storti, B.; Marchetti, L.; Beltram, F. *J. Am. Chem. Soc.* **2010**, *132*, 18158–18167.

(171) Albertazzi, L.; Brondi, M.; Pavan, G. M.; Sato, S. S.; Signore, G.; Storti, B.; Ratto, G. M.; Beltram, F. *PLoS One* **2011**, *6*, e28450.

(172) Kim, Y.; Kim, S. H.; Tanyeri, M.; Katzenellenbogen, J. A.; Schroeder, C. M. *Biophys. J.* **2013**, *104*, 1566–1575.

(173) Myung, J. H.; Gajjar, K. a; Saric, J.; Eddington, D. T.; Hong, S. *Angew. Chem. Int. Ed. Engl.* **2011**, *50*, 11769–11772.

(174) Jasmine, M. J.; Kavitha, M.; Prasad, E. *J. Lumin.* **2009**, *129*, 506–513.

(175) Herz, A. H. *Adv. Colloid Interface Sci.* **1977**, *8*, 237–298.

(176) Valdes-Aguilera, O.; Neckers, D. C. *Acc. Chem. Res.* **1989**, *22*, 171–177.

(177) Klajnert, B.; Stanisławska, L.; Bryszewska, M.; Pałecz, B. *Biochim. Biophys. Acta* **2003**, *1648*, 115–126.

(178) Lakowicz, J. R. *Principles of Fluorescence Spectroscopy*; Third Edit.; Springer: New York, NY, 2006.

(179) Archut, A.; Azzellini, G. C.; Balzani, V.; Cola, L. De; Vögtle, F. *J. Am. Chem. Soc.* **1998**, *120*, 12187–12191.

(180) Pistolis, G.; Malliaris, A.; Paleos, C. M.; Tsiourvas, D. *Langmuir* **1997**, *13*, 5870–5875.

(181) Maiti, P. K.; Çağın, T.; Lin, S.-T.; Goddard, III, W. A. *Macromolecules* **2005**, *38*, 979–991.

(182) Dougherty, C. A.; Furgal, J. C.; van Dongen, M. A.; Goodson, III, T.; Banaszak Holl, M. M.; Manono, J.; DiMaggio, S. *Chem. -A Eur. J.* **2014**, *20*, 4638–4645.

(183) Chwalek, K.; Tsurkan, M. V; Freudenberg, U.; Werner, C. *Sci. Rep.* **2014**, *4*, 4414.

(184) Chiew, G. G. Y.; Fu, A.; Perng Low, K.; Qian Luo, K. *Sci. Rep.* **2015**, *5*, 10801.

(185) Ghislin, S.; Obino, D.; Middendorp, S.; Boggetto, N.; Alcaide-Loridan, C.; Deshayes, F. *BMC Cancer* **2012**, *12*, 455.

(186) Nieman, K. M.; Kenny, H. a; Penicka, C. V; Ladanyi, A.; Buell-Gutbrod, R.; Zillhardt, M. R.; Romero, I. L.; Carey, M. S.; Mills, G. B.; Hotamisligil, G. S.; Yamada, S. D.; Peter, M. E.; Gwin, K.; Lengyel, E. *Nat. Med.* **2011**, *17*, 1498–1503.

(187) Lu, H.; Clauser, K. R.; Tam, W. L.; Fröse, J.; Ye, X.; Eaton, E. N.; Reinhardt, F.; Donnenberg, V. S.; Bhargava, R.; Carr, S. a; Weinberg, R. a. *Nat. Cell Biol.* **2014**, *16*, 1105–1117.

(188) Shen, K.; Luk, S.; Hicks, D. F.; Elman, J. S.; Bohr, S.; Iwamoto, Y.; Murray, R.; Pena, K.; Wang, F.; Seker, E.; Weissleder, R.; Yarmush, M. L.; Toner, M.; Sgroi, D.; Parekkadan, B. *Nat. Commun.* **2014**, *5*, 5662.

(189) Dura, B.; Voldman, J. *Curr. Opin. Immunol.* **2015**, *35*, 23–29.

(190) Lü, D.; Liu, X.; Gao, Y.; Huo, B.; Kang, Y.; Chen, J.; Sun, S.; Chen, L.; Luo, X.; Long, M. *PLoS One* **2013**, *8*.

(191) Wang, Z.; Wang, Y.; Farhangfar, F.; Zimmer, M.; Zhang, Y. *PLoS One* **2012**, *7*, 1–12.

(192) Ottone, C.; Krusche, B.; Whitby, A.; Clements, M.; Quadrato, G.; Pitulescu, M. E.; Adams, R. H.; Parrinello, S. *Nat. Cell Biol.* **2014**, *16*, 1045–1056.

(193) Wang, L.; Marquardt, T. *Nat. Protoc.* **2012**, *7*, 351–363.

(194) Kaji, H.; Camci-Unal, G.; Langer, R.; Khademhosseini, A. *Biochim. Biophys. Acta - Gen. Subj.* **2011**, *1810*, 239–250.

(195) Bhatia, S. N.; Balis, U. J.; Yarmush, M. L.; Toner, M. *FASEB J.* **1999**, *13*, 1883–1900.

(196) Dembele, L.; Franetich, J. F.; Lorthiois, a; Gego, a; Zeeman, a M.; Kocken, C. H.; Le Grand, R.; Dereuddre-Bosquet, N.; van Gemert, G. J.; Sauerwein, R.; Vaillant, J. C.; Hannoun, L.; Fuchter, M. J.; Diagana, T. T.; Malmquist, N. a; Scherf, a; Snounou, G.; Mazier, D. *Nat Med* **2014**, *20*, 307–312.

(197) Khetani, S. R.; Bhatia, S. N. *Nat. Biotechnol.* **2008**, *26*, 120–126.

(198) March Ng, S., Velmurugan, S., Galstian, A., Shan, J., Thomas, D., Sim, B. K. L., Mota, M. M., Hoffman, S. L., Bhatia, S. N., S. *Cell Host Microbe* **2013**, *14*, 104–115.

(199) Ploss, A.; Khetani, S. R.; Jones, C. T.; Syder, A. J.; Trehan, K.; Gaysinskaya, V. a; Mu, K.; Ritola, K.; Rice, C. M.; Bhatia, S. N. *Proc. Natl. Acad. Sci. U. S. A.* **2010**, *107*, 3141–3145.

(200) Shlomai, A.; Schwartz, R. E.; Ramanan, V.; Bhatta, A.; de Jong, Y. P.; Bhatia, S. N.; Rice, C. M. *Proc. Natl. Acad. Sci. U. S. A.* **2014**, *111*, 1–6.

(201) Bryant, S. J.; Nuttelman, C. R.; Anseth, K. S. *J. Biomater. Sci. Polym. Ed.* **2000**, *11*, 439–457.

(202) Lilly, J. L.; Romero, G.; Xu, W.; Shin, H. Y.; Berron, B. J. *Biomacromolecules* **2015**, *16*, 541–549.

(203) Karabacak, N. M.; Spuhler, P. S.; Fachin, F.; Lim, E. J.; Pai, V.; Ozkumur, E.; Martel, J. M.; Kojic, N.; Smith, K.; Chen, P.; Yang, J.; Hwang, H.; Morgan, B.; Trautwein, J.; Barber, T. a; Stott, S. L.; Maheswaran, S.; Kapur, R.; Haber, D. a; Toner, M. *Nat. Protoc.* **2014**, *9*, 694–710.

(204) Jones, K. H.; Senft, J. a. *J. Histochem. Cytochem.* **1985**, *33*, 77–79.

(205) *Immunocytochemical Methods and Protocols*; Javois, L. C., Ed.; 2nd ed.; Humana Press: Totowa, NJ, 1999.

(206) Thomas, S. W.; Joly, G. D.; Swager, T. M. *Chem. Rev.* **2007**, *107*, 1339–1386.

(207) Encinas, M. V.; Rufs, a. M.; Bertolotti, S. G.; Previtali, C. M. *Polymer (Guildf).* **2009**, *50*, 2762–2767.

(208) Fleming, G. R.; Knight, A. W. E.; Morris, J. M.; Morrison, R. J. S.; Robinson, G. W. *J. Am. Chem. Soc.* **1977**, *99*, 4306–4311.

(209) Lepoek, J. R.; Thompson, J. E.; Kruuv, J. *Biochem. Biophys. Res. Commun.* **1978**, *85*, 344–350.

(210) *Photosensitization*; Moreno, G.; Pottier, R. H.; Truscott, T. G., Eds.; Springer-Verlag Berlin Heidelberg, 1988.

(211) Davies, M. J. *Biochem. Biophys. Res. Commun.* **2003**, *305*, 761–770.

(212) Sheetz, M. P.; Koppel, D. E. *Proc. Natl. Acad. Sci. U. S. A.* **1979**, *76*, 3314–3317.

(213) Herrmann, K. S. *Microvasc. Res.* **1983**, *249*, 238–249.

(214) Mulroy, L.; Kim, J.; Wu, I.; Scharper, P.; Melki, S. a.; Azar, D. T.; Redmond, R. W.; Kochevar, I. E. *Investig. Ophthalmol. Vis. Sci.* **2000**, *41*, 3335–3340.

(215) Chan, B. P.; Kochevar, I. E.; Redmond, R. W. *J. Surg. Res.* **2002**, *108*, 77–84.

(216) Chan, B. P.; Amann, C.; Yaroslavsky, A. N.; Title, C.; Smink, D.; Zarins, B.; Kochevar, I. E.; Redmond, R. W. *J. Surg. Res.* **2005**, *124*, 274–279.

(217) Johnson, T. S.; O'Neill, A. C.; Motarjem, P. M.; Amann, C.; Nguyen, T.; Randolph, M. a.; Winograd, J. M.; Kochevar, I. E.; Redmond, R. W. *J. Surg. Res.* **2007**, *143*, 224–229.

(218) Eri Verter, E.; Gisel, T. E.; Yang, P.; Johnson, A. J.; Redmond, R. W.; Kochevar, I. E. *Investig. Ophthalmol. Vis. Sci.* **2011**, *52*, 9470–9477.

(219) Dubbelman, T. M. A. R.; De Goeig, A. F. P. M.; van Steveninck, J. *Biochim. Biophys. Acta* **1978**, *511*, 141–151.

(220) Verweij, H.; van Steveninck, J. *Photochem. Photobiol.* **1982**, *35*, 265–267.

(221) Lee, J. K.; Sikes, H. D. *Macromol. Rapid Commun.* **2014**, *35*, 981–986.

(222) Zhao, J.; Wu, W.; Sun, J.; Guo, S. *Chem. Soc. Rev.* **2013**, *42*, 5323–5351.

(223) Oster, G. *Nature* **1954**, *173*, 300–301.

(224) Kim, D.; Stansbury, J. W. *J. Polym. Sci. Part A Polym. Chem.* **2009**, *47*, 887–898.

(225) Fouassier, J. P.; Lalevée, J. *RSC Adv.* **2012**, *2*, 2621–2629.

(226) Popielarz, R.; Vogt, O. *J. Polym. Sci. Part A Polym. Chem.* **2008**, *48*, 3519–3532.

(227) Bhattacharyya, D.; Senecal, K.; Marek, P.; Senecal, A.; Gleason, K. K. *Adv. Funct. Mater.* **2011**, *21*, 4328–4337.

(228) Di Carlo, D.; Irimia, D.; Tompkins, R. G.; Toner, M. *Proc. Natl. Acad. Sci. U. S. A.* **2007**, *104*, 18892–18897.

(229) Godin, M.; Bryan, A. K.; Burg, T. P.; Babcock, K.; Manalis, S. R. *Appl. Phys. Lett.* **2007**, *91*, 123121.

(230) Grover, W. H.; Bryan, A. K.; Diez-Silva, M.; Suresh, S.; Higgins, J. M.; Manalis, S. R. *Proc. Natl. Acad. Sci. U. S. A.* **2011**, *108*, 10992–10996.

(231) Byun, S.; Son, S.; Amodei, D.; Cermak, N.; Shaw, J.; Kang, J. H.; Hecht, V. C.; Winslow, M. M.; Jacks, T.; Mallick, P.; Manalis, S. R. *Proc. Natl. Acad. Sci. U. S. A.* **2013**, *110*, 7580–7585.

(232) Lin, X.; He, Q.; Li, J. *Chem. Soc. Rev.* **2012**, *41*, 3584.

(233) Ozkumar, E.; Shah, A. M.; Cicilliano, J. C.; Emmink, B. L.; Miyamoto, D. T.; Brachtel, E.; Yu, M.; Chen, P.; Morgan, B.; Trautwein, J.; Kimura, A.; Sengupta, S.; Stott, S. L.; Karabacak, N. M.; Barber, T. A.; Walsh, J. R.; Smith, K.; Spuhler, P. S.; Sullivan, J. P.; Lee, R. J.; Ting, D. T.; Luo, X.; Shaw, A. T.; Bardia, A.; Sequist, L. V; Louis, D. N.; Maheswaran, S.; Kapur, R.; Haber, D. A.; Toner, M. *Sci. Transl. Med.* **2013**, *5*.

(234) Nagrath, S.; Sequist, L. V; Maheswaran, S.; Bell, D. W.; Irimia, D.; Ulkus, L.; Smith, M. R.; Kwak, E. L.; Digumarthy, S.; Muzikansky, A.; Ryan, P.; Balis, U. J.; Tompkins, R. G.; Haber, D. a; Toner, M. *Nature* **2007**, *450*, 1235–1239.

(235) Stott, S. L.; Hsu, C.; Tsukrov, D. I.; Yu, M.; Miyamoto, D. T.; Waltman, B. A.; Rothenberg, S. M.; Shah, A. M.; Smas, M. E.; Korir, G. K.; Floyd, F. P.; Gilman, A. J.; Lord, J. B.; Winokur, D.; Springer, S.; Irimia, D.; Nagrath, S.; Sequist, L. V; Lee, R. J.; Isselbacher, K. J.; Maheswaran, S.; Haber, D. A.; Toner, M. *Proc. Natl. Acad. Sci. U. S. A.* **2010**, *107*, 18392–18397.

(236) Kloxin, A. M.; Kasko, A. M.; Salinas, C. N.; Anseth, K. S. *Science* **2009**, *324*, 59–63.

(237) Lambert, C.; Sarna, T.; Truscott, T. G. *J. Chem. Soc. Faraday Trans.* **1990**, *86*, 3879–3882.

(238) Seret, A.; Van de Vorst, A. *J. Phys. Chem.* **1990**, *94*, 5293–5299.

(239) Tung, C.-H.; Wu, L.-Z.; Zhang, L.-P.; Chen, B. *Acc. Chem. Res.* **2003**, *36*, 39–47.

(240) Liu, Q.; Li, Y. N.; Zhang, H. H.; Chen, B.; Tung, C. H.; Wu, L. Z. *Chem. - A Eur. J.* **2012**, *18*, 620–627.

(241) Usui, Y.; Kobayashi, E.; Kazami, A.; Sakuma, S. *Bull. Chem. Soc. Jpn.* **1980**, *53*, 2716–2720.

(242) Pemberton, D. .; Johnson, a. . *Polymer (Guildf).* **1984**, *25*, 529–535.

(243) Grossweiner, L. I.; Rodde, A. F.; Sandberg, G.; Chrysochoos, J. *Nature* **1966**, *8041*, 1154–1156.

(244) Schweitzer, C.; Schmidt, R. *Chem. Rev.* **2003**, *103*, 1685–1757.

(245) Bolann, B. J.; Henriksen, H.; Ulvik, R. J. *Biochim. Biophys. Acta* **1992**, *1156*, 27–33.

(246) Bielski, B. H. J.; Allen, A. O. *J. Phys. Chem.* **1977**, *81*, 1048–1050.

Table A 1. Photopolymerization-based signal amplification: summary of reported limits of detection and the detection method used

References	Limit of detection	Detection method
5	0.005 biotinylated oligonucleotides/μm^2 (based on amount spotted and spot diameter)	Unaided eye on biosensor
6	10 biotinylated oligonucleotides/μm^2	Microscope/CCD camera
7	60 biotinylated oligonucleotides/μm^2	Optical microscope or unaided eye
28	14 eosins/μm^2, 7 (increased VP by 10x), 2.8 eosins/μm (acrylamide)	Visible to eye
20	~17 eosin/μm^2	Stained polymer (50 uM eosin solution)
13	Same as enzymatic method for flu	Unaided eye on biosensor
17	40 initiators/μm^2 (20 nm film)	Visible (1 hr hematoxylin stain)
153	~40 initiators/μm^2	Digital camera or stereomicroscope
18	0.16 biotin-antibody/μm^2	Fluorescence (say by eye and profilometry)
22	~10 EITC nucleotides/μm^2	Visible (1 hr hematoxylin stain)
8	31 (PEGA/PEGDA) and 0.16 (acrylamide) biotinylated antibodies/μm^2	Fluorescence
19	1: 100,000 anti-NPC	Fluorescence
10	15 biotin/μm^2	By eye (stained with eosin)
166	140 protein molecules/μm^2 (BCl)	By eye (stained with eosin)
105	Fraction omo bound at 100 nM omm-0.3 (of 900)=270 oligos/μm^2 (not sure if lower concentration was tested for polymerization)	Imaged with fluorescence scanner (stained with eosin)
21	7.2 nM	By eye (phenolphthalein)
30	10^{-3} g/L (printed concentration of Bio-BSA)	Profilometry/stained with Evans Blue

Table A 2. Summary of light sources, monomer compositions, and polymer film thicknesses for implementations of photopolymerization-based signal amplification

Reference	Light source	Intensity	Duration	Monomer	Maximum polymer height (initiator density)
[5]	ultraviolet light centred around 365nm from a Blak-Ray B Series-100A lamp.	5 mW/cm^2	10 min	97 wt% hydroxyethylacrylate/ 3 wt% ethyleneglycol dimethacrylate	n/a
[6]	400–500 nm, a Novacure collimated light source	8 mW/cm^2	20 min	PEGDA	240 nm
[7]	495–650-nm [2]	10 mW/cm^2 (increased to account for nanoparticle attenuation)	30 min (for max sensitivity)	PEGDA	<250 nm
[28]	495-650 nm	260 mW/cm^2 [3]	30 min	comparison	<180 nm (PEGDA), <1420 nm (acrylamide)
[20]	532 nm, LED	~35 mW/cm^2	~2 min [4]	PEGDA/VP/TEA	~30 um (optical microscopy)
[13]	UV light centered around 365 nm from a Blak-Ray B Series-100A lamp	5 mW/cm^2	12 min	97 wt% hydroxyethylacrylate/ 3 wt% ethyleneglycol dimethacrylate	Not measured
[17]	495–650-nm (Cite Hansen, Avens, et al. 2008)	10 mW/cm^2	30 min	PEGDA	<80 nm
[153]	495-650 nm	40 mW/cm^2	30 min	comparison	<1.6 mm (spotting sa-eosin onto NC,

[2] Collimated, 495–650-nm polychromatic light from Acticure light source, in-house 350–650-nm internal interference filter and a 490-nm stopband limit filter. Avens 2008: Acticure (Exfo) high pressure mercury lamp with an in-house internal bandpass filter (350– 650 nm) and an external 490 nm longpass filter (Edmund Optics) positioned at the end of a light guide and a collimating lens

[3] Light intensity increased to 540 mW/cm^2 for RT-IR

[4] Source: http://www.biotechniques.com/multimedia/archive/00042/320_42287a.pdf

					PEGDA), <200 nm (PEGDA) and <250 nm (acrylamide) with hybridization on sfb surfaces/hydrazide oligos
[18]	495-650 nm	40 mW/cm^2	30 min	acrylamide	<10^4 nm (fig. 2a)
[22]	495-650 nm	40 mW/cm^2	30 min	acrylamide	~300 nm (610±70 eosin/μm^2)
[8]	495-650 nm	40 mW/cm^2 (30 for cells)	30 min (20 for cells)	comparison	<250 nm (?), 10 microns on cells (both acrylamide)
[19]	495-650 nm	30 mW/cm^2	20 min	PEGDA	<250 nm (based on filament resolution)
[10]	522 nm LED (InDevR)	30 mW/cm^2	<100 sec	PEGDA	<~0.6 um
[166]	522 nm LED (InDevR)	30 mW/cm^2	100 sec	PEGDA	n/a
[105]	522 nm LED (InDevR)	30 mW/cm^2	~2 min	PEGDA	n/a
[21]	522 nm LED (InDevR) inverted	30 mW/cm^2	50/90 seconds	PEGDA	n/a
[30]	collimated, 530 nm LED light (Thorlabs, Newton NJ, model M530L3)	10 mW/ cm^2	20 min	PEGDA	<200 nm (epoxy surface)

Table A 3. Summary of PEGDA-based monomer compositions

Reference	PEGDA (mM)	MDEA/TEA (mM)	VP (mM)	Eosin (μM)
[6]	25 w% (435)	225 MDEA	37	0
[7]	434	225 MDEA	37 (pH 9)	0
[28]-standard formulation	22% (382.8, although later say 420)	210 MDEA	35 (pH 9)	-
[20]		TEA		
[17]-cite Hansen 2008	434	225 MDEA	37 (pH 9)	0
[153]	434	225 MDEA	37	0
[8]	1 wt% PEGDA, 21 wt% PEGA (620.5 mM) (100 nm	210 MDEA	35	0

	yellow/green nanoparticles)			
19	420	210 MDEA	35	0
10	200	150 (TEA)	100	0.3-0.7
166	200	150 (TEA)	100	0.5
105	200	150 (TEA)	100	Not specified
21	200	150 (TEA)	100	0.35 (and 1.6 mM phenolphthalein, pH 7.9)
30	25 wt% (435)	21 (TEA)	35	0

Table A 4. Summary of Acrylamide-based monomer compositions

Reference	Bisacrylamide	Acrylamide	MDEA/TEA	VP
28	130 mM	5.2 M	210 mM MDEA	35 mM
153	126 mM	5.2 M	225 mM MDEA	37 mM
18		40 wt% (5 mol% is N,N-methylenebisacrylamide)	210 mM MDEA	35 mM
22	126 mM	5.2 M	218 mM MDEA	36 mM
8	2 wt% crosslinker (130 mM)	5.2 M (20 nm yellow/green nanoparticles)	210 mM MDEA	35 mM

Table A 5. Summary of xanthene dye reactions reported in literature

Reaction	Rate constant	Reference/notes
$E^{\cdot-}$	$t_{1/2}=.35$ ms, $k=\ln(2)/t=1980$ s^{-1}	[121] Mills et al says there is 98% recovery of ground state by decay
$E^{\cdot+}$	$t_{1/2}=.6$ ms, $k=1155$ s^{-1}	[121]
E^{3*}	$t_{1/2}=.08$ ms *decay constant of 2000 thought to be less accurate than Kasche, $k=8664$ s^{-1}	[121]
$E^{\cdot-}$ (1st order relaxation)	9×10^2 s^{-1}	[132] cited by Fouassier 1991a, p.251
$E^{\cdot-}$ (2nd order relaxation)	8.7×10^8 $M^{-1}s^{-1}$	[132] cited by Fouassier
$E^{\cdot+}$ (2nd order relaxation)	8.8×10^7 $M^{-1}s^{-1}$	[132] cited by Fouassier
$E^{\cdot-}$ (decay)	6.5×10^3	[97] (half-life=30 µs)
$E^{\cdot+}$ (decay)		[97] (half-life=170 µs)
$RB^{\cdot-}$ (decay)	2×10^4 $M^{-1}s^{-1}$	[237] Rose Bengal (PBS)
$E^{3*} \xrightarrow{k_{deact}} E$	6×10^3 s^{-1}	[132]

Reaction	Value	Reference / Notes
$E^{3*} \xrightarrow{k_{deact}} E$	420 s^{-1}	113
$E^{3*} \xrightarrow{k_{deact}} E$	540 s^{-1}	110
$E^{3*} \xrightarrow{k_{deact}} E$	550/540 s^{-1}	133 (pH 8/11)
$E^{1*} \xrightarrow{k_{relax}} E + heat$	4.4x10^8 s^{-1}	113
$E^{1*} \xrightarrow{k_{relax}} E + light$	1.3x10^8 s^{-1}	113
$E^{1*} \xrightarrow{k_{relax}} E \ (+h\nu)$	$\le$ 1.05 x10^8 s^{-1}	131 water
$E^{1*} \xrightarrow{k_{isc}} E^{3*}$	5.8x10^7 s^{-1}	113
$E^{1*} \xrightarrow{k_{isc}} E^{3*}$	(8.4$\pm$0.8) x10^8 s^{-1}	131 water
$E^{1*} \xrightarrow{k_{isc}} E^{3*}$	10^8	97
$E^{3*} + E^{3*} \xrightarrow{k_{tt}} E^{3*} + E$	1.2x10^9 /9.8x10^8 M^{-1}s^{-1}	133 (pH 8/11)
$E^{3*} + E^{3*} \xrightarrow{k_{tt}} E^{3*} + E$	1.1x10^9 M^{-1}s^{-1}	110
$E^{3*} + E^{3*} \xrightarrow{k_{tt'}} E^{\cdot-} + E^{\cdot+}$	1.2x10^8 /1.3x10^8 M^{-1}s^{-1}	133 (pH 8/11)
$E^{3*} + E^{3*} \xrightarrow{k_{tt'}} E^{\cdot-} + E^{\cdot+}$	8x10^8 M^{-1}s^{-1}	132 rate constant summed with that for TT -> 2E
$E^{3*} + E^{3*} \xrightarrow{k_{tt'}} E^{\cdot-} + E^{\cdot+}$	1x10^8 M^{-1}s^{-1}	110
$E^{3*} \xrightarrow{k_{tt'}} E^{\cdot-} + E^{\cdot+}$	<3x10^4	97
$E^{3*} + E^{3*} \xrightarrow{k_{tg'}} 2E$	2k=2.4x10^9 M^{-1}s^{-1}	113
$E^{3*} + E^{3*} \rightarrow E + E$	1.9x10^9 M^{-1}s^{-1}	134 Nonradiative decay of triplet
$E^{3*} + E^{3*}$	1.1x10^9 M^{-1}s^{-1}	238
$RB^{3*} + RB^{3*}$	1.5x10^9 M^{-1}s^{-1}	238
$E^{3*} + E \xrightarrow{k_{tg}} E^{\cdot-} + E^{\cdot+}$	0.7x10^8 M^{-1}s^{-1}	110 Fisher et al. say that Kasche indicates this reaction accounts for 20% of triplet/triplet
$E^{3*} + E \xrightarrow{k_{tg}} E^{\cdot-} + E^{\cdot+}$	7.3x10^7 /7.1x10^7 M^{-1}s^{-1}	133 (pH 8/11)
$E^{3*} + E \xrightarrow{k} E^{\cdot-} + E^{\cdot+}$	8x10^8 M^{-1}s^{-1}	132 rate constant summed with T+E->2E
$E^{3*} + E \xrightarrow{k_{tg'}} 2E$	3x10^8 M^{-1}s^{-1}	110

Reaction	Rate	Reference/Notes
$E^{3*} + E \xrightarrow{k_{tg'}} 2E$	3.3×10^8 /7.9×10^8 $M^{-1}s^{-1}$	[133] (pH 8/11)
$E^{3*} + E$	4×10^8 $M^{-1}s^{-1}$	[121]
$RB^{3*} + RB$	7.6×10^8 $M^{-1}s^{-1}$	[103]
$E^{\cdot-} + E^{\cdot+} \xrightarrow{k_{rd}} 2E$	0.75×10^3 $M^{-1}s^{-1}$	[135] ethanol
$E^{\cdot-} + E^{\cdot+} \xrightarrow{k_{rd}} 2E$	8.8×10^7 $M^{-1}s^{-1}$	[132]
$E^{\cdot-} + E^{\cdot+} \xrightarrow{k_{rt}} 2E$	$8\times10^8 M^{-1}s^{-1}$	[120] aqueous pH 8.5
$F^{3*} + F^{\cdot-} \xrightarrow{k} F^{\cdot-} + F$	$k_6+k_7=1\times10^9$ $M^{-1}s^{-1}$	[136]fluorescein
$F^{3*} + F^{\cdot+} \xrightarrow{k} F + F^{\cdot+}$		[136]fluorescein
$E^{\cdot-} + E^{\cdot-} \xrightarrow{krr} E + EH_2$	$2.1\times10^6 M^{-1}s^{-1}$	[120] aqueous pH 8.5
$E^{\cdot+} + E^{\cdot+} \xrightarrow{krr} P$	$1\times10^8 M^{-1}s^{-1}$	[120] say P could be dimer
$RB^{3*} + O_2(\,^3\Sigma_g^-)$	1.6×10^9 $M^{-1}s^{-1}$	[103] all oxygen quenching reactions (20% superoxide and singlet o2)
$E^{3*} + O_2(\,^3\Sigma_g^-)$	1.1×10^9 $M^{-1}s^{-1}$	[97]
$E^{3*} + O_2(\,^3\Sigma_g^-) \xrightarrow{k_{et}} E^{\cdot+} + O_2^{\cdot-}(\ \xrightarrow{k_{ET}} E + O_2(\,^1\Delta_g))$	1.1×10^9 $M^{-1}s^{-1}$	[127] ethanol
$E^{3*} + O_2(\,^3\Sigma_g^-) \xrightarrow{k_{ET}} E + O_2(\,^1\Delta_g)$	1×10^9 /$1.8\times10^9 M^{-1}s^{-1}$	[133] (pH 8/11)
$E^{3*} + O_2(\,^3\Sigma_g^-) \xrightarrow{k_{ET}} E + O_2(\,^1\Delta_g)$	7×10^8 $M^{-1}s^{-1}$	[99]
$E^{3*} + O_2(\,^3\Sigma_g^-) \xrightarrow{k_{ET}} E + O_2(\,^1\Delta_g)$	$(1.3-2.1)\times10^9 M^{-1}s^{-1}$	[112] aqueous, attributing all of triplet/oxygen reaction to singlet oxygen
$E^{3*} + O_2(\,^3\Sigma_g^-) \rightarrow E + O_2$	$<10^8 M^{-1}s^{-1}$	[134]
$E^{3*} + O_2(\,^3\Sigma_g^-) \rightarrow E + O_2$	1.1×10^9 $M^{-1}s^{-1}$	[138] (pH 6-8) [139]cite Kasche 1967 [140]-give value for physical and chemical quenching and cite

		Kasche
$F^{3*} + O_2(^3\Sigma_g^-)$ $\rightarrow F + O_2(^3\Sigma_g^-)$	1.56×10^9 M^{-1}s^{-1}	[136]fluorescein, specify physical quenching
$E^{3*} + O_2(^3\Sigma_g^-) \rightarrow E + O_2$	1.6×10^6 M^{-1}s^{-1}	[113] aqueous
$E^{3*} + O_2(^3\Sigma_g^-) \xrightarrow{k_{et}} E^{\cdot+} + O_2^{\cdot-}$	Low efficiency-couldn't determine	[133] (pH 8/11)
$E^{3*} + O_2(^3\Sigma_g^-) \xrightarrow{k_{et}} E^{\cdot+} + O_2^{\cdot-}$	6×10^6 M^{-1}s^{-1},$< 10^7$ M^{-1}s^{-1}	[138] (pH 6-8) [139]
$E^{3*} + O_2(^3\Sigma_g^-) \xrightarrow{k_{et}} E^{\cdot+} + O_2^{\cdot-}$	$< 10^7$ M^{-1}s^{-1}	[99]
$E^{3*} + O_2(^3\Sigma_g^-) \xrightarrow{k_{et}} E^{\cdot+} + O_2^{\cdot-}$	9.1×10^3 M^{-1}s^{-1}	[113] (aqueous) [86]
$F^{3*} + O_2(^3\Sigma_g^-) \xrightarrow{k_{et}} F^{\cdot+} + O_2^{\cdot-}$	1.4×10^8 M^{-1}s^{-1}/1×10^7	[122] fluorescein (aqueous, pH 12/2)
$F^{3*} + O_2(^3\Sigma_g^-)$ $\rightarrow F^{\cdot+} + O_2^{\cdot-}$ (or HO_2)	1.4×10^8 M^{-1}s^{-1}	[136]fluorescein
$E^{\cdot-} + O_2(^3\Sigma_g^-)$	6×10^7 M^{-1}s^{-1}	[97] (70% acetonitrile) [112]
$E^{\cdot-} + O_2 \rightarrow E + HO_2$		[120]
$E^{\cdot-} + O_2 \rightarrow E + O_2^{\cdot-}$	10^7-10^9 M^{-1}s^{-1}	[112] low at low pH (based on half life)
$E^{\cdot-} + O_2 \rightarrow E + O_2^{\cdot-}$	No rate constant reported	[99,239,240]
$E^{\cdot+} - E^{\cdot-} + O_2$ $\rightarrow E^{\cdot+} + E + O_2^{\cdot-}$	3.7×10^6 M^{-1}s^{-1}	[241]
$F^{\cdot-} + O_2 \rightarrow F + O_2^{\cdot-}$	10^8 -10^9 M^{-1}s^{-1}	[122] fluorescein (aqueous)
$RB^{\cdot-} + O_2 \rightarrow RB + O_2^{\cdot-}$	1.5×10^8 M^{-1}s^{-1}	[237] Rose Bengal (PBS)
$E^{\cdot+} + O_2(^3\Sigma_g^-)$	8×10^8 M^{-1}s^{-1}	[97] (70% acetonitrile)
$E^{\cdot+} + O_2 \rightarrow P$		[120]
$F^{\cdot+} + O_2^{\cdot-} \rightarrow F + O_2(^3\Sigma_g^-)$		[122] fluorescein
$E + O_2(^1\Delta_g)$	10^7 M^{-1}s^{-1}	[123] methanol/acetonitrile, under illumination (so unclear which species quenching)
$O_2(^1\Delta_g) + E \rightarrow O_2(^3\Sigma_g^-) + E$ (EO2)	2.7×10^7 M^{-1}s^{-1}	[141] (50% acetonitrile/water) [124123]

$O_2(^1\Delta_g) \xrightarrow{k_d} O_2(^3\Sigma_g^-)$	$4.4 \times 10^5 \, s^{-1}$	[142] water (average)
$O_2(^1\Delta_g) \rightarrow O_2(^3\Sigma_g^-)$	$5.2 \times 10^4 \, s^{-1}$	[143] DMSO
$O_2(^1\Delta_g) \rightarrow O_2(^3\Sigma_g^-)$	$3.3 \times 10^4 \, s^{-1}$	[143] acetonitrile
$O_2(^1\Delta_g) \rightarrow O_2(^3\Sigma_g^-)$	$2.4 \times 10^5 \, s^{-1}$	[141]
$E^{\cdot+} + Q \xrightarrow{k} E + Qox$	Semioxidized reduced to ground with suitable reducing agent	[133]
$E^{3*} + TEA \xrightarrow{k}$	$7.3 \times 10^7 \, M^{-1}s^{-1}$	[127] triethanolamine in water[5]
$E^{3*} + TEA \xrightarrow{k}$	$4.2 \times 10^7 \, M^{-1}s^{-1}$	[128] triethanolamine in water, pH 9.5
$E^{3*} + TEA \xrightarrow{k} E^{\cdot-} + TEA^{\cdot+}$	6×10^5	[98] p.341 triethanolamine in eythl acetate/20% methanol
$E^{1*} + TEA \xrightarrow{k}$	$3.4 \times 10^9 \, M^{-1}s^{-1}$	[128] triethanolamine in water, pH 9.5
$E^{3*} + MDEA \xrightarrow{k} E^{\cdot-} + MDEA^{\cdot+}$	$4.3 \times 10^6 \, M^{-1}s^{-1}$	[97] Table 8 of Neckers 1993
$E^{3*} + MDEA \xrightarrow{k_2} E^{\cdot-} + MDEA^{\cdot+}$	4.3×10^6	[97]
$E^{3*} + MDEA \xrightarrow{k_1} E^{\cdot-} + MDEA^{\cdot+}$	$4.2 \times 10^4 \, s^{-1}$ (how are these the units?)	[146] acetonitrile
$E^{1*} + MDEA$	$8 \times 10^8 \, M^{-1}s^{-1}$	[97] 70% acetonitrile
$E^{1*} + MDEA \xrightarrow{k_2} E^{\cdot-} + MDEA^{\cdot+}$	8×10^7	[97]
$E^{1*} + MDEA \xrightarrow{k_2} E^{\cdot-} + MDEA^{\cdot+}$	$1.4 \times 10^8 \, M^{-1}s^{-1}$	[146] acetonitrile
$E^{\cdot-} + MDEA$	$5.6 \times 10^6 \, M^{-1}s^{-1}$	[97] 70% acetonitrile (semired. not measurable)
$E^{\cdot+} + MDEA \xrightarrow{k_2} E + MDEA^{\cdot+}$	2.3×10^4	[97]

---

[5] Faster than in ethanol (also faster than with erythrosine)

Reaction	Rate constant	Reference/Notes
$EH_2 + O_2 \xrightarrow{?} EH^{\cdot} + HOO^{\cdot}$		
$EH^{\cdot} + O_2 \xrightarrow{?} E + HOO^{\cdot}$ [14824245]		
$F^{\cdot+} + F^{\cdot+} \rightarrow dimer$		Lindqvist 1960 as specified by [120]
$FH^{\cdot} + FH^{\cdot} \rightarrow FH^- + F + H^+$	$1.1 \times 10^4 M^{-1} s^{-1}$	[147]
$EH^{\cdot} + EH^{\cdot} \rightarrow EH_2 + E$		[107145]
$E^{3*} + AM \xrightarrow{k} E^{\cdot-} + AM^{\cdot+}$	1×10^{10}	[98] p.340 p-phenylene diamine
$TEA^{\cdot} + O_2 \rightarrow TEA - OO^{\cdot}$	$4.9 \times 10^9 M^{-1} s^{-1}$	[149]-tertiary amine in benzene or cyclohexane.
$E + e^-_{aq} \xrightarrow{H+} E^{\cdot-}$	$5 \times 10^9 \text{-} 6 \times 10^{10} M^{-1} s^{-1}$	[120] water
$E + OH^{\cdot} \rightarrow E^{\cdot+} + OH^-$	$1.4 \pm 0.4 \times 10^{10} M^{-1} s^{-1}$	[243 120]
$EH^{\cdot} + RH \rightarrow EH_2 + R^{\cdot}$		[107] RH=MDEA
$O_2(^1\Delta_g) + O_2^{\cdot-} \rightarrow O_2(^3\Sigma_g^-) + O_2^{\cdot-}$	$1.6 \times 10^9 M^{-1} s^{-1}$	[143] DMSO
$O_2(^1\Delta_g) + O_2^{\cdot-} \rightarrow O_2(^3\Sigma_g^-) + O_2^{\cdot-}$	$(3.6 \pm 0.1) \, 10^7 M^{-1} s^{-1}$	[144] citing Rosenthal
$O_2(^1\Delta_g) + O_2^{\cdot-} \rightarrow O_2(^3\Sigma_g^-) + O_2^{\cdot-}$	$(7 \pm 6) \times 10^9 M^{-1} s^{-1}$	[143] acetonitrile (expect some superoxide loss since not stable in this solvent)
$O_2(^1\Delta_g) + O_2(^3\Sigma_g^-)$	$9.7 \times 10^2 M^{-1} s^{-1}$	[142] water, table 15, overall rate constant [244]
$O_2(^1\Delta_g) + (C_2H_5)_3N$	$1.3 \times 10^7 M^{-1} s^{-1}$	[142] methanol, table 6
$HO_2^{\cdot} + O_2^{\cdot-} + H_2O \rightarrow O_2(^3\Sigma_g^-) + H_2O_2 + OH^-$	$9.14 \times 10^7 M^{-1} s^{-1}$	[245]
$O_2^{\cdot-} + O_2^{\cdot-} \xrightarrow{2H+} O_2(^3\Sigma_g^-) + H_2O_2$	$2 M^{-1} s^{-1} / <0.2 / <0.3$	[150,151,246]
$HO_2^{\cdot} + HO_2^{\cdot} \rightarrow O_2(^3\Sigma_g^-) + H_2O_2$	$7.6 \times 10^5 M^{-1} s^{-1}$	[150,151]
$HO_2^{\cdot} + HO_2^{\cdot} \rightarrow O_2(^3\Sigma_g^-) + H_2O_2$	$2 \times 10^6 M^{-1} s^{-1}$	[152]